Optical-Level Structural Modelling of Membrane Mirrors for Spaceborne Telescopes

by

Brett Jeffrey de Blonk

B.S., Texas A&M University (1993)
M.S., Texas A&M University (1995)

Submitted to the Department of Aeronautics and Astronautics
in partial fulfillment of the requirements for the degree of

Doctor of Philosophy

at the

MASSACHUSETTS INSTITUTE OF TECHNOLOGY

June 2003

Author .....
Department of Aeronautics and Astronautics
May 9, 2003

Certified by .....
Edward F. Crawley
Professor and Department Head of Aeronautics and Astronautics
Committee Chairman

Certified by .....
Marthinus C. van Schoor
Visiting Associate Professor of Aeronautics and Astronautics

Certified by .....
David W. Miller
Associate Professor of Aeronautics and Astronautics

Certified by .....
Jesse A. Leitner
Distributed Space Systems Lead Engineer
NASA Goddard Spaceflight Center

Accepted by .....
Edward M. Greitzer
H.N. Slater Professor of Aeronautics and Astronautics
Chair, Committee on Graduate Students

Optical-Level Structural Modelling of Membrane Mirrors for Spaceborne Telescopes

by

Brett Jeffrey de Blonk

Submitted to the Department of Aeronautics and Astronautics
on May 9, 2003, in partial fulfillment of the
requirements for the degree of
Doctor of Philosophy

Abstract

The astronomy and Earth observation communities desire ever-larger space telescopes, but launch costs limit mass and technology limits size. Current research in large aperture mirrors largely supports deployed rigid optics, but efforts have already begun to develop technology that offers the possibility of a mass-optimal approach: a reflecting surface tens of microns thick over tens of meters in diameter. The manufacturing of membranes has advanced such that the community is just beginning to produce membranes with sufficient quality for optics, but the analysis of membranes is conducted with various models without verification of accuracy. Accurate structural modelling tools are required to create valid operational concepts, specify manufacturing tolerances, and define structural control needs. In the current work the accuracy of different membrane modelling tools is defined and quantified over a range of representative problems. Torsion-free, axisymmetric statics models are considered as a first step toward understanding three-dimensional dynamic behavior.

An inverse solver is developed through a new approach to the geometrically-exact model, with initial and final shapes as model inputs and load distribution as output. The current approach opens the possibility of manufacturing-driven initial shapes and performance-driven final shapes. The inverse solver is used to establish a series of benchmark problems with geometries traceable to doubly-curved telescope mirrors. Finite difference solutions to the benchmark problems lead to relationships between geometry, load, and model error; in the correlation with model error, geometry and load limits for optical-quality predictions are established for a set of models. Model error is defined according to a metric significant to optics, the area-averaged standard deviation of the pathlength error created from the inexact shape prediction. Hookean constitutive law is exactly derived for curved membranes, and constitutive relations from the literature are demonstrated to be inconsistent and contain more error than simpler, consistently-derived relations. Numerical considerations, from level of discretization to endpoint handling, are also discussed for high-accuracy solutions. The model error limits, constitutive relation derivations, and numerical-implementation considerations are combined into a guideline for modelling the optical-level structural behavior of curved membrane mirrors.

Thesis committee chairman: Edward F. Crawley
Title: Professor and Department Head of Aeronautics and Astronautics

Acknowledgments

First off is the administrative staff at MIT. They all worked very hard to find a good path through all of the unique challenges my degree program posed. Sharon-Leah Brown kept the inner workings of the Space Systems Laboratory going, and she provided manby levels of support to those of us students — known affectionately as her "kids." Kathi Cofield and Marilyn Good were stand-outs as assistants to Ed Crawley. They supported my tremendously from their front-line position in building 33, and my gratitude is extensive. The graduate administrators in the Aero/ Astro department were all I could hope for, and I got through this process with the unwavering support of Marie Stuppard. Mary Murray, too, helped make sure that I have stayed enrolled while my finances were being arranged.

Second are the students and faculty I met during my time in Cambridge. Getting to know the students was the single most important professional aspect of attending MIT. Of particular help and encouragement through the thesis ordeal were Michel Ingham (thanks for the defense help, Mitch!), Sean Kenny, Greg Mallory, and Homero Gutierrez, and many others probably should be mentioned. I also appreciate the support I received from various faculty in the department as I struggled at times with the thesis. I thank Ed Crawley for his show of support at a few critical moments. A very special thanks goes out to Tienie van Schoor for his tireless patience and encouragement in the last couple of years. The folks working for him at Midé Technology have been great to me, too.

Third are my co-workers at the Air Force Research Laboratory. From the early days with Bob Vondra and Mike Powers, the middle years with Jesse Leitner, and the later years with Robbie Robertson, Scott Erwin, and the rest of the branch, the lab has been very supportive and encouraging. Thanks, guys!

The best prize from my time in Boston is my fabulous bride, Karen, who has shown significant understanding and support to me through these years. My parents, Don and Gail de Blonk, have given me their love and have shown support in all the ways they could conceive, and I love them for that. My in-laws, Karnig and Carol Boyajian, have been very supportive and deserve recognition as well. Lastly I must recognize my friends and family, who have been patient these last several years while I have devoted myself rather exclusively to Karen and this thesis.

Thanks, y'all!

Contents

List of Figures

List of Tables

Nomenclature

Abbreviations

A-A	Area-Averaged
AMS	Axisymmetric Membrane Shell (model)
AEMS	Axisymmetric Exact Membrane Shell (model)
AILD	Axisymmetric Improved Large membrane Deflection (model)
ALD	Axisymmetric Large membrane Deflection (model)
ASD	Axisymmetric Small membrane Deflection (model)
BC	Boundary Condition
CFRP	Carbon-Fiber-Reinforced Plastic
EMS	Exact Membrane Shell (model)
ES	Exact Shell (model)
HST	Hubble Space Telescope
IR	Infrared (wavelength of light)
JWST	James Webb Space Telescope
LALD	Linearized Axisymmetric Large membrane Deflection (model)
N/A	Not applicable
NGST	Next-Generation Space Telescope (former name of "James Webb Space Telescope")
RMS	Root Mean Square (usually weighted by area)
ROC	Radius of Curvature
RSS	Root Sum Square (usually weighted by area)
STD	Standard Deviation (usually weighted by area)
ULE	Ultra-Low Expansion (glass)
3–D	Three-dimensional

Variables and Symbols

A	Area
BW	Beamwalk (the vector error remaining when ΔL is removed from the pointwise wavefront error; also the component of the pointwise vector wavefront error perpendicular to the direction of travel of the wavefront from the reference surface)
D	Diameter
$e_{\alpha\beta}$	Finite "Lagrangian" strain tensor
$\hat{\mathbf{e}}_n$	Unit vector in the normal direction
E	Elastic modulus
$f(x)$	Function f evaluated at value x
$f[k]$	Function f evaluated at k^{th} discrete point
F_{iJ}	Deformation gradient
$\mathbf{G}, \mathbf{g}$	Deformation gradient tensor for undeformed and deformed geometries, respectively
h_0, h	Undeformed and deformed thickness, respectively
ΔL	Change in pathlength (the component of the pointwise vector wavefront error in the direction of travel of the wavefront from the reference surface)
$\mathbf{M}, \mathbf{m}$	Vector representing mirror surface point-wise for reference and actual surfaces, respectively.
$\hat{\mathbf{N}}, \hat{\mathbf{n}}$	Unit normal vector in undeformed and deformed basis, respectively
$N_{\alpha\beta}, n_{\alpha\beta}$	Stress resultant in undeformed and deformed bases
$N^{(x)}_{\alpha\beta}$	Stress resultant of type "x"
p	Pressure reckoned with respect to the deformed basis
$\mathbf{P}, \mathbf{p}$	Integrated (resultant) force in undeformed and deformed basis, respectively
R, r	Radial position in the undeformed and deformed bases
R_α	Radius of curvature in α direction
q	Slope parameter
s_0, s	Arc length on undeformed and deformed boundary, respectively
u_i	Displacement in coordinate direction i

w	Displacement in axial or z-coordinate direction
Δw_r, Δw_z	Radial and piston (axial) components of the pointwise vector wavefront error
$\mathbf{WF}, \mathbf{wf}$	Vector representing wavefront surface point-wise for reference and actual surfaces, respectively
z	Axial Position
$Z_{[\cdot]}$	Performance metric based upon variable $(\cdot)$
α	Angle of surface with respect to $r-\theta$ plane for the actual mirror surface at point P
α_0, α_1	Angle of surface with respect to $r-\theta$ plane for the reference mirror surface at points P_0 and P_1
Δ	Differential error quantity
ϵ_α	Principal engineering strain in the coordinate direction α
κ	Curvature
ρ_0, ρ	Density for undeformed and deformed body, respectively
ρ_0^*, ρ^*	Area density for undeformed and deformed body, respectively
Ω_0, Ω	Area over which stress resultants act on the undeformed and deformed bodies

Subscripts and Superscripts

$(\cdot)_A$, $(\cdot)_{WF}$	Quantity of reference-mirror or reference-wavefront surface, respectively
$(\cdot)_0$	Quantity referenced to initial or "naught" configuration
$(\cdot)_I$, $(\cdot)_A$	Vector component in undeformed basis
$(\cdot)_i$, $(\cdot)_\alpha$	Vector component in deformed basis
$(\cdot)_{sph}$	Quantity referenced to spherical geometry or case
$(\cdot)^{(C)}$	Cauchy-type stress variable (used mostly for stress resultant)
$(\cdot)^{(1PK)}$	1^{st}-Piola-Kirchoff-type stress variable (used mostly for stress resultant)
$(\cdot)^{(2PK)}$	2^{nd}-Piola-Kirchoff-type stress variable (used mostly for stress resultant)
$\bar{(\cdot)}$	Over-bar indicates non-dimensional variable
$(\cdot)^A, (\cdot)^B$	Quantity associated with boundary cases (A) and (B)

Chapter 1

Introduction

Objective of Chapter:

1. To introduce and motivate the use of true membranes as primary mirrors for spaceborne telescopes;
2. To survey the literature relevant to the structural design of membrane primary mirrors; and
3. To provide an overview of the current work.

1.1 Motivation

The astronomy and Earth-observation communities both desire ever-increasing diameters for space telescopes because the diffraction-limited angular resolution of a telescope is directly related to the aperture diameter. Large telescopes also have a functional advantage; image-taking of ground targets by large telescopes in geostationary orbits, for example, could outperform smaller, similar-resolution telescopes in lower orbits by drastically decreasing the time required to revisit targets in a region of high interest. While the desired aperture size is increasing, the diameter of launch vehicle payload shrouds is not increasing. In order to achieve goals of low launch mass and large diameter, low-density telescope structures with high deployment ratios are required.

The combination of increasing aperture size and limited launch dimensions — both mass and volume — pushes the designs in the direction of minimum-mass and minimum-density telescope construction. In addition, launch costs constitute a significant fraction of the total cost of a spacecraft, and so using the smallest possible launch vehicle is considered desirable. For a reflector telescope this minimum-mass design apparently consists of a layer of material just thick enough to reflect the science wavelength and as little other mass as possible. Such a thin mirror exhibits such small bending stiffness that the mirror behaves as a true membrane over large diameters. Current membrane mirror concepts involve a low-density, high-quality plastic substrate membrane coated with a thin layer of reflecting metal.

During the time that telescopes have been used on-orbit, the designs have become progressively larger and less dense. Currently the $2.4m$ mirror of the NASA Hubble Space Telescope (HST) is the largest mirror on orbit, and the $6m$ James Webb Space Telescope (JWST)[1] is scheduled for launch during the next decade. While the HST represents a single large glass mirror whose size was restricted by launch vehicle dimensions and payload mass, the JWST mirror will consist of segments deployed and placed into correct figure[2] once on orbit. The area density of the JWST mirror will be an order of magnitude lower than the HST mirror, and future mirror systems are projected to continue this trend of decreasing density. Deployed optics technology can be found widely in the literature from the NASA-JPL Precision Segmented Reflector concept of the 1980s [63] to the JWST currently under development. The JWST will face problems of meter-scale deployment distances in combination with final distributed sub-micron operational tolerances. The structural control technology dveloped for JWST, specifically the phasing of lightweight mirror segments in zero-gravity, represents the next step in the development process for large, lightweight space telescopes.

A common measure for the mass performance of a telescope is the mass per area, or area density. Figure 1.1 presents a comparison of technologies in terms of telescope aperture diameter D and area density ρ^*. The upper left region of the plot represents systems in operation, the middle represents the current development for the JWST, and the lower

[1]Prior to 2002, the JWST was known as the Next Generation Space Telescope (NGST).

[2]In optics "figure" refers to the designed shape or figure. "Figuring" thus refers to the act of achieving the prescribed overall shape of the reflector.

right region represents future true-membrane mirrors. The current state-of-the-practice technology is represented by the Hubble Space Telescope, the current state-of-the-art by the JWST technology, and that projected by the polyimide membranes. Constant mass lines —indications of the launch vehicle requirement— are added to the plot by choosing mirror mass M in the following relation.

$$\begin{aligned} \rho^* &\equiv \frac{[\text{mass}]}{[\text{area}]} \\ &= \frac{4}{\pi D^2}[\text{mass}] \end{aligned}$$

With the constant-mass line that includes the HST down to the area density of a carbon-fiber-reinforced-plastic (CFRP) mirror, a $20m$ CFRP mirror would be feasible for the (large) HST launch mass. The plot also indicates that a telescope mirror built from the polyimide membranes will be an order of magnitude less massive than HST and yet an order of magnitude larger in diameter. A very important note about this argument is that consideration of dynamics has been omitted. While the lines of constant mass in Figure 1.1 are inversely related to diameter ($\propto \frac{1}{D^2}$), the lines of constant fundamental frequency have a direct relationship ($\propto D^4$) for the approximation of flat-plate dynamic behavior .

A "true membrane" mirror is defined as a sheet of material that is thin enough that the stretching response to loading dominates the bending response [31]. For most optical and infrared telescope applications, the performance criterion is that the total spatial and temporal RMS perturbation of the wavefront at the sensor be less than $\frac{1}{10}$ the science wavelength, approximately 0.4–4μm for the visible through the mid-wave IR. Telescopes with other science wavelengths are of interest to the scientific community but will not be emphasized here. Newer technologies such as holographic correction may relax this requirement upon the primary mirror shape by transferring the difficult problem of final shaping of the wavefront into a later element in the sequence of telescope optics [26]. *The structural control challenge is to place a membrane mirror with tens of microns thickness and tens of meters in dimension into the space environment with a sub-micron or micron level shape requirement.*

The use of a membrane reflector represents the apparent mass-optimal solution for space telescope mirrors, but insufficient analysis on membrane mirror implementation has been performed to fully verify this notion and predict the cost-optimal solution. True-membrane

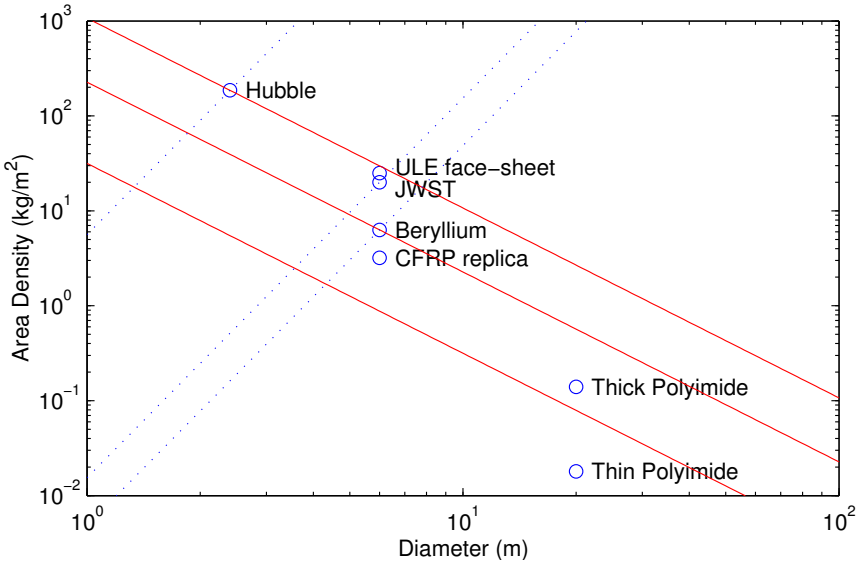

Figure 1.1: Technology comparison according to area density ρ^* and aperture diameter D. Solid constant-mass lines are added along with dashed constant-plate-frequency lines for each technology group. The group of $6m$-deployed-optics technology includes carbon-fiber-reinforced-plastic (CFRP) and ultra-low-expansion (ULE) glass.

mirrors consist of plastic film structures coated with a microns-thick layer of reflecting metal. The membrane mirror contributes the minimum amount of primary reflector mass, but the more important factor, the total system mass, also depends upon currently undefined control system and support structure needs. The membrane mirrors may also represent a cost-optimal solution. The glass mirrors used in current telescopes require an extensive polishing process that can literally last years for large diameters. Because the membranes utilize a different manufacturing technique, the inherent high cost of polishing may be eliminated. Thus the potential benefit of membrane mirrors is great. Since the use of membrane mirrors as primary telescope optics is only partly understood for space applications, the technology must be further developed in order to define the capabilities and limitations of the concept.

In addition to the static positioning difficulty, the dynamic response appears to present an engineering challenge. The membrane mirror is expected to be dense with dynamic modes in the sense that a drumhead membrane is more modally dense than a flat plate. The low stiffness of the membrane is expected to lead to a very sensitive response to disturbances. Any method to attenuate the disturbances will certainly add mass to the mirror, but mass

additions required to create a true-membrane primary mirror system need to be understood.

The use of membranes as telescope primary mirrors requires advancements in the structures-related fields of membrane manufacturing, structural dynamics and control, and precision mechanical modelling. *The goal of this thesis is to characterize the accuracy of structural modelling tools used to analyze and design membrane mirrors for spaceborne telescopes such that the static behavior, dynamic behavior, and the the systems design can be better understood.*

1.2 Literature Review

The literature provides insight in the history of membranes in space and enables an assessment of the state of the technology. This assessment is used to identify open issues for study and research.

1.2.1 History and State of the Technology

The history of membrane spacecraft components began with the inflated Echo spacecraft, one of NASA's first satellites [31]. After a long hiatus the interest in membranes for spacecraft has resurfaced under the moniker "Gossamer Technology". NASA currently funds a wide array of projects that support technology development for future large-area, low density spacecraft, including solar sails, antennas, solar concentrators, and optical telescopes [38]. Mikulas and Thomson [62] provide an assessment of the current state of the art in spacecraft structures, including a section on membranes. Gas-inflated structures have received the bulk of research attention in gossamer structures, and Satter and Freeland [75] provide an overview of challenges facing inflated structures.

The state of research into large membrane structures is best characterized as significant component technology development without significant unifying, definitive systems design. The system design to which most references are made is one particular on-orbit technology demonstration mission by NASA. The Inflatable Antenna Experiment, deployed from the space shuttle in 1996 [21], consisted of a $14m$ inflated antenna surface with inflated support structure. While not fully successful in its inflation, this experiment showed that large inflated structures can be deployed in the space environment and generated much interest in the space structures community. Another notable mention for systems work is the

Table 1.1: Technology readiness for many reflector systems, measured as the maximum diameter tested.

Category	Technology Demonstration	Component Tests	Space-Ready	Flown in Space
Mesh Antennas	$> 35m$	$> 35m$	$35m$	$35m$
Inflated Antennas and Solar Reflectors	$\sim 15m$	$\sim 15m$	$\sim 15m$	$14m$
Continuous Glass/ Stiff Mirror	$10m$	$10m$	$2.4m$	$2.4m$
Segmented Glass/ Stiff Mirror	$8m$	$6m$	—	—
Membrane Mirror	$\sim 1m$	0.1–0.5m	—	—

component-based whole-spacecraft design work of Robertson [72]; in that work the mass of the support structure and figure control subsystems are identified as having the most significant contributions to system mass, though the assumptions on the figure control system are rather uncertain.

Table 1.1 summarizes the technology readiness of several classes of optical and radio frequency reflectors. Mesh antennas have achieved the large sizes desired for optics, but the construction methods have surface-accuracy limits well above optical tolerances. Solar concentrator work feeds directly into optical reflector technology, but the tolerances are again far larger than those of optical telescopes. Continuous mirrors with $8m$ diameters have been spin-cast for terrestrial telescopes, and segmented-glass technology will be the next generation of large space telescopes. Membrane mirrors have had limited-diameter yet technically significant demonstrations to date.

The plausibility of using a membrane mirror surface has been investigated at the Air Force Research Laboratory (AFRL), and the results indicate that a useful mirror can be repeatedly and reliably figured from a membrane [56, 57, 58]. In these Air Force studies a circular membrane is mounted to an optically-polished ring and then figured using gas pressure and axisymmetric tension. The high shape quality of the ring greatly reduces shape errors that propagate toward the mirror center. The error between the achieved shape and the desired paraboloid is shown to be in the hundreds of wavelengths – not a final solution, but measured progress nonetheless.

The development path of the leading companies is to pursue inflated antennas [14, 12] as a first application of gossamer technology, but gas inflation does not appear to be a

viable concept for spaceborne mirrors; the conflict centers around whether the transmissive membrane that inflates opposite the mirror membrane will cause significant refractive errors in the wavefront. Carreras [13] indicates that an inflated mirror will not work as an optical surface because the clear lenticular surface will certainly introduce significant and complicated phase errors in the resulting wavefront. The same technology that produces high-quality reflectors also produces high-quality lenticular canopies, however, and so the path forward is not clear.

The deflection response of membranes to pressure loading has been studied by many groups over the last hundred years. Of most interest to the spacecraft community are the numerical PDE solutions of Mikulas [23] and the finite element results of Palisoc and Huang [69]. Membrane structures with much less accuracy than optical dimensions have been inflated in Earth orbit, and the concomitant analysis shows the capability to predict mechanical response and design the initial shapes according to desired performance [21, 25, 27, 68].

The nonlinear complication of membrane dynamic behavior arises from the product of in-plane tensile loads and curvature in the governing differential equation. Finite element procedures for including these tension effects on the structural dynamic behavior have been published in the study of civil engineering structures [79] and space structures [18]. Long inflated members have been shown to exhibit beam behavior in the absence of wrinkling [54], and predicting the modal behavior of inflated beam structures has proven relatively successful [53].

1.2.2 Review by Topic

1. Model Development

   (a) Libai and Simmonds [50] include comprehensive development of shell theory, from axisymmetric shells to general membranes and general shells. The vector equations of equilibrium are derived in addition to a number of constitutive relations.

   (b) Wilkes [88] applies the asymptotic expansion method to the membrane mirror problem. Once the relative powers have been determined through a process of engineering and mathematical judgement, these assumptions flow through every

equation such that all assumptions are definitively the same order.

Another result of this work is to show that an optical coating can be used to assist in the static shape forming of the material. The optical coating stress created an initial stress condition.

2. Comparative Modelling

   (a) Jenkins and Marker [34] discuss different solution approaches and provide a comparison between the Hencky series solution and the ABAQUS quarter-symmetry FEM results.

   (b) Greschik *et al* [23] compare the performance predictions of the deformed-coordinate shell equations to the results from other modelling assumptions (Hencky series approach, use of undeformed coordinates, shallow shell approximation). Because the authors do their computations in a modular C-language framework, they are able to swap different models, constitutive laws (wrinkling, viscoelasticity, *etc.*) and make numerical comparisons between the different assumptions. By comparing a simplified pathlength-error metric from the (few assumption) deformed-coordinate-equilibrium model to metrics resulting from the other models, the authors conclude that the several sets of modelling approaches are valid for antenna applications with a $0.1mm$ area-averaged pathlength error criterion. It would appear that each assumption investigated cannot be made, however, for optical-level investigations.

3. Static Forming

   (a) Kydoniefs [43], Hart-Smith and Crisp [29], and Vaughn [84] all show solutions for the inverse problem specialized to incompressible ($\nu = 0.5$) materials. Incompressibility leads to a simplification of the governing equations, and much progress in finite elasticity has been in the area of incompressible materials [78].

   (b) Juang and Huang [39] show one set of general equations that can be used for the nonaxisymmetric shape forming problem in which the initial and final shapes are predetermined. The initial angular position is posed as a function of the final angular position, and this variable choice leads to a lengthy mixed-form governing equation even with the assumption of axisymmetry. The most significant example

solution was a sphere-to-sphere numerical solution with a rigid outer ring. This solution method is not very tractable, and the large number of terms in the governing equations does not lend itself to numerical accuracy.

4. Thickness distribution

   (a) Meinel and Meinel [59] discuss a polynomial series approach to predicting the thickness distribution needed to inflate to a paraboloid from a flat.

   (b) Vaughn [84] calculates the radial thickness distribution required of a flat axisymmetric membrane to inflate to a parabola under constant pressure. The solution is only developed for incompressible materials.

5. Use of appropriate performance metric

   (a) Peters *et al* [70] show the RMS wavefront error for axisymmetric boundary displacements. They made an excellent use of proper performance in combination with an FEM prediction (quarter-symmetry model). Inflation from flat with constant pressure.

   (b) Greschik *et al.* [25] make the case that an acceptable performance metric is the RMS of twice the magnitude of the mirror piston error.

6. Electrostatic control. While electrostatic control brings challenges to the engineering design, the possibility of applying spatially distributed, high-bandwidth control makes electrostatic control a good technology to consider.

   (a) The electrostatic control of membrane mirrors received much attention during previous large-space-structure efforts by NASA, and the encouraging results indicate that the challenges are based in engineering design rather than fundamental physics. Deflection control is achieved as an electric potential is developed between two conducting surfaces, and the charge attraction results in a transverse pressure-type loading on the surfaces. One surface is the reflecting mirror, and the other is the control electrode or back-plane.

   A good review of electrostatically controlled membrane mirrors was published by Mihora and Redmond [61]. The equations that describe the behavior of charged membranes have been explored for both the continuous [39] and discrete [85]

cases, and a finite number of unstable modes can be shown to result from this configuration [45, 47, 46]. These efforts produced a method of linear quadratic stabilizing control that was successfully demonstrated in the laboratory.

More recent efforts frame the stability problem in a new way and include a Lyapunov-method controller that places the fundamental frequency in a stable regime [41]. The tight modal spacing that is characteristic of membrane behavior consistently presents a significant spillover challenge to the control system designer.

7. Solution methods for high precision

   (a) Rogers and Agnes [74] address the problem of accurate solution methods for the membrane problem, in which smoothness in the solution is very important. A set of finite element shape functions is determined in conjunction with the perturbation method that allows perturbative bending reactions to be included in the model. The governing equations are of the large-deflection type.

1.2.3 Discussion

The following general comments can be made about the field of membrane mirrors:

- A membrane mirror telescope is viable; no physics barriers have been established for the membrane mirrors.
- A true-membrane primary mirror is an enabling technology for space telescopes with diameters beyond 10 or 20 meters.
- Literature survey concludes that static shape forming of membrane mirrors is only partially understood; dynamic behavior—in the context of precision optical reflectors—has had little treatment in the literature.
- Solutions to the large membrane deflection equations have been exhaustively examined in the literature, especially for circular membranes, but not with an emphasis on accuracy. A typical approach is to rely upon finite element methods (FEMs) to produce a "truth" solution [36, 34].

The review of the available literature reveals many open structural control issues in the use of membrane mirrors for spaceborne telescopes.

1. *Model accuracy and solution precision* are not well-characterized in the literature in the context of optical-level shape predictions of membrane mirror structural response. The need for improved modelling tools affects all subsequent items on this list.

2. *Flexibility in the rim support* for membrane mirrors. In previous experiments with a membrane for optical applications, an optically polished rim surface has been used. Only one modelling effort has been found that considers the effect of a flexible frame, and the application was a radio-frequency antenna with tolerances significantly larger than optical [10].

3. The *ability of a membrane mirror to withstand the dynamic disturbances* of a spacecraft has not been shown. The response to reaction-wheel disturbances determines the image-taking performance of the system. Of particular interest for Earth-observing spacecraft is the performance of a telescope system during and after a slew (or reorientation) maneuver.

4. A *viable deployment concept* for membrane mirrors is not well understood. Current methods involve folding yet the resulting creases are not acceptable for optical surfaces. "Viability" in this context indicates that the surface accuracy and position requirements are met after surviving handling and launch loads.

5. The *spatial frequency tolerances on membrane properties* are not well understood. That is, how large can thickness or other stiffness-related variations (also in-plane tension?) be such that the optical figure is not significantly affected? In traditional active mirrors the manufacturing requirement is well-understood since the spatial cutoff frequency is around $\frac{1}{2}$ the inverse of the actuator spacing.

6. *Material characterization* of membranes in a space-like environment is required as inputs to the models, especially to deal with creep concerns.

1.3 Philosophy

Research into the modelling and actuation of membrane primary mirrors benefits the spaceborne telescope community by an increased understanding of the impact of reflector mass restrictions upon static and dynamic structural control requirements.

1.3.1 Research Path

The research in this thesis was originally motivated by the need for the dynamics analysis of a true membrane primary mirror. The thesis goals changed in time largely because of two reasons:

1. The steady-state stress resultant distribution is required for the dynamics analysis of a loaded membrane, just as the tension in a string influences dynamic behavior. Available solutions for the static behavior of membranes were not complete and did not span the design space. The first significant change in intended research direction thus occurred as suitable steady-state solutions were pursued in more depth.

2. One of the most significant problems in the more "standard" modelling tools (series solutions to large-membrane-deflection and finite element analysis) is lack of discussion regarding accuracy and precision. The level of modelling precision, or ability of the solution to represent the governing equations, increases with model complexity for common modelling approaches (more terms or a finer spatial discretization). The accuracy of those equations, however, is often not questioned in the literature. Investigating both the accuracy and precision of the modelling created many questions and led to significant changes in research direction.

1.3.2 Approach

The goal of telescope structural analysis is to take the system performance requirements and create requirements upon manufacturing tolerances, the structural supports, and the structural control system. Static and dynamic modelling tools are used to predict the mechanical response of the system to loading. Membrane primary mirrors present the structural analyst with characteristics rather unlike other more dense, standard structures, and so research must be performed to understand the design relationships for the new gossamer reflector systems.

Figure 1.2 provides a representation of the engineering design flow for membrane mirrors in the context of structural control. Inputs are mass and optical performance criteria, static disturbance levels, actuator choices, and dynamic disturbance levels. Output is a structural control design, here limited to the "perfect sensor" or full-state-feedback case for simplicity. Lack of achieving the steady-state performance goals leads to design feedback with the

loading configuration and design. The dynamic disturbance goals feed back to the control methodology, actuator configuration, and design.

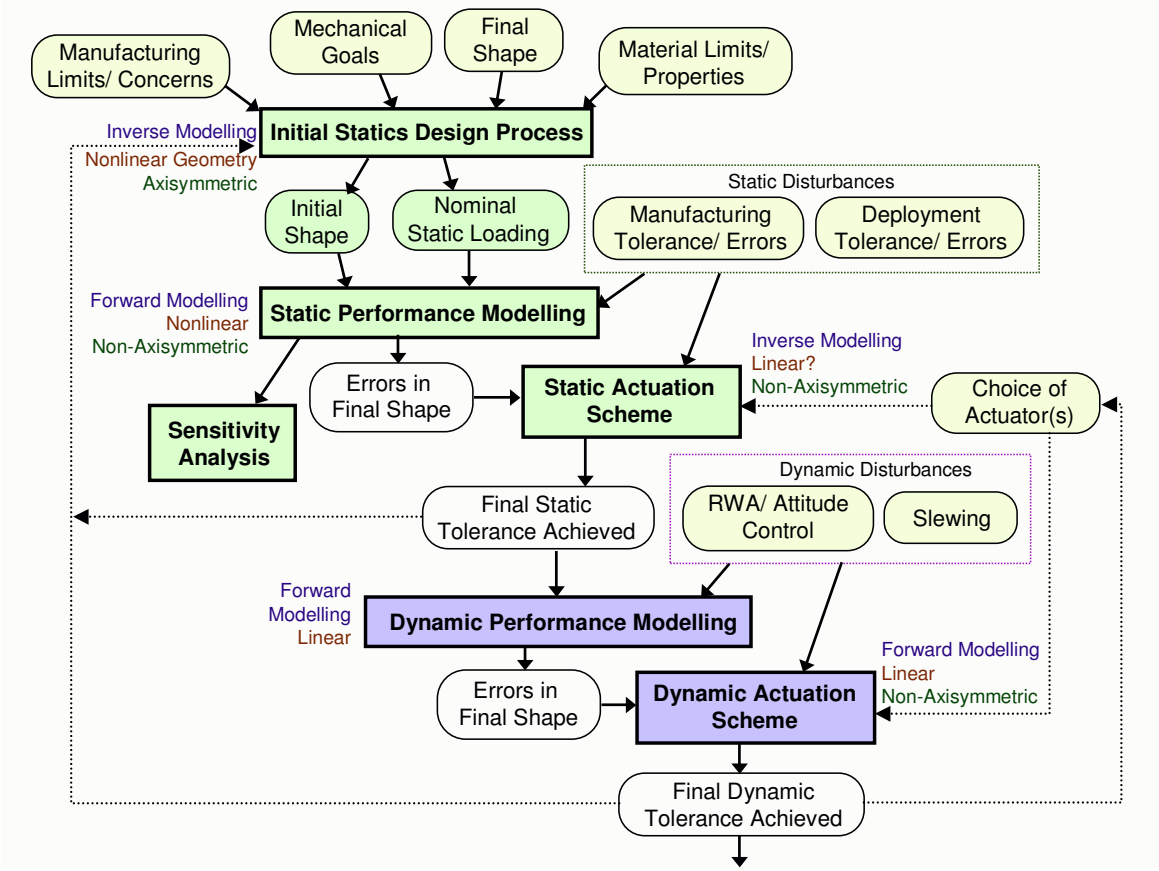

Figure 1.2: Engineering design flow for structural control of membrane mirrors. Issues relating to deployment and sensing have been omitted.

A systems approach is proposed for studying membrane mirror design and behavior. The primary mirror will both be a system in itself and a subsystem to the overall telescope. In the design and development phase of building a spaceborne telescope, the system engineer needs to understand the advantages and disadvantages of membrane mirrors for mitigating risk, optimizing performance, and reducing cost. Another critical aspect of the systems approach is gaining an understanding of how requirements upon one subsystem affect another subsystem in the context of structural control. For instance, the mass benefit of the membrane mirror may not be achievable if the mass requirements on actuators and sensors make the entire mirror system mass larger than the total mirror system mass for a

different technology.

The mass requirement limits the structure to true membranes, and the optical performance requirement specifies the precision of the operational shape. Since membranes are tension structures, the steady-state tension field influences the dynamic behavior, and so design decisions about geometry, materials, and actuation strategies affect both the static and dynamic characteristics of the membrane. Image-taking for a mirror is a steady-state process with static and dynamic disturbance rejection and drives the decisions relating to actuator and support characteristics. The models, techniques, and insight from this thesis work will be useful to future systems designers of membrane mirrors for spaceborne telescopes.

Modelling the performance of true-membrane primary mirrors can be pursued through two approaches.

- *Modelling for absolute capability.*

  The mechanics of the system need to be understood in order to understand the ultimate limitations of a membrane mirror. In terms of control, this approach is the perfect sensor/ perfect actuator problem.

- *Modelling for control.*

  The limitations of all system components are modelled inside a control design framework. Rather than compare modelling results to an abstract "exact solution," for example, the control problem uses the sensors as measurements of absolute error.

In this work the first approach is pursued because the the ultimate capability of membrane mirrors is important to understand prior to imposing the limitations of various sensor and actuator technologies.

1.4 Thesis Work

Within the design framework of Figure 1.2 is a flow of actual work tasks. These work tasks, represented in Figure 1.3, show how the different parts of the thesis are related. The circled numbers refer to thesis chapters as discussed here.

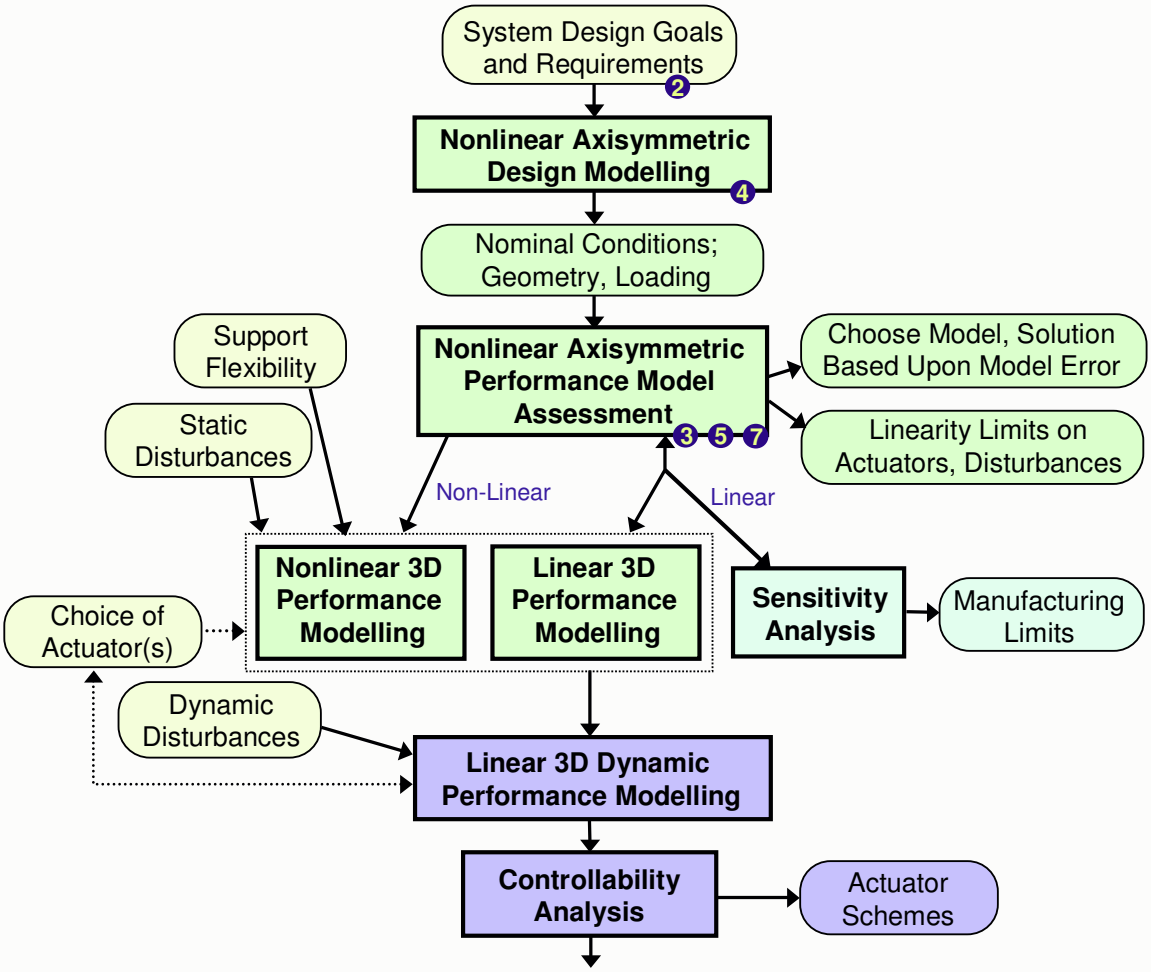

Figure 1.3: Research flow diagram for this thesis effort. The numbers indicate thesis chapters.

1.4.1 Scope

The scope of this research effort will be limited in order to concentrate on a reduced, core set of technical challenges.

- Issues specifically related to gores or seamed membranes will not be considered in this work.
- Issues related to material coatings will not be considered in this work.
- Membrane wrinkling, a significant non-linearity, will not be considered. A zero value in one of the principal stress resultants will be considered a lower limit of validity for analysis here.
- Thermal isolation is required to reduce the shape-distorting effects of thermal expansion. Electromagnetic isolation may also be required if electrostatic forces are to be used. The problem of a general thermal and electrical analysis will not be considered here.

1.4.2 Overview of Thesis and Thesis Contributions

The thesis is divided into three fundamental sections. In the first three chapters, the issues of membrane primary mirrors in spaceborne telescopes are introduced, and the model-accuracy problem is established. In the middle chapters the tools for the model accuracy assessment are developed and proven. In the last chapter the model-accuracy results are presented as the culmination of the document.

The contributions in this thesis relate to the quantification of error in the prediction of the static behavior of axisymmetric, doubly-curved membranes. A methodology is developed for quantifying the effects of membrane-mirror modelling decisions upon the static structural behavior at the optical level, and the methodology is demonstrated for the case of systems with unity focal ratio. Models from the literature are derived in a consistent framework such that the relationship between the models is understood and the exact assumptions can be correlated to shape prediction errors. The relationship between these errors and different parameters is shown and provides a method of predicting whether optical-quality predictions will be achieved for a given problem. Within the model comparison framework is a new method for an inverse problem, one in which the loading is

determined after the final shape is chosen for performance and the initial shape is chosen according to manufacturing needs. Extensions to the model-accuracy results also provide an indication of solution accuracy both for common solution methods such as finite elements and for dynamic shape predictions.

With this methodology a modelling guide is developed for the optical-quality shape prediction of membrane mirrors. In addition to the correlation of the equilibrium assumptions to the model, the guide also includes the results of an investigation into the constitutive theory and the lessons regarding numerical difficulties.

The constitutive theory is addressed through a formal mathematical approach in which changes in the reference frame are tracked exactly in the choice of variables. This new derivation provides the exact Hookean constitutive law for different strain measures and for stress resultants in different coordinate bases. The linearized model is shown to be more appropriate than a simply-justified model from the literature, which is also shown to use an inconsistent choice of variables. The use of the exact constitutive law is compared to different approximations in both the simple use of the constitutive law and application of the laws in the shape-prediction problem.

Modifications to standard numerical methods for optical modelling of membranes are identified and implemented because standard methods often add many orders of magnitude of error to the shape predictions. The modifications range from the simple (specification of the appropriate number of finite difference intervals) to the complex (lack of smoothness in the field-variable calculations near the endpoints). Each of the modifications is justified in the context of optical-level shape predictions, thereby keeping with the overall theme of the thesis.

Chapter 2

Systems-Level Design

Objective of Chapter:

To identify critical aspects of the structural system design for true-membrane primary mirrors, discuss the systems design space, and define a set of relevant boundary value problems.

In this chapter the system aspects of a spaceborne optical telescope are explored for the case of membrane primary mirrors. Engineering considerations for the structural requirements are discussed, as are the mission-critical performance metrics that provide a judgement of quality. The critical structural aspects of potential membrane mirror systems are condensed into a set of benchmark problems for use later in the thesis.

2.1 Design Specifications

Membrane primary mirrors stand approximately two generations beyond current technology, after deployed-glass and thin-shell-replica mirrors, and so the systems design has significant flexibility at this stage of technical maturity. Telescope system design is discussed here with an emphasis on the structure of the primary mirror; the requirements and technology unique to the aft optics and other individual components are left to other researchers. The primary mirror subsystem design must address a set of structures issues:

- Geometry (e.g. monolithic versus segmented),
- Mirror construction (e.g. seams),
- Deployment (e.g. segments, folds),
- Accuracy in the final shape (e.g. method of figure control), and
- Dynamic disturbance rejection.

Current research into membrane radio-frequency (RF) antennas and membrane optical reflectors, along with engineering needs, provide structural guidelines that will be common across different system concepts.

2.1.1 Desired Structural Qualities

Structures technology plays an important role for membrane mirrors because ability to maintain shape is paramount to telescope mission success. Solutions to the static shape-forming problem determine the steady-state reflector performance while the response to dynamic disturbance determines the ability to maintain that static performance. The structure will be affected by needs in the areas of optical performance, manufacturing, packaging and deployment, and mechanical state.

Optical Performance

If a large membrane mirror were to be inflated as part of a closed volume, a transparent film–the lenticular surface– would be inflated opposite the mirror. The science light would travel through this surface a minimum of two times at separate locations and angles, and maintaining an optical-quality wavefront through these transmissions would be extremely difficult [13]. A lenticular surface is therefore not desirable.

The shape of the mirror depends upon the optical prescription of the telescope, and a scan of the conferences in gossamer technology indeed reveals several different design paths. The most common primary mirror shape is parabolic, however, and so paraboloid mirrors are featured in this thesis. Other shapes tend to need special requirements placed upon other aspects of the system design. The methods used in the thesis are not limited to any one shape, however, and so other geometries could be explored in future work.

The performance of the membrane mirror is fundamentally the shape of the reflecting surface because the shape determines how an incoming wavefront is shaped and phased

at the detector. An optical prescription–the shape of each optical surface– is determined for the system according to the optical needs of the telescope mission, and the structural control system needs to minimize the error between the actual mirror surface and the mathematically-exact desired shape at all time. The science light is on the order of visible or infrared wavelengths, though, and so the mirror must maintain the correct shape to fractions of that wavelength. New wavefront-correction technology appears to be able to relax the static and dynamic wavefront requirements by about an order of magnitude but at the expense of signal intensity [58]. Shape precision is a tremendous design driver for the mirror system, and section 2.3 covers the topic of performance metrics in detail.

Manufacturing

A membrane mirror is an optical system component with large size and fine precision, and hence the manufacturing process will be non-trivial. A goal of the structural design process should be to balance the requirements between the ability to manufacture and the ability to apply loading to form a steady-state shape. For example, assumptions of constant pressure and low stress increase the difficulty of the manufacturing process because an aspheric initial shape is required. Assuming a spherical initial shape and paraboloidal final shape, however, increases the challenge for the steady-state actuator design because a radially-varying pressure-type loading is required. In order to appreciate the full design space, the design process should be opened to a variety of initial shapes so that the ability to manufacture an initial shape is considered as part of the systems design.

Large experiments to date such as the flight-tested Inflatable Antenna Experiment [21] created an approximation to an initially-curved mirror with carefully-manufactured strips or "gores" of material. The approximation of curved shapes with flat, tape-seamed gores does not, however, lead to an acceptable tolerance for optical applications [68]. Casting appears to be a feasible method for manufacturing accurate shapes [13, 59], though modern facilities for casting of glass mirrors limit precision curved shapes to about $8m$ in diameter. Moreover, no large membrane has been caste to date, and so the technical difficulties are uncertain.

Manufacturing quality is a significant concern for optical systems as well. The thickness of thin film has variations at some level in addition to discrete jumps at seams. Spatial variations in any of the material properties will lead to a corresponding spatial variation

in the response to loading. Variations in the shape of the material boundary changes the response of the material at some level. Minimum limits of quality in the spatial distribution of material and geometric properties will need to be assigned to the manufacturing process during systems design.

Thin-film coatings are commonly applied to optics to enhance the optical performance of the system. The application of a coating to a membrane can induce appreciable deformation due to residual stresses [58], and so the need for a coating must be assessed as part of a system design trade. Although the coating may increase the ultimate capability of the mirror, the coating-induced stresses may make the final shape unachievable. Recent research has shown that coatings can even be used to enhance the mechanical design [88].

Packaging and Deployment

The method of deployment is the most significant systems issue next to shape precision. The large ratio between the O($\geq 10m$) deployed mirror diameter and O($\leq 4m$) launch vehicle size combines with the O($50nm$) accuracy requirements of an IR/optical telescope to create a challenging deployment problem. Decisions about the deployment procedure affect the requirements upon actuation, structural support, and sensing, and so deployment is the most significant systems concern next to shape precision.

Stowage is an inherent part of the deployment method, and the loading of the membrane during the stowage and transportation process needs to be considered because events like folding can induce inelastic deformation and alter the membrane shape. The designers of optical and infrared systems will need to apply all the lessons learned in making inflated radio-frequency reflectors (RF antennas), such as the use of a rolling- rather than folding-type stowage scheme [12]. Cadogan *et al.* [12] directly assert the need to consider deployment as a design driver rather than an afterthought.

Decisions about deployment affect various aspects of the structural system. Rolling-type stowage may limit the allowable mirror curvature because of the loading imposed by rolling the doubly-curved surface into a singly-curved surface (*i.e.*, a paraboloid or spherical section into a cylinder). Rolling without folding also implies that the maximum dimension for a rolled optical component is limited by the launch vehicle; subapertures may be the only way to roll the mirror surfaces within this length restriction.

Mechanical State

Three factors define a loading regime of small positive principal stress resultants across the membrane:

1. *Wrinkling:* A non-positive principle stress resultant defines the wrinkled state of a membrane, and wrinkling by definition causes a large mirror shape error. A typical wrinkling scenario for an axisymmetric system is a positive radial stress resultant and a zero circumferential stress resultant. Positive stress resultants are therefore desired. See Jenkins *et al.* [37], Libai and Simmonds [50], and especially Adler [1] for a review of wrinkle field modelling.

2. *Creep:* The principle stresses should be small relative to material yielding to minimize the effect of creep in the viscoelastic membrane. Creep has been identified in the literature as an issue for membrane structures [20, 60]. Creep may be less of a problem for systems in which the spatial gradient of pressure can be adjusted; creep can be viewed as a change in initial shape, and the pressure distribution can be adjusted according to that new initial shape. The yielding behavior of membrane mirrors is not well understood currently for the space environment yet will need to be characterized to ensure long-term performance.

3. *Dynamic Response:* The magnitude of the in-plane stresses partially determines the response to out-of-plane dynamic disturbances, and so the stress resultants should be as large as creep concerns will allow.

2.1.2 Disturbance Environment

The need for fine pointing, tracking, and reorientation in spaceborne telescopes presents a significant dynamic disturbance environment for structural control. The attitude control system, which might include reaction wheels, will introduce harmonic disturbances to the system. Reorienting the spacecraft to new targets will provide perhaps the largest dynamic disturbance. Davis and Agnes [16] provide a summary of the disturbances acting upon a very-low-density, gossamer-type structure.

Reorienting the spacecraft also changes the thermal loading from the sun, and so the thermal environment must be considered as a disturbance. A shroud must be considered

as a reasonable means to achieve thermal isolation so that thermal gradients do not place a spatially-distributed (and maybe time-varying) load on the mirror. A shroud is significant to the system structural problem because a shroud would be a significant fraction of total telescope mass.

In addition to heating from the sun, the pressure of light from the sun applies a force that can have a significant effect on low-density structures made from membranes. If the solar pressure is taken to be the average solar flux [48] divided by the speed of light, then the equivalent solar pressure would be about $\sim 4.53 \times 10^{-6} \frac{N}{m^2}$. For a $20m$ telescope with an approximately $20m \times 20m$ shroud cross-section and mass concentrated at one end, the solar pressure produces a static moment of $\sim 0.018 N\text{-}m$.

2.1.3 Summary of Desired Properties

The knowledge about the desired and required qualities of the systems design can be summarized as guidelines:

- Manufacturing
  - The ability to manufacture the initial shape should be included in the design process. One possible rule is to avoid aspheric initial shapes.
  - Limits on the magnitude of spatially-distributed imperfections need to be imposed upon the manufacturing process according to the sensitivity of the mechanical response.
- Packaging and deployment
  - The stowage scheme should rely fundamentally on rolling the membrane while minimizing the amount of membrane folding.
  - In order to incorporate a rolling-type stowage scheme, "modest" curvature and launch-vehicle-size fundamental length are desired.
- Design
  - The principle stresses in the membrane mirror are positive and as large as possible without inducing material creep.

– The science light cannot transmit through a lenticular surface. This assumption rules out simple inflation of the primary.

2.2 Concepts for Precision Shape Control

Structural control research for membrane mirrors can be better understood through examination of the required structural components. Figure 2.1 shows an example configuration with a symmetric, monolithic primary mirror. Although some variations on the general design do exist, a membrane mirror telescope will likely have the components listed in this section. The numbers correspond to Figure 2.1.

1. Receiving optics in the direction of the mirror focus
2. Reflecting membrane mirror
3. Support rim at the membrane outer boundary
4. Method of applying a pressure-type loading to the membrane
5. Structure that connects the membrane mirror to the receiving optics
6. Outer membrane shroud for regulating the thermal and/ or electromagnetic environment

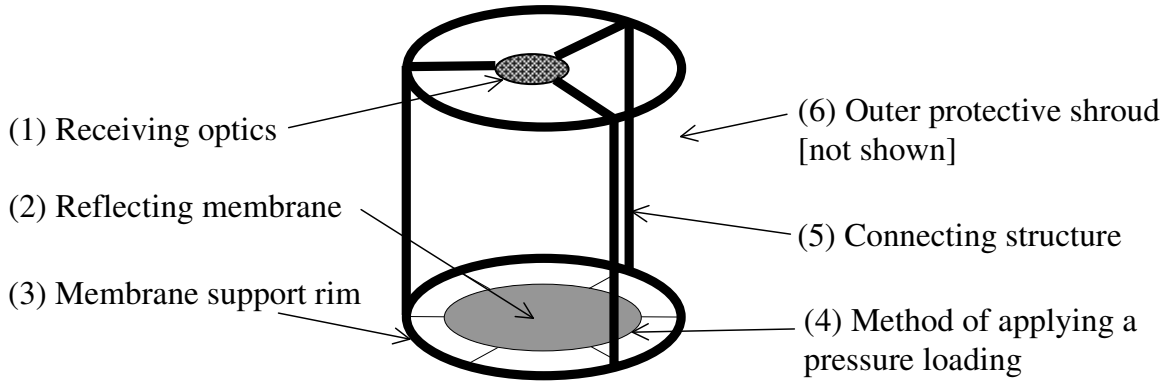

Figure 2.1: Illustration of structural components for a membrane mirror telescope.

2.2.1 Shape of Primary Mirror

The primary mirror can be made into many shapes, three classes of which are represented in Figure 2.2 as area projections. The most common shape or "planform" is circular—also called "filled" or "monolithic". An annular system is used to provide a light path for receiving optics located behind the primary mirror. Just as the removal of the center hole affects the spatial and spectral characteristics of the annular mirror, the reduction of the mirror to separate subapertures affects the spatial performance of the mirror but not the absolute ability to form images. While presenting separate alignment challenges to the structural control system, the subapertures also introduce flexibility into the system design. Each class of shape also has three reasonable subcases: the near-parabola and starting-from-flat are initial-shape cases discussed commonly in the gossamer spacecraft literature [23, 32] while the spherical initial shape is introduced as a near-parabolic initial shape with constant curvature in both principal directions.

With inflated struts as the frame elements, Figure 2.3 illustrates different concepts for the construction of a telescope with a filled or annular membrane primary mirror. In each case a ray is drawn to represent the path followed by the incoming signal. The membrane mirror is held by an inflated rim structure and may have a shroud for protection from thermal disturbances.

2.2.2 Structural Plant

The structural components can be divided into the primary mirror and the connecting structure.

Primary Mirror

Simple methods, *i.e.* a uniform membrane with uniformly applied pressure and fixed boundary conditions, do not produce an optical-quality membrane paraboloid. The literature provides three widely-discussed methods of static shape-forming of membrane paraboloids [68], [23]: (1) a near-paraboloid mirror loaded by a radially-constant pressure, (2) a flat mirror loaded with constant pressure and radial boundary displacements, and (3) an unloaded paraboloid membrane. Each method has difficulties either with manufacturing, deployment, shape, or dynamic behavior. This apparent difficulty in achieving a good solution

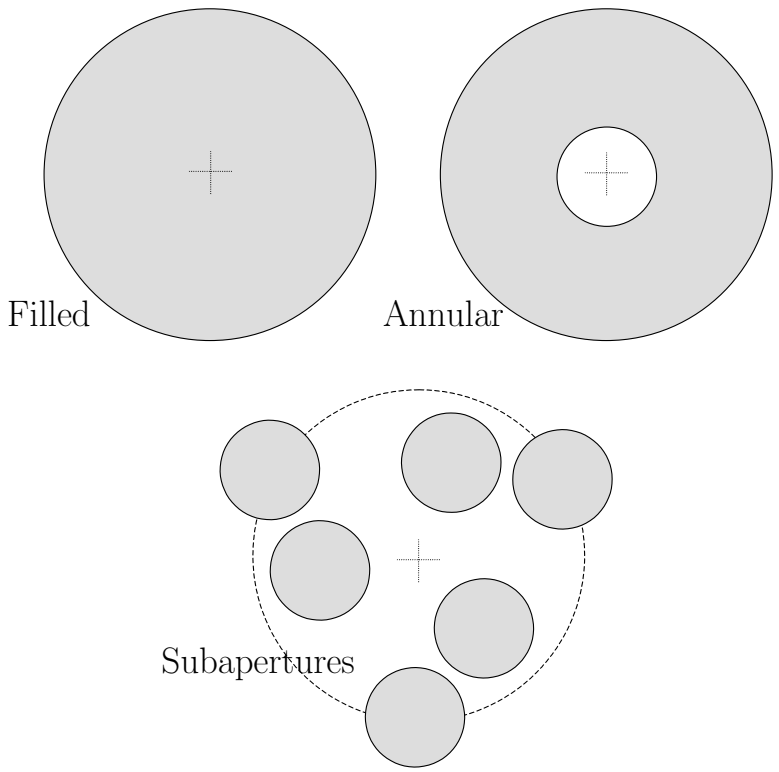

Figure 2.2: Shape of mirrors as viewed from focal point (the top view, also the mirror "planform"). Filled is the most common geometry in the literature, annular is most like current large mirror systems, and subapertures represent the most beneficial size for stowage and membrane dynamic behavior.

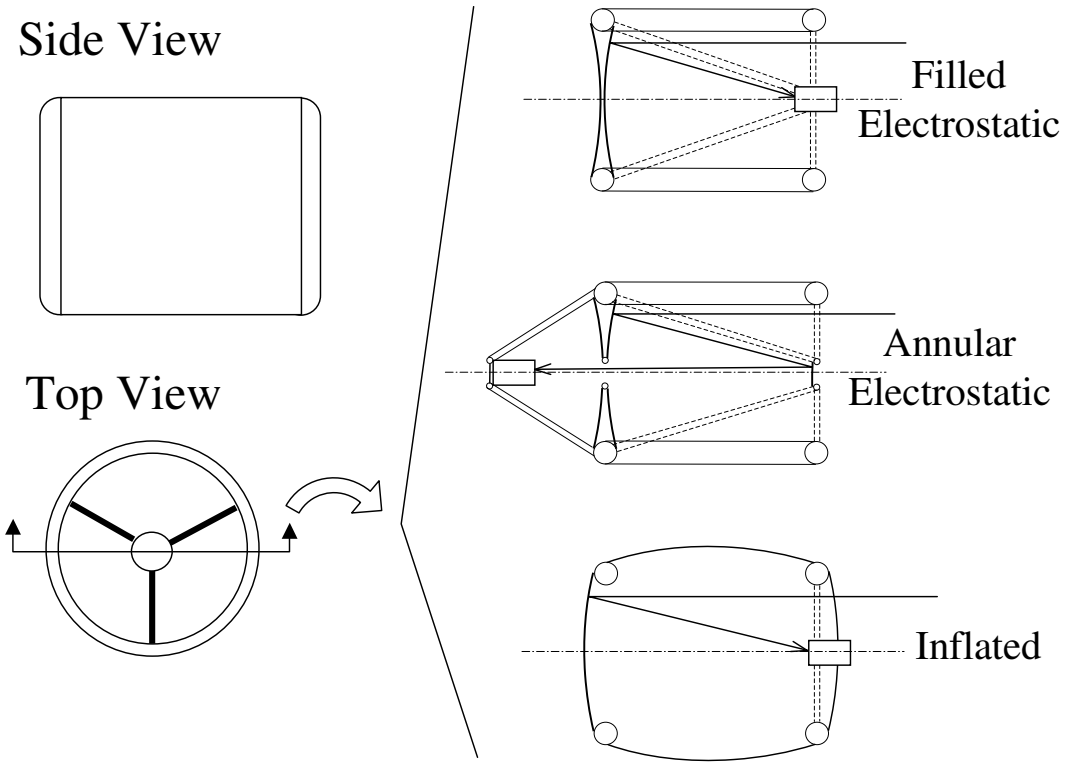

(a) Concepts with shroud

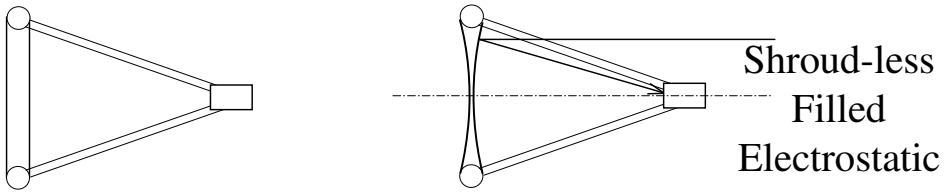

(b) Concepts without shroud

Figure 2.3: Cut-away illustrations of different concepts for single-reflector membrane mirror designs; for clarity only surfaces that intersect with the cut-away plane are shown. A single ray represents the light path for each design. Toroids are represented as circles and cylindrical struts as rectangles. Possible struts are drawn as dashed lines. "Inflated" is the only concept in which the signal must pass through a transmissive membrane prior to reaching the primary reflector.

indicates that more options need to be studied. With these three loading cases and the three planform shapes from Figure 2.2, a set initial-shape-plus-loading cases is identified in Section 2.4.

The geometry of the mirror combines with the boundary conditions provided by the rim and the pressure loading to define the mechanical state of the mirror, with the shape completely dependent upon the initial shape and loading. Moreover, the ability to manufacture the nominal initial shape and achieve the nominal final shape must be studied and proven through sensitivity analysis.

Connecting Structure

The structural support of the membrane primary mirror fulfills different yet interacting roles. First the rim must be positioned to tolerances similar to the mirror requirements over the entire circumference. Next the rim support must provide enough stiffness to be the reaction structure for the application of loads to the membrane mirror. Lastly, the rim support connects the membrane to the rest of the telescope structure and provide the conduit for the exchange of energy between spacecraft and mirror during dynamic excitation. Thus the membrane mirror rim support must provide a highly accurate and stable mirror boundary condition while receiving and rejecting disturbance inputs from other locations in the spacecraft. Figure 2.4 shows how the membrane may be attached continuously or at discrete points.

Using inflated film struts as supports for membrane mirrors promotes a uniform structural density, i.e. a film support for a film reflector. Previous experiments have shown inflated tubes to have beam-like behavior [53], and so the modelling of the support structure appears reasonably straightforward. One system study shows that a dynamics-based criterion on the support struts leads to a support mass that is a significant fraction of the total mass [72]. The ability to fold these structural members allows many stowage possibilities that accommodate the needs of the mirror.

2.2.3 Actuators

Actuators are required both for static shape-forming and for dynamic disturbance rejection; examples of three types of actuators for membrane mirror systems are given in Table 2.1. Discrete actuators can be added at the attachment points, as represented in the “Discrete”

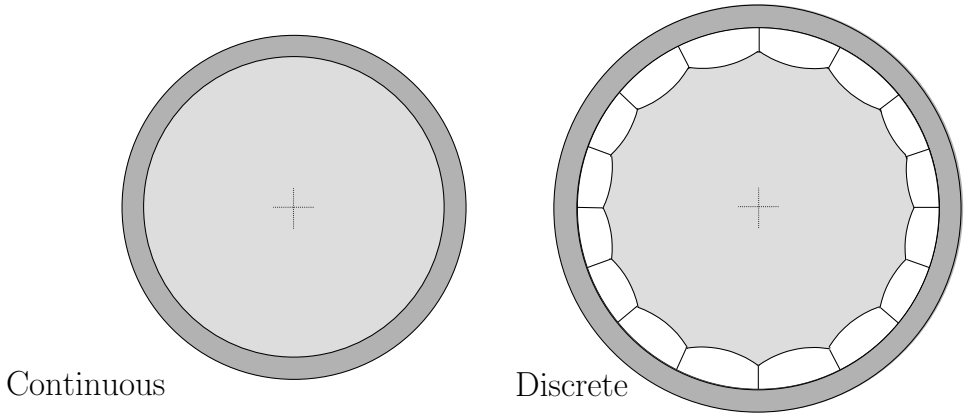

Figure 2.4: Illustration of different methods of attaching membranes to outer ring support structure. The rings are drawn such that the membrane areas are approximately equal.

case of Figure 2.4, or embedded in the support rim. Action at discrete points is fairly common to the structural control community while the action over a continuous surface deserves closer attention. With the need for extreme precision, non-contact actuator methods are preferred to eliminate print-through problems of contact actuators.

Distributed, non-contact actuators are desired for the membrane mirror. Distributed actuators provide a means of adjusting the local mirror shape, a feature that the constant pressure of gas inflation cannot provide. Non-contact actuation is derived from the two classes of interaction between some system input and mechanical load/ response.

1. Electromagnetic actuation:

   (a) Electrostatic forces (Electric field ⇒ force).

   (b) Piezoelectric strains (Charge ⇒ strain, with hysteresis).

   (c) Electrostrictive strains (Charge ⇒ strain, with hysteresis).

   (d) Magnetostrictive strains (Magnetic field ⇒ strain, with hysteresis).

   (e) Photostrictive strains (Light/ photons ⇒ strain, with hysteresis).

2. Thermal actuation:

   (a) Thermal expansion (Temperature ⇒ strain)

Table 2.1: Selection of actuators for membrane primary mirrors.

Type	Action	Actuator
Pressure-Type:	Over continuous surface	· Gas inflation · Active materials (manipulation of strain) · Electrostatic attraction
Attachment Cable Tension:	At discrete points	· Voice coil · Shape memory alloy · Piezoelectric crystals: stacks or fibers · Piezoelectric membrane
Support Ring:	Over continuous or discrete boundary	· Piezoelectric crystal on bending surfaces · Piezoelectric membrane or fibers on stretching surfaces · Cables internal to ring

(b) Shape memory response (Temperature ⇒ strain, with hysteresis)

Both electromagnetic and thermal fields can be applied to a membrane from a short distance, and so the use of such fields can be exploited through either a normal material response or a so-called "smart material" behavior. Electrostatic force actuation is the only method to provide the combination of (1) distributed actuation, (2) a means to introduce in-plane tension (as the reaction to pressure-type loading), and (3) a fairly wide temporal bandwidth of operation.

2.2.4 Sensors

The position of the membrane and the support structure will need to be provided as inputs to the closed-loop control system through a system of sensors. As with the actuators, the sensors either provide information across a region of the mirror or at discrete locations on the structure. Table 2.2 provides a selection of potential sensor types.

Because of the optical quality requirements on the mirror shape, the final mirror position will need to be measured optically. A capacitance sensor, measuring the distance to another conducting membrane, can assist in the membrane measurement task. Because the boundary of the stretching-dominated mirror has significant influence over the behavior of the mirror, knowledge of the boundary conditions is important to the structural control problem. Measurements that show how out-of-flat the rim is and how uneven the boundary tension provide the sensor information to make a closed-loop-control correction.

Table 2.2: Selection of sensors for membrane primary mirrors.

Type	Action	Sensor
Membrane Distortion	Over continuous surface	· Capacitance (requires second membrane) · Optical: wavefront sensor, interferometry of discrete targets, holographic target, white-light interferometer
Tension	At discrete points	· Strain gauge on cables, support structure · Piezoelectric crystal on cable tensioner · Piezoelectric membrane on membrane
Frame Distortion	Over continuous or discrete boundary	· Accelerometers · Micro-fabricated gyroscopes · Strain gauges

2.2.5 Controller

The goal of the overall control system will be to capture the optical figure of the telescope (from the state of maximum error), calibrate the mirror and telescope, and maintain that figure during all image-taking events. The achievement of optical figure can be conceptualized as a series of subsystem figure problems, from (1) the figure of the primary mirror, (2) the figure of any subsequent optics, and (3) the phasing between the primary mirror and subsequent optics. The difficulty of performing these control tasks is defined by how the whole system is built, and so questions of linearity, accuracy, and complexity must be addressed. At the level of the primary mirror subsystem, the control system needs to form the desired mirror shape and reject disturbances that alter that desired shape.

The selection of actuators and sensors is not a straightforward task for large membrane structures. Forming a shape in a low-stiffness system with micron-level precision over tens of meters is difficult. The type and distribution of both the actuators and sensors must be decided in accordance with the chosen structure and deployment system. For instance, the introduction of segments into the design also brings issues of sensing and actuating the segment boundaries.

2.3 Performance Metrics

In this section a metric is defined to represent the most important, mission-critical performance. Although optical systems are complicated and involve different types of errors

in any given system, the ability of the impinging wavefront to travel in its nominal direction and phase is the single most important property of a telescope system. With the bias phase error fairly easily removed within an optical system, the standard deviation (also "bias-removed RMS") of the pathlength error is the single most important performance metric [83]. Appendix A elaborates on this idea with a longer discussion and diagrams of the wavefront.

From Appendix A the metric is the area-averaged standard deviation of the pointwise wavefront error, or *pathlength STD metric* $Z_{[\Delta L_{STD}]}$.

$$\begin{aligned} \overline{\Delta L} &\equiv \frac{1}{A_{WF}} \int\limits_{A_{WF}} (\Delta L)\, dA_{WF} \\ &= \frac{1}{A_{WF}} \int\limits_{A_{WF}} [(\mathbf{W} - \mathbf{w}) \cdot \hat{\mathbf{e}}_L]\, dA_{WF} \\ Z_{[\Delta L_{STD}]} &\equiv \sqrt{\frac{1}{A_{WF}} \int\limits_{A_{WF}} \left(\Delta L - \overline{\Delta L}\right)^2 dA_{WF}} \end{aligned} \tag{2.1}$$

where A_{WF} is the axial projection of the area of the reference wavefront surface.

Two very different examples provide the boundaries for the numerical range of interest for the error.

1. Use of advanced correction techniques in the optical bench: one micron of error for a $20m$-diameter mirror.

$$\begin{aligned} \bar{\Delta}_1 &\equiv \frac{\Delta_1}{R_{out}} \\ &= \frac{1 \times 10^{-6} m}{10m} \\ &= 10^{-7} \end{aligned}$$

2. Standard optical error: for a wavelength of interest at $500nm$ over a $20m$-diameter mirror, the desired error is one-tenth the wavelength.

$$\begin{aligned} \bar{\Delta}_2 &\equiv \frac{\Delta_2}{R_{out}} \\ &= \frac{\frac{1}{10}(500 \times 10^{-9} m)}{10m} \\ &= 5 \times 10^{-9} \end{aligned}$$

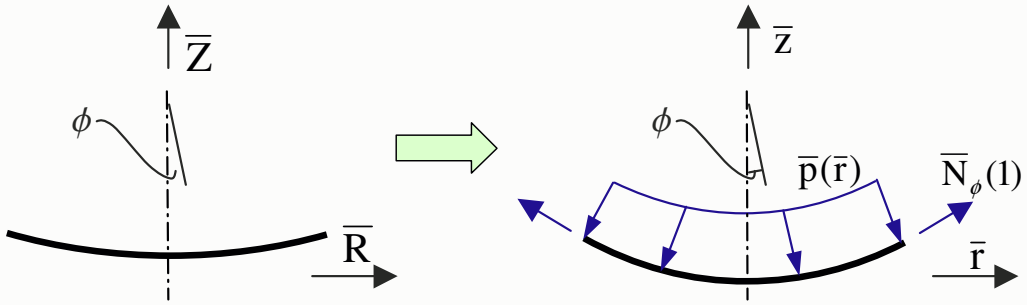

Figure 2.5: Representation of benchmark problems. The drawing shows a single meridian for the axisymmetric problem, with unloaded and loaded states.

The range of interest for the error is thus delimited by $\bar{\Delta}_1$ and $\bar{\Delta}_2$.

2.4 Benchmark Problems

Model accuracy results are not desired for every possible class of geometry and loading, and so a set of benchmark problems is chosen according to the loading and geometry guidelines from Sections 2.1–2.3.

The benchmark problems reflect the following assumptions:

- Each problem in this body of work will be axisymmetric over the entire domain $0 \leq \bar{r} \leq 1$, as represented in Figure 2.5. The axisymmetric condition limits the field variables to mathematically "even" distributions.
- The initial shape is load-free.
- Both a pressure and boundary load is applied to achieve the final shape.
- The boundary load is assumed to be the meridional stress resultant rather than a load at an arbitrary geometry. Moreover, for the statics problem, the boundary is always taken to be load-based (stress resultant) rather than displacement-based ("rigid", "flexible", etc).

Three geometries lead to a comprehensive set of four benchmark problems:

1. *Sphere to sphere*, or "constant pressure on a spherical cap," is the only solution in which an exact, closed-form solution is available. Although the closed-form solution is developed for a full sphere, the boundary conditions on a spherical cap can be specified so that the solution is identical to a cut-out section of a full sphere.

   A non-dimensional radius of $\bar{r}_{sph} = 4$ is used to specify the final shape because the shape is similar to an $f/1$ paraboloid. The 4 enters when the inverse of the second derivative, $4f_\infty$ for a parabola, is taken to approximate the radius of curvature.

2. *Flat to paraboloid* provides a tie to the classic problem in structural mechanics of constant pressure applied to a tensioned, flat membrane. Since the final shape of this constant-pressure case cannot be specified in closed-form to arbitrary accuracy, using the inverse solver of Chapter 4 for the constant-pressure case is inappropriate. Instead, however, a very similar problem is used here. The final shape is taken to be a paraboloid, and hence the applied pressure is allowed to vary with radius.

   In order to look at a range of pressure loads, the final shape is solved over a range of final focal ratios, from very high values down to 1, *i.e.* almost-flat shapes down a depth to radius ratio of around 1:8.

3. *Paraboloid to paraboloid* provides an example with the desirable combination of an optically-useful, highly-curved final shape with small loading. Both $f/1$ and $f/5$ final paraboloid shapes are considered, and a range of initial paraboloid shapes are used to cover a range of load magnitude. The paraboloid-forming case is considered the most general problem of the three geometries because neither the initial nor the final shape has a special symmetry.

   The unity focal ratio represents a filled or annular system as in Figure 2.2 while the larger focal ratio, $f/D = 5$, represents the subaperture case. Assuming that the subaperture case is a parabola rather than an off-axis shape is a reasonable approximation; this idealization is valid in the context of studying systems design trades though would need improvement prior to implementation. Figure 2.6 shows an illustration of the relative depth of the two focal ratios.

In each case a range of problems is solved by varying the initial and final shapes such that the range of loading varies from small to large.

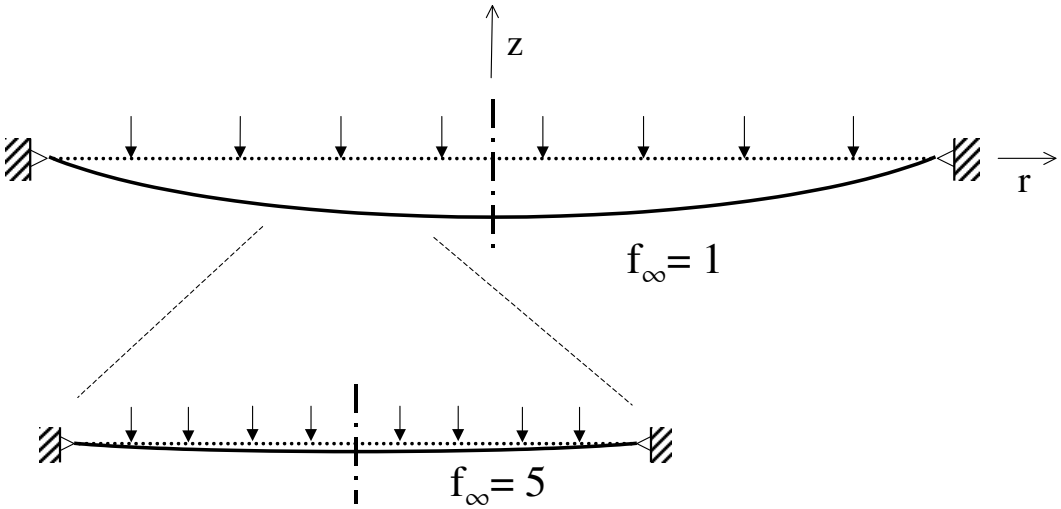

Figure 2.6: Illustrations of two focal-ratio cases, $f/D = \{1, 5\}$, drawn with approximate depth-to-width scale. The subaperture $f/D = 5$ case is shown as a cut of the deeper $f/D = 1$ case.

The dimensions used in this work will be based upon a primary mirror $10m$ or more in diameter and tens of microns thick. Appendix C shows representative properties for two different polyimide membrane cases; the range of property values reflects the different values reported by different research groups. Because the material has been rated for use in space, the NASA-Langley-developed LaRC-CP1 is used for the baseline case in this research. The choice of a polyimide membrane is consistent with other research in the field [68], though the behavior of such a membrane reflector in the space environment is not considered well-characterized.

2.5 Summary

The system aspects of membrane primary mirrors for spaceborne telescopes are discussed in detail, with an emphasis on the structures challenges. The basic geometry and requirements are given, and a list of desired properties are generated. The discussion about the possibilities for structural control helps to motivate the set of features needed in the model. The section on performance metrics shows that the standard deviation of the pathlength error is the most appropriate, most mission critical metric for comparison of two mirror

shapes.; hence the pathlength standard deviation is chosen for use later in the thesis.

From the system-level needs a set of benchmark problems is generated as problems of interest for further study. The sphere-to-sphere case is chosen because a closed-form solution is available, flat-to-paraboloid as a problem similar to existing work, and paraboloid-to-paraboloid as the most general case.

Chapter 3

Membrane Structural Models

Objective of Chapter:

To develop a family of membrane models within a consistent assumption framework and define the methodology used to quantify the optical-level predictive accuracy of models.

The term "model" describes an abstracted representation of a physical behavior. In this work the models are equations that are all directed at predicting the shape of membrane mirrors subject to representative loads. A model that describes structural behavior contains three parts.

1. *Equilibrium*: Stress-load equations
2. *Kinematic*: Strain-displacement equations
3. *Constitutive*: Stress-strain equations

The equilibrium and kinematic equations contain assumptions based upon geometry, and in this chapter the assumptions that define common membrane models are explicitly derived and placed into a framework for later comparison. Figure 3.1 represents the geometry of the doubly-curved membrane mirrors considered in this thesis, with curvilinear coordinate directions shown for a differential area.

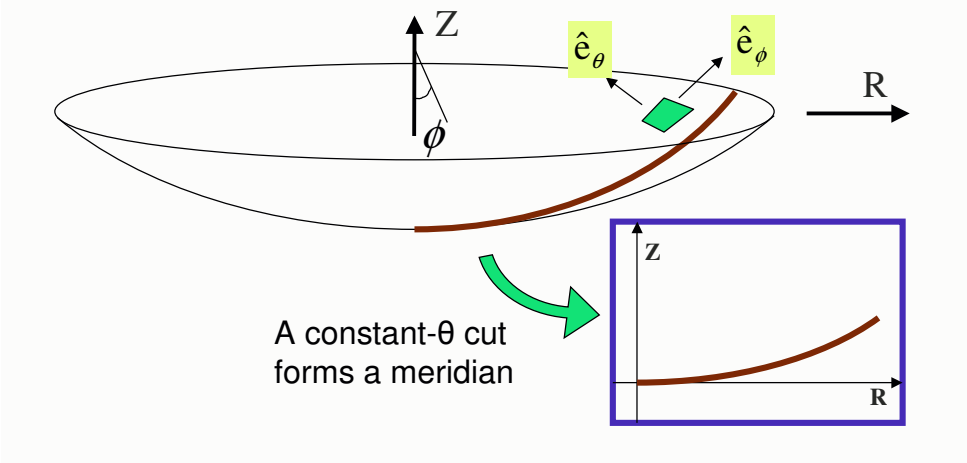

Figure 3.1: Geometry of doubly-curved mirrors: curvilinear surface coordinate directions $\hat{e}_\phi$ and $\hat{e}_\theta$ and example meridian.

3.1 Modelling Choices for Structural Control

In this section the requirements upon the membrane mirror models are discussed, solutions from the literature are acknowledged, and model error concepts are introduced.

3.1.1 Model Requirements

The modelling of membranes as primary mirrors appears to require a two-step modelling process: nonlinear predictions of static shape and linear predictions of dynamic response. A generic representation of a non-linear static response is given by

$$\mathbf{x}_{eqm} = \mathbf{x}_{eqm}(\mathbf{x}_0, \mathbf{F}_{eqm}) \tag{3.1}$$

where the equilibrium position $\mathbf{x}_{eqm}$ is calculated as a deformation from initial position $\mathbf{x}_0$.

Figure 3.2 provides a graphical flow that shows how inverse and forward modelling is used in the statics modelling process. Inverse modelling is used for initial determination of the mechanical state and for final correction, while forward modelling is used to assess the effects of disturbances and actuators on the system.

A linear dynamic system can be represented in state-space form as

$$\frac{d}{dt}(\mathbf{x} - \mathbf{x}_{eqm}) = \mathbf{A}(\mathbf{x} - \mathbf{x}_{eqm}) + \mathbf{B}_u\mathbf{u} + \mathbf{B}_w\mathbf{w} \tag{3.2}$$

$$\mathbf{y} = \mathbf{C}_y(\mathbf{x} - \mathbf{x}_{eqm}) + \mathbf{D}_{yu}\mathbf{u} + \mathbf{D}_{yw}\mathbf{w} \tag{3.3}$$

$$\mathbf{z} = \mathbf{C}_z(\mathbf{x} - \mathbf{x}_{eqm}) + \mathbf{D}_{zu}\mathbf{u} + \mathbf{D}_{zw}\mathbf{w} \tag{3.4}$$

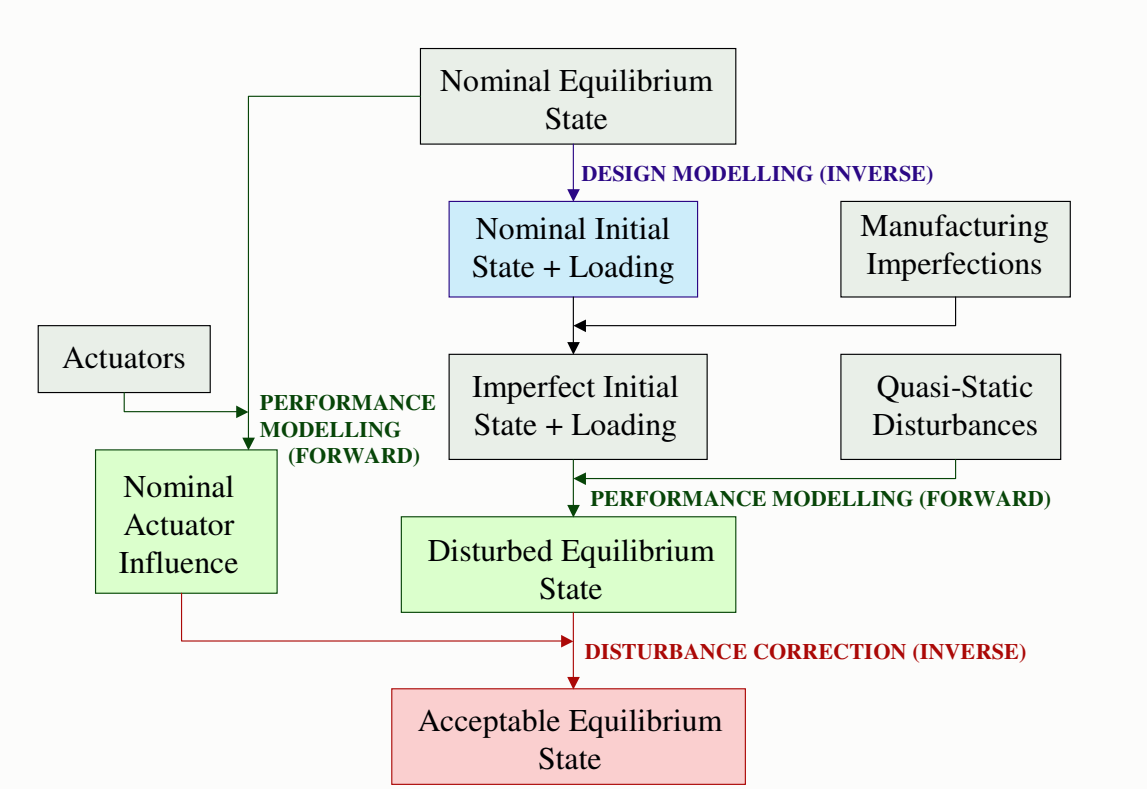

Figure 3.2: Statics modelling flow for true membrane mirrors that shows how imperfections, disturbances, and actuators affect the state of the membrane.

where $\mathbf{x}$ refers to the current shape. The goal for optics is to maintain the final shape $\mathbf{x}$ close enough to a target shape $\mathbf{x}_{target}$ so that the shape of the reflected wavefront is within a given tolerance. The initial problem is to form the equilibrium shape $\mathbf{x}_{eqm}$ close enough to $\mathbf{x}_{target}$, and the dynamics problem is solved to keep $\mathbf{x} - \mathbf{x}_{eqm}$ within the error tolerance.

A membrane mirror model has many uses for structural design and control:

1. Initial State:

   (a) *Initial Shape, $\mathbf{x}_0$, and Initial/ Nominal Loading, $\mathbf{F}_{eqm}$.* Just as for a string, the tension distribution in a membrane affects the dynamic response. Hence the static/ steady-state solution— initial shapes and corresponding loadings— must be well understood. For the case of a membrane under loading in the steady-state, the solution must be known to sub-micron accuracy for visible optics.

2. Final mirror shape performance:

   (a) *Performance = RMS deflection, $\mathbf{z}_{RMS}$.* The primary performance is the temporal and spatial RMS of the position error relative to the exact desired shape, in all cases here a paraboloid.

3. Response to dynamic loading:

   (a) *Free Modal Response/ Open-Loop Plant Characteristics, $\mathbf{A}_{OL}$.* What are the mode shapes and frequencies of a range of initial geometries? Of particular interest are (i) the cases from the earlier statics work and (ii) the no-tension case as offered by the AFRL/ Jenkins concepts.

   (b) *Open-Loop Response, $\mathbf{G}_{zw}$.* A spacecraft is subjected to reorientation (slew) and on-board disturbances. The effect of the disturbances upon the performance needs to be determined.

   (c) *How linear? $\dot{\mathbf{x}} = ?$* Once the linearized behavior is understood, the limits of the linear models should be explored. Geometrically exact steady-state models will provide guidance as to the loading levels for linear behavior. Because the most useful problems for optics involve small material strains, the dominant nonlinearity for these problems is the geometrical effect of large deflection upon the tension and strain fields.

4. Boundary conditions:

   (a) *Support Flexibility,* $\mathbf{A}_{OL}$. The support flexibility affects the dynamic modes (frequency and shape). The flexibility can be varied from approximately rigid to approximately free in order to observe the effect on the frequency and ordering of the dynamics modes.

   (b) *Controllability of Tension Actuators,* $\mathbf{B}_{u-tension}$. A common way to hold membranes is to connect them to a support ring at a discrete number of locations. What level of controllability do tension (strain) actuators at the supports provide?

   (c) *"Smart Ring,"* $\mathbf{B}_{u-ring}$. If the shape of the boundary is actuated, what influence do the actuators hold over the membrane dynamics?

5. Spatial variations:

   (a) *Material Non-uniformity,* $\delta E(r,\theta), \delta h(r,\theta)$. What effect do spatial variations in the material properties have on the final shape? This is primarily a statics issue. What is needed is some idea of the spatial-filtering ability of the structural control system so that the manufacturing requirements can be set.

   (b) *Pressure Errors,* $\delta p(r,\theta)$. How do spatial variations in the applied pressure field affect the final mirror shape? What are the spatial filtering characteristics of the membrane subject to the loading?

A couple of philosophical points about approach are worth noting at this point.

- The assumption framework in this chapter does not explicitly track the order of the assumptions but instead focuses on the effects of the assumptions on the predicted shape. The danger is that the assumptions made have not involved the highest-order relevant error. In efforts such as Wilkes [88], for example, the order of the error is tracked directly, but the trade-off comes in making an a priori assumption of the functional dependencies of the variables.

  Given that a series of assumptions is introduced to the modelling process, the current approach shows a tractable transition from exact to simple models and compares the effects with the most useful metric.

- Much attention is paid in the theories of shells to edge effects and the region of edge effects. It is proposed here that one of the purposes of the structural control is to maintain membrane boundary conditions such that a membrane state is always maintained (zero level of transverse load). Maintaining the membrane state aids in the predictability and smoothness of the solution.

  Inclusion of bending theory is thus required to predict the off-design response.

3.1.2 Published Solutions

Table 3.1 summarizes solutions from the literature for the "semi-inverse" static design problem. Although the solutions appear in the same table, the models used are slightly different in each of the different references. The columns of Table 3.1 divide the existing models into series and discretized-numerical solutions for the problem of determining the loading given initial and final shapes. Few solutions to these problems have been published, while the method of Chapter 4 is seen to cover the cases of interest.

Table 3.1: Axisymmetric solutions for static shape forming and design from the literature, divided according to problem geometry. Each method allows the designer to calculate the loading based upon chosen initial and final conditions.

Shape Transformation	Series Solution	Numerical
Flat ⇒ Paraboloid	Vaughn [84]	[Chapter 4]
Cone ⇒ Paraboloid		[Chapter 4]
Sphere ⇒ Paraboloid		[Chapter 4]
Sphere ⇒ Sphere		[Chapter 4], Juang and Huang [39]
Near-Paraboloid ⇒ Paraboloid		Greschik *et al.* [24], [Chapter 4]
Flat ⇒ Sphere	Hart-Smith and, Crisp [29]	[Chapter 4]

Equation development observed in the literature is recorded in Table 3.2 by problem type, linearity, and symmetry. A wide variety of models is thus available in the literature for shape forming, static performance, and dynamic performance, both axisymmetric and nonlinear cases. The connection between modelling choices and final prediction accuracy, however, is deficient in the literature.

Table 3.2: Division of *equation development* from the literature into axisymmetric vs. 3D and linear vs. nonlinear over the static forming, static performance, and dynamic performance responses.

	Linear (L) or Nonlinear (N), and Description	Axisym.	Full 3-D
Static Forming	N Solution approach with metric tensors and $\nu = 0.5$	[84]	[22]
	N Shell theory, with deformed equilibrium	[39, 17]	[39]
Static Performance	L Membrane theory	[82, 5]	[82]
	L Membrane theory; $n\theta$ Fourier solution		[67]
	N Exact theory in tensor notation	[50]	[11, 50]
	N Deep shell theory		[51, 77]
	N Large-deflection		[82]
	N "Elastic sheets" to curved membranes	[9]	
	N Membrane theory	[86]	
Dynamic Performance	L General tensor presentation		[11]
	L FEM		[49]
	L General presentation of assumed modes		[77]
	L Zonal model; ID from experiment		[32]
	N FEM: modal and time simulation		[79]

Similarly, Table 3.3 has rows and columns sectioned for problem type, linearity, and symmetry. Once again a variety of methods is observed in the literature, yet the discussions in the sources do not discuss accuracy either at all or at a level applicable to optics.

Table 3.3: Division of *solutions* from the literature into axisymmetric vs. 3D and analytical vs. numerical over the static forming, static performance, and dynamic performance responses.

	Analytical (A) or Numerical (N)	Axisym.	Full 3-D
Static Forming	A Exact ($\nu = 0.5$)	[29]	
	A Series ($\nu = 0.5$)	[84]	
	N Finite difference	[39, 24, 17]	
Static Performance	A Ritz/ Galerkin	[64, 15, 58]	
	A Ritz+	[64]	
	N Nonlinear Ritz	[81]	
	N Series	[30, 19, 87, 59]	
	N Finite difference	[64, 76, 24, 25]	
	N FEM		[6, 58, 69]
Dynamic Performance	A Exact		[42]
	A Exact as approx.		[44, 90]
	N Ritz/ Galerkin		[77]
	N FEM	[10, 69, 28, 33, 35]	[69]

3.1.3 Model Error Concepts

The challenge for modelling stems from the accuracy and precision needs of the final system. The optical performance of the telescope mirror will depend upon the exactness of the shape at the level of fractions of a micron, about 10^{-9} times the diameter or 10^{-3} times the thickness. While prediction accuracies on the order of 10^{-3} times the fundamental dimension are common in engineering, a 10^{9} scale difference between the fundamental structural length dimension and the performance tolerance dimension brings into question standard structural modelling practice. A basic question is whether optical-level behavior can accurately be predicted in this case; if not, an additional level of complexity might be needed in the control system.

Iterative solution methods such as nonlinear finite difference enable specification of a rather arbitrary precision, but the modelling assumptions will not support an arbitrary level

of precision. Quantifying the relative importance of the modelling assumptions establishes the accuracy of the modelling predictions.

The potential sources of inaccuracy in structural modelling can be divided into three classes:

- *Form of equations.* Reference equilibrium to the undeformed or deformed geometry? Use exact trigonometric quantities or polynomial approximations? Include both stretching and bending effects for a membrane? Solve multiple length scales independently?

- *Material/ manufacturing.* How do reasonable variations in thickness, elastic modulus, or Poisson's ratio affect the predicted deflection? What about manufacturing imperfections such as being slightly non-circular?

- *Loading and boundary condition inaccuracy.* (Input to the structural problem). To what tolerance can the loading and boundary conditions be applied?

Modelling uncertainties can be placed into three classes.

1. *Mathematics*: model and solution

2. *Material*: spatial variations in the material properties (the material response)

3. *Structural*: rim out-of-flatness, boundary tension variations, loading spatial variations (the material loading)

Mathematics is the first logical class to study because good modelling tools need to exist in order to study material and structural uncertainties.

Curved membrane mirrors are idealized as surfaces for mathematical analysis. Surfaces such as paraboloids and spherical caps have finite curvature in both principal coordinate directions, and the response of the surface to loading is predicted with shell theory. Predicting optical performance of $10m$ and larger membrane mirrors involves having $\mathrm{O}(10^{-8})D$ confidence in the deflection predictions. Precision and accuracy of the solution become very important.

The quality of modelling can be stated in terms of modelling and precision. For a modelling approach to be *accurate* enough, the model needs to be able to represent the actual system behavior to the required number of significant digits in the field quantities.

Modelling assumptions influence the model accuracy. How well the solution represents the model determines the modelling *precision*. Since the accuracy of the final prediction is largely dependent upon the modelling assumptions, the precision of the solution need not be greater than the accuracy of the solution method; *i.e.*, there is no need for 20-digit precision on a 4-digits-of-accuracy solution. The benchmark problems introduced in Section 2.4 provide a starting point for making these comparisons of accuracy and precision.

- *Modelling accuracy* indicates how well the equations predict the behavior of the physical system. In the context of membrane mirrors, the "behavior" is the shape change due to actuator and disturbance loading. The assumptions that lead to the governing equations, *i.e.* "the model," also establish the limiting accuracy to which solutions will predict the deflection response of the material.

- *Solution precision* indicates how well a solution represents the governing equations. Precision varies between solution methods and can often be increased by increasing the number of terms or degrees of freedom.

Figure 3.3 provides a notional plot of how modelling accuracy and solution accuracy are related. For a solution method such as finite elements, an increase in solution precision is gained from an increase in the number of elements. Other approximate solution methods will have similar behavior. The modelling assumptions limit the accuracy at which the solution represents the physical world, however, and the total error stems from both the assumptions and the solution method. This limit in possible accuracy is the model error or model accuracy.

The goal of the model selection process is to find the set of equations whose limiting modelling error is at least one order of magnitude less than the level of desired performance. For optical mirrors with an $O(10^{-8})$ performance-to-radius ratio, the modelling and solution procedures must have a combined error at or below this level.

3.2 Curved-Membrane Models

Many different types of models have been used by different authors in the literature of spacecraft reflectors made from large curved membranes. With the notable exception of the one paper that uses the axisymmetric exact membrane shell theory [23], none of the

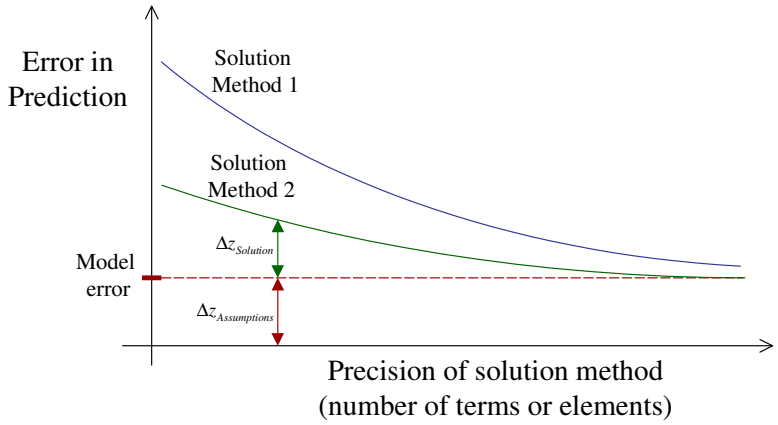

Figure 3.3: Notional representation of model error, divided into $\Delta z_{Assumptions}$, the limiting error due to modelling assumptions, and $\Delta z_{Solution}$, the error due to inaccuracy in the solution method. The solution accuracy is assumed to improve to a limiting value as the solution accuracy is increased.

authors has offered a justification of the model choice based upon the assumptions inherent in the chosen model. In this section the different models in use for curved membranes are developed from the most exact to the most approximate, with an explanation of the assumptions used to generate each subsequent model.

The series of models presented here are not unique. Rather, a different author might choose a different series of assumptions; a good example of a different series of approximations is the Donnell-Mushtari-Vlasov equations [77] that include a mixture of bending and extension assumptions. Another example of an approach is the small-strain theory presented in Reissner [71]. The present series of models was chosen because each has been used in the membrane literature.

3.2.1 Previous Study

The Greschik *et al* [23] paper presents the only work which is comparable to the current effort. Inverse and forward solvers are developed for the axisymmetric exact membrane theory, and the effect of introducing modelling assumptions is quantified for a discrete set of loading conditions.

The lessons from the study include:

- The final-shape errors increase as the pressure load increases.
- *The radial component of the deflection solution is important for assessing accuracy. Figure 7 (of [23]) shows that ignoring the axial component of the solution increases the error, especially away from the center ($r = 0$).*
- The small-angle assumption is more important for accuracy than approximating the constitutive model, using deformed versus undeformed basis, or assuming the pressure to only act in the axial direction.
- All of the assumptions appear to be important for the optical problem. For the initially-flat, inflated-to-250psi problem shows that each individual assumption leads to error larger than optical tolerances.

The error form in the cited study is

$$\int_A [2(z_{exact} - z_{approx})]^2 \, dA \tag{3.5}$$

The limitations of the study include:

1. Limited choice of geometries in the benchmark problems. Loads are applied to flat membranes to result in apex stresses of $\{125, 250, 500, 1000\}psi$ and to curved membranes of various final focal ratios to result in apex stresses of $\{500, 1000\}psi$.

2. Level of reported error. The paper is directed towards use of membranes for reflecting radio frequencies, and the stated error level of interest is $100\mu m$, well above optical levels. In general, the multi-micron error levels reported are much larger than the error levels of interest for optics.

   The forward solver used for model comparison had a limiting accuracy of $0.1\mu m$, and so the accuracy-comparison tables were discretized to $0.1\mu m$. The results are difficult to read at the optical level and do not show a continuous trends.

3. Comparison to existing solutions. While the individually-addressed model errors are interesting, the models in use by other researchers have these assumptions in various combinations.

3.2.2 Assumptions: Geometric and Moment-Free

Modelling assumptions for a structure are applied to the three basic types of equations that constitute the model:

1. Equilibrium (stress $\leftrightarrow$ load);
2. Kinematic (strain $\leftrightarrow$ displacement); and
3. Constitutive (stress $\leftrightarrow$ strain).

The assumptions that affect the equilibrium and kinematic equations are discussed in this section. For all of this work, the constitutive equations are assumed to follow that of linear elastic behavior of an isotropic material; wrinkling and orthotropic materials are outside the scope of this work. The most important assumption used in the current analysis is that the structure is free of distributed moments. This is the membrane assumption, that the structure responds to loading by extension rather than bending.

Many authors cite Reissner [71], who provides guidelines for differentiating bending-dominated and stretching-dominated (membrane) regions of parameter space. The results of Agnes and Wagner [2] also provide a way to estimate the validity of the membrane approximation.

- Reissner [71] shows that a stretching dominated response is observed for shallow spherical shells when

$$\frac{pR_{sph}^2}{Eh^2} \gg 1$$

for spherical radius R_{sph}. In terms of the non-dimensional variables used in this work and described in Appendix B, the inequality becomes

$$\frac{\bar{p}\bar{R}_{sph}^2}{\bar{h}} \gg 1$$

In the current work, a unit focal ratio and a relative thickness of $h = 10^{-6} r_{out}$ is of interest. For a focal ratio of one, the spherical radius is approximately four

($\bar{R}_{sph}(f/1) \approx 4$). These parameters lead to

$$\begin{aligned} \frac{\bar{p}(4)^2}{10^{-6}} &\gg 1 \\ \bar{p} &\gg 6.25 \times 10^{-8} \end{aligned}$$

This level of pressure is much smaller than the O(10^{-2}) level of nondimensional pressure used during the static design work, and so the stretching behavior dominates the response over the bending behavior.

- Agnes and Wagner [2], in combination with Rogers and Agnes [73], apply a matched asymptotic expansion solution from Nayfeh [66] in which an interior membrane solution is matched to an exterior bending solution. The tests in these papers apply for a large nondimensional thickness, $\sim O(10^{-3})$, and small in-plane load N_0. By using the standard definition for plate bending stiffness D, the perturbation term ϵ is defined

$$\epsilon = \sqrt{\frac{D}{R^{*2} N_0}} \tag{3.6}$$

and then transformed to

$$\epsilon \sim \sqrt{\frac{\bar{h}^2}{\bar{N}_0}} \tag{3.7}$$

The perturbation term for the experiment is O(10^{-1}), but an experimental system (as discussed in Chapter 2, Systems Design) will have a much smaller term, O(10^{-4}) or O(10^{-5}).

A closer examination of the solution reveals that the micron-level deflections of the experiment correspond to much smaller deflections in the scaled system, as well as a $10^{-3} \times r_{out}$ region in which the edge effect becomes noticeable ("noticeable" defined by solution shape function reaching a magnitude of O(10^{-6})).

3.2.3 Derivation of Nonlinear Models

The important mathematical relationships for shell analysis are reviewed in the stress-type discussion in Chapter 5 and the differential geometry discussion in Appendix D.

Figure 3.4 summarizes the different membrane models and modelling assumptions in

a flow chart. The assumptions are mostly geometric and affect both the equilibrium and kinematic relations. The form of the non-dimensional variables is given in Appendix B.

Table 3.4 lists the assumptions used to generate the series of equilibrium equations detailed in Fig 3.4, from geometrically exact shell theory to the classic axisymmetric, small-slope equations.

Table 3.4: Equilibrium equation assumptions for the series of models in Fig 3.4, listed in order of decreasing accuracy. Each row represents the addition of an assumption.

MODEL	CRITICAL ASSUMPTION
Exact Shell, Includes Bending (ES)	• No assumptions/ exact geometry
Exact Membrane Shell (EMS)	• Zero moment $M_{\alpha\beta}(\phi,\theta) \to 0$
Axisymmetric Exact Membrane Shell (AEMS)	• Axisymmetric initial geometry $\frac{\partial(R_\theta \sin\theta)}{\partial\theta} \to 0, g_{\phi\theta} = g_{\theta\phi} = 0$ • Axisymmetric response $n_{\phi\theta} \to 0$, $n_{\theta\phi} \to 0$
Axisymmetric Membrane Shell (AMS)	• Small strains; reference lengths changed to undeformed coordinates $1 + \varepsilon_{\phi\phi} \to 1$ and $1 + \varepsilon_{\theta\theta} \to 1$ $n_{\gamma\beta} \to N_{\gamma\beta}$, $r_\gamma \to R_\gamma$
Axisymmetric Improved Large Deflection (AILD) from Curved	• Small angle approximation (Order α_0^2 and higher $\to 0$) $\sin\alpha_0 \to \frac{dw}{dr}, \quad \cos\alpha_0 \to 1$ • Radial stress resultant rather than meridional $N_\phi(R)\cos\alpha_0 \to N_r(R)$
Improved Large Axisymmetric Deflection (AILD) from Flat	• Same as AILD from Curved, yet no initial slope $\left(\frac{dw}{dr}\right)_0 = 0$
Axisymmetric Large Deflection (ALD) from Curved	• Pressure approximated as an axial load $p_z \to p$ $p_r \to 0$
Axisymmetric Large Deflection (ALD) from Flat	• Same as ALD from Curved, yet no initial slope $\left(\frac{dw}{dr}\right)_0 = 0$
Axisymmetric Small Deflection (ASD) from Flat	• Stress resultants do not change with loading $N_r(r) \to N_0$ $N_\theta(r) \to N_0$

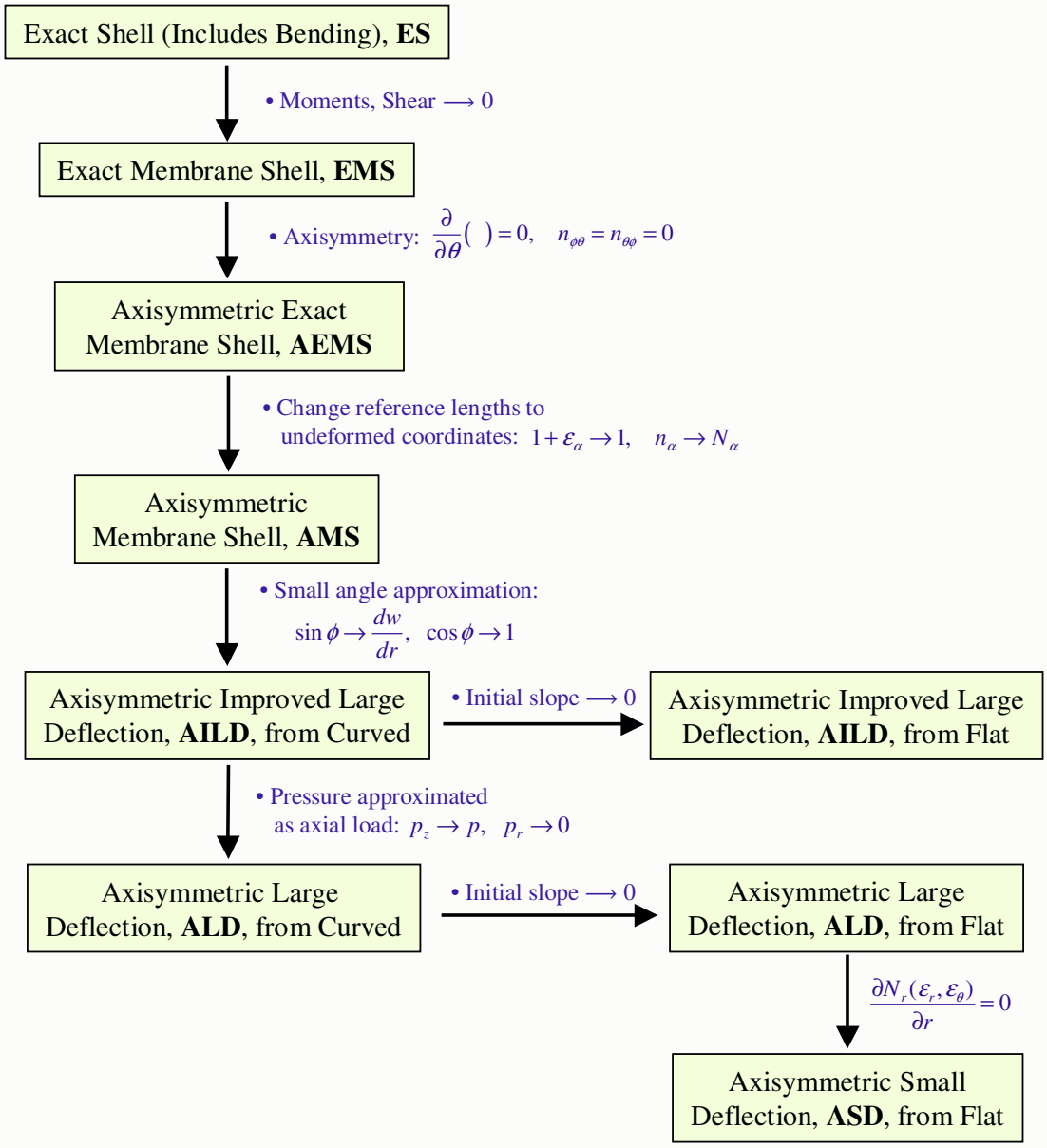

Figure 3.4: Taxonomy of membrane shell models. The top box represents the kinematically-exact theory, and each step down represents the use of one or more assumptions.

Exact Shell (ES)

From Chapter VIII of Libai and Simmonds the exact shell theory is given by a combination of the translational and rotational momentum equations.

$$\mathbf{n}^{\alpha}\big|_{\alpha} + \mathbf{p} = \frac{d\mathbf{l}}{dt} \tag{3.8}$$

$$\mathbf{m}^{\alpha}\big|_{\alpha} + \bar{\mathbf{y}}_{\alpha} \times \mathbf{n}^{\alpha} + \mathbf{m}_{ext} = \frac{d\mathbf{h}}{dt} \tag{3.9}$$

Linear momentum is represented by l, and angular momentum by h.

In this chapter only static models are considered. The time derivatives are hence set to zero for all subsequent models.

Exact Membrane Shell (EMS)

The exact membrane shell equations are found in the literature either as a simplification of exact shell theory [11] or as an independent development (Chapter VII of Libai and Simmonds [50]). The simplification comes from setting the moments to zero, and the implication is that the shear across the thickness of the membrane equals zero.

Again following the development of Libai and Simmonds [50], setting the moment to zero in Equations 3.8 and 3.9 and applying the formula for surface divergence leads to

$$\frac{1}{\sqrt{g}} \left(\sqrt{g}\mathbf{n}^{\alpha}\right)_{,\alpha} + \mathbf{p} = 0 \tag{3.10}$$

Axisymmetric Exact Membrane Shell (AEMS)

Following the development in sections VII.F and V.T of Libai and Simmonds, repeated with detail in Appendix E for convenience, the vector form for axisymmetric membrane shells is given by

$$\frac{d}{dr}\left(r n_{\phi\phi}\right) = n_{\theta\theta} \qquad \text{(Equilibrium)} \tag{3.11}$$

$$n_{\phi\phi}\kappa_{\phi} + n_{\theta\theta}\kappa_{\theta} = \frac{n_{\phi\phi}}{r_{\phi}} + \frac{n_{\theta\theta}}{r_{\theta}} = p \qquad \text{(Equilibrium)} \tag{3.12}$$

$$\frac{d}{dr}\left(r\kappa_{\theta\theta}\right) = \kappa_{\phi\phi} \qquad \text{(Compatibility)} \tag{3.13}$$

for pressure per deformed area p, Cauchy-type stress resultant tensor $n_{\alpha\beta}$, and principle curvatures κ_α.

The constitutive equations are based upon engineering stresses and strains, quantities referred to the undeformed basis, for plane stress and assumed isotropic response with elastic modulus E.

$$Eh\varepsilon_\theta = N_\theta - \nu N_\phi \tag{3.14}$$

$$Eh\varepsilon_\phi = N_\phi - \nu N_\theta \tag{3.15}$$

Transforming these equations into the deformed basis provides consistency to the governing equations.

$$Eh\varepsilon_\theta = n_\theta(1+\varepsilon_\phi) - \nu n_\phi(1+\varepsilon_\theta) \quad \text{(Constitutive)} \tag{3.16}$$

$$Eh\varepsilon_\phi = n_\phi(1+\varepsilon_\theta) - \nu n_\theta(1+\varepsilon_\phi) \quad \text{(Constitutive)} \tag{3.17}$$

The kinematic equations define the relation between displacement and strain.

$$\varepsilon_\phi = \frac{ds}{dS} - 1 \quad \text{(Kinematic)} \tag{3.18}$$

$$\varepsilon_\theta = \frac{r}{R} - 1 = \frac{u_r}{R} \quad \text{(Kinematic)} \tag{3.19}$$

The differential arc length is defined in the undeformed dS and deformed ds bases. Arc length is also related to angle ϕ, axial position z, and radial position r by the geometric relations $\{dr = ds\cos\phi(r), dz = ds\sin\phi(r), \kappa_\phi(r) = \frac{d\phi(r)}{ds}\}$.

Axisymmetric Membrane Shell (AMS)

"Axisymmetric membrane shell" represents first-approximation shell theory as discussed in Koiter [40] and can have many forms. The forms presented here follow Love [51] (see also Soedel [77] for a good re-derivation).

If the reference lengths for the variables are changed to the undeformed configuration,

the standard membrane shell model is found.

$$\frac{d}{dR}\left(RN_{\phi\phi}\right) = N_{\theta\theta} \qquad \text{(Equilibrium)} \tag{3.20}$$

$$\frac{N_{\phi\phi}}{R_\phi} + \frac{N_{\theta\theta}}{R_\theta} = P \qquad \text{(Equilibrium)} \tag{3.21}$$

for pressure per undeformed area P and first-Piola-Kirchoff-type stress resultant tensor $N_{\alpha\beta}$.

The constitutive equations are used in original form.

$$Eh\varepsilon_\theta = N_\theta - \nu N_\phi \qquad \text{(Constitutive)} \tag{3.22}$$

$$Eh\varepsilon_\phi = N_\phi - \nu N_\theta \qquad \text{(Constitutive)} \tag{3.23}$$

The kinematic equations define the relation between displacement and strain (see Baker [5]).

$$R_\phi \sin\phi \cos\phi \frac{d}{dR}\left(\frac{1}{\sin\phi}u_\phi\right) = R_\phi\varepsilon_\phi - R_\theta\varepsilon_\theta \qquad \text{(Kinematic)} \tag{3.24}$$

$$\varepsilon_\theta = \frac{u_r}{R} \qquad \text{(Kinematic)} \tag{3.25}$$

Axisymmetric Improved Large Deflection (AILD) from Curved

In the next set of assumptions, the models switch to cylindrical coordinates r and z from curvilinear surface coordinates ϕ and θ. The following steps are taken:

- The two AMS equilibrium equations, Eqns 3.20 and 3.21, are added in two different combinations so as to eliminate (1) the curvature term and (2) the circumferential stress resultant. This process, in combination with the following approximations, produces the two new equilibrium equations.
- The radial stress resultant N_r is used instead of the meridional stress resultant $N_{\phi\phi}$.

$$N_r(R) = N_{\phi\phi}(R)\cos\phi \tag{3.26}$$

- The slope is represented as a combination of the initial slope $\left(\frac{d\bar{W}}{dR}\right)_0$ and slope

change $\Delta\frac{d\bar{W}}{dR}$.

$$\frac{dW}{dR} = \left(\frac{dW}{dR}\right)_0 + \Delta\frac{dW}{dR} \tag{3.27}$$

- A small-angle-approximation is used for angle $\alpha(R)$, and terms of order α^2 and higher are eliminated in the sine and cosine approximations. The angle α is approximated by the slope $\frac{dW}{dR}$ in the small-angle approximation.

The equilibrium equations are

$$\frac{d}{dR}\left[R\ N_r^{tot}(R)\right] = N_\theta^{tot}(R) + P(R)R\frac{dW}{dR} \quad \text{(Equilibrium)} \tag{3.28}$$

$$\frac{d}{dR}\left[R\ N_r^{tot}(R)\left(\left(\frac{dW}{dR}\right)_0 + \Delta\frac{dW}{dR}\right)\right] = P(R)\ R \quad \text{(Equilibrium)} \tag{3.29}$$

The axisymmetric strain-displacement relations are

$$\varepsilon_r = \frac{dU}{dR} + \left(\frac{dW}{dR}\right)_0 \Delta\frac{dW}{dR} + \frac{1}{2}\left(\Delta\frac{dW}{dR}\right)^2 \quad \text{(Kinematic)} \tag{3.30}$$

$$\varepsilon_\theta = \frac{U}{R} \quad \text{(Kinematic)} \tag{3.31}$$

The constitutive equations for this model involve use of the $\alpha^2 \to 0$ approximation.

$$Eh\varepsilon_\theta(R) = N_\theta(R) - \nu N_r(R) \quad \text{(Constitutive)} \tag{3.32}$$

$$Eh\varepsilon_r(R) = N_r(R) - \nu N_\theta(R) \quad \text{(Constitutive)} \tag{3.33}$$

The compatibility equation is then found by combining the strain-displacement equations 3.30–3.31 and the constitutive equations.

$$N_r(R) = \frac{d}{dR}\left(RN_\theta(R)\right) + \left(\frac{dW}{dR}\right)_0 \Delta\frac{dW}{dR} + \frac{1}{2}\left(\Delta\frac{dW}{dR}\right)^2 \quad \text{(Compatibility)} \tag{3.34}$$

Axisymmetric Improved Large Deflection (AILD) from Flat

The equations are the same as above, with the initial slope terms set to zero, $\left(\frac{d\bar{W}}{d\bar{R}}\right)_0 = 0$. Equations 3.30, 3.28, and 3.29 are thus changed from the previous model.

$$\frac{d}{dR}\left[R\ N_r^{tot}(R)\right] = N_\theta^{tot}(R) + P(R)R\left(\Delta\frac{dW}{dR}\right) \text{ (Equilibrium)} \quad (3.35)$$

$$\frac{d}{dR}\left[R\ N_r^{tot}(R)\left(\Delta\frac{dW}{dR}\right)\right] = P(R)\ R \quad \text{(Equilibrium)} \quad (3.36)$$

$$\varepsilon_r = \frac{dU}{dR} + \frac{1}{2}\left(\Delta\frac{dW}{dR}\right)^2 \quad \text{(Kinematic)} \quad (3.37)$$

$$\varepsilon_\theta = \frac{U}{R} \quad \text{(Kinematic)} \quad (3.38)$$

$$Eh\varepsilon_\theta(R) = N_\theta(R) - \nu N_r(R) \quad \text{(Constitutive)} \quad (3.39)$$

$$Eh\varepsilon_r(R) = N_r(R) - \nu N_\theta(R) \quad \text{(Constitutive)} \quad (3.40)$$

Axisymmetric Large Deflection (ALD) from Curved

Assuming the pressure term to act in only the radial direction leads to the ALD equations from the AILD equations. The only change to the equations thus appears from eliminating the $\bar{P}(\bar{R})\bar{R}\frac{d\bar{R}}{d\bar{R}}$ term from Equation 3.28. Equation 3.29 still applies. The strain-displacement relations are the same as Equations 3.30 and 3.31, and the constitutive equations are unchanged.

$$\frac{d}{dR}\left[R\ N_r^{tot}(R)\right] = N_\theta^{tot}(R) \quad \text{(Equilibrium)} \quad (3.41)$$

$$\frac{d}{dR}\left[R\ N_r^{tot}(R)\left(\left(\frac{dW}{dR}\right)_0 + \Delta\frac{dW}{dR}\right)\right] = P(R)\ R \quad \text{(Equilibrium)} \quad (3.42)$$

$$\varepsilon_r = \frac{dU}{dR} + \left(\frac{dW}{dR}\right)_0\Delta\frac{dW}{dR} + \frac{1}{2}\left(\Delta\frac{dW}{dR}\right)^2 \quad \text{(Kinematic)} \quad (3.43)$$

$$\varepsilon_\theta = \frac{U}{R} \quad \text{(Kinematic)} \quad (3.44)$$

$$Eh\varepsilon_\theta(R) = N_\theta(R) - \nu N_r(R) \quad \text{(Constitutive)} \quad (3.45)$$

$$Eh\varepsilon_r(R) = N_r(R) - \nu N_\theta(R) \quad \text{(Constitutive)} \quad (3.46)$$

Axisymmetric Large Deflection (ALD) from Flat

As with the AILD model, the transition to the flat initial shape in the ALD model involves the removal of the initial slope term, or $\left(\frac{d\bar{W}}{d\bar{R}}\right)_0 = 0$.

$$\frac{d}{dR}\left[R\ N_r^{tot}(R)\right] = N_\theta^{tot}(R) \qquad \text{(Equilibrium)} \tag{3.47}$$

$$\frac{d}{dR}\left[R\ N_r^{tot}(R)\left(\Delta\frac{dW}{dR}\right)\right] = P(R)\ R \qquad \text{(Equilibrium)} \tag{3.48}$$

$$\varepsilon_r = \frac{dU}{dR} + \frac{1}{2}\left(\Delta\frac{dW}{dR}\right)^2 \qquad \text{(Kinematic)} \tag{3.49}$$

$$\varepsilon_\theta = \frac{U}{R} \qquad \text{(Kinematic)} \tag{3.50}$$

$$Eh\varepsilon_\theta(R) = N_\theta(R) - \nu N_r(R) \qquad \text{(Constitutive)} \tag{3.51}$$

$$Eh\varepsilon_r(R) = N_r(R) - \nu N_\theta(R) \qquad \text{(Constitutive)} \tag{3.52}$$

If the two strain-displacement relations are combined in such a way as to eliminate displacement $\bar{U}(\bar{R})$, with substitution of the constitutive equations, the compatibility equation is found to be

$$\bar{N}_r(\bar{R}) = \frac{d}{d\bar{R}}\left(\bar{R}\bar{N}_\theta(\bar{R})\right) + \frac{1}{2}\left(\frac{d\bar{W}}{d\bar{R}}\right)^2 \qquad \text{(Compatibility)} \tag{3.53}$$

Axisymmetric Small Deflection (ASD) from Flat

In the small-deflection problem the initial stress resultant is assumed to not vary as the load is applied. In addition, with the flat membrane the radial stress resultant will be constant, or $\frac{d}{d\bar{R}}\left(\bar{N}_r\bar{R}\right) = 0$. The equilibrium equations are thus changed slightly from Equations 3.47 and 3.48.

$$N_r^{tot} = N_\theta^{tot} \qquad \text{(Equilibrium)} \tag{3.54}$$

$$N_r^{tot}\frac{d}{dR}\left(R\Delta\frac{dW}{dR}\right) = P(R)\ R \qquad \text{(Equilibrium)} \tag{3.55}$$

$$\varepsilon_r = \frac{dU}{dR} + \frac{1}{2}\left(\Delta\frac{dW}{dR}\right)^2 \qquad \text{(Kinematic)} \tag{3.56}$$

$$\varepsilon_\theta = \frac{U}{R} \qquad \text{(Kinematic)} \tag{3.57}$$

$$Eh\varepsilon_\theta(R) = N_\theta(R) - \nu N_r(R) \qquad \text{(Constitutive)} \tag{3.58}$$

$$Eh\varepsilon_r(R) = N_r(R) - \nu N_\theta(R) \qquad \text{(Constitutive)} \tag{3.59}$$

3.2.4 Derivation of Linear Perturbation Models

Each of the preceding equations can be linearized. To linearize the equations, each of the field variables is assumed to be a linear perturbation with a zero initial value, or $(\cdot) \Rightarrow \Delta(\cdot)$. Second-order terms are set to zero ($\mathrm{O}(\Delta^2) \rightarrow 0$). The exception is that the initial curvatures and initial slope are nonzero.

$$\kappa_{\phi\phi} \rightarrow (\kappa_{\phi\phi})_0 + \Delta\kappa_{\phi\phi} \tag{3.60}$$

$$\kappa_{\theta\theta} \rightarrow (\kappa_{\theta\theta})_0 + \Delta\kappa_{\theta\theta} \tag{3.61}$$

$$\frac{dW}{dR} \rightarrow \left(\frac{dW}{dR}\right)_0 + \Delta\frac{dW}{dR} \tag{3.62}$$

Linearized Exact Membrane Shell (LEMS)

The linearized version of these equations can be found in the appendix of Budiansky [11].

Linearized Axisymmetric Exact Membrane Shell (LAEMS)

$$\frac{d}{dR}\left(R\Delta n_{\phi\phi}\right) = \Delta n_{\theta\theta} \quad \text{(Equilibrium)} \tag{3.63}$$

$$\kappa_\phi \Delta n_{\phi\phi} + \kappa_\theta \Delta n_{\theta\theta} = \Delta p \quad \text{(Equilibrium)} \tag{3.64}$$

$$\frac{d}{dR}\left(\kappa_{\theta\theta}\Delta r + R\Delta\kappa_{\theta\theta}\right) = \Delta\kappa_{\phi\phi} \quad \text{(Compatibility)} \tag{3.65}$$

$$Eh\Delta\varepsilon_\theta = \Delta n_\theta - \nu\Delta n_\phi \quad \text{(Constitutive)} \tag{3.66}$$

$$Eh\Delta\varepsilon_\phi = \Delta n_\phi - \nu\Delta n_\theta \quad \text{(Constitutive)} \tag{3.67}$$

$$\Delta\varepsilon_\phi = \frac{ds}{dS} - 1 \quad \text{(Kinematic)} \tag{3.68}$$

$$\Delta\varepsilon_\theta = \frac{\Delta u_r}{R} \quad \text{(Kinematic)} \tag{3.69}$$

Linearized Axisymmetric Membrane Shell (LAMS)

Through this general linearization process, the LAMS model is shown to be identical to LAEMS model. In addition, the LAMS model is also identical to the AMS model, thereby showing that the AMS model is already linear.

$$\frac{d}{dR}\left(R\Delta N_{\phi\phi}\right) = \Delta N_{\theta\theta} \quad \text{(Equilibrium)} \tag{3.70}$$

$$\frac{\Delta N_{\phi\phi}}{R_\phi} + \frac{\Delta N_{\theta\theta}}{R_\theta} = \Delta p \quad \text{(Equilibrium)} \tag{3.71}$$

$$Eh\Delta\varepsilon_\theta = \Delta N_\theta - \nu\Delta N_\phi \quad \text{(Constitutive)} \tag{3.72}$$

$$Eh\Delta\varepsilon_\phi = \Delta N_\phi - \nu\Delta N_\theta \quad \text{(Constitutive)} \tag{3.73}$$

$$R_\phi \sin\phi\cos\phi\frac{d}{dR}\left(\frac{1}{\sin\phi}\Delta u_\phi\right) = R_\phi\Delta\varepsilon_\phi - R_\theta\Delta\varepsilon_\theta \quad \text{(Kinematic)} \tag{3.74}$$

$$\Delta\varepsilon_\theta = \frac{\Delta u_r}{R} \quad \text{(Kinematic)} \tag{3.75}$$

Linearized Axisymmetric Improved Large Deflection (LAILD) from Curved

$$\frac{d}{dR}\left(R\ \Delta N_r(R)\right) = \Delta N_\theta(R) + R\left(\tfrac{dW}{dR}\right)_0 \Delta P(R) \text{ (Equilibrium)} \tag{3.76}$$

$$\frac{d}{dR}\left[R\Delta\ N_r(R)\left(\frac{dW}{dR}\right)_0\right] = R\Delta P(R) \quad \text{(Equilibrium)} \tag{3.77}$$

$$Eh\Delta\varepsilon_\theta(R) = \Delta N_\theta(R) - \nu\Delta N_r(R) \quad \text{(Constitutive)} \tag{3.78}$$

$$Eh\Delta\varepsilon_r(R) = \Delta N_r(R) - \nu\Delta N_\theta(R) \quad \text{(Constitutive)} \tag{3.79}$$

$$\Delta\varepsilon_r = \tfrac{d\Delta U}{dR} + \left(\tfrac{dW}{dR}\right)_0 \Delta\tfrac{dW}{dR} \quad \text{(Kinematic)} \tag{3.80}$$

$$\Delta\varepsilon_\theta = \tfrac{\Delta U}{R} \quad \text{(Kinematic)} \tag{3.81}$$

Linearized Axisymmetric Improved Large Deflection (LAILD) from Flat

In the flat case, the governing equations collapse to a set of nonsensical expressions for no initial stress resultant. The "from Flat" model hence does not exist.

Linearized Axisymmetric Large Deflection (LALD) from Curved

$$\frac{d}{dR}\left(R\ \Delta N_r(R)\right) = \Delta N_\theta(R) \quad \text{(Equilibrium)} \tag{3.82}$$

$$\frac{d}{dR}\left[R\Delta\ N_r(R)\left(\frac{dW}{dR}\right)_0\right] = R\Delta P(R) \quad \text{(Equilibrium)} \tag{3.83}$$

$$Eh\Delta\varepsilon_\theta(R) = \Delta N_\theta(R) - \nu\Delta N_r(R) \quad \text{(Constitutive)} \tag{3.84}$$

$$Eh\Delta\varepsilon_r(R) = \Delta N_r(R) - \nu\Delta N_\theta(R) \quad \text{(Constitutive)} \tag{3.85}$$

$$\Delta\varepsilon_r = \tfrac{d\Delta U}{dR} + \left(\tfrac{dW}{dR}\right)_0 \Delta\tfrac{dW}{dR} \quad \text{(Kinematic)} \tag{3.86}$$

$$\Delta\varepsilon_\theta = \tfrac{\Delta U}{R} \quad \text{(Kinematic)} \tag{3.87}$$

Linearized Axisymmetric Large Deflection (LALD) from Flat

As with the LAILD model, the governing equations collapse to a set of nonsensical expressions for no initial stress resultant. The "from Flat" model hence does not exist.

3.3 Model Accuracy and Solution Precision

The model hierarchy established in section 3.2.3 is used as the framework to assess the cumulative effect of modelling assumptions upon solution accuracy and precision. The only well-known exact solution for curved membranes describes the uniform expansion of a spherical membrane shell subject to constant pressure; other well-known solutions involve models with various assumptions, often with a near-flat geometry. The goal of this work is to explore model accuracy and solution precision for parabolic mirrors; and so, to avoid the geometric limitations of the known exact solutions, the geometrically-exact model will be used to generate reference problems.

3.3.1 Approach

The procedure for quantifying the level of modelling error from different modelling assumptions is summarized by the flow diagram in Figure 3.5. The boundary condition, initial shape, and final shape are chosen initially, from which the inverse solver determines the required pressure loading. For an arbitrary choice of shapes, the pressure loading will vary radially. The boundary conditions, initial shape, and pressure loading are then applied to an approximate model to determine an approximate final shape. The difference in shapes between the exact and approximate final shapes is significant; the difference directly represents the prediction error of the approximate model. This approach quantifies the effects of modelling assumptions for any chosen class of geometries and loads.

The connection to mission-critical optical performance is found in the "Performance Model" block of Figure 3.5. For error much larger than the tolerances of the optical telescope of interest, the final shape prediction error is sufficient to characterize the error trends. For smaller error, however, as explained in section 2.3, the most appropriate error metric is a ray-traced optical performance metric. A comparison of optical-type errors in the models and solutions quantifies the impact of modelling decisions upon the mission-critical performance. The area average is taken as an optics standard that condenses the spatial information into a single number, and the standard deviation is used in order to de-emphasize the mean error.

These quantified measures of error will be correlated to the modelling assumptions, as summarized in Figure 3.4, to determine an appropriate range of utility for the model.

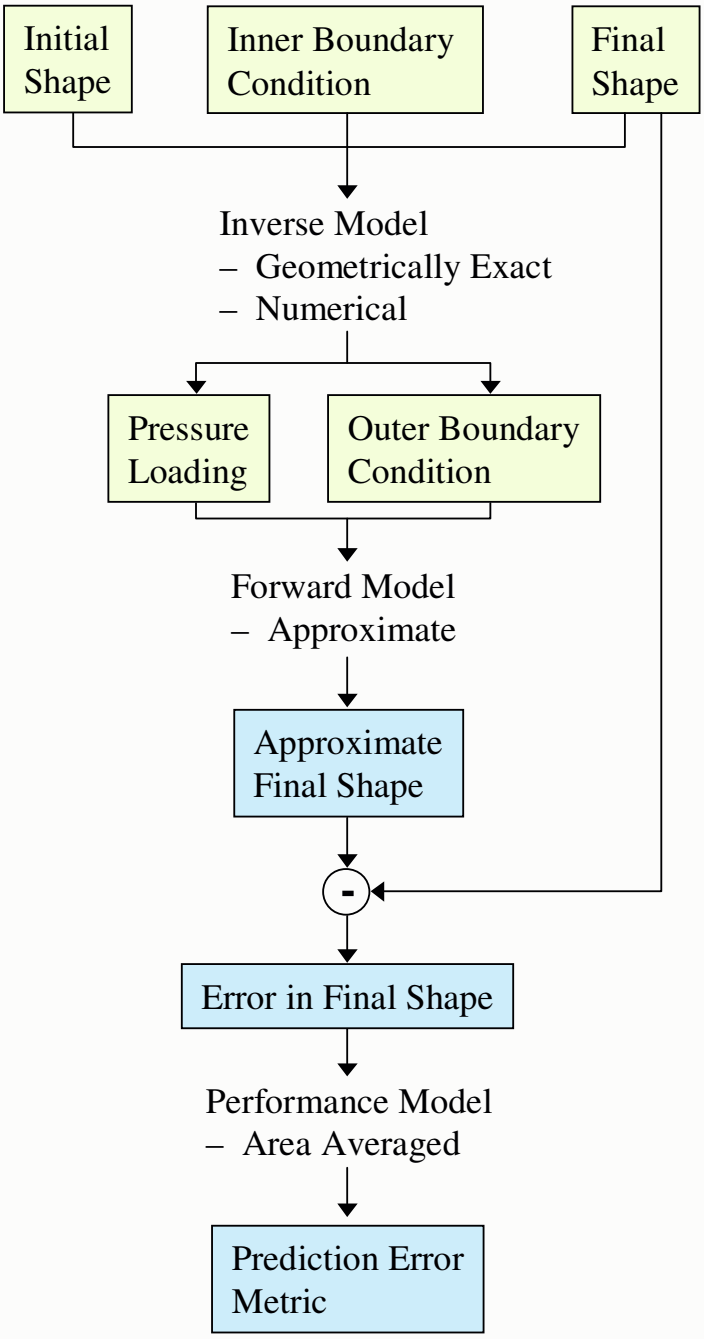

Figure 3.5: Analysis flow for comparing solutions from "approximate" models — models with assumptions – to solutions from a geometrically exact model.

Moreover, for a single given set of initial shape, boundary conditions, and loading, the use of multiple solution methods leads to a solution method comparison as represented notionally in Figure 3.3.

3.3.2 Inverse Solver

The inverse solver for the geometrically exact model of Figure 3.5 is taken directly from the inverse-design work in Chapter 4 (also [17] and [24]). The initial shape and final shape are chosen independently, but the boundary conditions are prescribed as functions of the shape change.

The Galerkin solution of Croll [15] is used to generate the meridional stress resultant at $\bar{r} = 0$. Although not physically a boundary location, the zero radial position ($\bar{r} = 0$) is used as a mathematical boundary condition. Both the initial and final shapes are assumed to be deflection solutions for a flat initial geometry, and the difference in stress resultant solutions for the two cases produces an estimate for the boundary stress resultant.

$$\bar{N}_m(0) = C\frac{1}{256}\frac{(3-\nu)}{(1-\nu)}\left[\left(\frac{1}{f_F}\right)^{\frac{2}{3}} - \left(\frac{1}{f_I}\right)^{\frac{2}{3}}\right] \tag{3.88}$$

for initial and final focal ratios, f_I and f_F. Since Equation 3.88 is only an estimate, the constant C is included to ensure a positive load and positive stress resultants over the whole range of $\bar{r}$. This small, positive constant ($C \approx 1$) is adjusted manually for each class of problem.

The circumferential stress resultant is set to the same value as the meridional stress resultant, $\bar{N}_c(0) = \bar{N}_m(0)$. Since the inverse solver requires a strain boundary condition, the constitutive equations are used to transform from stress resultants to strains. In addition, the conditions at only one boundary are specified, as described in Chapter 4. The boundary condition at $\bar{r} = 1$ is an output of the inverse solver.

3.3.3 Solution Methods

In order to compare model properly against each, without the bias of differing implementations, a common solution technique is required. *Finite differences will be used as the common solution method for quantifying the limiting modelling error* for the following reasons:

- The finite difference method is considered a standard solution technique for differential equations;
- The finite difference method can be implemented in all of the models and problem classes of interest; and
- The precision of a finite difference method is based upon the difference between points on the grid. Hence the precision of the solution can reliably be increased by increasing the density of points. Other solution methods, such as the assumed modes methods, are limited in ultimate predictive accuracy by a priori decisions about the shape functions.

3.4 Summary

In this chapter model concepts are introduced by discussions of model requirements, examples from the literature, and model error. Model accuracy is defined as the fundamental limit on the accuracy of the prediction from the best solution to the model equations, and solution precision is defined as the additional error due to the solution method.

A hierarchy of models is established through a methodical derivation process, and the different models are identified with past efforts from the literature. With this hierarchy the set of assumptions that feed into a given model are explicitly given. A similar set of models is given for linearized versions of the same models.

A framework for measuring and assessing the prediction error, decomposed into model error and solution precision, using comparisons of static axisymmetric models to the geometrically exact static axisymmetric results. Various solution methods from the literature are explored, but the finite difference method is chosen as a standard method that promised to eliminate the solution precision error for a sufficiently large number of intervals.

Chapter 4

Axisymmetric Shape Forming

Objective of Chapter:

To expand the static shape-forming design space for doubly-curved membranes by investigating combinations of initial geometry, material properties, and loading that produce shapes desired for telescope primary mirrors.

Current design concepts for large, spaceborne membrane reflectors specify aspheric initial shapes with intrinsic manufacturing and deployment difficulties. The development in this chapter expands the accepted design space of membrane mirror initial shapes by showing how a radial distribution in load or stiffness can produce a final parabolic shape from spherical, conical, or flat initial shapes. More than just solve a few design cases, the inverse solver resulting from this work enables a rich set of geometries to be considered in the assessment of model accuracy.

4.1 Introduction

Structural behavior plays an important role for membrane primary mirrors because the static shape-forming determines the reflector performance whereas the response to dynamic disturbance determines the ability to maintain that static performance. The need for fine pointing, tracking, and reorientation in spaceborne telescopes presents a significant dynamic

disturbance environment for structural control. The strong connection between statics and dynamics is due to the significant dependence of the dynamic behavior upon the steady-state mechanical conditions determined in the shape-forming problem.

The term "shape forming" refers to achieving a final desired shape in a structure after load has been applied. Because the final shape is pre-determined by other design influences — here the design of the optical system, either the initial shape or the load is determined via solutions of the governing equations. With the normal or "forward" solution defined as the determination of the deformed shape from initial shape and loads, the "inverse" solution then refers to the determination of initial shape or load with knowledge of the final shape. The shape forming problem for membrane mirrors thus pertains to the use of an inverse solver to find desirable combinations of initial shape, boundary conditions, and load given a final shape.

The current modelling need is to apply the governing equations in light of systems-level concerns to (1) produce a design tool for systems design decisions and (2) create a numerical tool for assessment of model accuracy. Figure 3.5 shows how the inverse solver is an integral part of the model accuracy analysis in this thesis.

4.1.1 Assumptions

The equations that govern the inverse design of the static, geometrically-exact behavior of axisymmetric membrane shells are developed here in a non-dimensional form useful both for numerical scaling and for direct application to design. The equations correspond to the Axisymmetric Exact Membrane Shell (AEMS) model shown in Figure 3.4 and derived in detail in Appendix E.

The following assumptions are consistently used in this chapter:

- *Axisymmetry* – Implication for stress resultant tensor is a zero shear stress resultant component, with circumferential and meridional stress resultants as the principle values.

- *Torsion-free loading* – The loading does not lead to displacements in the circumferential direction.

- *No wrinkling* – Implication is that solutions with negative stress resultant solutions are considered invalid and hence discarded.

- *Material selection* – The membrane material NASA LaRC CP-1 is chosen as a representative membrane material; the material properties are found in Appendix C. An elastic modulus of $2.17 \times 10^9 Pa$ and a yield strength of $9.99 \times 10^7 Pa$ mean a non-dimensional elastic modulus $\frac{E}{\sigma_Y}$ just above 20; for simplicity—and because the error in the modulus measurements is not even known— the non-dimensional value of 20 is used here for elastic modulus. The Poisson's ratio is taken to be $\nu = 0.35$ for the design studies in this chapter.

- *Geometry* – The mirror system under study is assumed to have unity focal ratio in accordance with the discussions in Chapter 2. In addition, mostly annular geometries are considered in this chapter. The inner boundary is chosen without optimization to be at $\bar{r} = 0.2$ as a location with little loss in total reflecting area. The boundary conditions are specified at this inner boundary point, and so an inner boundary is shown to be useful as another design parameter. It is noted, however, that the solver developed here also applies to the filled geometries that are used in the other chapters (see Figure 2.2).

The discussions in Chapter 2 provide the following goals for the shape and mechanical state of a membrane mirror.

- Initial shape easy to manufacture
- Principle stresses positive
- Principle stresses as large as possible without creep
- Folding requirement for stowage minimized

In this chapter a membrane design guideline of small yet positive principle stress resultants is applied to produce a set of non-dimensional static-forming cases with favorable mechanical states.

4.1.2 Scope

Simple methods, i.e. a flat membrane with uniformly applied pressure and fixed boundary conditions, do not produce an optical-quality membrane paraboloid shape; a good explanation of the resulting "W-profile error" is given by Meinel and Meinel [59]. *The literature*

provides three widely-discussed methods of static shape-forming of paraboloid membrane mirrors [23, 68]:

1. Mirror with near-paraboloid prescription loaded by a radially-constant pressure;
2. Flat mirror loaded with constant pressure and radial boundary displacements (final shape is notably still not a paraboloid); and
3. Unloaded paraboloid membrane.

Each method has difficulties with manufacturing, deployment, final shape, and/ or dynamic behavior. This apparent difficulty in achieving a good solution — and lack of clear path forward — indicates the need to explore more static-forming approaches.

The cases studied in this chapter are all represented in Table 4.1. Cone, flat, and sphere initial shapes are selected because of ease-of-manufacture due to symmetry and potential benefits in deployment. The case of a near-paraboloid initial shape, Case 7 in Table 4.1, is included as a comparison to more conventional ways of viewing the shape-forming problem. The near-paraboloid results are available in the literature [25] and so are not developed here. For a desired non-dimensional stress resultant of 0.05 and a final shape of an $f/1$ paraboloid the pressure and boundary load are found to be $\bar{p} = 0.02291$ and $\bar{F}_v = 0.001150$. The design space is searched by comparing the mechanical state of many sets of the design parameters–initial shapes and boundary conditions– but only one solution set per case is presented in this chapter.

Figure 4.1 summarizes the static shape forming choices as a flow of design choices. The design choices lead to three different types of problems:

- Constant pressure and prescribed initial shape (Case 7 of Table 4.1)
- Prescribed pressure and chosen initial shape (Cases 1–3 of Table 4.1)
- Prescribed extensional stiffness and chosen initial shape (Cases 4–6 of Table 4.1)

Two static structural response cases are explored in accordance with foreseeable technology.

- The application of a radially-varying pressure prescription is shown to form a final paraboloid shape for constant extensional stiffness.

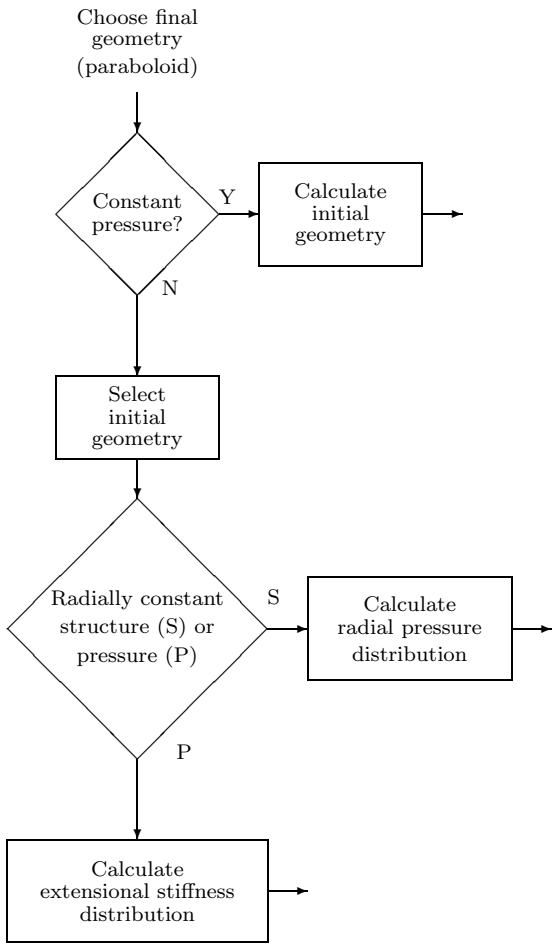

Figure 4.1: Description of solution choices once a final geometry has been determined. An arrow to the right indicates that the type of problem has been determined.

Table 4.1: Shape-forming cases in which the final geometry is a paraboloid. The shapes are all annular, i.e. each has a center cut-out.

Case	Initial Shape	Pressure	Extensional Stiffness
1	Flat	Prescribed: $\bar{p}(\bar{r})$	Constant
2	Cone	Prescribed: $\bar{p}(\bar{r})$	Constant
3	Spherical	Prescribed: $\bar{p}(\bar{r})$	Constant
4	Flat	Constant	Prescribed: $Eh(r)$
5	Cone	Constant	Prescribed: $Eh(r)$
6	Spherical	Constant	Prescribed: $Eh(r)$
7	Prescribed: Near-Paraboloid	Constant	Constant

While current experience with membrane structures tensioned in space lies primarily with pressure provided uniformly by a gas [21], electrostatic control provides a means to apply a pressure gradient. The electrostatic control of membrane mirrors received much attention during previous large-space-structure efforts by NASA [61], and the encouraging results indicate that the challenges are based in engineering design rather than fundamental physics. Deflection control is achieved as two surfaces are charged to opposite polarity, and the charge attraction results in a transverse pressure-type loading on the surfaces. Thus a radially-varying pressure is deemed to be feasible for membrane mirrors.

- Similarly, the application of constant pressure to membranes with a radially-varying extensional stiffness prescription is shown to form a final paraboloid shape. With the extensional stiffness the product of elastic modulus and thickness, this distribution can be achieved by either a distribution of strength or a varying thickness.

These solutions are achieved in this chapter by reducing the governing equations of the exact membrane shell model to a pair of first-order, nonlinear differential equations in the principle strains. After the solver development, the solutions to the example cases from Table 4.1 are discussed. The solution process is shown to be verified, too.

4.2 Inverse Solver

In this section the equations for the inverse solver are developed and results from the cases of Table 4.1 are presented. The last section shows how the implementation of the inverse solver has been verified.

4.2.1 Governing Equations

Figure 4.2 outlines the solution method used for the inverse solver as a process flow of field variables and equations. The final shape is selected according to required performance,

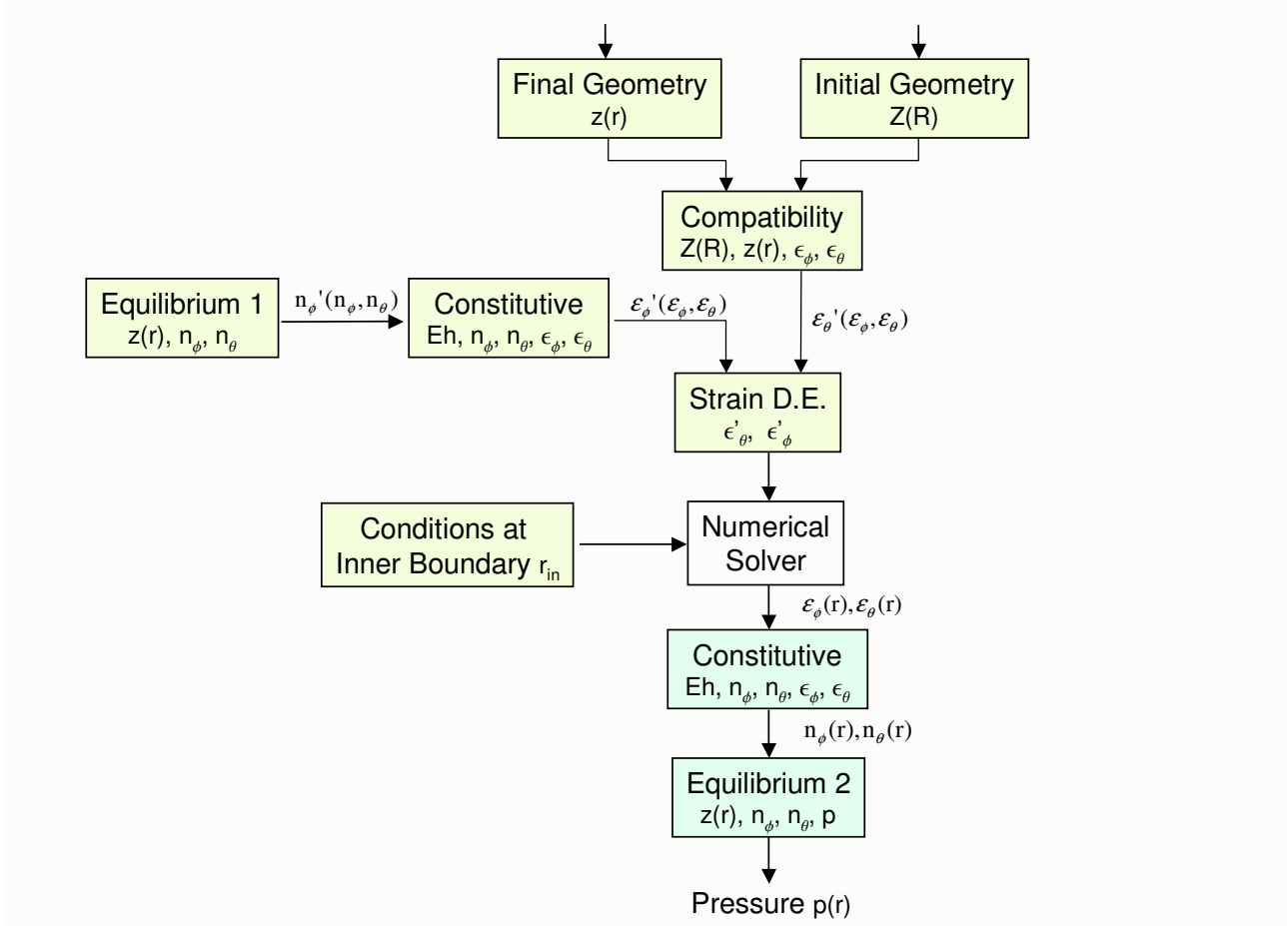

Figure 4.2: Inverse solution process to calculate the pressure distribution for the static shape-forming problem. All variables are non-dimensional although the over-bar notation is omitted.

and the initial shape is chosen independently so as to satisfy unrelated needs such as manufacturing. The kinematic relations provide a unique form of the compatibility equation

that incorporates both initial and final geometries. The combination of the compatibility equation, one of the two equilibrium equations, and the constitutive equations results in a pair of nonlinear, first-order differential equations in terms of principle strains. With the addition of a boundary condition either in the form of a pair of strains (or, equivalently, a pair of stress resultants that are mapped into strains), the strain distribution is calculated via a numerical solver. The constitutive equations map the strains into the stress resultants, and the one unused equilibrium equation allows the pressure distribution to be calculated.

The modelling approach taken here is similar to Chapter 14 of Timoshenko [82] with several important modifications from Greschik *et al* [23]. A similar approach that is only applied to a sphere-to-sphere geometry is found in Juang and Huang [39]. Figure 4.3 shows the geometry of the unloaded and loaded membranes, and Appendix B non-dimensional form. The choice of non-dimensional quantities is determined according to the form of the equations and a desire to have well-conditioned values. The result is a set of variables whose magnitudes are near unity; the stress resultants $\bar{n}_\phi$ and $\bar{n}_\theta$ (integral of stress through the thickness, also the "membrane stress") are particularly useful because the non-dimensional form can be directly used in "percent of yield stress" analysis. *In later chapters the denominator term for non-dimensional pressure and stress resultant will be extensional stiffness Eh rather than the product of thickness and yield strength $h\sigma_Y$.* The difference in choice of normalizing denominator is the difference between Tables B.1 and B.2 in Appendix B. Equivalent to setting $\frac{E}{\sigma_Y}$=1 here, the change to use of extensional stiffness is made for the model-accuracy problem because one variable fewer can be specified in the problem.

For a paraboloid with a z-axis as the axis of rotation and a focal length of $2f_\infty r_{out}$, the dimensioned final shape is given by

$$z(r) = b_0 + \frac{1}{8f_\infty r_{out}} r^2 \tag{4.1}$$

The non-dimensional form is given by

$$\bar{z}(\bar{r}) = \frac{b_0}{r_{out}} + \frac{1}{8f_\infty} \bar{r}^2 \tag{4.2}$$

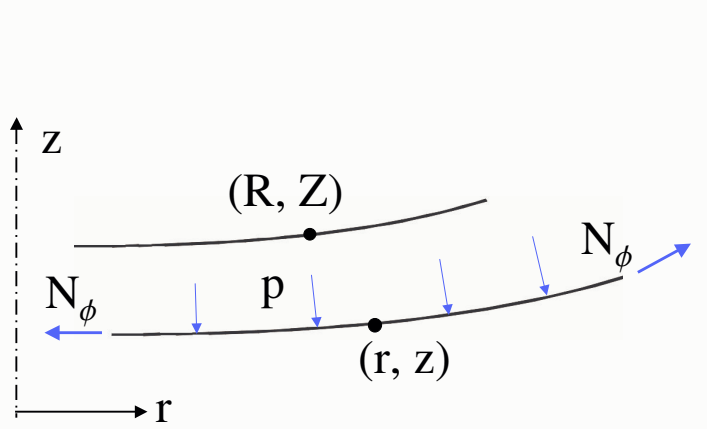

Figure 4.3: Mechanical diagram that shows a meridian of an annular membrane section. A point at $(\bar{R}, \bar{Z})$ moves to the location $(\bar{r}, \bar{z})$ after loading.

with the geometry further defined by curvature $\bar{\kappa}$ and angle from the radial axis α.

$$\tan\alpha = \frac{\bar{r}}{4f_\infty} \tag{4.3}$$

$$\bar{\kappa} = \frac{\frac{\partial^2 \bar{w}}{\partial \bar{r}^2}}{\left(1+(\frac{\partial \bar{w}}{\partial \bar{r}})^2\right)^{\frac{3}{2}}} \tag{4.4}$$

The initial conical shape is described by

$$\bar{Z}(\bar{R}) = \bar{a}_0 + \bar{a}_1 \bar{R} \tag{4.5}$$

and the initial spherical shape is given by

$$\bar{Z}(\bar{R}) = \bar{c}_0 - \sqrt{\bar{r}_{sph}^2 - \bar{R}^2} \tag{4.6}$$

The initial shape for a flat configuration is the same as for the cone but with a zero slope $\bar{a}_1 = 0$. The two equilibrium equations from the AEMS model are repeated from Equations 3.11 and 3.12.

$$\bar{p} = \bar{n}_\phi \bar{\kappa} + \frac{\bar{n}_\theta \sin\alpha}{\bar{r}} \tag{4.7}$$

$$\bar{n}_\theta = \frac{d}{d\bar{r}}\left(\bar{r}\bar{n}_\phi\right) \tag{4.8}$$

No small-angle assumptions are made in the equations, and so this development is geometrically exact. The constitutive relations are defined as in Greschik et al [23] as

$$\bar{E}\epsilon_\theta = \bar{n}_\theta(1+\epsilon_\phi) - \nu\bar{n}_\phi(1+\epsilon_\theta) \tag{4.9}$$

$$\bar{E}\epsilon_\phi = \bar{n}_\phi(1+\epsilon_\theta) - \nu\bar{n}_\theta(1+\epsilon_\phi) \tag{4.10}$$

The extension terms of the form [1+strain] in Eqns 4.9 and 4.10 are included to effect the transformation from the undeformed basis into the deformed basis in which equilibrium is considered. Chapter 5 has a thorough discussion on constitutive relations that shows Eqns 4.9 and 4.10 to have an inexact form for linear Hookean behavior. The error in form, however, is also shown to have a negligible effect on the shape prediction error, and so these constitutive relations are considered sufficiently valid for the problems and models in this thesis. The strains are defined by the stretching of a differential arc length $\bar{r}d\theta$ and differential meridional path $d\bar{s}$.

$$\epsilon_\theta(\bar{r}) = \frac{\bar{r}}{\bar{R}} - 1 \tag{4.11}$$

$$\epsilon_\phi(\bar{r}) = \frac{d\bar{s}}{d\bar{S}} - 1 \tag{4.12}$$

The curvature and trigonometric functions are also useful to the current development.

$$\bar{\kappa} = \frac{d\alpha}{d\bar{s}} \tag{4.13}$$

$$\frac{d\bar{r}}{d\bar{s}} = \cos\alpha(\bar{r}) \tag{4.14}$$

$$\frac{d\bar{z}}{d\bar{s}} = \sin\alpha(\bar{r}) \tag{4.15}$$

Consequence of No Pressure Loading

The lack of a pressure-type load can lead to a wrinkled state. Non-positive stress resultants at any point indicate a wrinkling condition and a need for a more specialized model that those in this thesis. With a need for shape precision in the final structure of membrane mirrors, wrinkling is unallowable and so non-positive stress resultants should be avoided. This condition of non-positive stress resultants thus means that a pressure-type loading is required. This point is explicitly shown by solving for the stress resultants in Eqns 4.7 and 4.8 given a zero value of pressure and a non-zero vertical line load $\bar{F}_v$ at the inner

boundary.

$$\bar{n}_\phi(\bar{p}=0) = 4f_\infty \bar{F}_v \bar{r}_{in} \frac{\sqrt{1+\left(\frac{\bar{r}}{4f_\infty}\right)^2}}{\bar{r}^2} \tag{4.16}$$

$$\bar{n}_\theta(\bar{p}=0) = -4f_\infty \bar{F}_v \bar{r}_{in} \frac{1}{\bar{r}^2\sqrt{1+\left(\frac{\bar{r}}{4f_\infty}\right)^2}} \tag{4.17}$$

The only function in the stress resultant solutions that can be non-positive is $\bar{F}_v$. With each stress resultant dependent upon an opposite sign of $\bar{F}_v$, one stress resultant is necessarily negative. A wrinkling condition exists under such loading, and a wrinkling analysis is therefore required to determine deformation behavior.

Differential Equations

The differential form of Eqn 4.11 is taken as

$$d\bar{R} = \frac{d\bar{r}}{1+\epsilon_\theta(\bar{r})} - \frac{\bar{r}}{(1+\epsilon_\theta(\bar{r}))^2}\frac{d\epsilon_\theta(\bar{r})}{d\bar{r}}d\bar{r} \tag{4.18}$$

Eqn 4.18 is substituted in Eqn 4.12 to get

$$d\bar{R}(1+\epsilon_\phi(\bar{r}))\sqrt{(\frac{d\bar{Z}}{d\bar{R}})^2+1} = d\bar{r}\sqrt{(\frac{d\bar{z}}{d\bar{r}})^2+1} \tag{4.19}$$

When Eqn 4.18 is substituted for $d\bar{R}$ in Eqn 4.19, the differential equation of circumferential strain is found in terms of strain components, initial geometry, and final geometry.

$$\frac{d\epsilon_\theta(\bar{r})}{d\bar{r}} = \frac{1+\epsilon_\theta(\bar{r})}{\bar{r}}\left(1-\frac{1+\epsilon_\theta(\bar{r})}{1+\epsilon_\phi(\bar{r})}\sqrt{\frac{(\frac{d\bar{z}}{d\bar{r}})^2+1}{(\frac{d\bar{Z}}{d\bar{R}})^2+1}}\right) \tag{4.20}$$

The differential equation for the meridional strain is found by solving Eqns 4.9 and 4.10 for the stress resultants in terms of the strains, and these results are substituted into Eqn 4.8 to form a differential equation in terms of strain. With a substitution for $\frac{d\epsilon_\theta(\bar{r})}{d\bar{r}}$ by Eqn 4.20, the differential equation is determined.

$$\frac{d\epsilon_\phi(\bar{r})}{d\bar{r}} = \frac{1+\epsilon_\theta(\bar{r})}{1+\epsilon_\phi(\bar{r})}\left(\frac{1}{\bar{r}}\right)\left((\epsilon_\theta-\nu)+(\nu-\epsilon_\phi)\sqrt{\frac{(\frac{d\bar{z}}{d\bar{r}})^2+1}{(\frac{d\bar{Z}}{d\bar{R}})^2+1}}\right) \tag{4.21}$$

Together Eqns 4.20 and 4.21 form a system of first-order, nonlinear differential equations

Table 4.2: Parameters for radially-varying pressure cases. "$\bar{a}_1$" is the slope in Eqn 4.5. Final focal ratio is $f/1$ in each case.

Case	Initial Shape	Parameter	$\bar{n}_\theta(\bar{r}=0.2)$	$\bar{n}_\phi(\bar{r}=0.2)$
1	Flat	$\bar{a}_1 = 0$	0.3	0.3
2	Cone	$\bar{a}_1 = 0.15$	0.04	0.04
3	Spherical	$\bar{r}_{sph} = 4$	0.05	0.05
7	Near-Paraboloid	$\bar{p} = 0.02291$		

that can be numerically integrated once boundary conditions are chosen. Although strains are needed as boundary conditions, stress resultant boundary conditions can be chosen and mapped to strain boundary conditions through the use of Eqns 4.9 and 4.10.

4.2.2 Prescribed, Radially-Varying Pressure

The first static forming design problem is examined is the calculation of the radial distribution of pressure-type load required to move a membrane from a given initial shape into a given final shape. Here Eqns 4.20 and 4.21 are solved for Cases 1–3 of Table 4.1 subject to the parameters in Table 4.2. The constant in each shape equation is set such that the position at the outer rim is at $\bar{z} = 0$. The difference between initial and final shapes is presented in Figure 4.4 for each case in Table 4.2 and indicates that a range of load magnitudes will be required. The near-paraboloid case will be discussed in a later subsection but is included in the plots for reference. The spherical and near-paraboloid cases are close to the final paraboloid while the flat undergoes the largest deflection.

The pressure distributions required for each initial shape are presented together in Figure 4.5. Consistent with the differences in shape, the spherical and near-paraboloid require rather little pressure to form a paraboloid as compared to the flat and more modest cone case. The large loading required to make a flat into a paraboloid makes it an undesirable case for the current choice of membrane material. The stress resultant and strains for the same cases as in Figure 4.5 are shown in Figures 4.6–4.7. The basic trend for stress resultants and strains in the same as for pressure; the shapes that start out near a paraboloid require much less loading. The distribution of stress resultant and strain is, however, different for each initial shape and has some dependency upon the choice of inner boundary load.

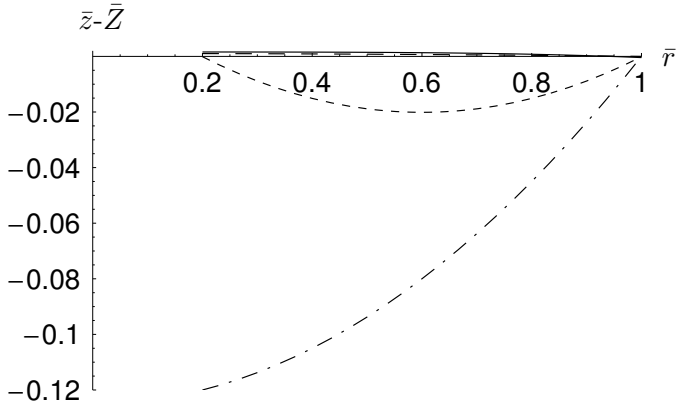

Figure 4.4: *Prescribed-pressure design* — Shape differences between final shape and spherical (—), conical (- -), and flat (– · –) initial shapes, Cases 1–3 of Table 4.1. The near-paraboloid Case 7 is shown (– –) for comparison.

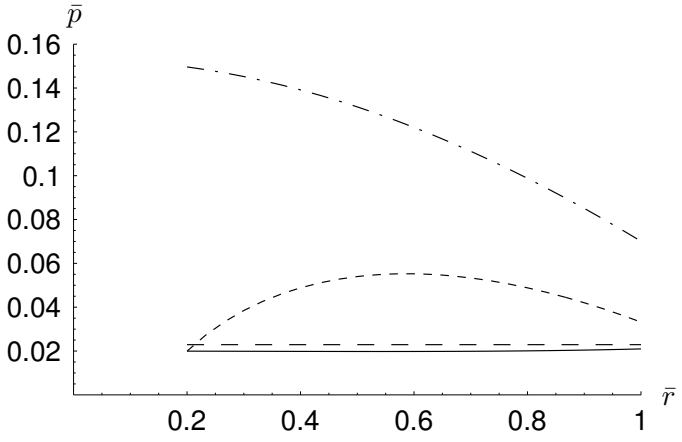

Figure 4.5: *Prescribed-pressure design* — Radially-varying pressure distributions for spherical (—), conical (- -), and flat (– · –) initial shapes, Cases 1–3 of Table 4.1. The near-paraboloid Case 7 is shown (– –) for comparison.

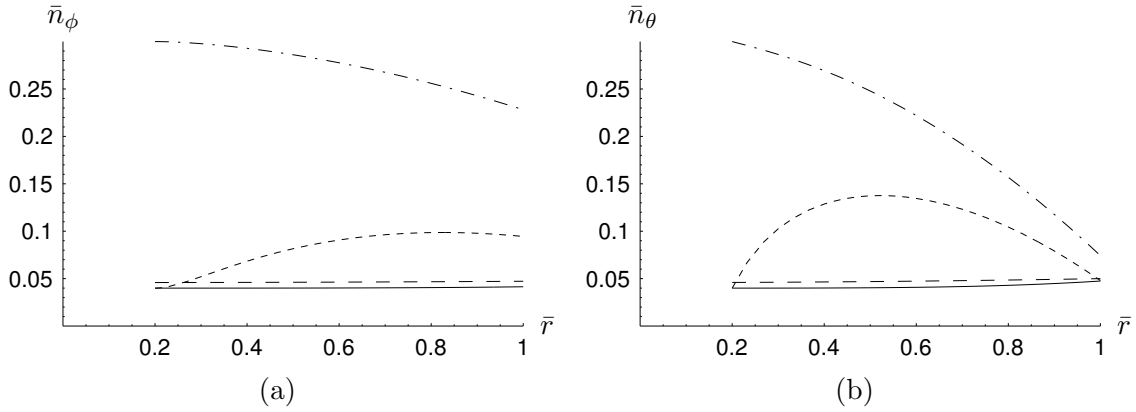

Figure 4.6: *Prescribed-pressure design* — Radially-varying distributions of (a) meridional stress resultant and (b) circumferential stress resultant for spherical (—), conical (- -), and flat (– · –) initial shapes, Cases 1–3 of Table 4.1. The near-paraboloid Case 7 is shown (– –) for comparison.

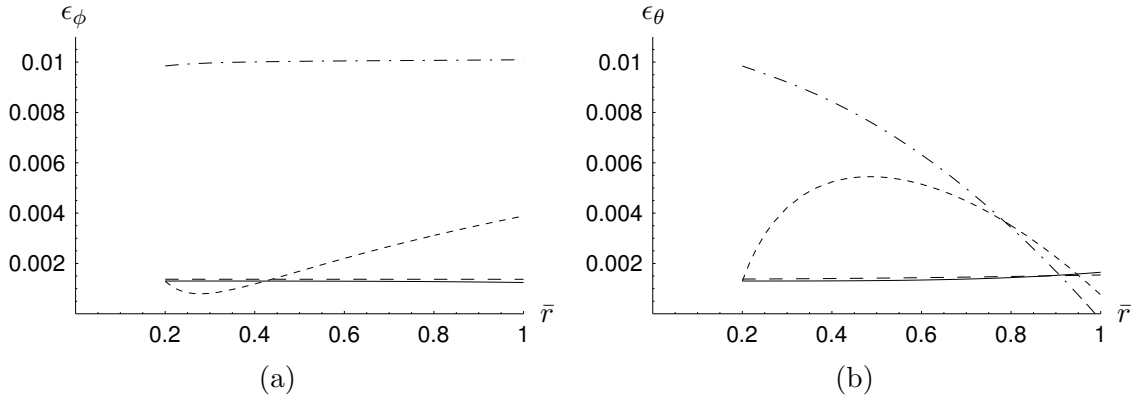

Figure 4.7: *Prescribed-pressure design* — Radially-varying distributions of (a) meridional strain and (b) circumferential strain for spherical (—), conical (- -), and flat (– · –) initial shapes, Cases 1–3 of Table 4.1. The near-paraboloid Case 7 is shown (– –) for comparison.

Table 4.3: Parameters for radially-varying extensional stiffness cases. $\bar{a}_1$ is the slope in Eqn 4.5. Final focal ratio is $f/1$ in each case.

Case	Initial Shape	Pressure	Parameter	$\epsilon_\phi(\bar{r}=0.2)$	$\epsilon_\theta(\bar{r}=0.2)$
4	Flat	0.111	$\bar{a}_1 = 0$	0.01	0.01
5	Cone	0.047	$\bar{a}_1 = 0.15$	0.0015	0.0015
6	Spherical	0.024	$\bar{r}_{sph} = 4$	0.002	0.002

4.2.3 Prescribed, Radially-Varying Extensional Stiffness

If the extensional stiffness rather than pressure is allowed to vary with radial position, a set of designs can be found in which the initial shape forms the final shape under constant pressure. Several methods are possible: electromagnetic energy that degrades the stiffness in the prescribed pattern, laser removal of material to implement a thickness pattern, etc. Although the method for achieving a distributed extensional stiffness is not a well-understood problem, the solution will be presented here in order to show its merit.

The constant-pressure case is essentially the same as the radially-varying case, except that the equations are solved in a slightly different order. Since the pressure is constant and the extensional stiffness is variable, the extensional stiffness is determined after the equilibrium equation is applied to generate the stress resultants. The strains are explicitly given as boundary conditions this time because the variable extensional stiffness prevents a constant mapping between the strains and stress resultants.

In addition, since the thickness is used to normalize several of the quantities, the dimensioned form of the equations is necessary. The equations look the same without the over-bars, but the non-dimensional stiffness $\bar{E}$ becomes the extensional stiffness Eh. Since the problem is fully analogous to the non-dimensional problem, the non-dimensional formulation is used. The parameters used for the extensional-stiffness problems are listed in Table 4.3. Similar plots are shown as for the radially-varying pressure case.

The difference between initial and final shapes for each case is the same as given earlier in Figure 4.4. Figure 4.8 shows the relative change in extensional stiffness required for a constant pressure loading. The function values are divided by the respective area-averaged-RMS values in order to emphasize the relative distribution of extensional stiffness. This represents, for example, the thickness distribution that could be imparted onto an easily manufactured shape.

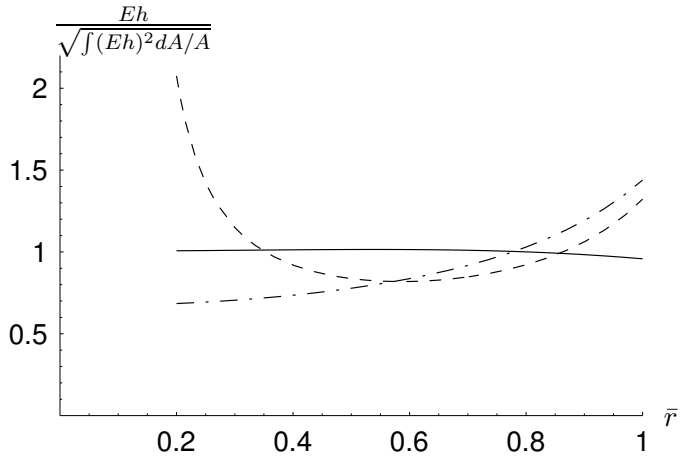

Figure 4.8: *Prescribed-extensional-stiffness design* — Radially-varying distributions of extensional stiffness for spherical (—), conical (- -), and flat (– · –) initial shapes, Cases 4–6 of Table 4.1.

Figures 4.9 through 4.10 represent the mechanical state in the final membrane for each of the cases. The distributions are different than in the prescribed-initial-shape case (Case 7), but the predictable trend of low strain (stress resultant) for the sphere and large strain (stress resultant) for the flat continues.

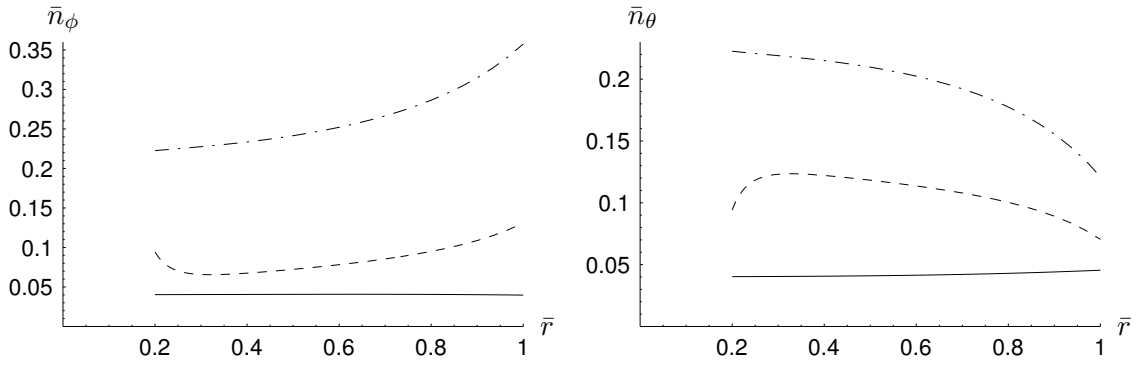

Figure 4.9: *Prescribed-extensional-stiffness design* — Radially-varying distributions of (a) meridional stress resultant and (b) circumferential stress resultant for spherical (—), conical (- -), and flat (– · –) initial shapes, Cases 4–6 of Table 4.1.

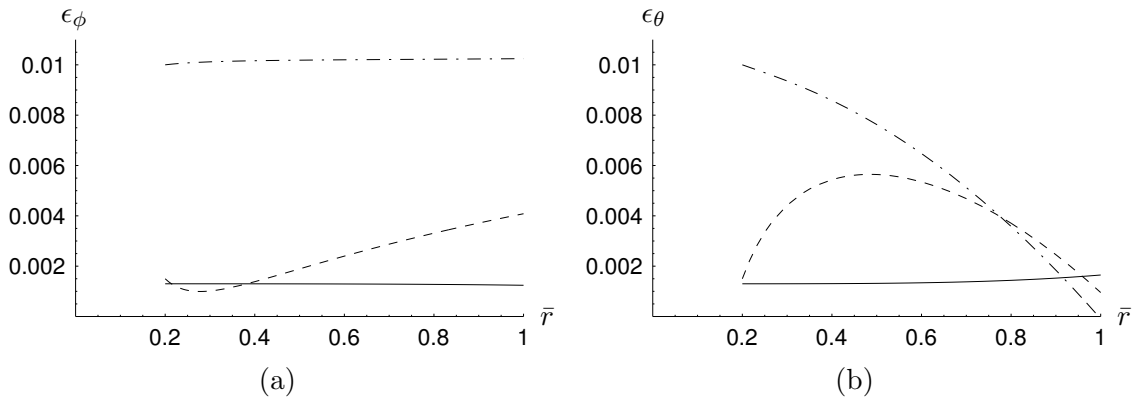

Figure 4.10: *Prescribed-extensional-stiffness design* — Radially-varying distributions of (a) meridional strain and (b) circumferential strain for spherical (—), conical (- -), and flat (– · –) initial shapes, Cases 4–6 of Table 4.1.

4.2.4 Verification of Numerical Implementation

The inverse solver is implemented in Mathematica software with high-accuracy and high-precision solvers taken from the included libraries. The accuracy of the solution is checked by two approaches that provide an absolute measure of the success of the solution.

- The residuals of the governing equations consistently have values that are either zero or numerically zero ($O(10^{-16})$) over the whole range of radial position. One example, forming a $\bar{r}_{sph}$=4 spherical cap from a $\bar{R}_{sph}$=3.999 cap, results in a residual for Eqn 4.7 that is identically zero for all $\bar{r}$. A similar example with forming an $f/5$ paraboloid from an $f/5.000001$ paraboloid results in $O(10^{-27})$ maximum error over $0 \leq \bar{r} \leq 1$.

- Constant-pressure expansion of a sphere is the only exact solution with a closed form that applies to this geometry. Have shown that my numerical implementation finds the pressure to be constant to $\sim 10^{-16}$ accuracy. Figure 4.11 provides an example from the solution to the $\bar{r}_{sph}$=4-forming problem; the error is $O(10^{-16})$, and so the percent difference between exact and numerical is seen to be $O(10^{-16}\%)$.

4.2.5 Observations on Shape Forming

The shape-forming design process, from developing the equations to implementing the solutions for a range of shapes, has led to a number of comments and observations relevant to the shape-forming problem.

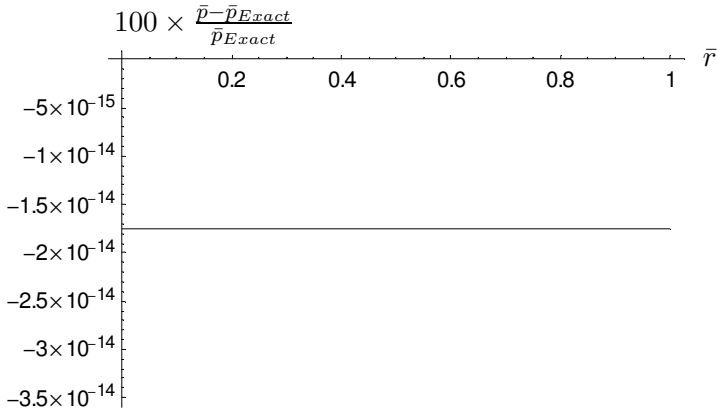

Figure 4.11: $\bar{R}_{sph}$=3.8-to-$\bar{r}_{sph}$=4 problem — Percent difference between calculated pressure distribution and exact pressure value.

- Solution method/ approach:
  - With all of the geometric parameters chosen, a degree of freedom still exists in the problem. The designer can influence the stress-resultant distribution noticeably by the choice of the boundary condition (magnitude and location). Increasing and decreasing the boundary load has the accompanying effect of increasing and decreasing the stress resultant distribution.
  - The design results contained in this effort are not formally optimized. A parametric analysis led to the final choices in initial shapes and boundary loads.
- Numerical implementation:
  - The non-dimensional form of the equations presented here is also useful numerically because the values of the variables have been conditioned well. That is, the variables implemented here all have values within a few orders of magnitude of one.
  - Both the meridional and circumferential strains are specified at the boundary because the work here is inverse design rather than a standard boundary-value problem. Although the circumferential stress resultant/ strain cannot be applied mechanically, the value can be chosen as part of a design effort to find favorable solutions. Because of this freedom in the solution, the numerical solution is easier

to obtain due to the fact that the boundary conditions are specified at only one location.

  - Use of the outer boundary $\bar{r} = 1$ to specify boundary loads often leads to solutions with values that diverge near the inner boundary. Specifying the boundary condition at the inner boundary is found to be the most practical in terms of finding the better solutions in less time.

- Extension of the results:

  - The non-dimensional framework of this process leads to interesting questions about the most favorable material properties. Yield stress provides an example. Two materials with the same elastic modulus yet different yield strengths produce two different non-dimensional solutions to this non-linear problem. Studying the non-dimensional results can lead to identification of better materials choices.

  - Sphere-to-paraboloid represents the best combination of easy-to-manufacture initial shape and reasonable distributed load. In fact, a sparse-aperture mirror can be formed from subapertures with spherical initial shapes (see Figure 2.2). The individual subapertures can be rolled for stowage to eliminate the need for folds. Each subaperture can be manufactured identically, and the pressure gradients required to form paraboloid subapertures are shown here to be small. Hence useful directions in system design can be taken from the shape-forming results.

4.3 Summary

A non-dimensional formulation of the static shape-forming method with good numerical qualities is presented. The optical engineer can determine the final shape, and manufacturing concerns can determine the initial shape. The designer can work with symmetric initial-shape designs and seek a solution with the most advantageous mechanical property distribution. The innovation comes in considering distributions in the pressure-type load or in the extensional stiffness. The design of the mechanical state is aided by the form of the equations; the form of the stress resultant is useful for example, because direct decisions can be made with respect to yielding concerns based upon the non-dimensional modulus of the material.

Spherical and conical initial shapes are shown to be usable for membrane mirrors when the final shape is required to be parabolic. The specified final shape is achieved either through a combination of varying-pressure and constant extensional stiffness or through a combination of constant pressure and radially-varying extensional stiffness.

Aside from shape-forming design, the inverse solver developed here is capable of solving a wide range of problems at a very high level of accuracy. This implementation of an inverse solver, with a demonstrated $O(10^{-14}\%)$ or better level of error, can be used to determine model accuracy as part of the model accuracy methodology laid out in Chapter 3.

Chapter 5

Constitutive Law

Objective of Chapter:

To analyze mathematically and compare numerically different assumptions underlying the constitutive equations for membranes in the context of predicting the optical-level deflection behavior of doubly-curved membrane mirrors.

5.1 Introduction

Along with the equilibrium and kinematic relations, the constitutive law forms a critical aspect of every structural model. The high-accuracy requirements of membrane mirror shape predictions demands that the constitutive law be examined for significant contributions to error. To examine the error of simplified relations, the exact constitutive law for a simple case is first examined. Linear elastic Hookean behavior, the most common linear elastic relation from material tests and the most commonly used in the literature, provides the best constitutive law for further study.

Deriving the equations for a non-axisymmetric solver highlight the case where the distinction between the use of first- and second-Piola-Kirchoff-type stresses become important. The practical issue is performing the geometric update on the shear-stress-resultant term in the middle of an iterative solver. Most of the literature lists the governing equations as first-Piola-Kirchoff-type stresses, and the complications arise in making geometric updates

to the shear terms (the first Piola-Kirchoff stress resultant tensor is non-symmetric). This issue of choosing the stress type is unresolved. Although these issues with the 3–D problem motivated some of the current work, the 3–D problem is beyond the scope of this document.

The constitutive relations from literature relevant to large membrane optics thus contain error when considering exact mathematical definitions. The discrepancy that motivated this work was the lack of symmetry in the stress resultant tensor during derivation of the non-axisymmetric models. Inconsistent definition and use of the Piola-Kirchoff stress resultant types lead to this problem, and the transformation to Cauchy-type stress resultant is not always mathematically consistent. In this chapter the definitions found in the relevant literature are compared with a mathematical development based upon continuum mechanics. This consistent development provides two lessons:

1. The required change in the form of the often-used constitutive and stress-resultant-transformation equations to become mathematically consistent.

2. For membrane shells, the impact of different constitutive-equation forms upon the :

   (a) Direct prediction of stress resultants;

   (b) Prediction of pressure from the inverse solver; and

   (c) Prediction of optical-quality shape when subjected to mechanical loads.

While the constitutive-law used in the literature indeed results in more error than even the linear law, the effect upon shape prediction for a range of constitutive law transformations is shown to be insignificant compared to the prediction errors due to geometric assumptions in the equilibrium equations.

5.2 Mathematical Description

In this section different stress-resultant types are defined. The differences arise from the transformation between coordinate bases as the reference lengths move from the undeformed body to the deformed body. Proper stress resultant and strain types are then applied to the constitutive equations. Substitution of small-strain expressions under the assumption of the axisymmetric membrane shell problem highlights the differences between the the various stress-resultant and strain definitions.

5.2.1 Definition of Stress Resultant Types

Although stress is a common load-per-area measure of internal loading in structural analysis, the nearly-two-dimensional nature of shells leads to a load-per-length measure: the stress resultant. Although the load and the length each require a reference basis to which the quantities are reckoned, the differentiation of basis and stress resultant types can be ignored in a typical small-strain analysis. With high quality predictions desired for optics, however, such approximations may introduce unacceptable levels of error to the shape prediction.

In this document the different stress resultant types are developed in a method that follows the stress-type derivation in a classic continuum mechanics text (Section 5.3 of Malvern [55]). Each stress type — Cauchy, first Piola-Kirchoff, and second Piola-Kirchoff — is shown to have an analog stress resultant type. Part (a) of Table 5.1 shows how the different types of stress are classified according to the reference basis of the resulting force and the reference basis of the area over which the force acts; similarly part (b) shows the analog quantities for stress resultant types.

Table 5.1: Description of (a) stress types and (b) stress resultant types according to the reference frame of the area or length and the reference basis of the resultant force.

(a) Stress

Stress Type	Reference frame of area over which stress is reckoned	Reference frame of equivalent force
Cauchy	Deformed	Deformed
First Piola-Kirchoff	Undeformed	Deformed
Second Piola-Kirchoff	Undeformed	Undeformed

(b) Stress Resultant

Stress Resultant Type	Reference frame of length over which stress resultant is reckoned	Reference frame of equivalent force
Cauchy	Deformed	Deformed
First Piola-Kirchoff	Undeformed	Deformed
Second Piola-Kirchoff	Undeformed	Undeformed

Figure 5.1 shows how the deformation changes the reference basis for the vectors. The

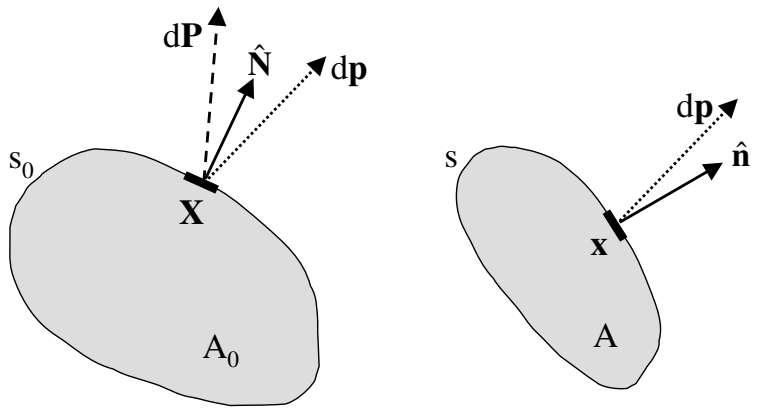

Figure 5.1: Representation of the difference between undeformed and deformed bases for normal directions $\{\hat{\mathbf{N}}, \hat{\mathbf{n}}\}$ and for resulting forces $\{d\mathbf{P}, d\mathbf{p}\}$. The surface, initially represented by the undeformed basis with area A_0 and one-dimensional linear boundary s_0, moves to a new position with a new deformed basis with area A and boundary s. $d\mathbf{p}$ is added to the undeformed body for illustration of need for transformations. Based upon Figure 5.8 of Malvern [55].

boundary point with initial position $\mathbf{X}$ moves to $\mathbf{x}$ in the deformed configuration, and the unit normal changes accordingly. The differential force that represents the stress resultant over the differential deformed length is shown as $d\mathbf{p}$; $d\mathbf{p}$ is also represented on the undeformed configuration to explicitly show a force in a deformed basis on the undeformed boundary.

The most important quantity for understanding the coordinate transformation from undeformed to deformed basis is the deformation gradient tensor $\mathbf{F}$. Capitol subscripts indicate the undeformed basis, and lower-case the deformed. Standard Einsteinian notation is used such that the i^{th} component of vector $\mathbf{x}$ is x_i .

$$\mathbf{F} = F_{iJ} = \frac{\partial x_i}{\partial X_J} \tag{5.1}$$

In dealing with surfaces, however, only the two curvilinear directions along the surface are relevant (the other direction has a 1 on the diagonal when maintaining full 3D notation).

Greek subscripts indicate two components.

$$\mathbf{F} = F_{\alpha B} = \frac{\partial x_\alpha}{\partial X_B} \tag{5.2}$$

From this definition come two other relations.

$$\begin{aligned} dx_\alpha &= F_{\alpha B} dX_B \\ dX_B &= F^{-1}_{B\alpha} dx_\alpha \end{aligned}$$

In a direct analog to how the differential lengths are represented, the differential forces $\{d\mathbf{P}, d\mathbf{p}\}$ are related by the deformation gradient.

$$dP_B = F^{-1}_{B\alpha} dp_\alpha \tag{5.3}$$

With the definitions from Table 5.1, the normal force vector resulting from the total stress over the thickness is found for each stress resultant type. For Cauchy-type stress resultant $\mathbf{N}^{(C)} = N^{(C)}_{\alpha\beta}$, Eqn 5.3 becomes

$$\begin{aligned} d\mathbf{P} &= \mathbf{F}^{-1} \cdot \left[(\hat{\mathbf{n}} \cdot \mathbf{N}^{(C)}) ds \right] \\ &= \hat{\mathbf{n}} \cdot \mathbf{N}^{(C)} \cdot \left(\mathbf{F}^{-1} \right)^T ds \end{aligned} \tag{5.4}$$

For first-Piola-Kirchoff-type stress resultant $N^{(1PK)}_{\alpha\beta}$, Eqn 5.3 becomes

$$\begin{aligned} d\mathbf{P} &= \mathbf{F}^{-1} \cdot \left[(\hat{\mathbf{N}} \cdot \mathbf{N}^{(1PK)}) ds_0 \right] \\ &= \hat{\mathbf{N}} \cdot \mathbf{N}^{(1PK)} \cdot \left(\mathbf{F}^{-1} \right)^T ds_0 \end{aligned} \tag{5.5}$$

Finally, for second-Piola-Kirchoff-type stress resultant $N^{(2PK)}_{\alpha\beta}$, Eqn 5.3 becomes

$$d\mathbf{P} = \hat{\mathbf{N}} \cdot \mathbf{N}^{(2PK)} ds_0 \tag{5.6}$$

Next a relation is borrowed from three-dimensional elasticity (see section 4.5 of Malvern [55])

$$\hat{n}_\alpha d\Omega = \frac{\rho_0}{\rho} \frac{\partial X_B}{\partial x_\alpha} \hat{N}_B d\Omega_0 \tag{5.7}$$

for differential cross-sectional-area Ω of the membrane. The area and density quantities are factored according to the thickness, e.g. $d\Omega_0 = h_0 ds_0$ and $d\Omega = hds$. Introducing the area density ρ^* and eliminating the thickness variables leads to an expression that relates the undeformed and deformed arc lengths.

$$\begin{aligned} \hat{n}_\alpha h ds &= \frac{\rho_0^*/h_0}{\rho^*/h} \frac{\partial X_B}{\partial x_\alpha} \hat{N}_B h_0 ds_0 && (5.8) \\ \hat{n}_\alpha ds &= \frac{\rho_0^*}{\rho^*} \frac{\partial X_B}{\partial x_\alpha} \hat{N}_B ds_0 && (5.9) \end{aligned}$$

Equation 5.9 is also written in vector notation as

$$\hat{\mathbf{n}} ds = \frac{\rho_0^*}{\rho^*} (\mathbf{F}^{-1})^T \cdot \hat{\mathbf{N}} ds_0 \qquad (5.10)$$

To relate two stress resultants, Equations 5.4 and 5.5 are set equal to each other. Eqn 5.10 is then used to relate deformed arc length ds to undeformed arc length ds_0.

$$\begin{aligned} \hat{\mathbf{N}} \cdot \mathbf{N}^{(1PK)} \cdot \left(\mathbf{F}^{-1}\right)^T ds_0 &= \hat{\mathbf{n}} \cdot \mathbf{N}^{(C)} \cdot \left(\mathbf{F}^{-1}\right)^T ds \\ \hat{\mathbf{N}} \cdot \mathbf{N}^{(1PK)} ds_0 &= \hat{\mathbf{n}} \cdot \mathbf{N}^{(C)} ds \\ &= \hat{\mathbf{N}} \cdot (\mathbf{F}^{-1} \cdot \mathbf{N}^{(C)}) \frac{\rho_0^*}{\rho^*} ds_0 \\ \hat{\mathbf{N}} \cdot \left[\mathbf{N}^{(1PK)} - \frac{\rho_0^*}{\rho^*} \mathbf{F}^{-1} \cdot \mathbf{N}^{(C)} \right] ds_0 &= 0 \\ \mathbf{N}^{(1PK)} &= \frac{\rho_0^*}{\rho^*} \mathbf{F}^{-1} \cdot \mathbf{N}^{(C)} \qquad (5.11) \end{aligned}$$

To define the Cauchy stress resultant in terms of the first Piola Kirchoff type, pre-multiply Eqn 5.11 by the deformation gradient $\mathbf{F}$.

$$\mathbf{N}^{(C)} = \frac{\rho^*}{\rho_0^*} \mathbf{F} \cdot \mathbf{N}^{(1PK)} \qquad (5.12)$$

The process is similar to relating the second-Piola-Kirchoff-type stress resultant to the

Cauchy type.

$$\begin{aligned}
\hat{\mathbf{N}} \cdot \mathbf{N}^{(2PK)} ds_0 &= \hat{\mathbf{n}} \cdot \mathbf{N}^{(C)} \cdot \left(\mathbf{F}^{-1}\right)^T ds \\
&= \hat{\mathbf{N}} \cdot (\mathbf{F}^{-1} \cdot \mathbf{N}^{(C)}) \frac{\rho_0^*}{\rho^*} \cdot \left(\mathbf{F}^{-1}\right)^T ds_0 \\
\hat{\mathbf{N}} \cdot \left[\mathbf{N}^{(2PK)} - \frac{\rho_0^*}{\rho^*} \mathbf{F}^{-1} \cdot \mathbf{N}^{(C)} \cdot \left(\mathbf{F}^{-1}\right)^T\right] ds_0 &= 0 \\
\mathbf{N}^{(2PK)} &= \frac{\rho_0^*}{\rho^*} \mathbf{F}^{-1} \cdot \mathbf{N}^{(C)} \cdot \left(\mathbf{F}^{-1}\right)^T \qquad (5.13)
\end{aligned}$$

Alternatively, pre- and post-multiply Eqn 5.13 by the deformation gradient $\mathbf{F}$.

$$\mathbf{N}^{(C)} = \frac{\rho^*}{\rho_0^*} \mathbf{F} \cdot \mathbf{N}^{(2PK)} \cdot \mathbf{F}^T \qquad (5.14)$$

Combining Eqns 5.12 and 5.14 leads to the relationship between the first and second Piola-Kirchoff stress resultants.

$$N_{A\beta}^{(1PK)} = N_{AB}^{(2PK)} \frac{\partial x_\beta}{\partial X_B} \qquad (5.15)$$

The transformations on the stress resultants thus look the same as the transformation on the stresses; the difference is the ratio of *area* density and the fact that the deformation gradient on the membrane surface is a second-order tensor. For reference, the different stress types transform as follows [55]:

$$\sigma^{(C)} = \frac{\rho}{\rho_0} \mathbf{F} \cdot \sigma^{(1PK)} \qquad (5.16)$$

$$\sigma^{(C)} = \frac{\rho}{\rho_0} \mathbf{F} \cdot \sigma^{(2PK)} \cdot \mathbf{F}^T \qquad (5.17)$$

5.2.2 Application to Axisymmetric Membrane Shells

In this subsection the relationship between meridional stress resultant types for axisymmetric shells is calculated as an aid to understanding how to implement the transformations. The deformation gradient for the two-dimensional shell problem comes from Eqn 5.2 and the assumption of axisymmetry; most notable is that axisymmetry precludes shear terms. In accordance with Figure 3.1, the curvilinear coordinate system follows the two lines of principal curvature on the surface and uses the two principal radii of curvature: radial position R as in a cylindrical coordinate system and meridional radius of curvature R_ϕ

perpendicular to the shell.

The deformation gradient tensor is thus calculated via Eqn 5.2

$$\begin{aligned} F_{\alpha B} &= \frac{\partial x_\alpha}{\partial X_B} \\ &= \begin{bmatrix} \frac{\partial x_\phi}{\partial X_\phi} & \frac{\partial x_\phi}{\partial X_\theta} \\ \frac{\partial x_\theta}{\partial X_\phi} & \frac{\partial x_\theta}{\partial X_\theta} \end{bmatrix} \\ &= \begin{bmatrix} \frac{\partial x_\phi}{\partial X_\phi} & 0 \\ 0 & \frac{\partial x_\theta}{\partial X_\theta} \end{bmatrix} \\ &= \begin{bmatrix} \frac{r_\phi d\phi}{R_\phi d\phi} & 0 \\ 0 & \frac{r d\theta}{R d\theta} \end{bmatrix} \end{aligned} \tag{5.18}$$

The engineering strains are defined by the ratio of radii such that Eqn 5.18 becomes

$$F_{\alpha B} = \begin{bmatrix} 1+\epsilon_\phi & 0 \\ 0 & 1+\epsilon_\theta \end{bmatrix} \tag{5.19}$$

Next, the ratio of area densities $\{\rho_0^*, \rho^*\}$ for a differential element in the undeformed and deformed configurations is considered for the areas $\{A_0, A\}$. For a constant mass over a differential area,

$$\begin{aligned} \frac{\rho^*}{\rho_0^*} &= \frac{dm/dA}{dm/dA_0} \\ &= \frac{dA_0}{dA} \\ &= \frac{dX_\phi dX_\theta}{dx_\phi dx_\theta} \qquad (5.20) \\ &= \frac{1}{(1+\epsilon_\phi)} \frac{1}{(1+\epsilon_\theta)} \qquad (5.21) \end{aligned}$$

Under axisymmetric conditions the meridional stress resultant, in terms of meridional and sagittal angles ϕ and θ, is found from Eqn 5.14.

$$\begin{aligned} N_{\phi\phi}^{(C)} &= \frac{\rho^*}{\rho_0^*} \frac{\partial x_\phi}{\partial X_\phi} N_{\phi\phi}^{(2PK)} \frac{\partial x_\phi}{\partial X_\phi} \\ &= \frac{1}{(1+\epsilon_\phi)(1+\epsilon_\theta)} \left[(1+\epsilon_\phi) N_{\phi\phi}^{(2PK)} (1+\epsilon_\phi) \right] \\ &= \frac{1+\epsilon_\phi}{1+\epsilon_\theta} N_{\phi\phi}^{(2PK)} \end{aligned} \tag{5.22}$$

Similarly, the relationship between the Cauchy and first-Piola-Kirchoff stress resultants is rewritten from Eqn 5.12,

$$N_{\alpha\beta}^{(C)} = \frac{\rho^*}{\rho_0^*}\frac{\partial x_\alpha}{\partial X_A}N_{A\beta}^{(1PK)} \tag{5.23}$$

For axisymmetry the meridional stress resultant becomes

$$\begin{aligned} N_{\phi\phi}^{(C)} &= \frac{\rho^*}{\rho_0^*}\frac{\partial x_\phi}{\partial X_\phi}N_{\phi\phi}^{(1PK)} \\ N_{\phi\phi}^{(C)} &= \frac{1}{(1+\epsilon_\phi)(1+\epsilon_\theta)}\left[(1+\epsilon_\phi)N_{\phi\phi}^{(1PK)}\right] \\ &= \frac{1}{(1+\epsilon_\theta)}N_{\phi\phi}^{(1PK)} \end{aligned} \tag{5.24}$$

Eqns 5.22 and 5.24 combine to provide the relationship between the first and second Piola-Kirchoff stress resultants.

$$N_{\phi\phi}^{(1PK)} = (1+\epsilon_\phi)\,N_{\phi\phi}^{(2PK)} \tag{5.25}$$

Under axisymmetry the double-subscript will be reduced to a single, e.g. $N_{phi}^{(C)} = N_{\phi\phi}^{(C)}$.

5.2.3 Comparison to the Literature

The labelling of stress resultant types in the literature is not always consistent with this mathematical development. In Jenkins *et al.* [37], for example, the stress resultant transformation labelled as Cauchy-to-second-Piola-Kirchoff-type is consistent with the Cauchy-to-first-Piola-Kirchoff-type transformation shown in Section 5.2.2. Often the distinction between first- and second-type Piola-Kirchoff stress resultant is not given explicitly in the literature.

The consistent stress resultant definitions for the three types are used to provide a guide to selections from the literature. In Table 5.2 the variables from the source are shown with the consistent definition. The Kirchoff stress resultant quantity found in Budiansky [11] and Libai and Simmonds [50] does not actually have a commonly-defined stress-type analog.

Table 5.2: Stress resultant notation in the literature, with the current notation shown for comparison. The variables used in each reference are given in the nomenclature of the reference.

Reference	Stress Resultant Type			
	Cauchy	1^{st} Piola-Kirchoff	2^{nd} Piola-Kirchoff	Kirchoff
Libai and Simmonds, §VII.F [50]	$\bar{N}^{\alpha\beta}$			$N^{\alpha\beta}$
Budiansky [11]	$N^{\alpha\beta}$			$n^{\alpha\beta}$
Malvern, Ch. 5 [55]$^\flat$	T_{ij}	T^0_{Ij}	$\tilde{T}_{IJ}$	
Jenkins *et al.*, [37]	$n_{\alpha\beta}$	$N_{\alpha\beta}{}^\ddagger$		
Greschik *et al.*, [23]	N_α	n_α		
[This document]	$\{N^{(C)}_{\alpha\beta}, n_\alpha\}$	$N^{(1PK)}_{\alpha\beta}$	$N^{(2PK)}_{\alpha\beta}$	

†This quantity is transformed by the change in volume, also represented by the metric tensor determinant ratio, $N_{\alpha\beta} = \sqrt{\frac{g}{G}}\bar{N}_{\alpha\beta} = \frac{\rho_0}{\rho}\bar{N}_{\alpha\beta}$. See Appendix D for more on the metric tensor.

$^\flat\mathbf{T}$ represents the *stress* tensor, not the stress resultant.

‡The 1^{st} Piola-Kirchoff-type stress resultant, as defined consistently here, is labelled in the reference as the 2^{nd} Piola-Kirchoff-type stress resultant.

5.2.4 Constitutive Laws for Axisymmetric Membrane Shells

A common assumption in elasticity, especially when accuracies on the order of 5% are desired, is to assume small strains and ignore the terms that distinguish between the stress and strain types. The current context is the high-quality shape prediction of optical performance, however, and so the proper treatment of the constitutive law is pursued. In this section a proper form of linear, Hookean constitutive law is derived for different stress resultant types, and through the derivation process a set of different forms is created.

Continuum mechanics texts such as Malvern [55] emphasize the importance of matching a proper strain type with a conjugate stress type in the constitutive law. *The fundamental concept is that the value of the strain energy must be invariant to form, and the result is that the stress resultant types of the previous section must be paired with particular types of strain tensors in the constitutive relations.* This need to relate conjugate pairs in the constitutive law is not reflected in some of the literature.

The linear, Hookean constitutive law is formally a relation between the 2^{nd}-Piola-Kirchoff stress and the Lagrangian strain [55]; both are referenced to the initial, undeformed basis. A review of the ASTM standard for tensile testing of plastic sheets [4] confirms this approach. That is, the standard practice for membranes is to reference the undeformed basis by using the original, undeformed dimensions to transform the force/ displacement data into stress (resultant)/ strain curves. For the axisymmetric problem the two constitutive relations are thus

$$e_\phi = \frac{1}{Eh_0}\left(N_\phi^{(2PK)} - \nu N_\theta^{(2PK)}\right) \tag{5.26}$$

$$e_\theta = \frac{1}{Eh_0}\left(N_\theta^{(2PK)} - \nu N_\phi^{(2PK)}\right) \tag{5.27}$$

The Lagrangian strain terms e_α are finite strains referenced to the undeformed coordinate system. The strains are found from a relation with the change in arc length ds on the surface during deformation.

$$ds^2 - ds_0^2 = 2dX_A e_{AB} dX_B \tag{5.28}$$

Substitution for the differential arc length into each side of Eqn 5.28 leads to a useful

definition for e_{AB} in the case of axisymmetric membrane shells.

$$\begin{aligned}\left[(r_\phi d\phi)^2 + (r d\theta)^2 - (R_\phi d\phi)^2 - (R d\theta)^2\right] &= 2\left[e_\phi dX_\phi^2 + e_\theta dX_\theta^2\right] \\ &= 2\left[e_\phi R_\phi^2 d\phi^2 + e_\theta R^2 d\theta^2\right] \\ d\phi^2\left[r_\phi^2 - R_\phi^2 - 2e_\phi R_\phi^2\right] + d\theta^2\left[r^2 - R^2 - 2e_\theta R^2\right] &= 0 \end{aligned} \tag{5.29}$$

From Eqn 5.29 the Lagrangian strain components for axisymmetric membrane shells are found by setting each of the coefficients of the differential-angle terms to zero.

$$e_\phi = \frac{1}{2}\frac{r_\phi^2 - R_\phi^2}{R_\phi^2} \tag{5.30}$$

$$e_\theta = \frac{1}{2}\frac{r^2 - R^2}{R^2} \tag{5.31}$$

The form of Eqns 5.30 and 5.31 may then be rewritten.

$$\begin{aligned} e_\phi &= \frac{1}{2}\left(\frac{r_\phi}{R_\phi} - 1\right)\left(\frac{r_\phi}{R_\phi} + 1\right) \\ &= \left(\frac{r_\phi}{R_\phi} - 1\right)\left[\frac{1}{2}\left(\frac{r_\phi}{R_\phi} - 1\right) + 1\right] \\ &= \left(\frac{r_\phi}{R_\phi} - 1\right) + \frac{1}{2}\left(\frac{r_\phi}{R_\phi} - 1\right)^2 \end{aligned} \tag{5.32}$$

The sagittal strain is found similarly.

$$e_\theta = \left(\frac{r}{R} - 1\right) + \frac{1}{2}\left(\frac{r}{R} - 1\right)^2 \tag{5.33}$$

To relate these ratios of radii to a strain quantity, an alternative approach is considered. With the displacement vector **u** defined as a difference in position vectors,

$$u_\alpha \equiv x_\alpha - X_\alpha \tag{5.34}$$

Eqn 5.28 can be reformulated in terms of derivatives of displacements in the coordinate directions [55].

$$e_{\alpha\beta} = \frac{1}{2}\left(\frac{du_\alpha}{dX_\beta} + \frac{du_\beta}{dX_\alpha} + \frac{du_\gamma}{dX_\beta}\frac{du_\alpha}{dX_\beta}\right) \tag{5.35}$$

The quadratic terms are ignored to define the linear component of the Lagrangian strain, also well-known as the "engineering strain" $\epsilon_{\alpha\beta}$.

$$\epsilon_{\alpha\beta} \equiv \frac{1}{2}\left(\frac{du_\alpha}{dX_\beta} + \frac{du_\beta}{dX_\alpha}\right) \tag{5.36}$$

The engineering strains are thus defined according to the simple relative change in fundamental lengths.

$$\begin{aligned} \epsilon_\phi &= \frac{dx_\phi - dX_\phi}{dX_\phi} = \frac{ds - dS}{dS} \\ &= \frac{r_\phi}{R_\phi} - 1 \end{aligned} \tag{5.37}$$

$$\begin{aligned} \epsilon_\theta &= \frac{dx_\theta - dX_\theta}{dX_\theta} = \frac{rd\theta - Rd\theta}{Rd\theta} \\ &= \frac{r}{R} - 1 \end{aligned} \tag{5.38}$$

Substituting the definition for the engineering strains, Eqns 5.37 and 5.38, into the Lagrangian strain tensor $e_{\alpha\beta}$ of Eqn 5.32 and 5.33 provides the relation of the engineering strain to the finite-strain for axisymmetric membranes.

$$e_\phi = \epsilon_\phi + \frac{1}{2}\epsilon_\phi^2 \tag{5.39}$$

$$e_\theta = \epsilon_\theta + \frac{1}{2}\epsilon_\theta^2 \tag{5.40}$$

Whenever the quadratic term is eliminated, the small-strain approximation is explicitly implemented. Returning to the Hookean constitutive law of Eqns 5.26 and 5.27, the equations are rearranged in terms of stress resultants.

$$N_\phi^{(2PK)} = \frac{Eh_0}{1-\nu^2}\left(e_\phi + \nu e_\theta\right) \tag{5.41}$$

$$N_\theta^{(2PK)} = \frac{Eh_0}{1-\nu^2}\left(e_\theta + \nu e_\phi\right) \tag{5.42}$$

From Eqns 5.22 and 5.24, the different stress resultant types are related to each other in

the following way.

$$\begin{aligned} N_\phi^{(C)} &= \tfrac{1}{1+\epsilon_\theta} N_\phi^{(1PK)} &= \frac{1+\epsilon_\phi}{1+\epsilon_\theta} N_\phi^{(2PK)} \\ N_\theta^{(C)} &= \tfrac{1}{1+\epsilon_\phi} N_\theta^{(1PK)} &= \frac{1+\epsilon_\theta}{1+\epsilon_\phi} N_\theta^{(2PK)} \end{aligned}$$

The 2^{nd}-Piola-Kirchoff-type stress resultants $N_\alpha^{(2PK)}$ are now replaced with the equivalent expression from the constitutive law, Eqns 5.41 and 5.42, to form the "Exact" constitutive law.

$$\begin{aligned} N_\phi^{(C)}\big|_{(Exact)} &= \frac{1+\epsilon_\phi}{1+\epsilon_\theta}\left(\frac{Eh_0}{1-\nu^2}\right)(e_\phi + \nu e_\theta) \\ &= \frac{Eh_0}{1-\nu^2}\left(\frac{1+\epsilon_\phi}{1+\epsilon_\theta}\right)\left[\left(\epsilon_\phi + \frac{1}{2}\epsilon_\phi^2\right) + \nu\left(\epsilon_\theta + \frac{1}{2}\epsilon_\theta^2\right)\right] \qquad (5.43) \\ N_\theta^{(C)}\big|_{(Exact)} &= \frac{1+\epsilon_\theta}{1+\epsilon_\phi}\left(\frac{Eh_0}{1-\nu^2}\right)(e_\theta + \nu e_\phi) \\ &= \frac{Eh_0}{1-\nu^2}\left(\frac{1+\epsilon_\theta}{1+\epsilon_\phi}\right)\left[\left(\epsilon_\theta + \frac{1}{2}\epsilon_\theta^2\right) + \nu\left(\epsilon_\phi + \frac{1}{2}\epsilon_\phi^2\right)\right] \qquad (5.44) \end{aligned}$$

With small strains ($|\epsilon_\alpha| \ll 1$), the consistent expressions for the Cauchy stress resultant can be expanded as a series of the two engineering strains. The "Quadratic" constitutive law comes from keeping terms in the series up to second order in engineering strain.

$$\begin{aligned} N_\phi^{(C)}\big|_{(Quadratic)} &= \frac{Eh_0}{1-\nu^2}\left(\epsilon_\phi + \nu\epsilon_\theta + \frac{3}{2}\epsilon_\phi^2 - \frac{1}{2}\nu\epsilon_\theta^2 - (1-\nu)\epsilon_\phi\epsilon_\theta\right) \qquad (5.45) \\ N_\theta^{(C)}\big|_{(Quadratic)} &= \frac{Eh_0}{1-\nu^2}\left(\epsilon_\theta + \nu\epsilon_\phi + \frac{3}{2}\epsilon_\theta^2 - \frac{1}{2}\nu\epsilon_\phi^2 - (1-\nu)\epsilon_\phi\epsilon_\theta\right) \qquad (5.46) \end{aligned}$$

If only the linear terms are kept, the "Linear" constitutive law is formed.

$$\begin{aligned} N_\phi^{(C)}\big|_{(Linear)} &= N_\phi^{(1PK)}\big|_{(Linear)} &= N_\phi^{(2PK)} = \frac{Eh_0}{1-\nu^2}\left(\epsilon_\phi + \nu\epsilon_\theta\right) \qquad (5.47) \\ N_\theta^{(C)}\big|_{(Linear)} &= N_\theta^{(1PK)}\big|_{(Linear)} &= N_\theta^{(2PK)} = \frac{Eh_0}{1-\nu^2}\left(\epsilon_\theta + \nu\epsilon_\phi\right) \qquad (5.48) \end{aligned}$$

This linear approximation derived in a consistent manner leads to equivalence among the stress resultant types. Although not the goal of this analysis, *Eqns 5.47 and 5.48 show that the use of engineering strains rather than Lagrangian strains is not consistent with making a distinction between stress resultant types.*

Lastly, the so-called "Classic" constitutive equation is considered; the name refers to the previous use of this relation by the author [17] and others [23]. The basic assumption is that the "Classic" constitutive equation provides a relation between the engineering strain and the 1^{st}-Piola-Kirchoff stress resultants.

$$\begin{aligned} N_{\phi}^{(C)}\big|_{(Classic)} &= \frac{1}{1+\epsilon_\theta} N_{\phi}^{(1PK)} \\ &= \frac{1}{1+\epsilon_\theta}\left(\frac{Eh_0}{1-\nu^2}\right)\left(\epsilon_\phi + \nu\epsilon_\theta\right) \qquad (5.49) \\ N_{\theta}^{(C)}\big|_{(Classic)} &= \frac{1}{1+\epsilon_\phi} N_{\theta}^{(1PK)} \\ &= \frac{1}{1+\epsilon_\phi}\left(\frac{Eh_0}{1-\nu^2}\right)\left(\epsilon_\theta + \nu\epsilon_\phi\right) \qquad (5.50) \end{aligned}$$

In summary, the constitutive laws in terms of the Cauchy stress resultants and the engineering strain are given in four categories:

1. "Exact" (Eqns 5.43 and 5.44);
2. "Quadratic" (Eqns 5.45 and 5.46);
3. "Linear" (Eqns 5.47 and 5.48); and
4. "Classic" (Eqns 5.49 and 5.50).

5.3 Quantification of Error

The previous section details the mathematics behind the four different constitutive laws. In this section the errors are quantified in the context of modelling doubly-curved membrane shells similar in shape to telescope primary mirrors. The errors from not using the "Exact" constitutive law are shown to follow the expected trends and yet not generally be as significant as the error introduced from the equilibrium and kinematic assumptions in the models.

Consistent with the rest of the thesis, two example geometries are considered:

- Forming a spherical cap from a spherical cap by applying a constant pressure: the final shape has spherical radius $\bar{r}_{sph} = \frac{r_{sph}}{r_{out}} = 4$, and the initial spherical radius is smaller than 4 (i.e., the final shape is flatter). The stress-resultant boundary condition is set such that the cap behaves like a cutout of a filled sphere.

- Forming a paraboloidal shell from a shallower paraboloidal shell: the final shape has focal ratio $f_\infty = \frac{f}{2r_{out}} = 1$, and the initial shape has a larger focal ratio.

The constitutive models are each implemented in the inverse solver because the difference between bases and different constitutive laws is important for the geometrically-exact inverse solver. Axisymmetry is assumed. The product of the inverse solver is the radially-varying pressure distribution required to push the initial shape into the final shape. The sphere-forming problem is used to verify the numerical inverse solver, while the parabola-forming problem provides a real mirror shape for study. The different constitutive models are used to create a series of corresponding pressure distributions, and these pressure distributions are applied in the same "forward" model to get a final shape. The final shape predictions are then compared to quantify the impact of constitutive model choice on the final shape prediction.

With reference to the taxonomy of models in Chapter 3, three models are used in this chapter:

- The Axisymmetric Exact Membrane Shell (AEMS) model for the inverse solver;
- The Axisymmetric Membrane Shell (AMS) model to generate shape predictions of the example problems; and
- The Linearized Axisymmetric Large Deflection (LALD) model, also for shape predictions of the example problems.

With no distinction between coordinate bases, the AMS and LALD models only use linear constitutive laws.

5.3.1 Stress Resultants from Strain Distributions

With the different constitutive laws in Section 5.2.4 given as functions of strains (see Eqns 5.43–5.50), the most direct implementation of a membrane constitutive law is to determine the stress resultant as a function of strain. The different stress resultant distributions corresponding to the four laws — "Exact", "Quadratic", "Linear", and "Classic" — are calculated and compared here to quantify the difference for problems of interest.

Figure 5.3 shows the area-averaged Root-Mean-Square (RMS) error in the prediction of meridional stress resultant N_ϕ. To be consistent with the rest of the thesis, the abscissa

is the mean pressure applied to form the final shape. The distributions of principal strain, the same for each constitutive equation, come from the Mathematica-based inverse solver so as to create a realistic set of values. The error is calculated as a relative error away from the stress resultants calculated via the consistently "Exact" constitutive equations. The *relative* error is seen to be linear for the "Linear" and "Classic" laws, consistent with the fact that a quadratic-level error is divided by the stress resultant. Similarly, the expected cubic level of error for the "Quadratic" law is supported by a quadratic relative error.

Figure 5.2 shows data from the ($\bar{r}_{sph} = 4$)-sphere-forming problem and Figure 5.3 from the $f/1$-parabola-forming problem. In Figure 5.2 the "Linear" and "Classic" points lie on nearly identical lines as for the parabola-forming problem, but the "Quadratic" law is observed to have a numerically-zero error. As seen in the equations, the sphere-expansion problem has the unique geometry and loading for which the quadratic expression is identical to the exact.

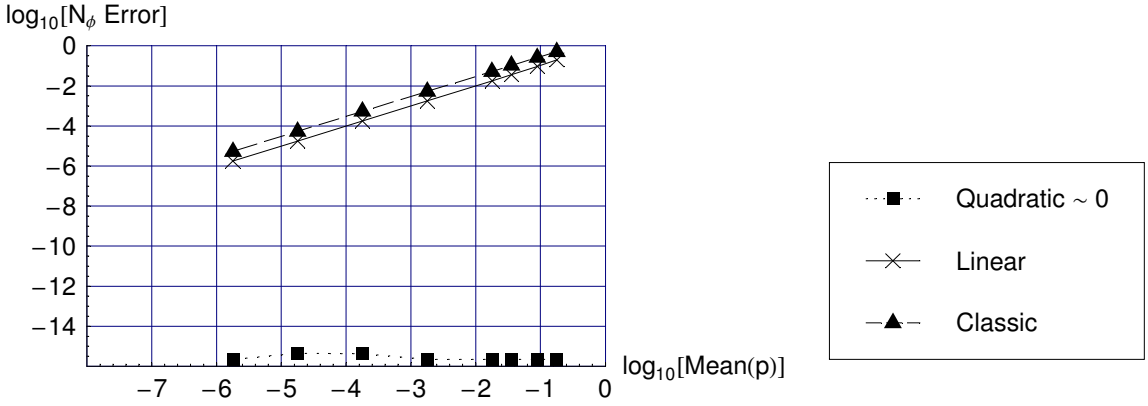

Figure 5.2: *Sphere-to-$\bar{r}_{sph} = 4$-sphere forming.* Area-weighted-RMS error in the prediction of meridional stress resultant $\bar{N}_\phi$ relative to that from the "Exact" law, $\frac{\bar{N}_\phi - (\bar{N}_\phi)_{Exact}}{(\bar{N}_\phi)_{Exact}}$, as a function of mean applied pressure. The "Quadratic" law has a zero error to the level of numerical precision.

Figure 5.4 has slightly different axes, with the circumferential stress resultant prediction error plotted against average strain. The trends are uniformly similar to the trends observed in the meridional-stress-resultant-versus-pressure plots, and so the full permutation of plots is omitted here for brevity.

The error in Figures 5.3, 5.2, and 5.4 is seen to be small: less than 1% relative error

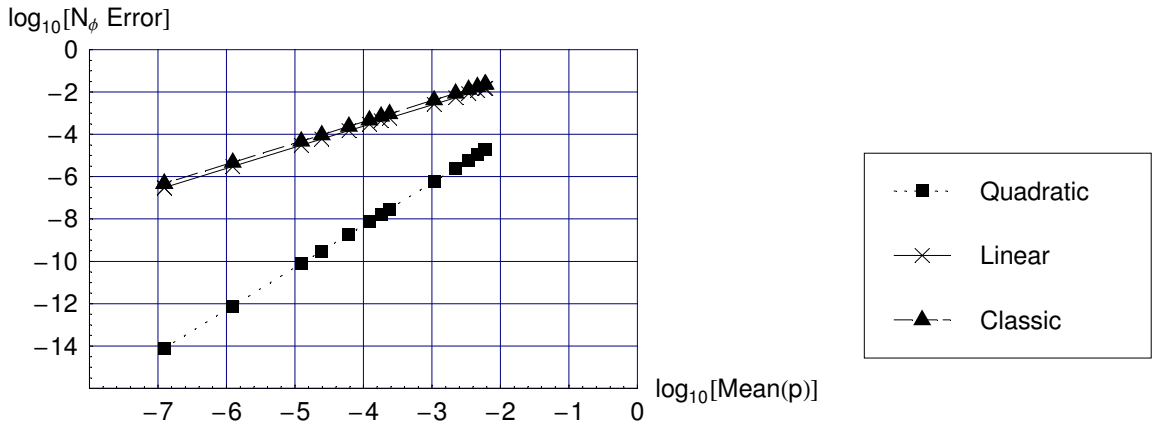

Figure 5.3: *Parabola-to-f/1-parabola forming.* Area-weighted-RMS error in the prediction of meridional stress resultant $\bar{N}_\phi$ relative to that from the "Exact" law, $\frac{\bar{N}_\phi - (\bar{N}_\phi)_{Exact}}{(\bar{N}_\phi)_{Exact}}$, as a function of mean applied pressure.

in most of the parabola-forming problems, for example. Such a small difference in the prediction of stress resultant provides the first indication that the difference between the constitutive models is not significant for the geometric and loading problems of interest for forming curved membrane mirrors. *The results also provide the first indication that use of the "Classic" constitutive law may introduce more error that use of even the "Linear" law.*

5.3.2 Implementation in Inverse Solver: Pressure Solution

As a more significant comparison, the four constitutive models are each implemented in an inverse solver; the result is four different pressure distributions for each initial shape/ final shape combination. The sphere-forming problem is used for this comparison for one underlying reason: the answer can be found in closed form, and this closed-form solution can be used to verify the numerical inverse-solver code.

The exact equations for the equilibrium of a sphere subject to constant pressure are found by writing the classic pressure-vessel-expansion expressions in the deformed basis rather than the undeformed basis typical of small-strain analysis.

$$\bar{p}|_{Exact} = \frac{2\bar{N}^{(C)}}{\bar{r}_\phi} \tag{5.51}$$

In this section the functional dependence of the field variables upon position (either ra-

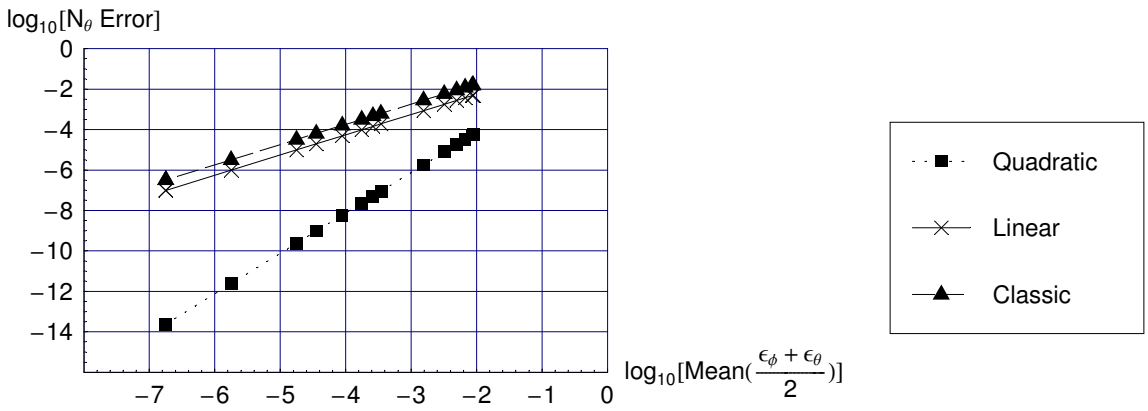

Figure 5.4: *Parabola-to-f/1-parabola forming.* Relative area-weighted-RMS error in the prediction of meridional stress resultant $\bar{N}_\phi$ as a function of a given strain set, $\frac{\bar{N}_\theta - (\bar{N}_\theta)_{Exact}}{(\bar{N}_\theta)_{Exact}}$.

dial position R or angular position ϕ) is omitted for readability. The exact constitutive equations, Eqns 5.43 and 5.44, become

$$\begin{aligned} \bar{N}^{(C)} &= \frac{1}{1-\nu} e \\ &= \frac{1}{1-\nu}\left(\epsilon + \frac{1}{2}\epsilon^2\right) \end{aligned} \tag{5.52}$$

The subscripts have been dropped for convenience because the two principal tensor components are equal: $\bar{N}^{(C)} = \bar{N}^{(C)}_\phi = \bar{N}^{(C)}_\theta$ for the stress resultants and similar for engineering strain ϵ and Lagrangian strain e. The engineering strain is defined by a change in arc lengths according to Eqns 5.37–5.38, and so the stress resultant transforms accordingly.

$$\bar{N}^{(C)} = \frac{1}{2}\frac{1}{1-\nu}\left[\left(\frac{\bar{r}_\phi}{\bar{R}_\phi}\right)^2 - 1\right] \tag{5.53}$$

The equilibrium equation, Eqn 5.51, can thus be solved for pressure in terms of change in radius.

$$\bar{p}|_{Exact} = \frac{1}{1-\nu}\left(\frac{1}{\bar{r}_\phi}\right)\left[\left(\frac{\bar{r}_\phi}{\bar{R}_\phi}\right)^2 - 1\right] \tag{5.54}$$

Eqn 5.54 thus represents the pressure for both the "Exact" and "Quadratic" laws because the deformation is such that the stress resultant is exactly a quadratic expression in engi-

neering strain.

For the "Linear" law, Eqn 5.52 is made linear consistent with Eqns 5.47 and 5.48, with a corresponding change to the pressure.

$$\begin{aligned}
\bar{N}^{(C)} &= \frac{1}{1-\nu}\left(\epsilon + \frac{1}{2}\epsilon^2\right) \\
&= \frac{1}{1-\nu}\left(\frac{\bar{r}_\phi}{\bar{R}_\phi} - 1\right) \\
\bar{p}|_{Linear} &= \frac{2}{\bar{r}_\phi}\bar{N}^{(C)} \\
&= \frac{2}{1-\nu}\left(\frac{1}{\bar{r}_\phi}\right)\left(\frac{\bar{r}_\phi}{\bar{R}_\phi} - 1\right)
\end{aligned} \tag{5.55}$$

The pressure for the "Classic" law is found in a similar way using Eqns 5.49 and 5.50.

$$\begin{aligned}
\bar{N}^{(C)} &= \left(\frac{1}{1+\epsilon}\right)\frac{1}{1-\nu^2}\left(\epsilon + \nu\epsilon\right) \\
&= \frac{1}{1-\nu}\left(\frac{\epsilon}{1+\epsilon}\right) \\
&= \frac{1}{1-\nu}\left(1 - \frac{\bar{R}_\phi}{\bar{r}_\phi}\right) \\
\bar{p}|_{Classic} &= \frac{2}{\bar{r}_\phi}\bar{N}^{(C)} \\
&= \frac{2}{1-\nu}\left(\frac{1}{\bar{r}_\phi}\right)\left(1 - \frac{\bar{R}_\phi}{\bar{r}_\phi}\right)
\end{aligned} \tag{5.56}$$

The inverse solver is implemented in Mathematica without any arbitrary constraints upon the solution, and still the solver returns values of pressure equal over the entire domain to each of the relations represented by Eqns 5.54, 5.55, and 5.56. That is, the area-averaged value of the relative error is around 10^{-16} or less – and hence numerically zero. In most cases the differences are exactly 0. *The inverse solver code is thus again verified.*

In the axisymmetric inverse solver used here both strain components at the inner boundary ($\bar{R} = 0$) are specified. This strain can either be chosen directly or as a function of the Cauchy stress resultant $\bar{N}^{(C)}$. In the "Linear" and "Classic" laws, the inverse solution for engineering strains in terms of stress resultants is easy to solve and leads to a closed-form relation. The "Exact" law is nonlinear and has no solution. In the "Quadratic" law, the expression is only acknowledged to be accurate to cubic order. An inverse polynomial function to cubic order is a deterministic problem, and so, for the "Quadratic" law, the

inverse expressions are as follows. Although this is a boundary condition with all variables evaluated at $\bar{R} = 0$, the "at $\bar{R} = 0$" function notation is omitted for brevity.

$$\begin{aligned} \epsilon_\phi|_{(Quadratic)} &= \bar{N}_\phi^{(C)} - \nu\bar{N}_\theta^{(C)} \\ &\quad - \left(\frac{3}{2}+\nu\right)\left(\bar{N}_\phi^{(C)}\right)^2 + \left(\nu+\frac{1}{2}\nu^2\right)\left(\bar{N}_\theta^{(C)}\right)^2 + \left(1+\nu-\nu^2\right)\bar{N}_\phi^{(C)}\bar{N}_\theta^{(C)} \end{aligned} \tag{5.57}$$

$$\begin{aligned} \epsilon_\theta|_{(Quadratic)} &= \bar{N}_\theta^{(C)} - \nu\bar{N}_\phi^{(C)} \\ &\quad - \left(\frac{3}{2}+\nu\right)\left(\bar{N}_\theta^{(C)}\right)^2 + \left(\nu+\frac{1}{2}\nu^2\right)\left(\bar{N}_\phi^{(C)}\right)^2 + \left(1+\nu-\nu^2\right)\bar{N}_\theta^{(C)}\bar{N}_\phi^{(C)} \end{aligned} \tag{5.58}$$

Specifying the stress resultant as the inner boundary condition with a "Quadratic" constitutive law therefore means that a third-order error is added to the problem prior to the numerical solution.

To explore the differences between the constitutive laws and the boundary specifications, the six cases of Table 5.3 are used. Each case was implemented in the inverse solver for the $\bar{r}_{sph} = 4$-sphere-forming problem over a range of initial radii, and the relative difference from the exact pressure of Eqn 5.54 is plotted in Figure 5.5. In confirmation of the implementation, the "Exact" case (4) is numerically zero (error magnitude $< 10^{-16}$). For the sphere-forming case, the "Quadratic" cases (2–3) are identical in form to the "Exact", and this fact is reflected in the numerically-zero error in the plot. The two "Classic" cases (5–6) have identical answers, as expected.

Table 5.3: Table of inverse-solver cases. The constitutive law types are consistent with Section 5.2.4.

Case	Constitutive Law	Boundary Condition Variables at $R = 0$
1	Linear	$\{\bar{N}_\phi, \bar{N}_\theta\}$
2	Quadratic	$\{\bar{N}_\phi, \bar{N}_\theta\}$
3	Quadratic	$\{\epsilon_\phi, \epsilon_\theta\}$
4	Exact	$\{\bar{N}_\phi, \bar{N}_\theta\}$
5	Classic	$\{\epsilon_\phi, \epsilon_\theta\}$
6	Classic	$\{\bar{N}_\phi, \bar{N}_\theta\}$

Figure 5.5 compels further investigation because the error magnitudes in many of the cases are above the 10^{-6} magnitude that arises in optical structures. The most interesting result here, however, is that *the "Classic" cases actually result in greater error that the "Linear" case.* This is the second quantified indication that choosing the "Classic" constitutive

law may actually degrade rather than improve the solution.

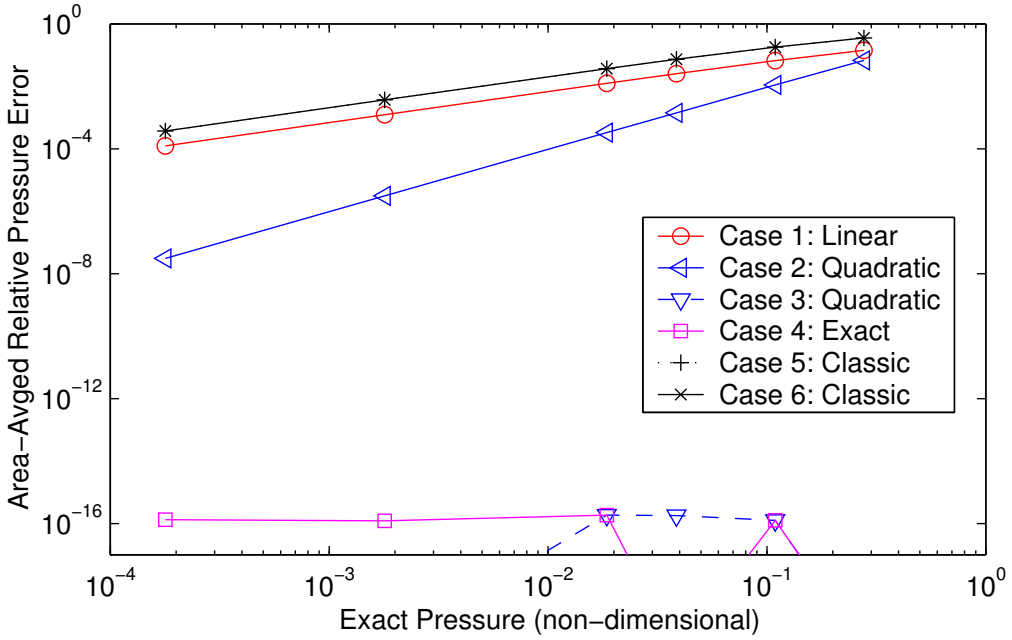

Figure 5.5: $\bar{r}_{sph}$=4-forming problem: Pressure prediction error due to choice of constitutive model in the inverse solver versus exact value of non-dimensional pressure from Eqn 5.54. The error is area-averaged to create a single metric for each loading state. Table 5.3 explains the difference in equation form and boundary condition implementation between the six cases.

5.3.3 Implementation in the Full Design Problem: Shape Prediction

In the last section the constitutive cases are compared by implementation in the full design problem, defined as the shape prediction of the nominal geometry and loading determined via the inverse solver. The different pressures from the inverse solvers are implemented in so-called "forward" models to see if the constitutive law in the inverse solver leads to any significant error in the shape predictions. This type of result indicates the significance of the difference in constitutive laws when a full design analysis, from the inverse statics solution to eventually study of the "forward" dynamics and control problem, is performed.

As discussed in Section 2.3, the STD-pathlength shape-error metric is used to compare the shape solution to the exact shape. Figure 5.6 shows that the difference between the constitutive-law cases is inconsequential for the parabola-forming design problem. The non-dimensional error range of interest for optical mirrors, 5.0×10^{-9} to 0.1×10^{-6}, is delineated

by dotted lines.

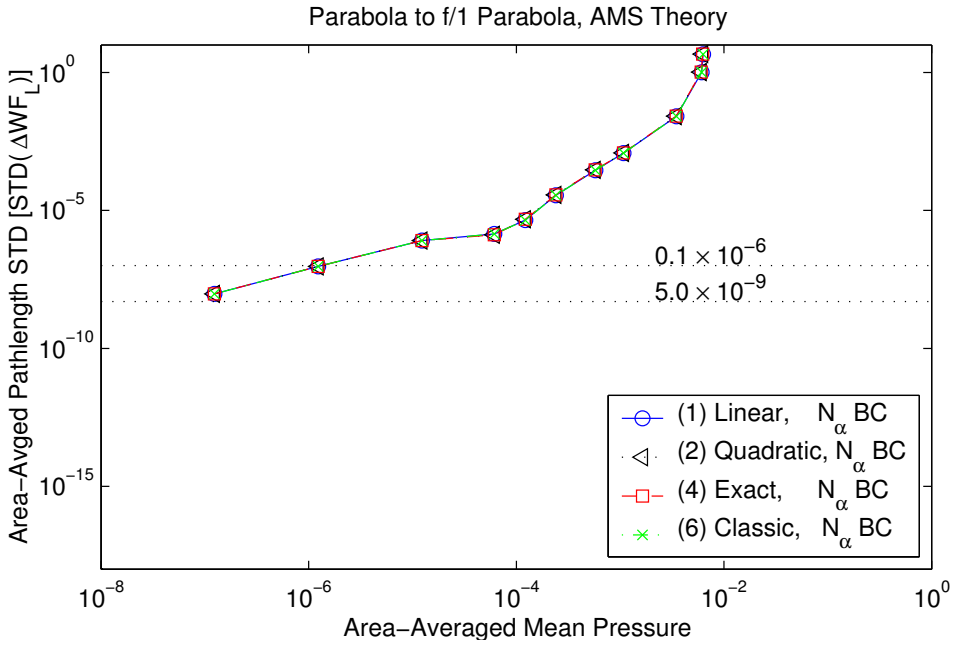

Figure 5.6: Standard-Deviation-of-Pathlength error metric as a function of mean applied pressure for *AMS-theory* discretized-integral solutions to the $f/1$-*parabola-forming problem* with $N = 3200$ intervals. Consistent with Table 5.3, the six case numbers represent different constitutive laws and boundary conditions used in the inverse solver.

Figure 5.7 represents a similar problem yet with a surprising result. When the "Classic" constitutive model is used in the inverse solver (Cases 5–6), the AMS-theory model returns an answer with optical-level accuracy over the full range of pressure load. The results appear to be either a sort of fluke caused by mutual error cancellation or a special result of AMS theory. This behavior is not observed in the $f/1$-parabola-forming geometry of Figure 5.6 or the LALD-theory results.

Figures 5.8 and 5.9 also show results for the parabola- and sphere-forming problems, though in this case for the LALD theory. The fundamental observation for the two plots is the same as for Figure 5.6: no appreciable difference is observed between any of the six cases. The error from the equilibrium and kinematic equations in the models is thus observed to be more significant than the error in the applied pressure load.

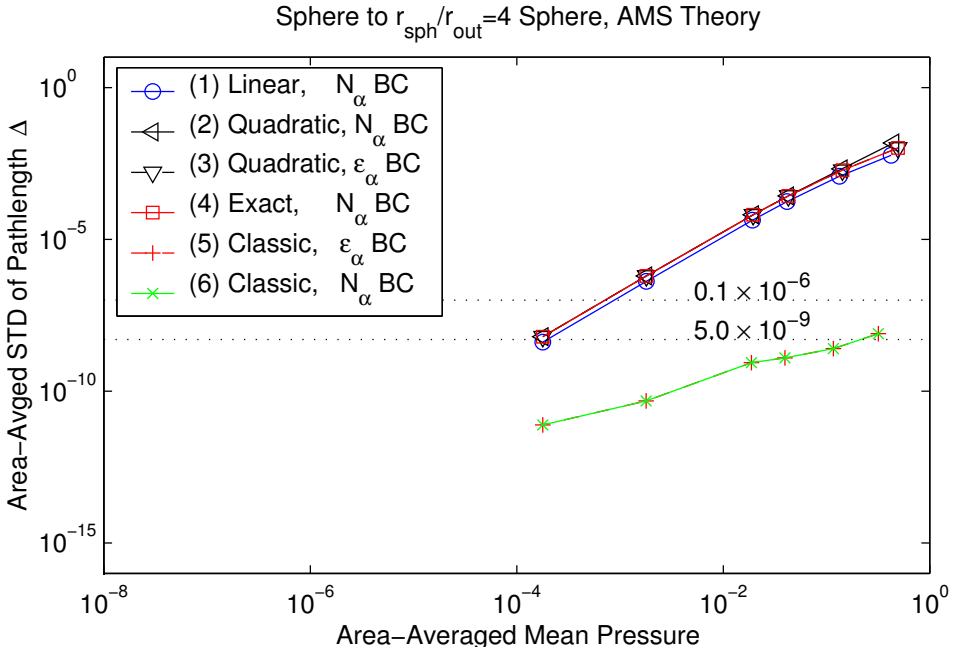

Figure 5.7: Standard-Deviation-of-Pathlength error metric as a function of mean applied pressure for *AMS-theory* finite difference solutions to the $\bar{r}_{sph} = 4$-*sphere-forming problem* with $N = 3200$ intervals. Consistent with Table 5.3, the six case numbers represent different constitutive laws and boundary conditions used in the inverse solver.

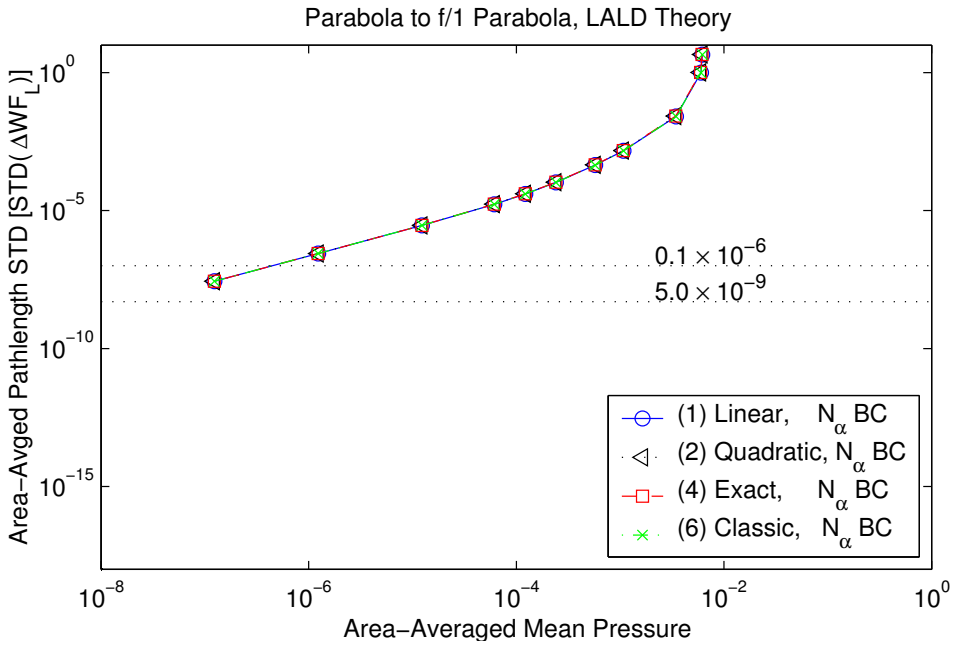

Figure 5.8: Standard-Deviation-of-Pathlength error metric as a function of mean applied pressure for *LALD-theory* finite difference solutions to the $f/1$-*parabola-forming problem* with $N = 3200$ intervals. Consistent with Table 5.3, the six case numbers represent different constitutive laws and boundary conditions used in the inverse solver.

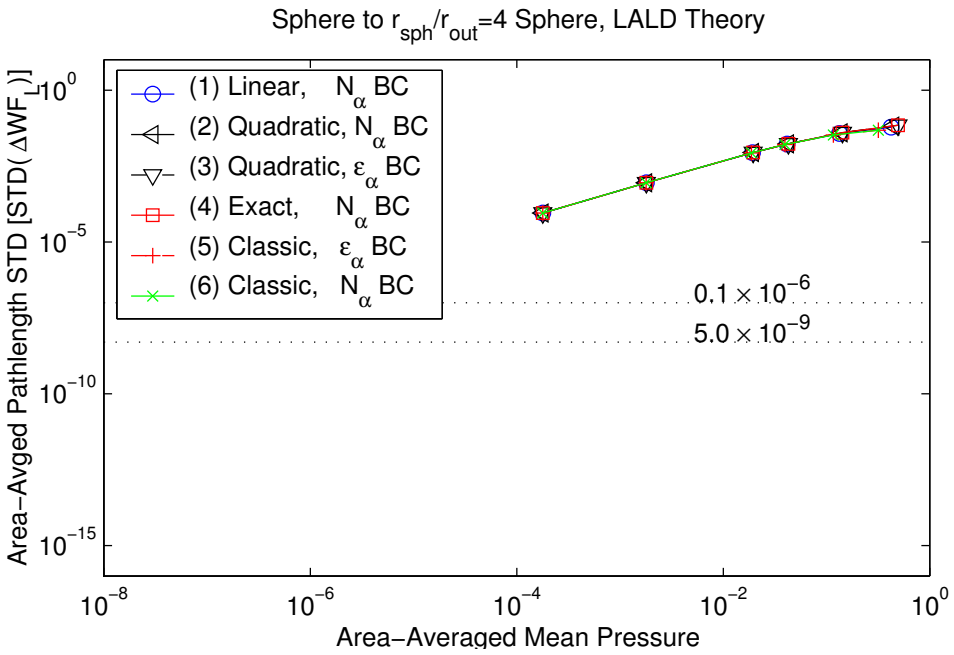

Figure 5.9: Standard-Deviation-of-Pathlength error metric as a function of mean applied pressure for *LALD-theory* finite difference solutions to the $\bar{r}_{sph} = 4$-*sphere-forming problem* with $N = 3200$ intervals. Consistent with Table 5.3, the six case numbers represent different constitutive laws and boundary conditions used in the inverse solver.

5.3.4 Functional Order of Error

As a check of accuracy and consistency, the results for the different cases were compared to the "Exact" case (4) and plotted in Figures 5.10 and 5.11 for the AMS and LALD models, respectively. Figure 5.10 shows that the functional dependence changes as the load decreases through the "hump" in the curve. In the "Linear" and "Classic" cases, the error appears to change linearly with strain for small loads and then as a constant for large loads. This change to a constant near a non-dimensional pressure load of 10^{-4} corresponds with the region in which the error function undergoes a sign change (see Chapter 7). The functional dependence of the "Quadratic" case is difficult to judge because of the features in the functions. Figure 5.11 shows a similar result for LALD theory except that the transition to higher-order error is gradual. In the LALD case the "Quadratic" case is seen to have quadratic functional dependence at small loads and then transition to a higher-order dependence at large loads. At smaller loads the difference between the exact error metrics and the other cases thus follows the expected order-of-strain trend for both the AMS and LALD models.

Hookean constitutive law is based upon a quadratic formulation of strain energy with a linear stress-strain relationship. The first improvement would seem to be the addition of cubic terms, thus indicating a quadratic relationship between stress and strain. A quadratic expression is a mathematically-even function, however, while an isotropic material would be expected to have a mathematically-odd stress-strain relationship (a quadratic term would indicate a positive force resulting from a negative strain, and so a cubic term would actually be the next logical addition).

This logic may not apply, however, to the no-compression-allowed world of membranes. Moreover, in special cases such as highly wrinkled/ crushed membranes, a quadratic term may be important. An example is found in Murphey and Mikulas [65], where a series expansion of an exponential constitutive law is used for a wrinkled membrane.

The most conservative error in the constitutive law is thus taken to be on the order of the engineering strain, or $O(1+\epsilon)$. A less conservative yet justifiable approach would be to consider the error to be on the order of $(1+\epsilon^2)$. Figures 5.10 and 5.11 show both of these strain trends plotted. Only experimental data can settle the question definitively.

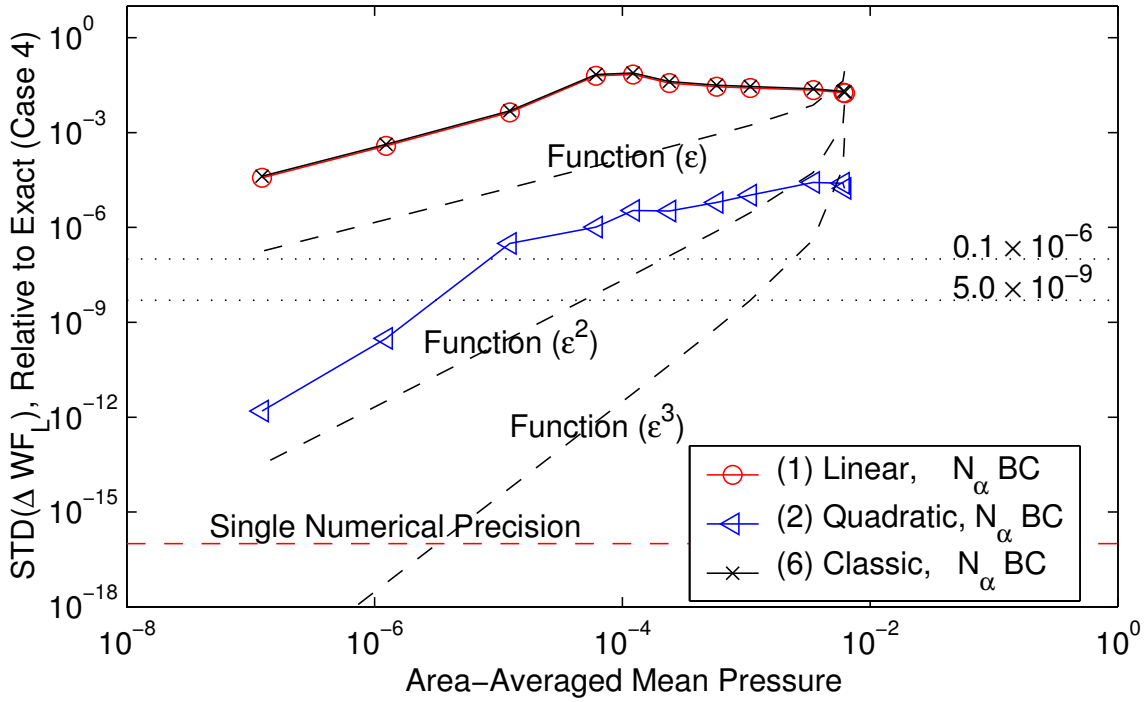

Figure 5.10: Standard-Deviation-of-Pathlength error metrics, *relative to the error metric from the "Exact" inverse-solver case*, as a function of mean applied pressure for $N = 3200$ AMS-theory solutions to various inverse-solver-based initial conditions. Consistent with Table 5.3, the six case numbers represent different constitutive laws and boundary conditions used in the inverse solver. The linear, quadratic, and cubic functions of the mean strain are also plotted to help identify trends.

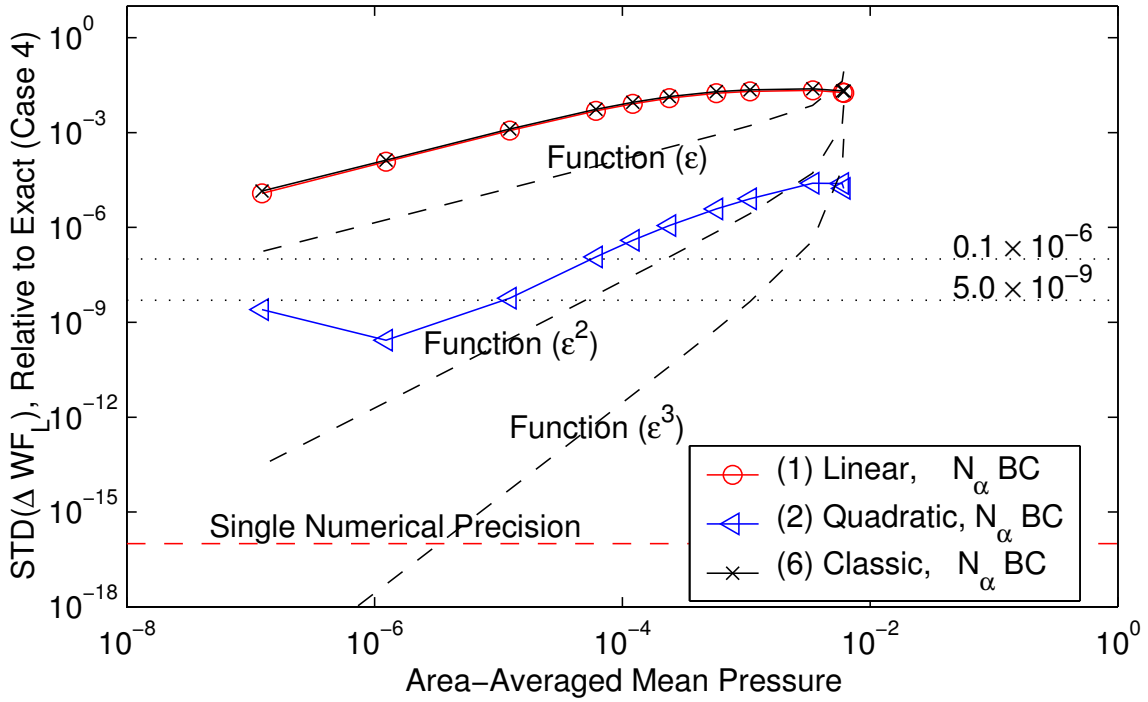

Figure 5.11: Standard-Deviation-of-Pathlength error metrics, *relative to the error metric from the "Exact" or "Case (4)" inverse-solver case*, as a function of mean applied pressure for $N = 3200$ LALD-theory solutions to various inverse-solver-based initial conditions. Consistent with Table 5.3, the six case numbers represent different constitutive laws and boundary conditions used in the inverse solver. The linear, quadratic, and cubic functions of the mean strain are also plotted to help identify trends.

5.4 Summary

In this chapter the exact Hookean constitutive law is written in term of proper complementary variables, the second-Piola-Kirchoff stress resultant and the Lagrangian strain, and then rewritten in terms of other stress resultant and strain types. Stress resultant types explored are Cauchy, first Piola-Kirchoff, and second Piola-Kirchoff, and the constitutive law choices are linear, quadratic, exact, and "classic". To assess the importance of distinguishing between the types of stress and strain in the constitutive law, a set of three membrane shell problems is used: (i) prediction of stress resultant distribution from a strain distribution, (ii) prediction of pressure distribution in an inverse solver, and (iii) prediction of final deformed shape. For each problem the results from the different constitutive laws are compared to the results from the exact relationship.

The following observations and recommendations are drawn from these comparisons:

- Consistency in the equations used in modeling must be considered. When ignoring the difference between engineering strains and Lagrangian strains, no distinction need be made between stress resultant types (see Eqns 5.47 and 5.48).

- The error from not using the exact Hookean constitutive law in the inverse solver is observed to be much less than the error from the equilibrium and kinematic assumptions in the AMS and LALD models.

- In predicting the pressure required to deform from one membrane shell into another, the "Classic" form of the constitutive equations results in greater error than even the "Linear" case. With consistently more error in the "Classic" than the "Linear" constitutive formulation, the consistent-linear form should be used as the first-level approximation. The consistently-derived quadratic expression should be used as the next level of fidelity in the constitutive law.

- The difference between the stress resultant types can be ignored for the inverse solver in combination with most simple models. The error introduced to the loading generated by an approximate inverse solver does not significantly change the accuracy of the resulting shape prediction for the models studied, even at the small scale required for optics. That is, the error in the constitutive law is largely overshadowed by the error inherent in the model.

The work in this chapter includes the following contributions.

- Derivation of relation between stress resultant types as analogs to stress types.
- Mathematical description of inconsistency in constitutive relations currently found in the literature. A constitutive law found in the literature from a well-known author is shown to be mathematically inconsistent and is shown to potentially add more error than even the simplest linear law.
- Quantification of error resulting from simplifications to the constitutive equations. The error is on the order of strain yet in the full design problem may be swamped by the error from other assumptions.

Chapter 6

Implementation

Objective of Chapter:

To identify problems with the implementation of the optical-accuracy numerical solutions and demonstrate the effectiveness of the measures taken to mitigate the problems.

6.1 Introduction

Modelling structural behavior to optical-level accuracy requires a careful analysis of the numerical solutions so that the origins of the error can be understood and properly handled. Decisions used in standard, "textbook" analyses can and do introduce prediction errors that are significant under the fine length scales of large optical structures. While the goal of this thesis is to quantify the error due to modelling assumptions, the study of the shape prediction errors has also led to quantification and subsequent identification of problems in the numerical implementation of the solutions. The problems share a common theme — that seemingly reasonably implementation decisions may lead to error that is significant at the performance level of interest for large optical membrane structures.

As with the work on constitutive laws in Chapter 5, the work in this chapter was motivated by efforts to implement solutions to advanced models. These efforts exposed problems with the implementation of the simpler models, and an understanding of the

problems led to development of measures to mitigate or eliminate the source of the errors. The problems arise in three areas:

1. *The AMS-model integral solution.* The boundary condition in this solution must be applied one way under the Axisymmetric Membrane Shell (AMS) model when the domain includes $R = 0$. In Section 6.2 the integral solution is derived, and numerical results are presented in support of the chosen boundary condition approach.

2. *Use of proper coordinate basis for loads.* In the first generation of finite difference solutions, the pressure was taken directly from the inverse solver, reckoned with respect to the deformed-coordinate basis. Section 6.3 includes numerical results that quantify the improvement in prediction error when the load is transformed into the (appropriate) undeformed basis prior to application in the undeformed state.

3. *Endpoint manipulation of solution for smoothness.* The most difficult challenge to finding a good solution for the AMS model lies with a discrete jump in the solution near the endpoints of the domain. Section 6.4 discusses both the origin of this problem within the finite difference expressions and a smoothing procedure.

Modifications to the standard implementation of the solutions are herein shown to decrease the prediction errors. Example cases are given with the spherical-cap-expansion benchmark problem because the exact solution is available.

Simple shape-comparison metrics quantify the prediction errors due to implementation of the example cases. The prediction error $Z_{[\cdot]}$, labelled also as a "model accuracy result" or a "prediction error metric", is a comparison of the deflection derived from a geometrically-exact inverse solver to the deflection calculated through a finite difference solution. For predicted axial displacement $\bar{w}(\bar{r})$, the root-mean-square (RMS) metric is defined by

$$\begin{aligned} \Delta\bar{w}(\bar{r}) &\equiv \bar{w}(\bar{r}) - \bar{w}_{Exact}(\bar{r}) \\ Z_{[\Delta\bar{w}-RMS]} &\equiv \sqrt{\frac{1}{\bar{A}}\int_{\bar{A}}\left[\Delta\bar{w}(\bar{r})\right]^2 d\bar{A}} \end{aligned}$$

Similarly for the standard deviation (STD), the expression is

$$\begin{aligned} \overline{\Delta\bar{w}} &\equiv \frac{1}{\bar{A}}\int_{\bar{A}} \Delta\bar{w}(\bar{r})d\bar{A} \\ Z_{[\Delta\bar{w}-STD]} &\equiv \sqrt{\frac{1}{\bar{A}}\int_{\bar{A}}\left[\Delta\bar{w}(\bar{r}) - \overline{\Delta\bar{w}}\right]^2 d\bar{A}} \end{aligned}$$

The structural performance metrics $Z_{[\Delta\bar{w}-RMS]}$ and $Z_{[\Delta\bar{w}-STD]}$ are used consistently for shape comparison in this chapter.

6.2 AMS Boundary Conditions

The solutions using the AMS model exhibit a discrepancy according to how the outer boundary condition is handled for the case of a filled membrane shell. Through numerical comparison a displacement boundary condition rather than load boundary condition is shown to be appropriate.

6.2.1 Integral Solution

Figure 6.1 represents the mechanical problem under consideration. The radial position variable $\bar{R}$ and radii of curvature functions $\{\bar{R}_\phi(\bar{R}), \bar{R}_\theta(\bar{R})\}$ are given in terms of the undeformed configuration. In addition, the stress resultants $\bar{N}_{\alpha\beta}(\bar{R})$ and pressure $\bar{P}(\bar{R})$ are forces per undeformed length, i.e. the geometry is reckoned with respect to the undeformed basis. For the Axisymmetric Membrane Shell (AMS) theory, the equilibrium equations are given by Equations 3.20 and 3.21 for the case of no initial load.

The first step in the integral solution is to determine the expression for meridional stress resultant $\bar{N}_{\phi\phi}(\bar{R})$. Substitution of Eqn 3.20 into Eqn 3.21 eliminates the circumferential stress resultant $\bar{N}_{\theta\theta}(\bar{R})$.

$$\frac{\bar{N}_{\phi\phi}(\bar{R})}{\bar{R}_\phi(\bar{R})} + \frac{d}{d\bar{R}}\left[\bar{R}\ \bar{N}_{\phi\phi}(\bar{R})\right]\bar{R}_\theta(\bar{R}) \quad = \quad \bar{P}(\bar{R}) \tag{6.1}$$

With a pre-multiplication by $\bar{R}$ and the substitution $\bar{R} = \bar{R}_\theta \sin\phi(r)$, Eqn 6.1 becomes

$$\frac{\bar{R}\ \bar{N}_{\phi\phi}(\bar{R})}{\bar{R}_\phi(\bar{R})} + \sin\phi(\bar{R})\frac{d}{d\bar{R}}\left[\bar{R}\ \bar{N}_{\phi\phi}(\bar{R})\right] \quad = \quad \bar{P}(\bar{R})\ \bar{R} \tag{6.2}$$

The critical step comes in relating the sine of the perpendicular angle ϕ to the meridional

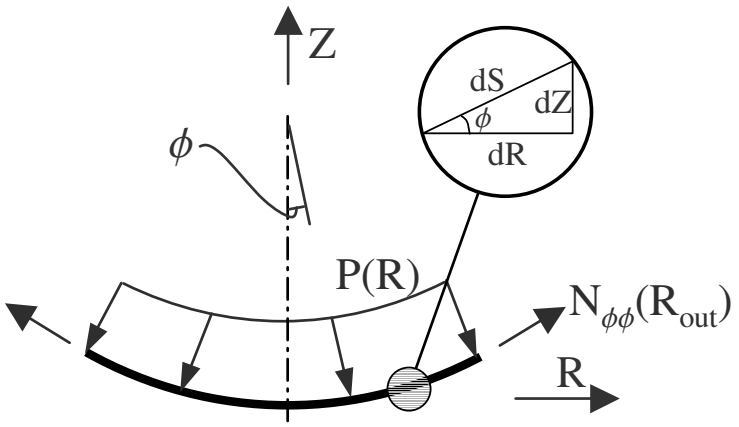

Figure 6.1: Diagram of representative mechanics problem under consideration. The drawing shows a single meridian of shell axisymmetric about the Z-axis labelled with axial position Z, radial position R, angle ϕ from the center line, pathlength position S, pressure $P(R)$, and boundary stress resultant $N_{\phi\phi}(R_{out})$; all quantities are reckoned with respect to the undeformed basis.

radius of curvature $\bar{R}_\phi(\bar{R})$.

$$\begin{aligned}
\frac{d}{d\bar{R}}\sin\left[\phi(\bar{R})\right] &= \cos\left[\phi(\bar{R})\right]\frac{d\phi(\bar{R})}{d\bar{S}}\frac{d\bar{S}}{d\bar{R}} \\
&= \cos\left[\phi(\bar{R})\right]\bar{\kappa}_\phi(\bar{R})\frac{1}{\cos\left[\phi(\bar{R})\right]} \\
&= \bar{\kappa}_\phi(\bar{R}) \\
&= \frac{1}{\bar{R}_\phi(\bar{R})}
\end{aligned} \tag{6.3}$$

for curvature $\bar{\kappa}_\phi(\bar{R})$. With Eqn 6.3, Eqn 6.2 becomes

$$\frac{d}{d\bar{R}}\left(\bar{R}\sin\left[\phi(\bar{R})\right]\bar{N}_{\phi\phi}(\bar{R})\right) = \bar{P}(\bar{R})\bar{R} \tag{6.4}$$

With the use of an arbitrary variable of integration ρ, over $\bar{R}_1 \le \rho \le \bar{R}_2$, Eqn 6.4 becomes

$$\rho\ \ \sin\left[\phi(\rho)\right]\ \ \bar{N}_{\phi\phi}(\rho)\Big|_{\rho=\bar{R}_1}^{\bar{R}_2} = \int_{\bar{R}_1}^{\bar{R}_2}\bar{P}(\rho)\rho d\rho \tag{6.5}$$

Equation 6.5 provides the functional solution for $\bar{N}_{\phi\phi}(\bar{R})$ when either $\bar{R}_1$ or $\bar{R}_2$ is set to the

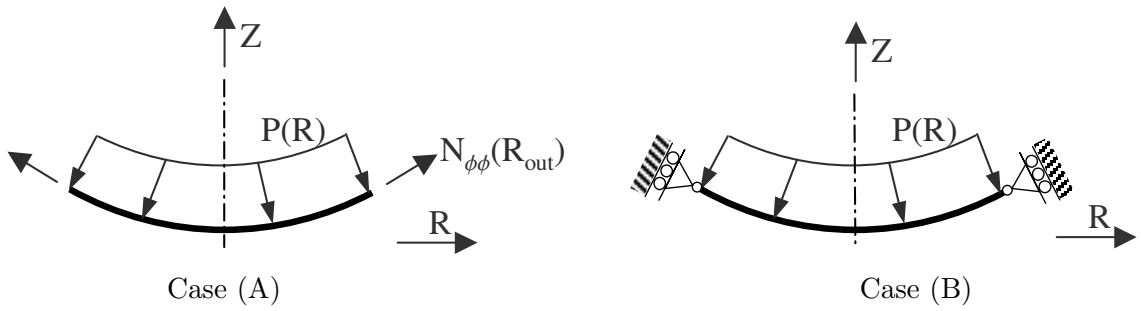

Figure 6.2: Diagram of representative mechanics problem with (A) a stress resultant boundary condition and (B) a displacement boundary condition (the so-called "membrane boundary condition").

general point $\bar{R}$.

6.2.2 Boundary Condition Options

The two potential boundary conditions for this problem are (A) the specification of the boundary stress resultant $\bar{N}_{\phi\phi}(1)$ that is consistent with the inverse design work in this thesis and (B) the specification of zero tangential boundary displacement $\bar{u}_{\phi}(1) = 0$ that is usually called the "membrane boundary condition" when used with membrane shell models. Figure 6.2 provides a graphical description of the difference, and Table 6.1 provides a mathematical summary based upon Eqn 6.5.

The quandary comes when assessing the accuracy of the AMS theory for the membrane mirror benchmark problems. Case (A) more closely matches the mechanical conditions used in the inverse solutions of Chapter 4, but Case (B) is a more common use of membrane theory. The difference between the cases is observed by examining the stress resultant solution near the origin $\bar{R} = 0$.

The two solutions for $\bar{N}_{\phi\phi}(\bar{R})$, as listed in Table 6.1, each include a $\bar{R}^{-1}$-dependent term, and so the limits as $\bar{R} \to 0$ are derived via L'Hôpital's Rule. This limit is explained physically by taking the sum of the static forces acting in the Z-direction. The pressure and stress resultants are linked; if the Z-component of the meridional stress resultant does not equal the area-integral of the corresponding pressure, the missing force quantity must appear over some range of $\bar{R}$. In this case the solution goes to infinity at $\bar{R} = 0$ for all but one exact case of boundary load — the load for which the Case (A) and (B) solutions are

Table 6.1: Mathematical comparison of solutions for representative mechanics problem with (A) a stress resultant boundary condition and (B) a "membrane boundary condition." The integral $\bar{N}_{\phi\phi}(\bar{R})$ solution comes directly from Eqn 6.5, with $\phi_{out} \equiv \phi(1)$.

	Case (A): Specified Boundary Load	Case (B): Displacement BC ("Membrane BC")
Boundary Condition	$\bar{N}_{\phi\phi}(1)$ specified	$\bar{u}_{\phi}(1) = 0$
Initial integral point $\bar{R}_1$	$\bar{R}$	0
Final integral point $\bar{R}_2$	1	$\bar{R}$
$\bar{N}_{\phi\phi}(\bar{R})$ Solution	$\left\{ \frac{1}{\bar{R}\ \sin\left[\phi(\bar{R})\right]} \left[\sin\left[\phi_{out}\right] \bar{N}_{\phi\phi}(1) - \int_{\bar{R}}^{1} \rho \bar{P}(\rho) d\rho \right] \right\}$	$\frac{1}{\bar{R}\ \sin\left[\phi(\bar{R})\right]} \int_0^{\bar{R}} \rho \bar{P}(\rho) d\rho$
Is it finite? ($\lim_{\bar{R}\to 0} \left[\bar{N}_{\phi\phi}(\bar{R})\right]$)	No† $[\pm\infty]$	Yes $\left[\frac{1}{2}\bar{P}(0)\bar{R}_{\phi}(0)\right]$

†The exception is the unique value of $\bar{N}_{\phi\phi}(1)$ for which $\bar{N}^{A}_{\phi\phi}(\bar{R}) = \bar{N}^{B}_{\phi\phi}(\bar{R})$.

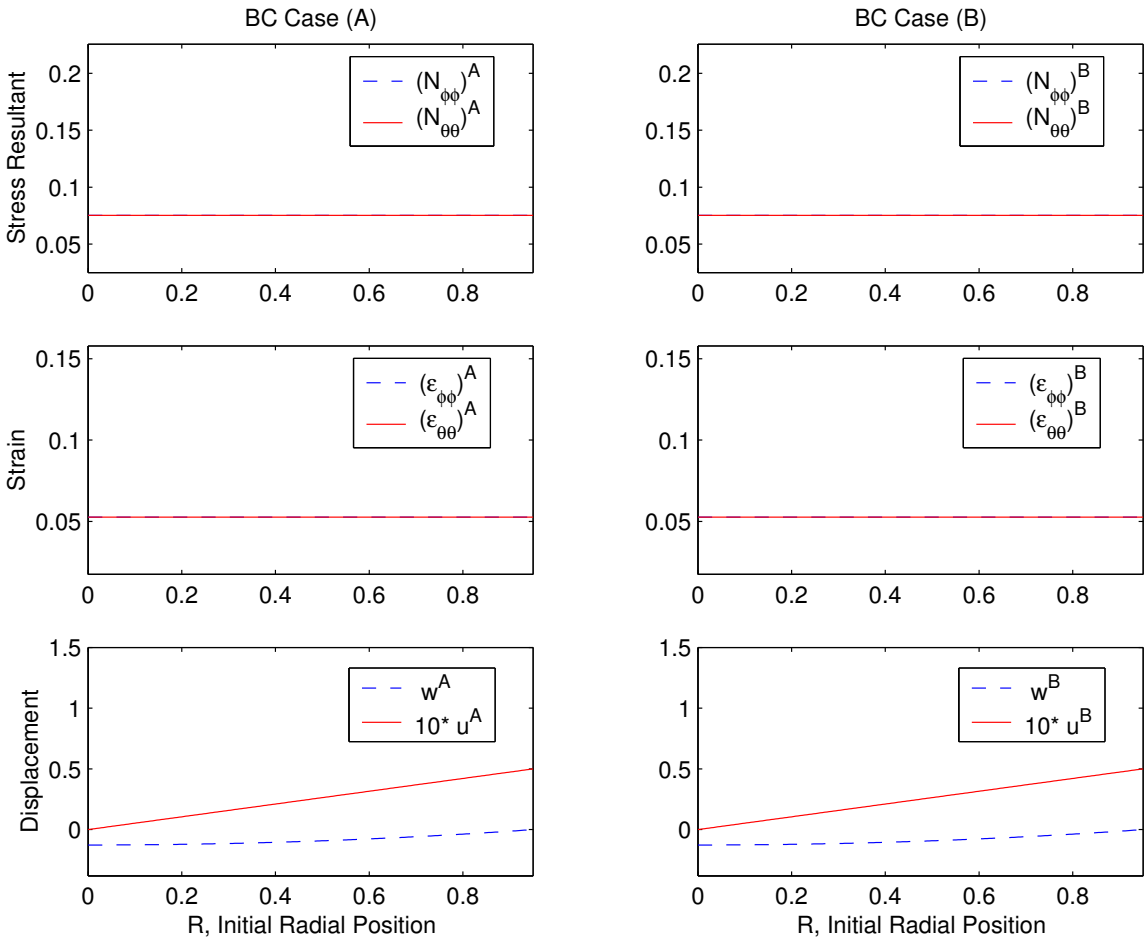

Figure 6.3: Comparison of numerical solution predictions for stress resultant, strain, and displacement given two different boundary conditions in the AMS solution. Case (A), the stress resultant BC, is used for the results in column 1, and Case (B), the displacement BC, in column 2. No difference between the predictions is observed. The problem considered is the spherical-cap benchmark with radius $\bar{R}_{sph} = 3.8 \rightarrow \bar{r}_{sph} = 4$ and 200 intervals.

equal.

6.2.3 Numerical Example

A discrete numerical form of the integral solution is used to demonstrate the issue. Figure 6.3 shows the solutions for different field variables for the spherical-cap benchmark problem with initial radius $\bar{R}_{sph} = 3.8$ and final radius $\bar{r}_{sph} = 4$. The field variable solutions are identical because the boundary condition $\bar{N}_{\phi\phi}(1)$ applied Case (A), taken from the inverse solver, is the exact value at which the two solutions equal each other.

An extension to this analysis shows that any specified boundary load other than the

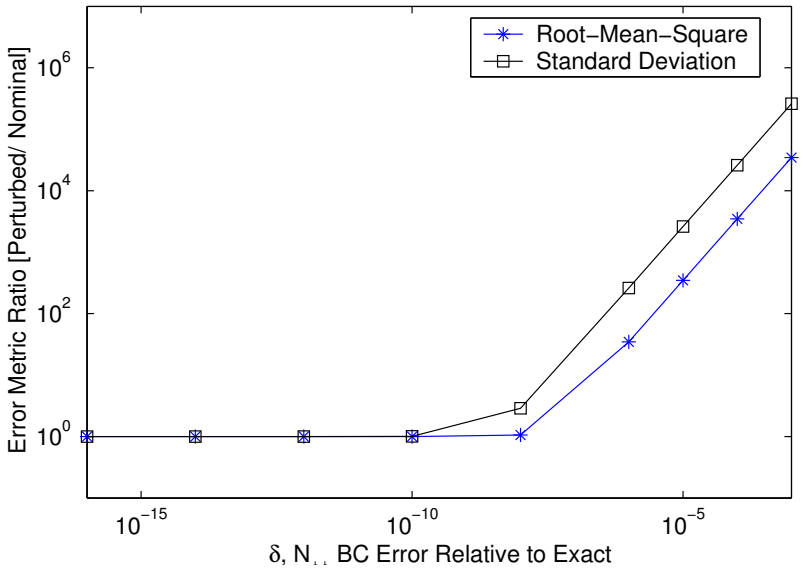

Figure 6.4: Relative growth of prediction error metrics as a function of additive error δ, for $\bar{N}_{\phi\phi}(1) = \bar{N}_{\phi\phi}(1)\big|_{exact}(1+\delta)$. The metrics from Case (B), the membrane-boundary case from Table 6.1, are used to normalize the quantities to the values with the exact BC. The problem considered is the spherical-cap benchmark with radius $\bar{R}_{sph} = 3.8 \rightarrow \bar{r}_{sph} = 4$ and 200 intervals.

exact leads to an infinite solution. To quantify this effect for the membrane shell cases of interest, a small relative error δ is added to the exact boundary specification,

$$N_{\phi\phi}(R_{out}) \quad = \quad N_{\phi\phi}(R)\Big|_{exact}(1+\delta) \tag{6.6}$$

and the accompanying growth in prediction error is observed. Figure 6.4 shows the relative growth of two structural prediction error metrics, area-averaged root-mean-square (RMS) and standard deviation (STD), for one case of spherical cap expansion. At a relative error of $\rho \sim O(10^{-10}$–$10^{-8})$, the prediction error ratio begins to grow rapidly. At a relative boundary error around $\delta \sim 10^{-5}$, for example, the error in the prediction is observed to increase by three orders of magnitude. This error growth correlates to the number of discrete points near $\bar{R} = 0$ that represent the solution going to infinity. The small-δ plateau does equal the error found in the solution employing the $\bar{u}_{\phi}(1) = 0$ displacement condition. Figure 6.5 shows that the basic BC-error-to-prediction-error trend holds over a range of initial-shape dimensions.

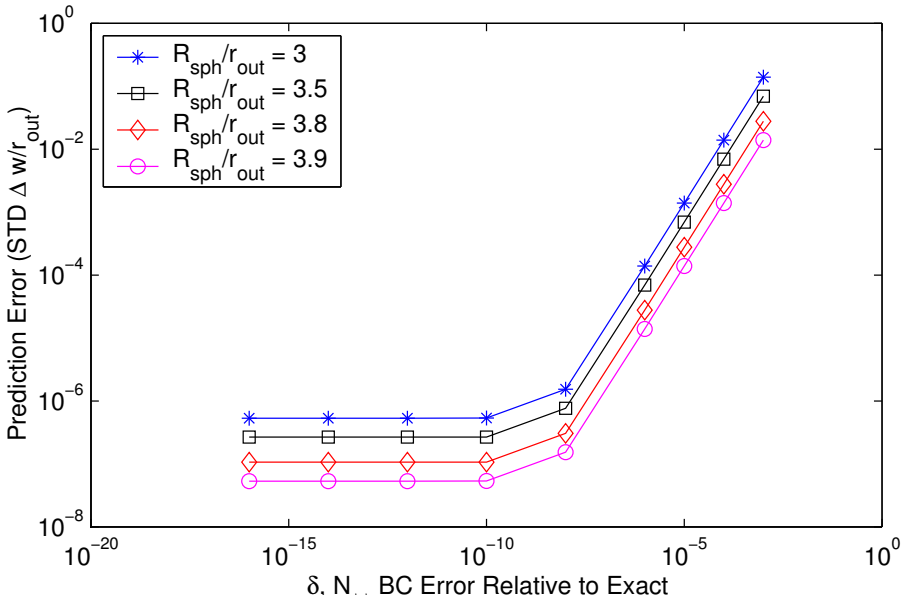

Figure 6.5: Growth of *standard deviation of prediction error* as a function of additive error δ, for $\bar{N}_{\phi\phi}(1) = \bar{N}_{\phi\phi}(1)\big|_{exact}(1+\delta)$. The problem considered is the spherical-cap benchmark with radius $\bar{R}_{sph} = 3.8 \rightarrow \bar{r}_{sph} = 4$ and 200 intervals.

These results show that specifying the outer-boundary stress resultant in AMS theory leads to a tenuous solution technique without robustness. The chance that an $O(10^{-6})$ level error might exist in the boundary is enough to warrant using the membrane boundary condition. Another perspective is that the boundary options are limited once (1) the undeformed basis is used and (2) a no-bending/ no-moment condition is applied. Finally, using a load BC to assess the limiting prediction error of AMS theory presents a mechanics problem consistent with the inverse solution but a poor and unreasonable implementation of the AMS theory; the resulting error cannot be correlated to model assumptions. Moreover, incremental solution methods used for nonlinear, geometrically-exact analysis that is highly sensitive to small error increases the chances of finding a non-sensical solution.

Case (B), the membrane boundary condition with no specification on the boundary stress resultant, should be used as the standard boundary condition for AMS-theory solutions.

6.3 Coordinate Basis for Load

The infinity solutions discussed in Section 6.2 arise when the exact boundary condition is not applied. The critical process for determining the exact boundary condition is the basis transformation, the same undeformed-to-deformed transformation that is discussed in Chapter 5. A boundary condition that is not properly transformed from the deformed to undeformed coordinate basis will result in an error that is significant at the scale of optical quality considered in this thesis. The lesson about proper coordinate basis in the boundary condition extend as well to all of the load conditions on a membrane shell.

One of the first assumptions used in developing most mathematical models of structural behavior is that lengths are reckoned with respect to undeformed coordinates. This assumption leads to tractable models and common field quantities such as engineering stress. Highly-accurate deflection predictions of compliant structures may not allow these assumptions. The inverse solver for the model-accuracy problems uses quantities referred to the deformed basis. This section explains how not transferring the loads from the inverse solver to the undeformed basis results in a significant addition to the prediction error. Applying load in the wrong basis hence leads to an incorrect assessment of the limiting predictive accuracy for a model.

6.3.1 Derivation of Basis Transformation

A notional argument for the form of the basis transformation motivates the basic structure of the transformation. The pressure load is transformed from the deformed basis into the undeformed by

$$\begin{aligned}
[\text{Pressure}]\big|_{\text{Undeformed}} &= \frac{[\text{Normal Force}]}{[\text{Undeformed Area}]} \\
&= \frac{[\text{Normal Force}]}{[\text{Deformed Area}]}\frac{[\text{Deformed Area}]}{[\text{Undeformed Area}]} \\
&= [\text{Pressure}]\big|_{\text{Deformed}}\,(1+[\text{Strain 1}])\,(1+[\text{Strain 2}])
\end{aligned}$$

In contrast to the stress resultant transformation in Chapter 5, the normal force term on a surface does not change form. In specific mathematical terms, the deformation gradient tensor has a one on the diagonal and zeros in the off-diagonal positions.

The spherical-cap-expansion problem used consistently in this chapter is considered now for a more specific example. With a constant pressure and local shape symmetry, the stress resultants and strains will be the same in each principal direction, i.e. $\bar{N}_{\phi\phi}(\bar{R}) = \bar{N}_{\theta\theta}(\bar{R}) = \bar{N}$. The subscripts and the dependence on $\bar{R}$ are eliminated for convenience. The behavior is governed in AMS theory by

$$n = \frac{1}{2}pr_{sph} \tag{6.7}$$

$$\epsilon = \frac{1}{Eh}(1-\nu)N \tag{6.8}$$

$$N = n(1+\epsilon) \tag{6.9}$$

$$P = p(1+\epsilon)^2 \tag{6.10}$$

$$r_{sph} = R_{sph}(1+\epsilon) \tag{6.11}$$

The variables are stress resultant N, strain ϵ, extensional stiffness Eh, pressure P, and radius of curvature R_{sph}, with lower case variables for quantities reckoned with respect to the undeformed basis and upper case for the deformed basis. Since strain is the quantity used to translate between deformed and undeformed bases, the equations are solved for strain. Deformed-basis pressure p and undeformed-basis radius of curvature R_{sph} are the desired dependent variables because these parameters properly specify the problem. For

outer radius $R = r_{out}$ the strain is represented by

$$\begin{aligned}\epsilon &= \frac{1-(1-\nu)\frac{pr_{out}}{Eh}\frac{R_{sph}}{r_{out}} - \sqrt{1-2(1-\nu)\frac{pr_{out}}{Eh}\frac{R_{sph}}{r_{out}}}}{(1-\nu)\frac{pr_{out}}{Eh}\frac{R_{sph}}{r_{out}}} \\ &= \frac{1-\sqrt{1-2(1-\nu)\bar{p}\bar{R}_{sph}}}{(1-\nu)\bar{p}\bar{R}_{sph}} - 1 \end{aligned} \tag{6.12}$$

where pressure and radius of curvature have been transformed into nondimensional quantities $\bar{p}$ and $\bar{R}_{sph}$. The geometrically-exact strain of Equation 6.12 is thus found in closed form, and the undeformed-basis pressure $\bar{P}$ is found via Equation 6.10. In the following section this correction of the pressure into the undeformed basis is implemented, and the resulting model prediction errors between the naive and proper methods are compared.

6.3.2 Numerical Example

For the spherical-expansion problem under study in this chapter, Figure 6.6 shows that the standard deviation of the deflection prediction error is much lower when the undeformed basis is used. The mean pressure for each case is used as the abscissa because previous work showed this quantity tends to be the best parameter for comparison. *The correction to the undeformed basis results in multiple orders of magnitude decrease in the estimation of model prediction error.*

More than just showing that the error is lower when using the proper basis, Figure 6.6 shows that the use of the wrong basis adds so much error that the expected trends are not observable. In the undeformed-basis results, the finer-discretization, $N = 1000$ cases have smaller prediction error than the $N = 200$; smaller interval sizes are expected to be more accurate in finite difference, and so this trend is consistent with expectation. The errors for the deformed-basis results are the same for the two different intervals, and so the error from an incorrect basis is seen to be so great that the underlying model-error trends are not observable.

In addition to smaller magnitude, the trend of error versus load is seen in Figure 6.6 to have a smaller slope in the undeformed-basis results. In fact, the slope of the pressure-versus-error relationship decreases by almost half from the deformed basis to the undeformed basis. A proper use of coordinate basis hence means that the model will be valid for problems of optical-level accuracy over a larger range of load than would have been predicted with the

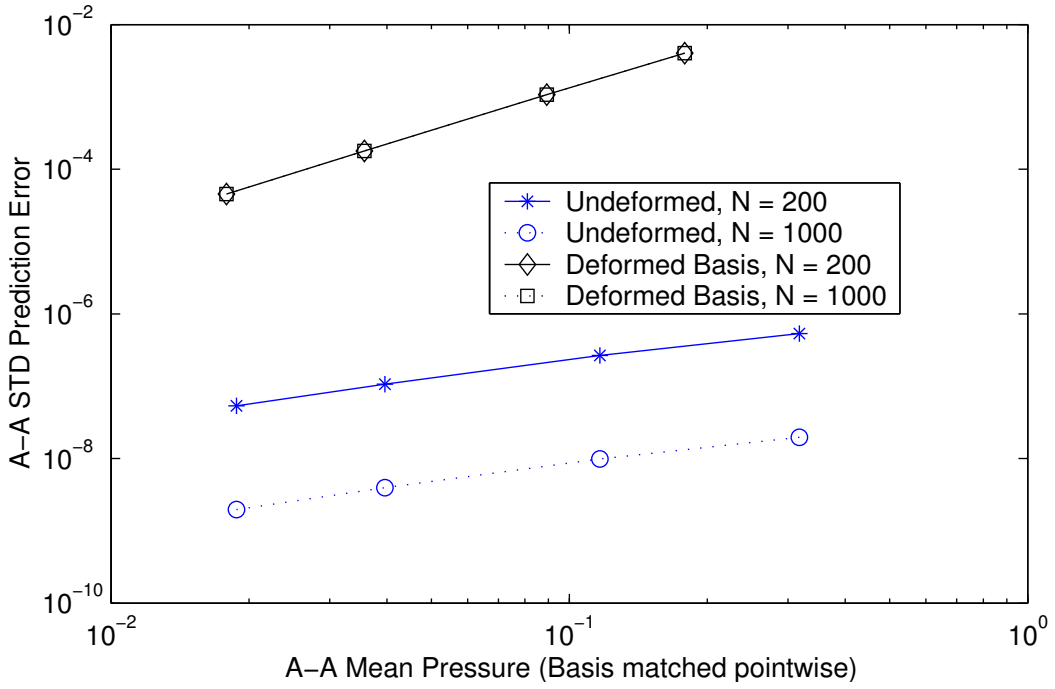

Figure 6.6: Comparison of model prediction error STD metrics according to mean pressure, for pressure in each the deformed and undeformed bases (undeformed is appropriate for all but the geometrically-exact theories). The problem considered is the spherical-cap benchmark with radius $\bar{R}_{sph} = 3.8 \rightarrow \bar{r}_{sph} = 4$ and intervals of 200 and 1000.

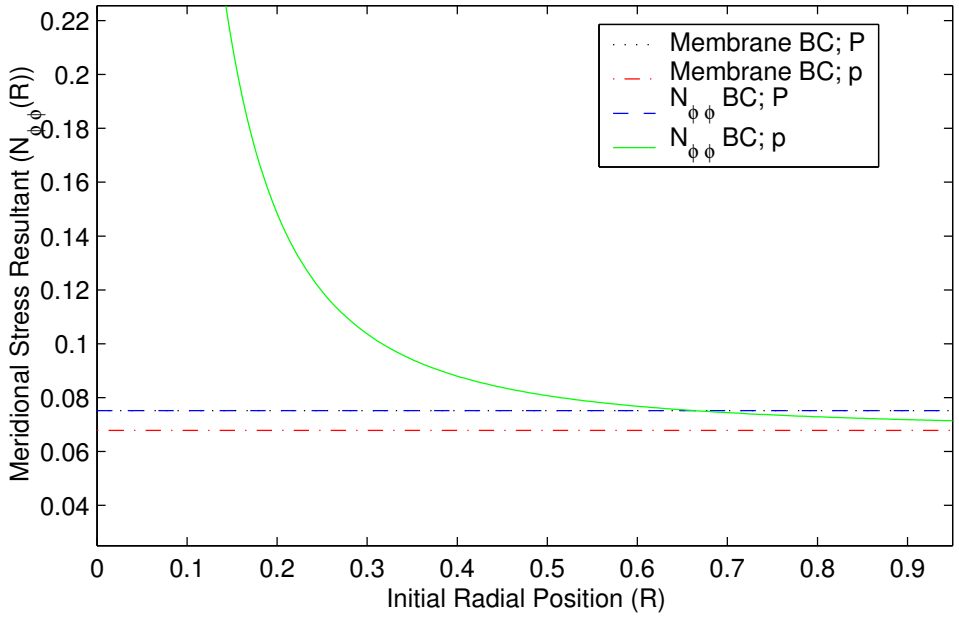

Figure 6.7: Solution for meridional stress resultant $\bar{N}_{\phi\phi}(\bar{R})$ for two different boundary conditions and two different coordinate bases for the load. This plot shows that the correct, constant-response solution is found when the load is transformed into the undeformed basis. The problem considered is the spherical-cap benchmark with 200 intervals and radius $\bar{R}_{sph} = 3.8 \rightarrow \bar{r}_{sph} = 4$.

deformed-basis results.

The choice of coordinate basis also ties back to the boundary-condition results of Section 6.2. Figure 6.7 shows the solution for the stress resultant distribution for different combinations of boundary conditions and load bases. When the pressure is transformed into the undeformed basis, the two different BC conditions return an identical solution. This solution trend is the same as seen in Figure 6.3. For pressure in the deformed basis, however, (1) the membrane-BC case returns a solution with a bias error and (2) the load-BC case returns a solution that goes to infinity at $\bar{R} = 0$ (Equation 6.5 and Table 6.1 provide the details). The "exact boundary condition load" discussed as impractical in Section 6.2 is hence determined from the inverse solver results through a proper transformation of coordinate basis.

The switch to undeformed basis is necessary for consistency with most membrane models, and the impact of missing this detail is significant: the values of

prediction error metrics with load properly represented in the undeformed basis are many orders of magnitude lower than the results from the load in a deformed basis.

6.4 Smoothness of the Solution

The straightforward use of finite difference expressions to calculate the discrete geometric field variable distribution required for the AMS integral solution leads to a numerical discrepancy. The values of the radii of curvature near the endpoints make a slight jump in the initial state, but this lack of smoothness in the undeformed configuration leads to a very noticeable jump in the radii of curvature in the final state. In this section the problems with smoothness of the solution at the endpoints is explained, and a method to smooth the solution is introduced. The effect upon the solution is explained in terms of the both the field variable distribution and mirror performance metrics.

6.4.1 Observed Jumps in the Field Variables

A discrete jump is observed in the stress resultant and other field variables at the endpoints. Neither the membrane governing equations nor the boundary conditions provide any indication that the structural response will be discontinuous, and so the numerical solution technique appears suspect.

Figure 6.8 shows the calculated radii of curvature in both the undeformed and deformed states for the benchmark problem of constant-pressure expansion on a spherical cap. The "undeformed" case shows the radii of curvature prediction prior to loading, and the "deformed" case shows the ROC prediction after loading. Figure 6.9 shows the errors of Figure 6.8 relative to the exact values over a logarithmic scale. These relative error plots show how a jump in the value at the endpoints, not even perceivable in the undeformed function values of Figure 6.8, evolve into more significant errors in the predicted deformed state. Similar results are observed in the $N = 1000$-interval case, and so the $N = 1000$ results are not shown here.

Numerical errors in the calculation of the geometric field variables at the endpoints lead to errors significant to the optical-level predictions of the deformed shape. Specialized methods are required to smooth the solution near the endpoints.

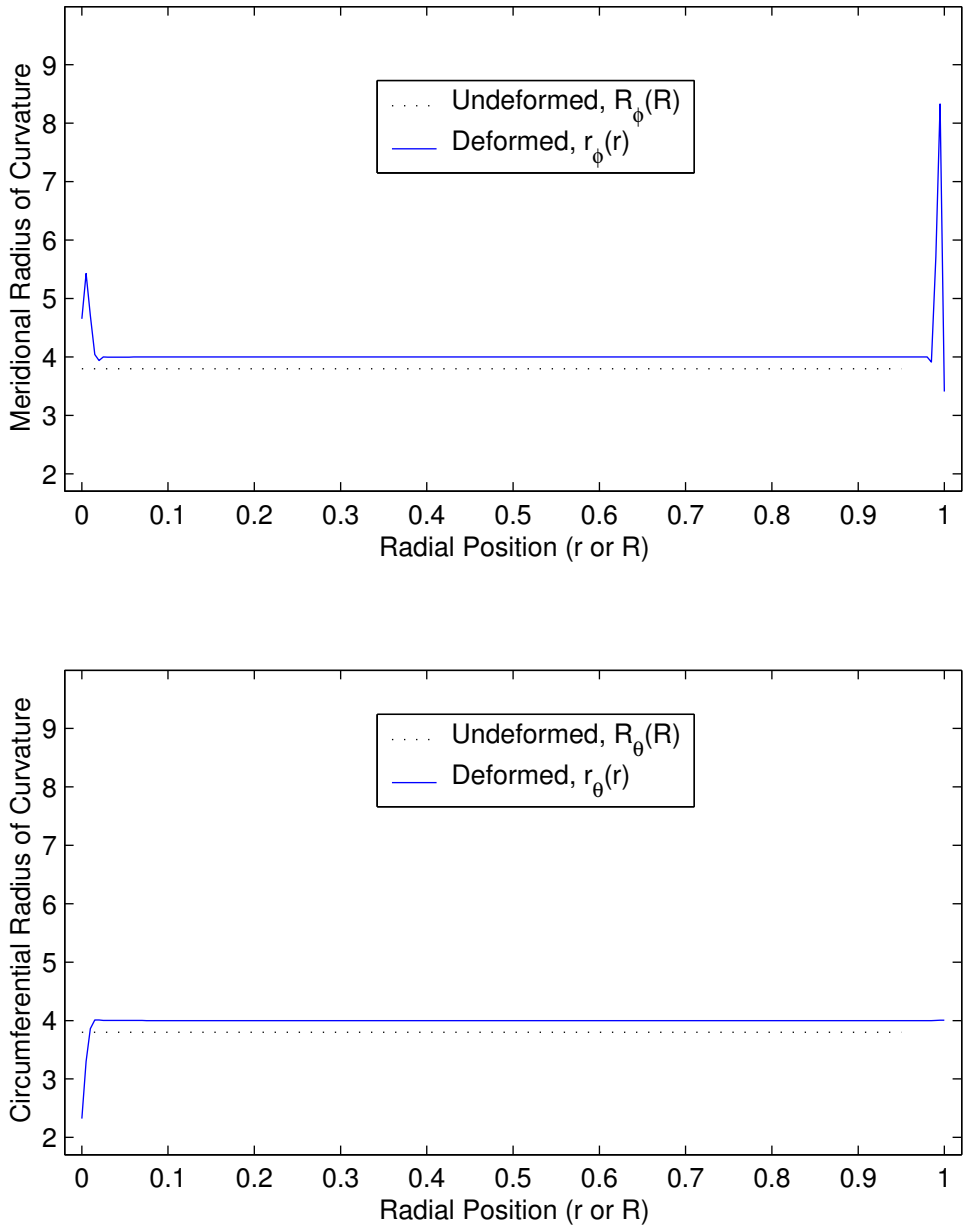

Figure 6.8: Numerically-calculated radii of curvature (ROC) for the spherical-cap-expansion problem. The top plot shows the meridional ROC $\bar{R}_\phi(\bar{R})$, and the bottom shows the circumferential ROC $\bar{R}_\theta(\bar{R})$. The problem considered is the spherical-cap benchmark with 200 intervals and radius $\bar{R}_{sph} = 3.8 \rightarrow \bar{r}_{sph} = 4$.

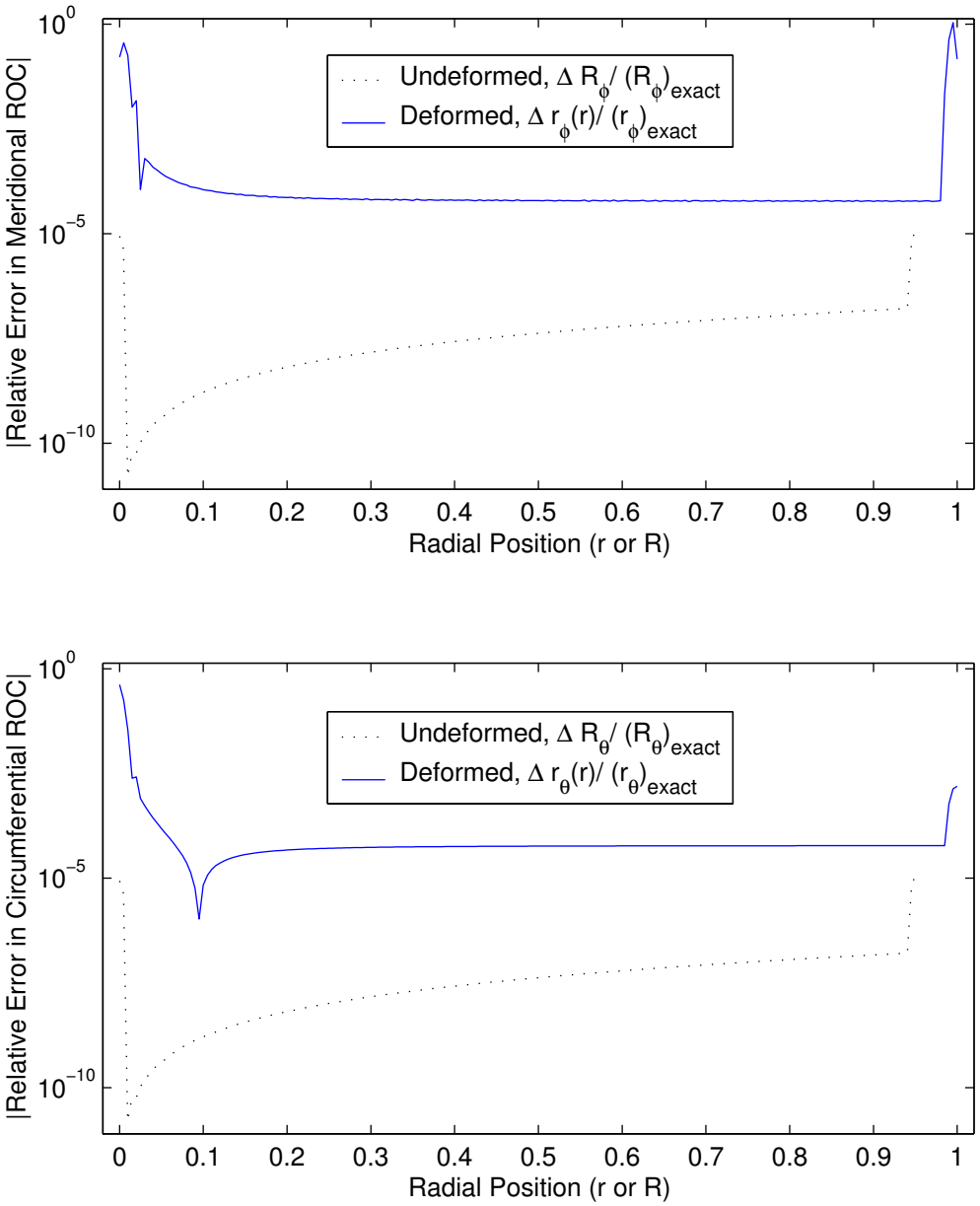

Figure 6.9: Error in the numerically-calculated radii of curvature (ROC) relative to the exact value for the spherical-cap-expansion problem. The top plot shows the meridional ROC $\bar{R}_\phi(\bar{R})$, and the bottom shows the circumferential ROC $\bar{R}_\theta(\bar{R})$. The problem considered is the spherical-cap benchmark with 200 intervals and radius $\bar{R}_{sph} = 3.8 \rightarrow \bar{r}_{sph} = 4$.

6.4.2 Identification of Numerical Issue

The radius of curvature term $\bar{R}_\phi(\bar{R})$ is used to calculate deflection due to pressure loading in the AMS theory as developed in Section 6.2 and summarized by Case (B) in Table 6.1. The exact form of the curvature along a meridian, using the geometry of Figure 6.1, is given by

$$\begin{aligned} \bar{\kappa}_\phi(\bar{R}) &= \frac{1}{\bar{R}_\phi(\bar{R})} = \frac{\frac{d^2\bar{Z}(\bar{R})}{d\bar{R}^2}}{\left[1+\left(\frac{d\bar{Z}(\bar{R})}{d\bar{R}}\right)^2\right]^{\frac{3}{2}}} \\ \bar{R}_\phi(\bar{R}) &= \frac{\left[1+\left(\frac{d\bar{Z}(\bar{R})}{d\bar{R}}\right)^2\right]^{\frac{3}{2}}}{\frac{d^2\bar{Z}(\bar{R})}{d\bar{R}^2}} \end{aligned} \tag{6.13}$$

Thus both first and second derivatives of the meridian shape function $\bar{Z}(\bar{R})$ are required.

In the numerical implementation, finite difference expressions with order $(\Delta\bar{r})^2$ error are used. Central difference expression errors are used for all of the interior points, with a switch to forward and backward difference expressions near $\bar{R} = 0$ and $\bar{R} = 1$, respectively. This switch in expressions is the basis of the lack of smoothness in the field variable calculations.

6.4.3 Method to Smooth Solution

A good approach to handling the jumps in values is to perform a cubic extrapolation from the neighboring points to guarantee that the function values are smooth. The function value from cubic extrapolation at a single point is determined from the values of the function at the nearest four points.

To check the accuracy of this implementation, the benchmark problem considered is the extension of a spherical cap. In terms of the curvature calculations that feed the solution integral for the AMS model, this problem reduces to calculating curvature on a spherical line segment divided into discrete intervals. In an effort not represented in this thesis, the finite difference expressions for an irregularly-spaced grid were derived. These new, more complicated expressions are verified through testing of polynomials and sinusoids, and the new code predicts the derivatives within the error tolerances of the expressions.

Figure 6.10 shows how the size of the interval $\Delta\bar{R}$ used over $0 \leq \bar{R} \leq 1$ affects the numerical accuracy of the radius of curvature prediction for finite difference expressions

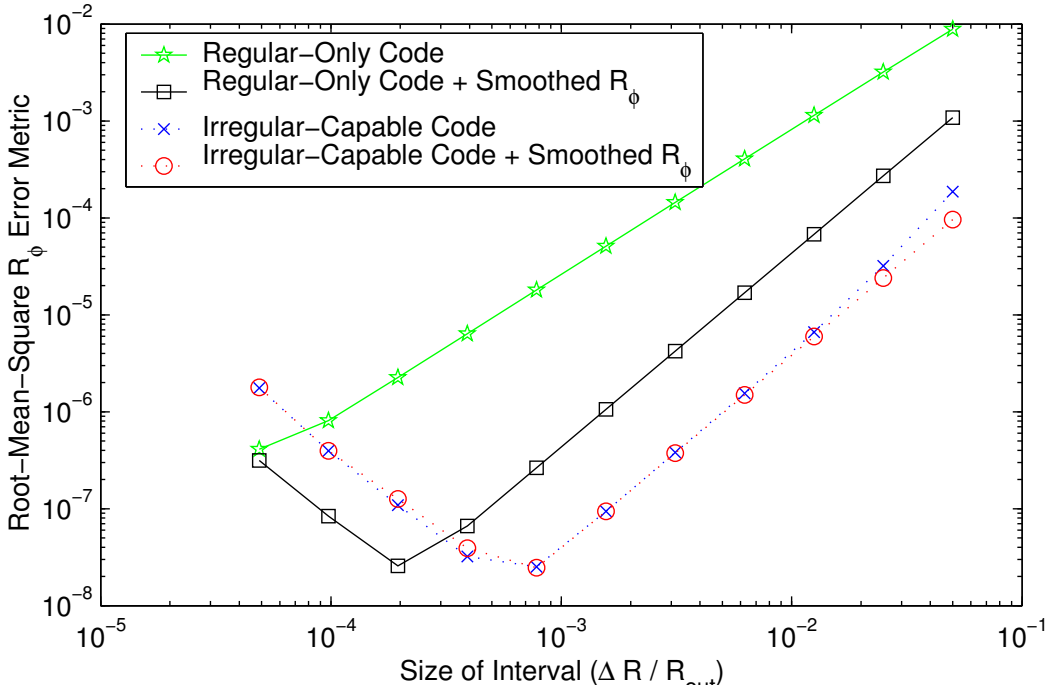

Figure 6.10: Comparison of radius-of-curvature $\bar{R}_{sph}$ calculation errors for different sets of algorithms over a range of finite difference interval sizes. The exact curve is a spherical line segment over $0 \leq \bar{R} \leq 1$ for which $\bar{R}_{sph} = 3$. The RMS error metric is defined by the discrete version of $\sqrt{\frac{1}{\bar{A}} \int_{\bar{A}} \left(\bar{R}_\phi(\bar{R}) - \bar{R}_{sph}\right)^2 d\bar{A}}$.

using either the assumptions of regular or irregular spacing in the grid. "Smoothing" indicates that the two extreme points at either end of the line segment were calculated via cubic extrapolation. The input to the code is a spherical line segment with regularly-spaced discrete intervals. With the assumption that this segment is a meridian of an axisymmetric spherical shell, the root-mean-square metric is taken as an area integral for exact spherical radius $\bar{R}_{sph}$.

$$[\bar{R}_\phi \text{ RMS Error}] \quad = \quad \sqrt{2 \int_0^1 \left[\bar{R}_\phi(\bar{R}) - \bar{R}_{sph}\right]^2 \bar{R} \; d\bar{R}} \tag{6.14}$$

Figure 6.11 presents similar information except that the abscissa is the number of points.

Figures 6.10 and 6.11 provide 3 lessons:

1. Below approximately 1000 intervals ($\Delta\bar{R} \sim 10^{-3}$), the code for calculating derivatives

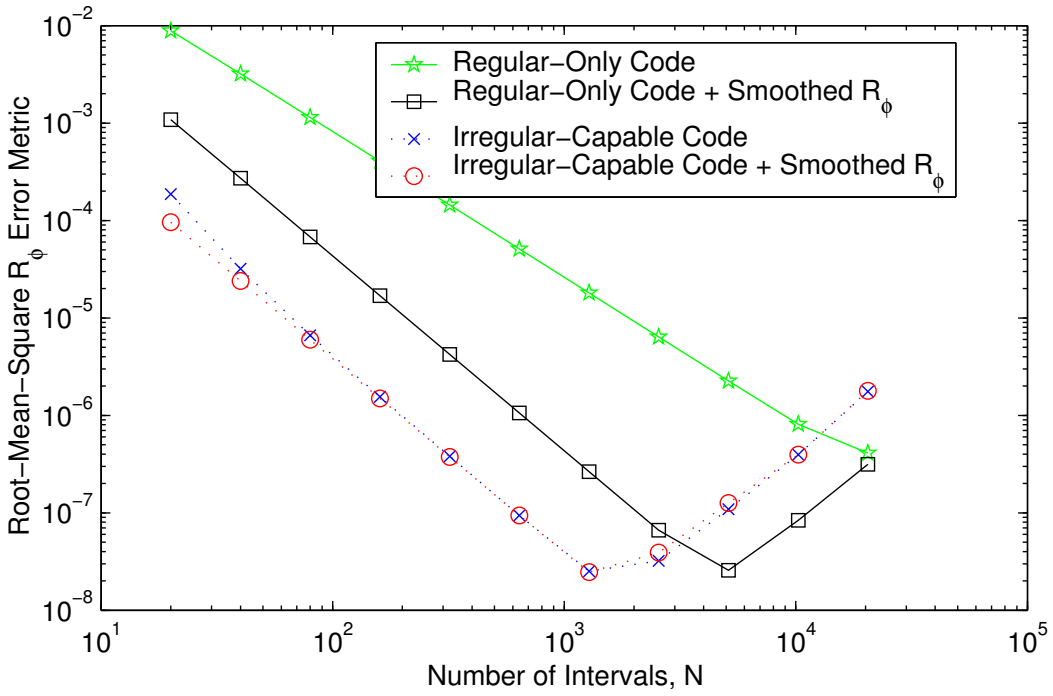

Figure 6.11: Comparison of radius-of-curvature $\bar{R}_\phi$ calculation errors for different sets of algorithms over a range of total finite difference interval counts. Data is the same as Figure 6.10.

for grids with irregularly-spaced points predicts the radius of curvature to better accuracy than the code for grid with regularly-spaced points. This is because the irregularly-spaced-grid code includes central difference expressions with $(\Delta\bar{R})^4$-level error for equal intervals; this expression is used because the error is one to two orders larger for irregular intervals. *The irregularly-spaced-capable code calculates the field variables correctly*, albeit with a numerical limitation on the interval size.

2. Around 1000 intervals, the prediction error for radius of curvature begins to grow in all but the un-smoothed, regularly-spaced-grid code. A growth in the error is expected at some small interval size because the large number of multiplication and addition operations in the irregularly-spaced-grid difference code propagates errors.

3. Smoothing the endpoint and neighbor values of $\bar{R}_\phi[k]$, $k = \{1, 2, N, N+1\}$, reduces the prediction error 1–2 orders of magnitude for the regularly-spaced-grid code yet not significantly for the irregularly-spaced grid code.

With the need for smoothing the calculation of field quantities near the endpoints now established, the method of smoothing must be understood and chosen. Figure 6.12 shows the error in the radius-of-curvature calculation at the endpoints for a variety of smoothing methods. The basic difference between the methods is whether the endpoints of the component functions $\frac{d\bar{W}}{d\bar{R}}(\bar{R})$ and $\frac{d^2\bar{W}}{d\bar{R}^2}(\bar{R})$ have been altered by extrapolating; Table 6.2 describes which points were calculated by extrapolation. Case (A) represents the previous implementation in which the slope is a known quantity and the second derivative only comes from a numerical first derivative. With the incremental solver, however, only the shape will be known explicitly, and so the first and second derivatives are both calculated numerically. Figure 6.12 shows that some of the cases leave significant errors at the endpoints; note that this endpoint error is fundamentally the same issue as recorded in Figures 6.6 and 6.7. Cases (B), (J), and (K) result in the same error at the endpoints, while Cases (L) and (M) result in a decrease in error. It is noted that the intervals for these numerical examples are made slightly irregular by the addition of an order $\sim 10^{-6}\bar{R}_{out}$ additive perturbation.

While smoothing the endpoints of the component functions $\frac{d\bar{W}}{d\bar{R}}$ and $\frac{d^2\bar{W}}{d\bar{R}^2}$ does affect the endpoint error in $\bar{R}_\phi[k]$, the error is improved more by smoothing the outer two points of $\bar{R}_\phi$. In this case "smoothing" refers to finding the function value at a point via cubic-polynomial extrapolation from neighboring points. The implementation uses the following

Table 6.2: Description of the different cases implemented for handling the endpoint errors in the field variables: delineation of the different extrapolations. Figures 6.12 and 6.13 provide a graphical comparison.

(a) Slope

Case	Number of Points Extrapolated			
	$\frac{d\bar{W}}{d\bar{R}}[1]$	$\frac{d\bar{W}}{d\bar{R}}[2]$	$\frac{d\bar{W}}{d\bar{R}}[N]$	$\frac{d\bar{W}}{d\bar{R}}[N+1]$
A	0	0	0	0
B	1	0	0	1
J	1	0	0	0
K	1	0	0	0
L	1	0	0	0
M†	1	0	0	0

(b) Curvature

Case	Number of Points Extrapolated			
	$\frac{d^2\bar{W}}{d\bar{R}^2}[1]$	$\frac{d^2\bar{W}}{d\bar{R}^2}[2]$	$\frac{d^2\bar{W}}{d\bar{R}^2}[N]$	$\frac{d^2\bar{W}}{d\bar{R}^2}[N+1]$
A	0	0	0	0
B	0	0	0	1
J	0	0	0	1
K	0	0	1	1
L	1	1	1	1
M†	1	1	1	1

dependencies:

$$\bar{R}_\phi[1] = f_1\Big(\bar{R}_\phi[3],...,\bar{R}_\phi[6],\bar{R}[1],\bar{R}[3],...,\bar{R}[6]\Big) \quad (6.15)$$

$$\bar{R}_\phi[2] = f_1\Big(\bar{R}_\phi[3],...,\bar{R}_\phi[6],\bar{R}[2],\bar{R}[3],...,\bar{R}[6]\Big) \quad (6.16)$$

$$\bar{R}_\phi[N] = f_N\Big(\bar{R}_\phi[N-4],...,\bar{R}_\phi[N-1],\bar{R}[N-4],...,\bar{R}[N-1],\bar{R}[N]\Big) \quad (6.17)$$

$$\bar{R}_\phi[N+1] = f_N\Big(\bar{R}_\phi[N-4],...,\bar{R}_\phi[N-1],\bar{R}[N-4],...,\bar{R}[N-1],\bar{R}[N+1]\Big) \quad (6.18)$$

Figure 6.13 shows the results of smoothing for the different cases discussed in Table 6.2. Although the original function $\bar{R}_\phi(\bar{R})$ is different for each case, the prediction error for the smoothed $\bar{R}_\phi(\bar{R})$ is approximately the same across all the cases. When the results are smoothed by extrapolation from the neighboring points, the field variables are observed to no longer have discrete jumps in prediction error.

Although the use of extrapolation does not have a mathematical justification beyond the desire for a smooth solution, an analysis of the finite difference error shows that the cubic extrapolation is mathematically legitimate and sound. The justification for this corrective measure comes from the very definition of the finite difference operators. In the derivation, the Taylor series expansion of the function is taken at each point. By application of Taylor's Theorem [80], the error in the series representation of a function is defined by the first omitted derivative term, evaluated at some undetermined point in the interval in question.

To estimate this error, the finite difference expressions are revisited. Adding another term to the Taylor series expansion allows the error term to be tracked through the derivation of the finite difference expressions, and an error estimate of the finite difference expression is thereby generated. For an example with an easier-to-read case, the following is the first term of the error series for the forward difference form of a second derivative ($O(\Delta x^2)$ error) in the case of regularly-spaced intervals.

$$\delta y(x,x_0) = \frac{2f(x_0) - 5f(x_0+\Delta x) + 4f(x_0+2\Delta x) - f(x_0+3\Delta x)}{\Delta x^2} \quad (6.19)$$

The error expressions for irregularly-spaced intervals contain a much larger number of terms and are not repeated here. In the current context, the error expressions are used as bounds over which the current values can be changed to extrapolated values.

Case L from Table 6.2, in which four points are modified by cubic extrapolation, is used

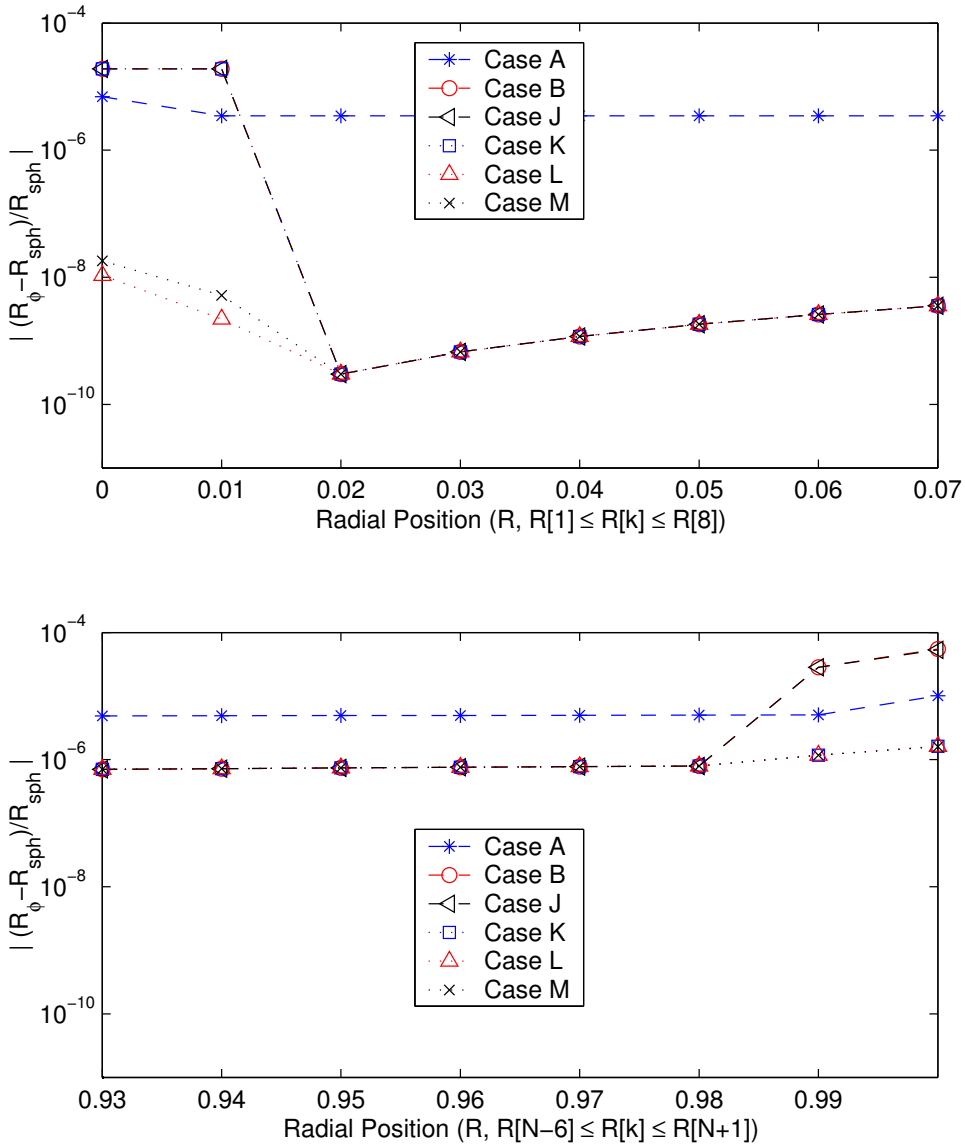

Figure 6.12: Comparison of meridional ROC $\bar{R}_\phi([k])$ calculation errors near each endpoint for different numerical techniques. The abscissa shows the error relative to the exact value for the case of no direct extrapolation of $\bar{R}_\phi([k])$ at the extreme two points; Figure 6.13 provides a comparison for the *case of extrapolated endpoints*. The top plot shows the error at the $\bar{R} = 0$ end of the domain, and the bottom plot shows $\bar{R} = 1$. 100 intervals are used over $0 \le \bar{R} \le 1$ for a spherical line segment with exact radius of curvature 3.8.

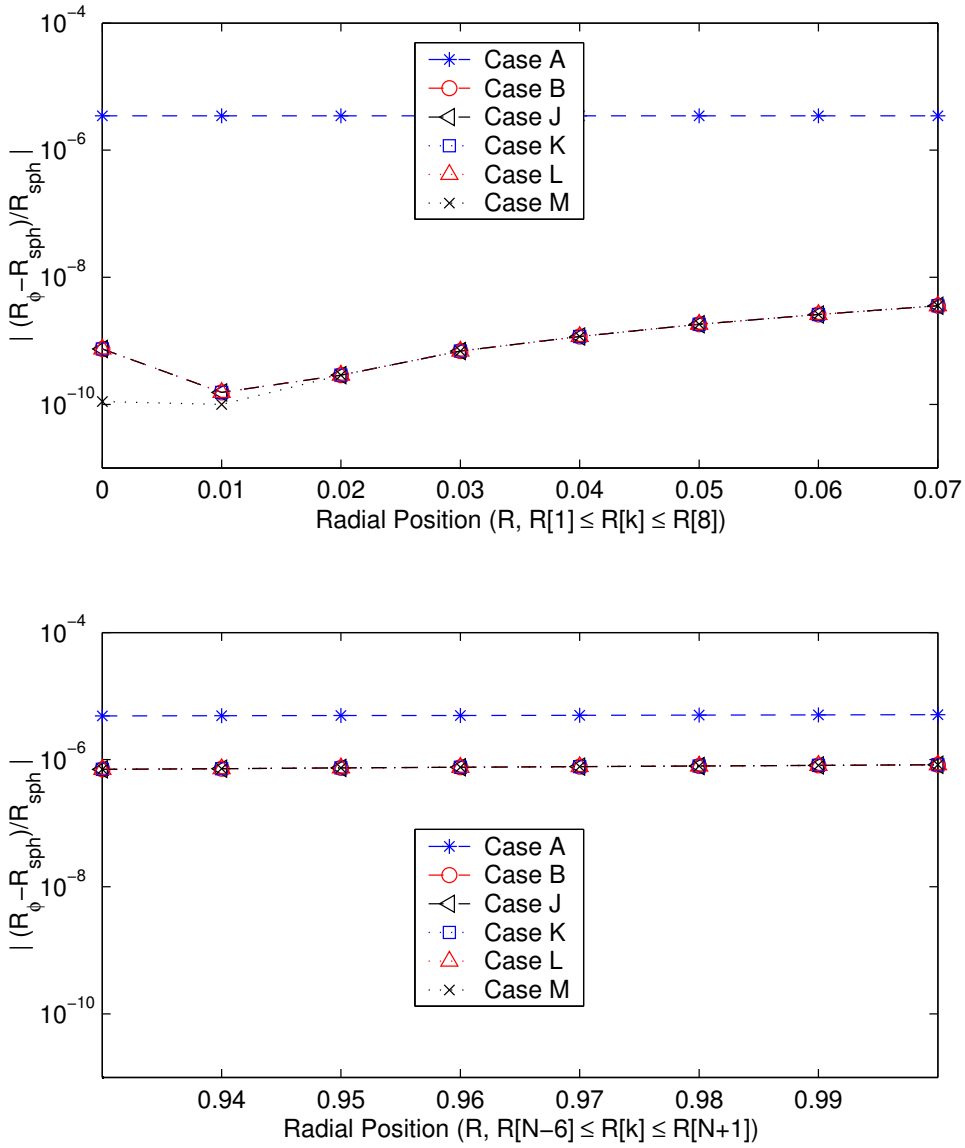

Figure 6.13: Comparison of meridional ROC $\bar{R}_\phi([k])$ calculation errors near each endpoint for different numerical techniques. The abscissa shows the error relative to the exact value for the case of no direct extrapolation of $\bar{R}_\phi([k])$ at the extreme two points; Figure 6.13 provides a comparison for the *case of no extrapolation*. The top plot shows the error at the $\bar{R} = 0$ end of the domain, and the bottom plot shows $\bar{R} = 1$. 100 intervals are used over $0 \leq \bar{R} \leq 1$ for a spherical line segment with exact radius of curvature 3.8.

to examine the extrapolation of points in the $\frac{d^2\bar{W}}{d\bar{R}^2}(\bar{R})$ function relative to the expression for maximum error. Note that this "maximum error" quantity is an estimate because the exact error specified in Taylor's Theorem is based upon the final derivative (third derivative in this case) evaluated at some point near the expansion. Since the final derivative is evaluated at the expansion point for convenience in this work, the resulting quantity is only an estimate of the error bound.

In Figure 6.14 the change in current function value due to cubic extrapolation is normalized by the estimate of the finite difference error and plotted over a range of exact ROC values. Each connected set of points represents a difference point from the set of $\{1, 2, N, N+1\}$. The example case in Figure 6.14, with one set of random interval perturbations, shows that the values found by cubic extrapolation generally lie within the bounds of the finite difference error expression. Plotted against radius of curvature are lines which represent the second derivative $\frac{d^2\bar{W}}{d\bar{R}^2}[k]$ predicted by different extrapolation schemes; the scale of the derivative has been normalized by the predicted error bound. For the $N = 100$ interval case, the extrapolated values are within the error bounds for the reported radii of curvature. For the $N = 1000$ interval case in Figure 6.15, however, the error is observed to become larger than the error estimate for radii of curvature above $\bar{R}_{sph} \sim 6$. The result is encouraging because the error lies within an order of magnitude of the error estimate. Figures 6.14 and 6.15 show that the mathematical basis for the cubic extrapolation is sound because the extrapolated values generally lie within the error bound estimate for the function.

In this implementation the values of the derivative functions $\frac{d\bar{W}}{d\bar{R}}(\bar{R})$ and $\frac{d^2\bar{W}}{d\bar{R}^2}(\bar{R})$ are only changed as much as the estimated error bound. For radius-of-curvature endpoint values, however, no such restrictions are placed on the values of ROC resulting from extrapolation.

Use of cubic extrapolation is recommended to smooth the endpoint predictions of differential-type field variables. The differences between the values predicted by finite difference and the values modified by extrapolation are consistent with the error tolerance of the finite difference expressions in the geometric and loading cases of interest.

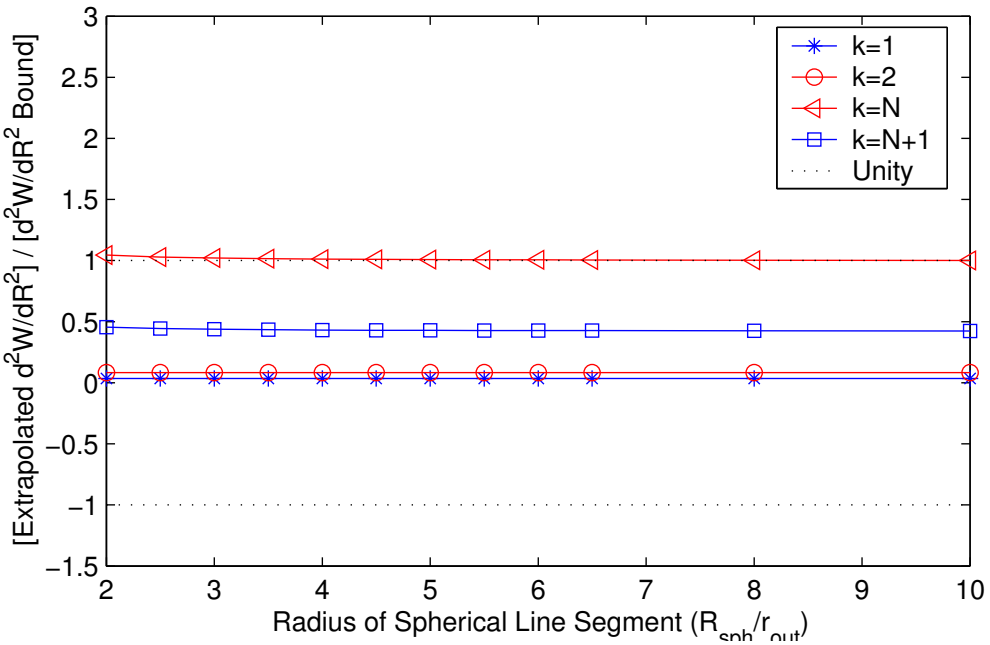

Figure 6.14: Change to finite difference expressions for $\frac{d^2\bar{W}}{d\bar{R}^2}(\bar{R})$ according to cubic extrapolation relative to the finite difference error estimate. The case under study is a spherical line segment where the abscissa is the spherical radius. Lines are drawn to represent the extrapolation at four discrete locations: $k = \{1, 2, N, N+1\}$. The 100-interval grid is irregularly-spaced by the addition of a $O(10^{-6}\Delta\bar{R})$ random "noise", and so this plot is representative rather than unique. Figure 6.15 provides the 1000-interval case.

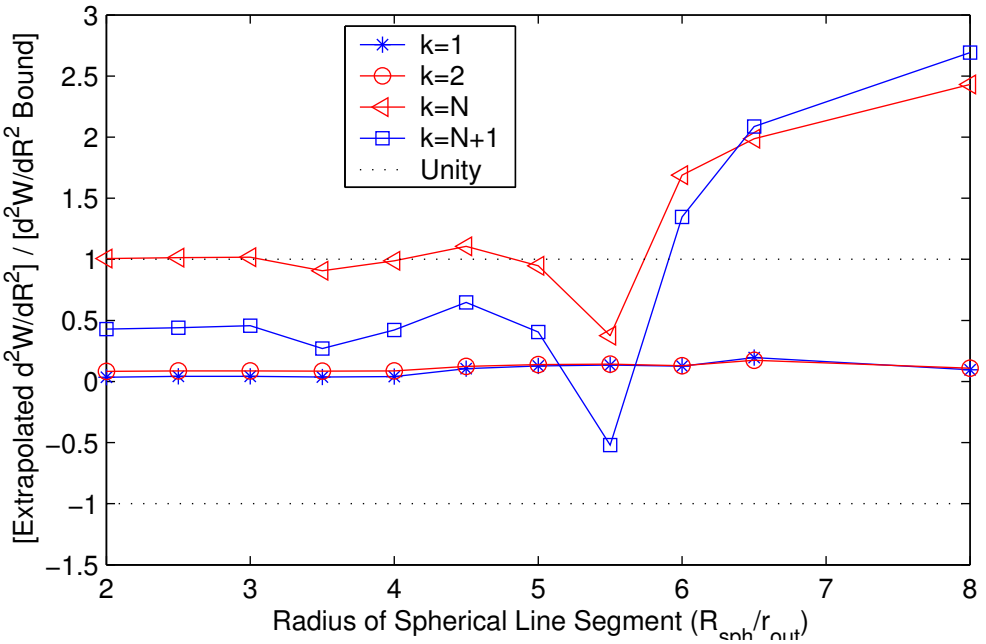

Figure 6.15: Change to finite difference expressions for $\frac{d^2\bar{W}}{d\bar{R}^2}(\bar{R})$ according to cubic extrapolation relative to the the finite difference error estimate. The case under study is a spherical line segment where the abscissa is the spherical radius. Lines are drawn to represent the extrapolation at four discrete locations: $k = \{1, 2, N, N+1\}$. The 1000-interval grid is irregularly-spaced by the addition of a $10^{-6}\Delta\bar{R}$-magnitude random "noise", and so this plot is representative rather than unique. Figure 6.14 provides the 100-interval case.

6.5 Summary

In this chapter a set of lessons have been developed for the implementation of optical-quality shape predictions of large membrane shells. In each case the use of the spherical-cap benchmark problems provides a method to quantify the effect of the incorrect or less desirable implementation choices upon a relevant membrane optics problem.

1. *The displacement or "membrane" boundary condition should be used as the standard boundary condition for AMS-theory solutions.*

   Specification of a stress resultant boundary condition leads to a solution with infinite or near-infinite endpoint values unless one exact value of the boundary condition is applied. Finite deflection predictions for pressure loading of zero-initial-load, filled, doubly-curved membranes using AMS theory require that the boundary stress resultant be part of the solution rather than part of the problem specification.

2. *A load in the deformed basis, such as that from an inverse solver, must be converted into the undeformed basis for most membrane models.*

   Correcting the load to the undeformed basis, a step that is consistent with the assumptions of AMS and other models, leads to a prediction error orders of magnitude smaller than the prediction error when using the deformed-basis loads. In addition, the error grows more slowly with pressure load than if the deformed-basis load is applied. Correcting the pressure load to the undeformed basis also shows that the prediction error continued to decrease between 200- and 1000-interval discrete solutions. Discretization-based behavior was observed to plateau at a much lower number of intervals when the pressure value from the deformed basis was applied.

3. *Without some modifications to the standard finite difference expressions near the endpoints, the seemingly-minor differences between the numerical expressions lead to a significant prediction error at the endpoints. Cubic extrapolation provides a good method for smoothing the results that is mathematically reasonable and that reduces the model prediction error.*

   The rapid changes in the discrete deflection solution for AMS theory at the endpoints is attributed to the method of calculating differential field variables near the

endpoints. A cubic extrapolation of the endpoint values of discretized geometric-field-variables removes the error incurred by switching finite difference expressions near the endpoints. The differences between the values predicted by finite difference and the values modified by extrapolation are consistent with the error tolerance of the finite difference expressions in the geometric and loading cases of interest.

The implementation lessons of this chapter have been applied to the code that is used to generate the final model-error results.

Chapter 7

Model Accuracy

Objective of Chapter:

To compare the accuracy and precision of different models to better understand both the utility and limitations of different modelling assumptions and solutions for the prediction of optical-level behavior of membrane mirrors.

The methods, lessons, and cases regarding model accuracy discussed in the previous chapters are implemented together in this chapter. Model accuracy results are quantified for each of the benchmark problems from Section 2.4 and then summarized in a modelling guideline.

7.1 Introduction

In Chapter 3 a taxonomy of models is developed, and in Section 3.3 a methodology is described for evaluating the error due to model assumptions. The components in the analysis flow of Figure 3.5 are developed and refined in Chapters 4–6. The theme behind the model accuracy analysis is to compare the predictions of simplified models for relevant benchmark problems with the results from a geometrically-exact model. Each combination of load, geometry, and model leads to a single metric that quantifies the mission-critical-type error in the prediction; the plots of these error metrics represent the fundamental result of this model-assessment effort for large membrane mirrors.

The model error plots shown in this chapter have many common features:

- Each solution precision plot represents a single problem with a pre-determined initial and final shape.
- In accordance with the model error discussions in Section 2.3, the ordinate on most plots is the area-averaged standard deviation of the wavefront error in the pathlength direction.
- Three parameters constitute most of the abscissas on the plots:
  - Area-averaged mean of the pressure, $\bar{p}$,
  - Area-averaged mean of the average strain, $\frac{\epsilon_\phi+\epsilon_\theta}{2}$, and
  - Total displacement at the outer boundary, $|\bar{\mathbf{u}}(1)|$.
- The dashed lines indicate the transition region over which the prediction error achieves optical quality; two lines are used because the factors that define the non-dimensional threshold are specified by a range of interest. In Section 2.3 this range of values is generated to represent the upper and lower estimates of the error that is small enough to be labelled "optical quality." In non-dimensional units of tolerance over final outer radius, the range is 0.1×10^{-6} to 5.0×10^{-9}. Error near the larger threshold is considered to be near optical quality, and error near the smaller threshold is considered optical quality for most cases of interest. Restated, error less than the chosen thresholds indicates a combination of model and parameter space that results in optical-quality shape predictions.
- The individual results of the finite number of load cases are represented by symbols on the results plots. Line segments connect these symbols for readability, i.e. the resulting lines are not intended to represent a continuum of solutions.
- Model accuracy is assessed for three models:
  - Axisymmetric Membrane Shell (AMS),
  - Axisymmetric Large Deflection (ALD), and
  - Linearized Axisymmetric Large Deflection (LALD).

All solutions are determined numerically through finite difference type solutions. While the AMS and LALD models are linear, the ALD model is nonlinear and thus requires more complicated solution steps. The solutions for the ALD models require the most active programming effort between cases because the relative convergence values and relaxation parameters need to be manually adjusted per case (the ALD solution method is taken from Sheplak and Dugundgi [76]). These parameters are determined by choosing values that correspond to the smallest prediction error. The prediction error over different parameters is observed to lie in a finite set of values, and parameters corresponding to the minimum error are chosen for this study. This approach is supported by the asymptotic relationship observed between the LALD and ALD model error.

The results are presented for the set of relevant benchmark problems from Section 2.4, the parameter space for optical quality in the models is discussed, and the model-accuracy results are summarized into a modelling guideline.

7.2 Results

In this section the model errors, as defined in Section 2.3, are presented for a set of three different models with solutions to four benchmark problems. Each problem is solved all over a range of load magnitudes. Quantifying the model error down to the level of optical tolerances thus provides a guide to usage of the models for optical-quality shape predictions. The time required to calculate the solution is also recorded as a means of indicating efficiency in the solution method.

7.2.1 Solution Precision for Finite Difference

Figures 7.1– 7.2 represent solution precision for finite difference approach through plots of the shape prediction error for three models over the set of finite difference intervals $N = \{24, 50, 100, 200, 400, 800, 1600, 3200, 6400\}$. With the finite difference method, the errors in the solution are based upon the interval size; increasing the number of points is thus expected to reliably decrease the prediction error.

The example sphere-forming problem of Figure 7.1, the forming of a $\bar{r}_{sph} = 4$ spherical cap from a $\bar{R}_{sph}$ spherical cap, provides a few lessons about precision of the solution:

- The AMS-model prediction errors decrease significantly with interval number and

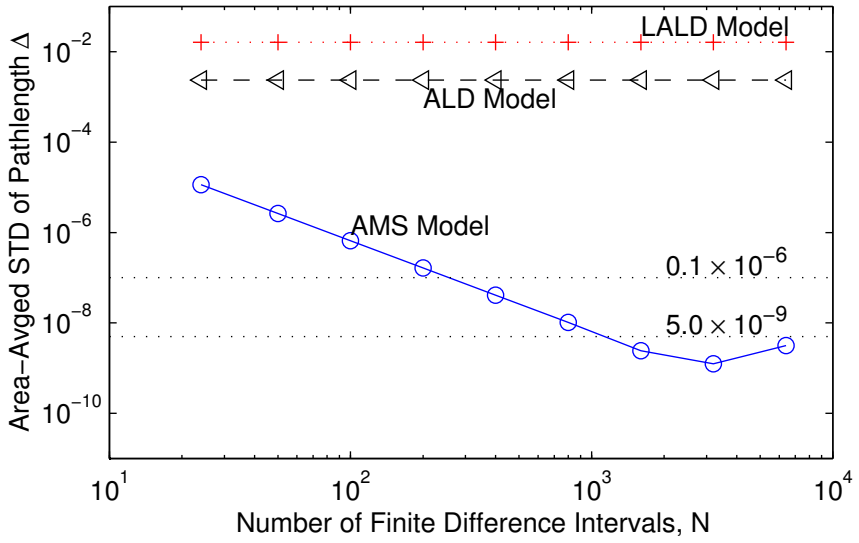

Figure 7.1: *Sphere-to-$\bar{r}_{sph}$=4-Sphere* benchmark problem, solution precision results — Model prediction error, as measured by the area-averaged standard-deviation of pathlength error, over a range of finite difference intervals. Final radius is $\bar{r}_{sph} = 4$, and initial radius is $\bar{R}_{sph} = 3.8$.

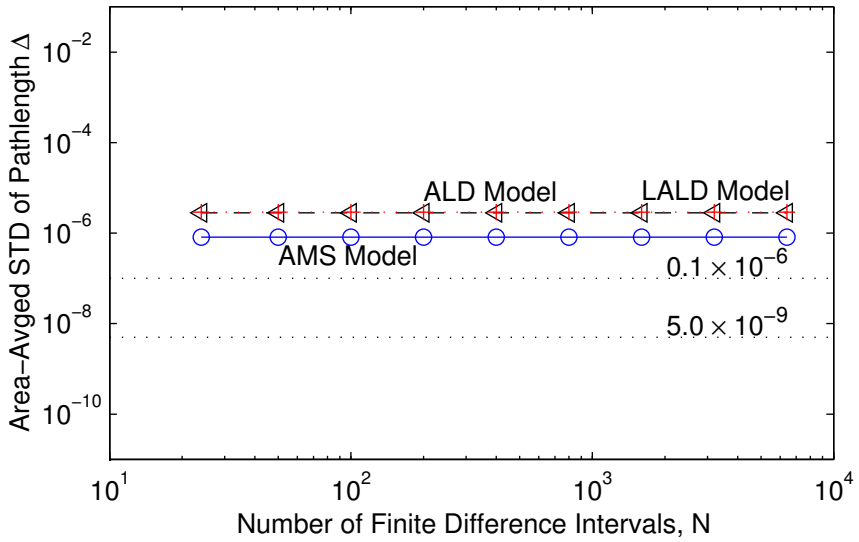

Figure 7.2: *Parabola-to-f/1-Parabola* benchmark problem, solution precision results — Model prediction error, as measured by the area-averaged standard-deviation of pathlength error, over a range of finite difference intervals. Final focal ratio is $f_\infty = 1$, and the initial focal ratio is $f_\infty = 1.001$.

achieve optical quality for thousands of finite difference intervals.

- The increase in error from $N = 3200$ to $N = 6400$ intervals is apparently due to the smallness of the numbers involved, the complexity of the finite difference expressions, and numerical clipping from implementation on a computer. The calculation of field variables exhibits the same trend, as shown in Figure 6.11.

- The prediction errors for the ALD and LALD models do not change significantly between 24 and 6400 intervals; this lack of dependency upon interval size indicates that the errors from geometric model assumptions are larger than the numerical errors in the solution implementation.

Solution-precision results for an initial shape of $\bar{R}_{sph}$=3.99 provide no additional information and are hence omitted here; the similarity of the error relationships for different initial shapes indicates that the results of Figure 7.1 hold for a wide range of initial shapes.

Figure 7.2 presents results for the parabola-to-parabola benchmark problems with geometry and loads almost identical to the sphere-forming benchmark problem, but none of the solutions here shows a significant change in prediction error with interval size. That is, the error for the smallest number of intervals is approximately equal to the error for the largest interval count. Results for an initial shape of $f/1.1$ are similar to Figure 7.2 and hence are omitted. Again the errors from the geometric assumptions dominate the numerical errors due to the solution. With the starkly different results for the AMS model between the similar $\bar{r}_{sph}$=4-sphere-forming and $f/1$-parabola-forming benchmark problems, the sphere-to-sphere problem appears to be a special geometry for which the AMS model is particularly accurate. The less accurate results of the similar parabola-forming case indicate that the results of the sphere-to-sphere benchmark problem using the AMS model cannot be considered for determining thresholds of optical quality for a general loading.

In consideration of all solution-precision plots, $N = 3200$ is the best choice of interval count for pressure-loaded, curved membranes to ensure that the prediction errors due to numerical issues are smaller than errors allowable for optical quality. For the subsequent model accuracy results in this section, $N = 3200$ is the standard number of intervals used. With the exception of the AMS-model predictions of the sphere-to-sphere problem, however, the solution precision plots show that the prediction error is approximately the same for tens of thousands of intervals or tens of intervals. This lack of perceptible change indicates that

the errors due to discretization are smaller than the errors due to geometric assumptions; the calculated error can thus be attributed to the modelling choices and assumptions.

7.2.2 Benchmark 1: Sphere to $\bar{r}_{sph}$=4 Sphere

Figure 7.3 shows how the shape prediction error changes with mean pressure load for benchmark problem #1, the forming of a $\bar{r}_{sph}$=4 spherical cap from the constant-pressure-induced expansion of a smaller spherical cap. The set of initial radii are $\bar{R}_{sph} = \{3, 3.5, 3.8, 3.9, 3.99, 3.999, 3.9999, 3.99999\}$. The error for the AMS model remains below even the lower limit of the optical range for most load cases, whereas the errors for the large-deflection models, ALD and LALD, only begin to approach the upper limit of the optical range for mean pressure $\bar{p} < O(10^{-6})$. The error from the ALD model is consistently less than the error of the LALD model, though not significantly, and thus shows that the nonlinear ALD is an improvement on the linear model.

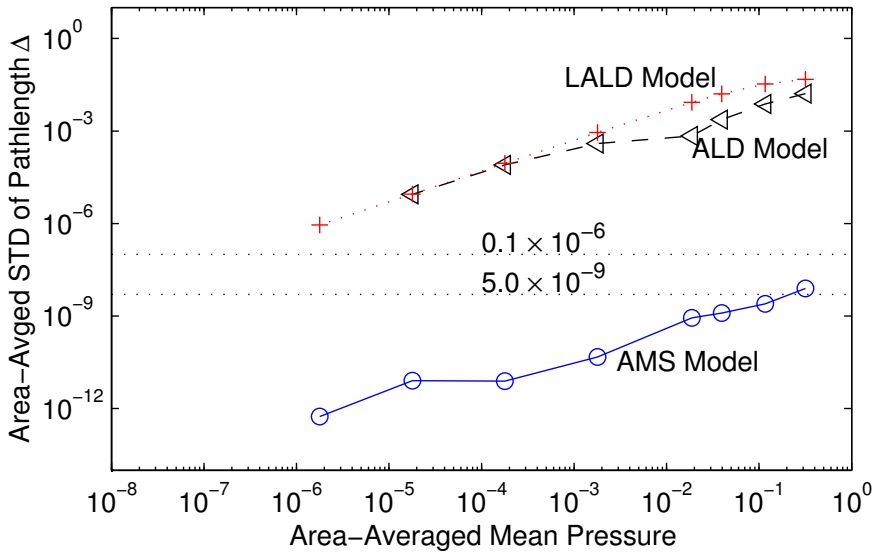

Figure 7.3: *Sphere-to-$\bar{r}_{sph}$=4-Sphere* benchmark problem, model accuracy results—Model prediction error, as measured by the area-averaged standard-deviation of pathlength error, over a range of load cases. The final radius is $\bar{r}_{sph} = 4$ in each case.

7.2.3 Benchmark 2: Flat to Paraboloid

For the initially-flat benchmark problem #2, the linear models – LALD and AMS – cannot be applied due to a one-over-zero type of error that would result. For the ALD solution, Figures 7.4 and 7.5 show how the prediction error changes with pressure load and final focal ratio, respectively, for the set of final focal ratios $f_\infty = \{100, 50, 20, 10, 5, 2, 1\}$. Similar to previous results, the predictions begin to show optical quality below pressures $\bar{p} < O(10^{-6})$. With a switch in abscissa from Figure 7.4, Figure 7.5 shows that the ALD model approaches an optical-quality prediction for forming rather shallow final shapes – shallower than $f/20$ (i.e., larger focal ratio than 20) at the high end of the threshold and less than $f/100$ at the lower end.

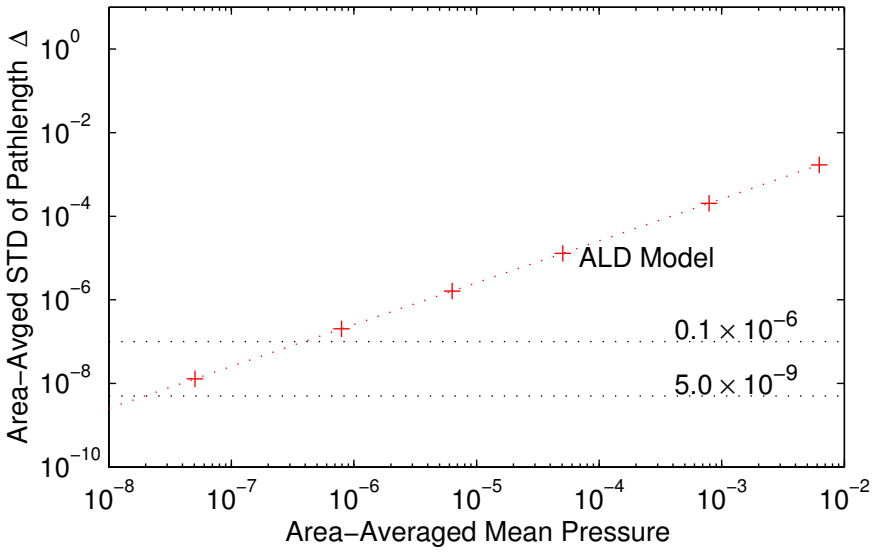

Figure 7.4: *Flat-to-Paraboloid* benchmark problem, model accuracy results—Model prediction error, as measured by the area-averaged standard-deviation of pathlength error, over a range of load cases.

7.2.4 Benchmark 3: Paraboloid to $f/1$ Paraboloid

Figure 7.6 shows prediction-error results for a similar final geometry and similar load range to the spherical-cap problem results shown in Figure 7.3, though in this problem the shapes are paraboloids. Of the benchmark problems, the paraboloid-forming problems are the most interesting because the initial and final shapes both have the least symmetry and, with the

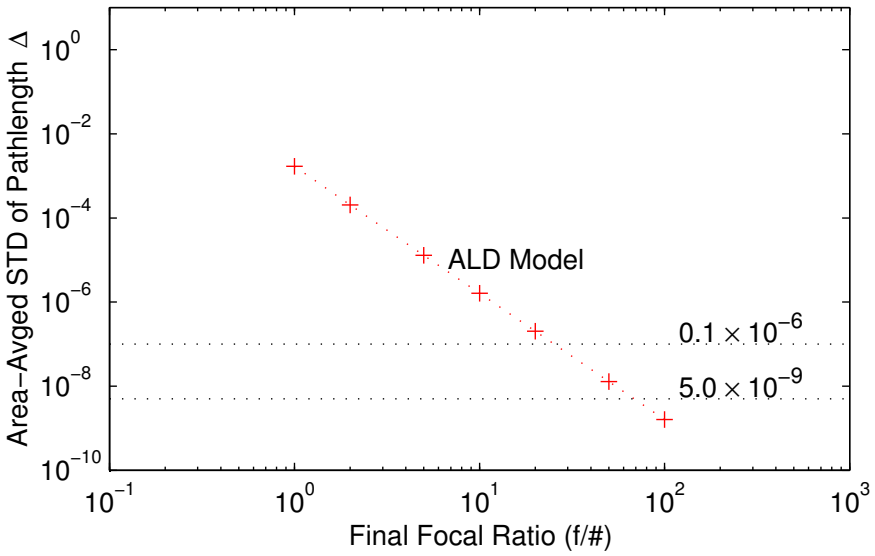

Figure 7.5: *Flat-to-Paraboloid* benchmark problem, model accuracy results—Model prediction error, as measured by the area-averaged standard-deviation of pathlength error, over a range of load cases.

current direction in research, cover the most interesting range of shapes and loads. The final focal ratio is held constant at $f/1$, and the set of initial focal ratios is {10, 5, 2, 1.5, 1.25, 1.1, 1.02, 1.015, 1.01, 1.005, 1.002, 1.001, 1.0001, 1.00001, 1.000001}. The AMS model again has the smallest shape prediction error for a significant load range, $\bar{p} < 10^{-3.5}$, with the ALD model exhibiting the smallest error above that pressure mark. The AMS-model predictions enter the optical-error range of interest below $\bar{p} < O(10^{-6})$ while the errors of the ALD and LALD models enter the optical range for a load three times smaller.

The two linear models in Figure 7.6, ALD and AMS, merge to have the same prediction error above $\bar{p} > 10^{-3}$. The extremely large errors in the ALD and AMS solutions, near $O(1)$ non-dimensional error, are included to show how very large the error can be when using these linear models to predict large deflections from relatively flat initial shapes. Errors on the scale of the radius represent a loading and geometry regime in which the models are no longer valid but are recorded here to illustrate the impact of relying upon the wrong model.

Figure 7.7 presents the same results as Figure 7.6, except that the abscissa is the difference in focal ratios between the final and initial parabolic shapes. The initial focal ratio must be very similar to the final, here shown to be $O(10^{-4})$, for the deformed-shape predic-

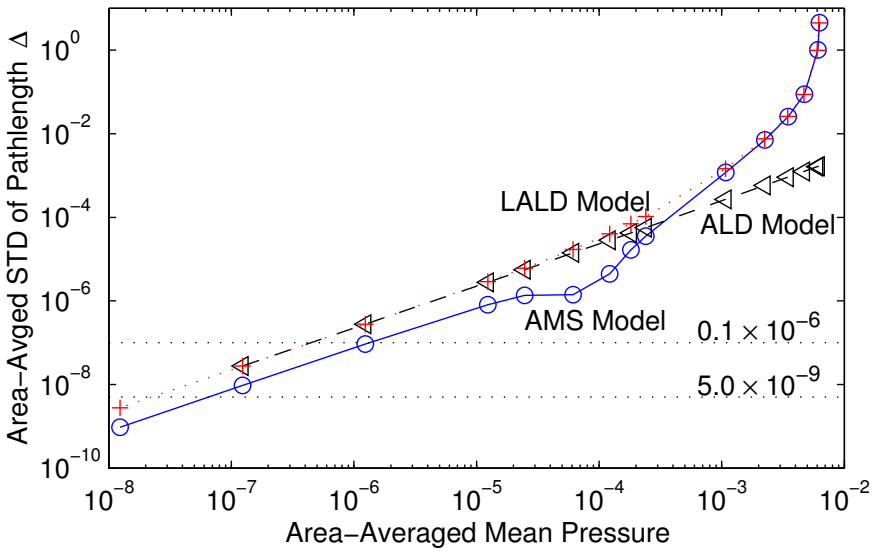

Figure 7.6: *Paraboloid-to-f/1-Paraboloid* benchmark problem, model accuracy results — Model prediction error, as measured by the area-averaged standard-deviation of pathlength error, over a range of load cases. The final focal ratio is $f_\infty = 1$ in each case.

tions to begin to have optical quality. Restated, the shape predictions from these models will be optical quality for loadings smaller than that from the $f/1.0001$-to-$f/1$ problem.

In Figure 7.8 three different abscissas provide a comparison of the same model-error problem sets. For loads that result in prediction errors much larger than optical level, the error trends are very different for the three different abscissas. The mean-pressure and total-boundary-displacement curves show a rapid increase in error for the LALD and AMS models at large loads, while the log-log relationship between strain and error remains linear in the strain curve.

7.2.5 Benchmark 4: Paraboloid to $f/5$ Paraboloid

Figures 7.9 and 7.10 present the prediction-error results for a shallower geometry than the spherical-cap or $f/1$-forming problems of Figures 7.3 and 7.6. The final focal ratio is $f/5$, and the set of initial focal ratios is {30, 10, 5.3, 5.1, 5.03, 5.01, 5.003, 5.001, 5.0001, 5.00001, 5.000001}.

In Figure 7.9 the same model error problems are compared over three different abscissas. The set of plots represents the same variables as in Figure 7.8, and the results are indeed

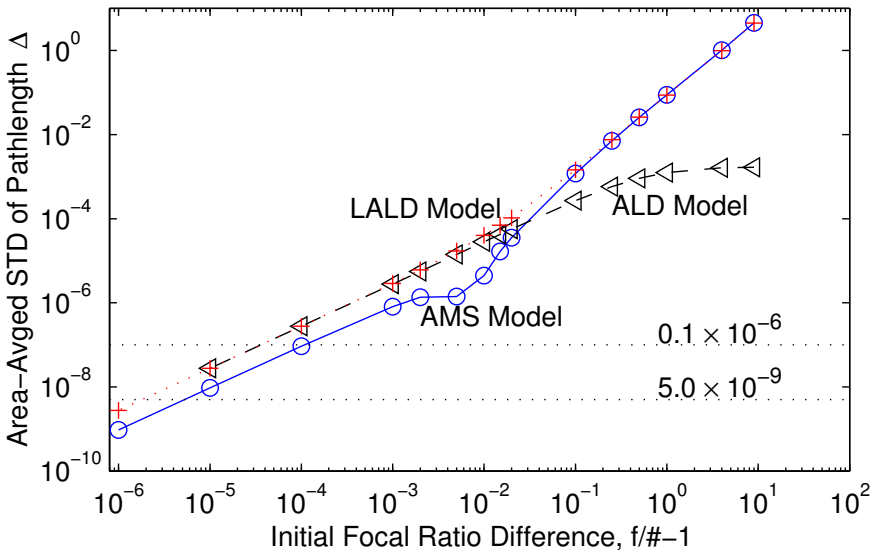

Figure 7.7: *Paraboloid-to-f/1-Paraboloid* benchmark problem, model accuracy results — Model prediction error, as measured by the area-averaged standard-deviation of pathlength error, over a range of focal ratio differences. The final focal ratio is $f_\infty = 1$ in each case.

similar. The limits of key parameters for optical-quality predictions of mirror shape are approximately the same for the $f/5$ and $f/1$ final shapes.

Figure 7.10 presents the same cases as Figure 7.9, except that the abscissa is the difference in focal ratios between the final and initial parabolic shapes. Although the plot is similar to the $f/1$-forming results from Figure 7.7, the modelling error for the $f/5$-forming case remains under the optical quality thresholds for a much larger focal ratio difference, around $O(10^{-2})$.

A feature unique to the AMS-model error in all of the $f/1$-forming and $f/5$-forming problems is the local minimum in the error near $\bar{p} \sim 10^{-4}$ and $\bar{p} \sim 10^{-8}$, respectively. This dip in the trend indicates a region of loading in which the character of the error function changes; the accompanying rapid increase in error/load relationship provides further evidence of this change. The difference between AMS and exact solutions switches at that load from having a mostly-positive to mostly-negative sign. The results from the $f/5$-forming problem in Figure 7.11 show how the mostly-flat error distribution hits a local minimum during this transition from positive to negative error.

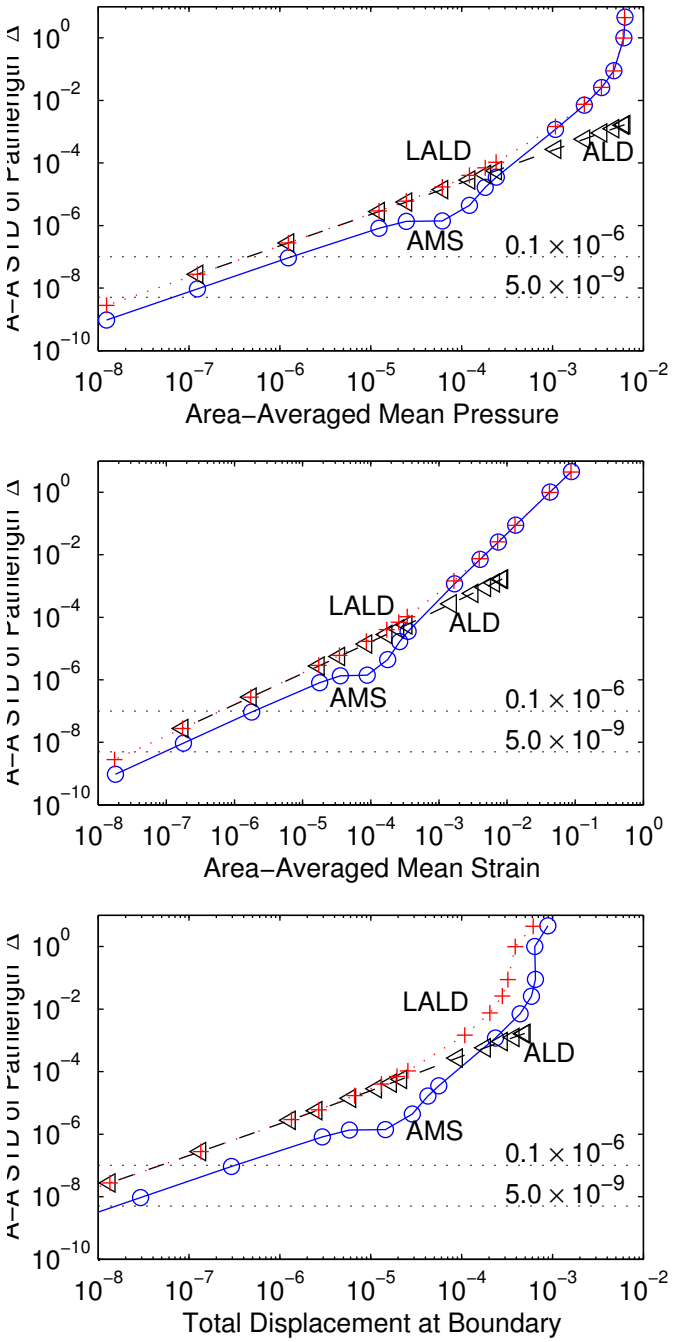

Figure 7.8: *Paraboloid-to-f/1-Paraboloid* benchmark problem, model accuracy results — Model prediction error, as measured by the area-averaged standard-deviation of pathlength error, for three different abscissas: (a) Area-averaged mean pressure, (b) Area-averaged mean strain, and (c) Total displacement at $\frac{r}{r_{out}}$=1.

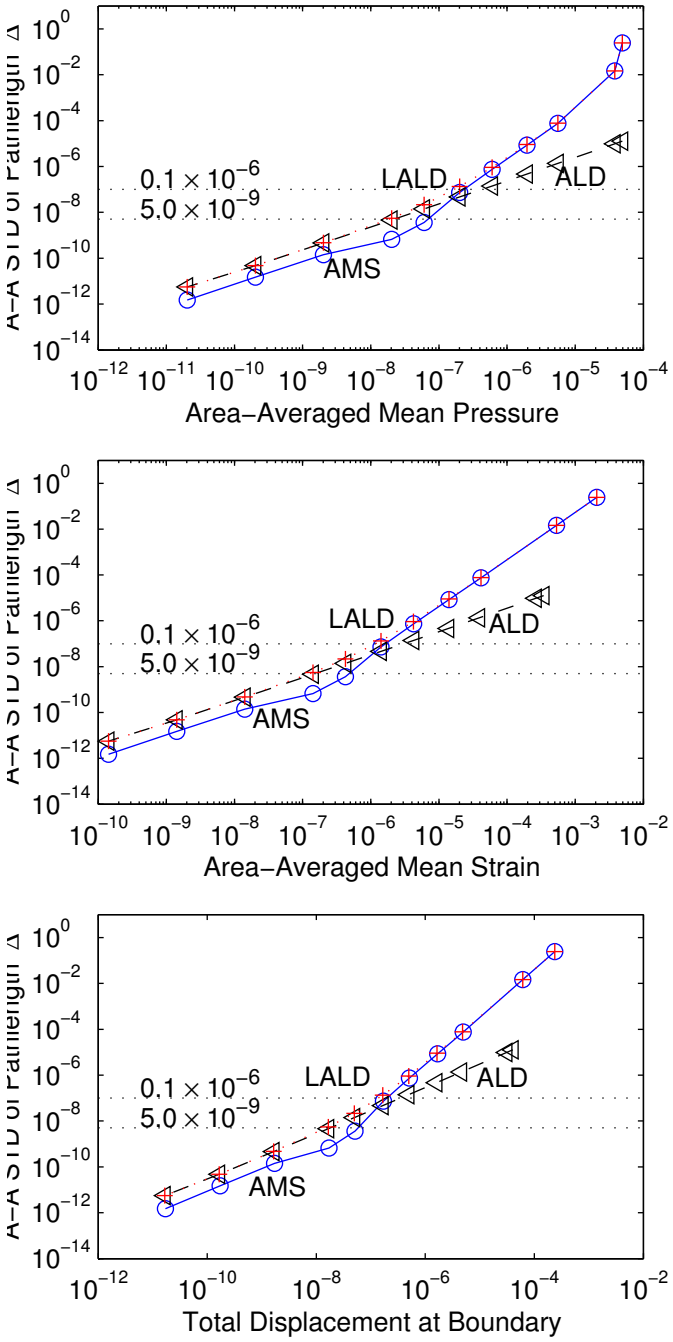

Figure 7.9: *Paraboloid-to-f/5-Paraboloid* benchmark problem, model accuracy results — Model prediction error, as measured by the area-averaged standard-deviation of pathlength error, for three different abscissas: (a) Area-averaged mean pressure, (b) Area-averaged mean strain, and (c) Total displacement at $\frac{r}{r_{out}}$=1.

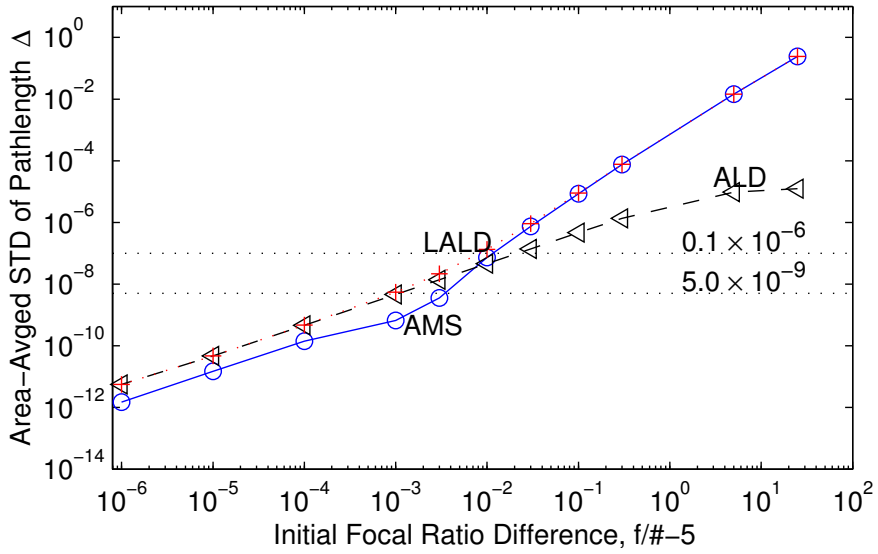

Figure 7.10: *Paraboloid-to-f/5-Paraboloid* benchmark problem, model accuracy results — Model prediction error, as measured by the area-averaged standard-deviation of pathlength error, over a range of focal ratio differences.

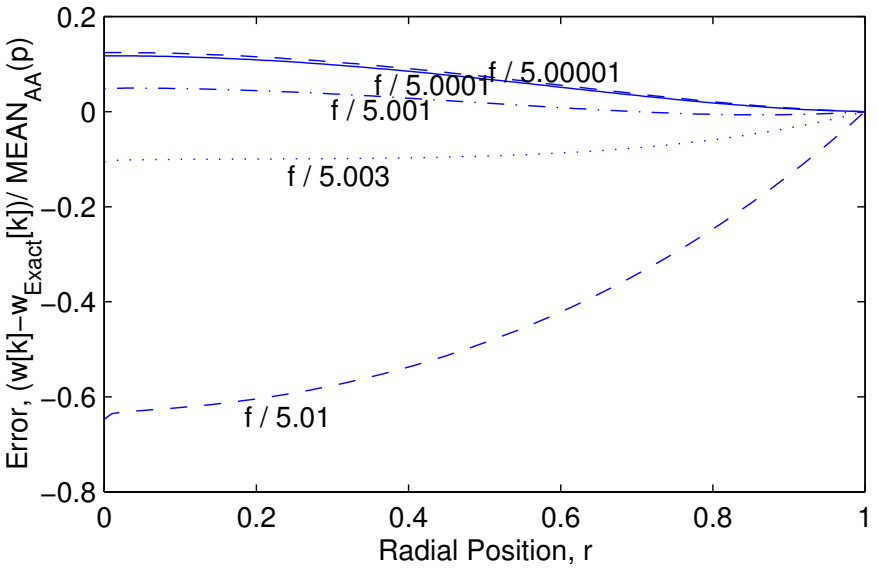

Figure 7.11: *Paraboloid-to-f/5-Paraboloid* benchmark problem, axial error distribution — Model prediction error, as measured with the axial shape error normalized by mean pressure, versus radial position. Each line represents an initial focal ratio and hence a different load function.

7.2.6 Time Required to Generate Solutions

Another difference between the models is the time required to generate each solution. Since all finite difference solutions are calculated in MATLAB with a single function call, the "tic"/ "toc" command pair is used on either side of the function call to generate the solution time required. The overhead time required to pre- and post-process the solution is not included. It is noted here that the solution methods presented have not been studied specifically to determine time-optimal methods.

For the flat-to-paraboloid problem, Figure 7.12 indicates the significant increase in solution time required from 200 to 3200 intervals. At small loads, the increase in solution time signals the numerical difficulties incurred when many of the field variables are numerically small. The same parameters are plotted in Figure 7.13 for the $f/5$-forming problem, yet all models are represented. The AMS and LALD solution time do not change with load, and the LALD times are the fastest. The ALD calculation times again increase for small loads and far surpass the times required to calculate AMS and LALD solutions.

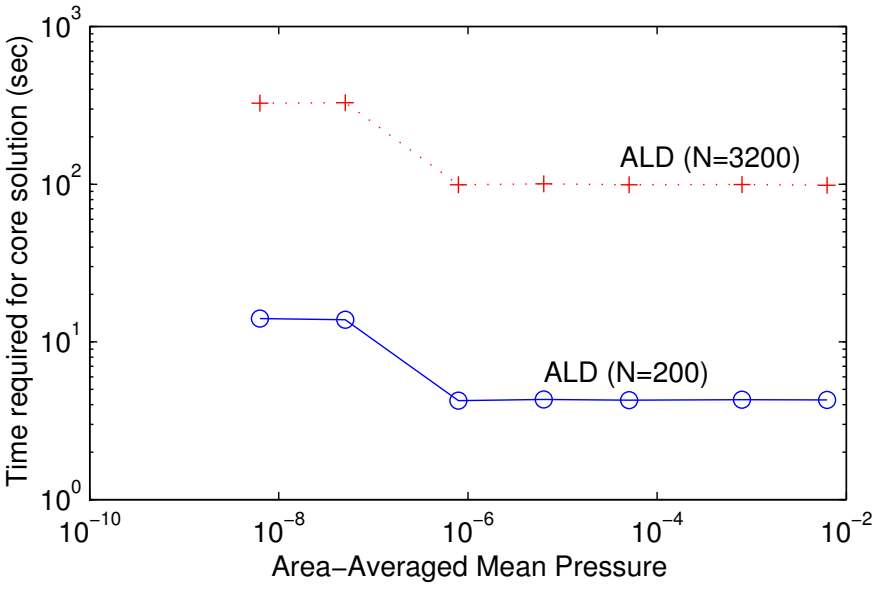

Figure 7.12: *Flat-to-Paraboloid* benchmark problem, calculation time results—Time to calculate core solution over a range of load cases.

All of the models are again represented in the $f/1.001$-to-$f/1$ solution-precision results of Figure 7.14. The calculation time for the ALD solution steadily increases with the number

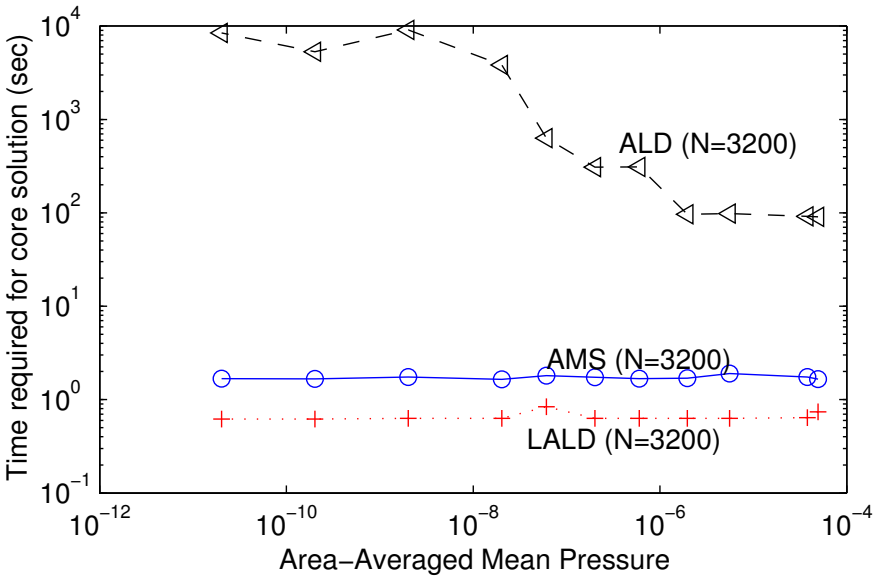

Figure 7.13: *Paraboloid-to-f/5-Paraboloid* benchmark problem, calculation time results — Time to calculate core solution over a range of nondimensional pressures. The final focal ratio is $f_\infty = 5$ in each case.

of intervals, but the AMS and LALD results increase much more gradually with interval count. The increase for AMS and LALD is so gradual that a hundred-fold increase in the interval count produces less than a ten-fold increase in solution time required.

7.3 Discussion

7.3.1 Parameter Space for Optical-Quality Predictions

Choosing the parameters for comparing the models is crucial to creating model accuracy thresholds useful for other problems. Previously-shown results are combined here to better understand the parameter-error trends for different models and geometries.

Figure 7.15 shows the same set of parameters as in Figures 7.8 and 7.9, but in this case the plots contain all four of the benchmark-problem solutions. The relationship between error and mean pressure exhibits a fairly consistent correlation with exceptions for the larger error in the AMS and LALD $f/5$-forming results and the optical-quality error in the AMS solution for $\bar{r}_{sph}$=4-forming. That is, mean pressure is the parameter for which the model error limits are reached at the approximately the same values for different geometries. *The*

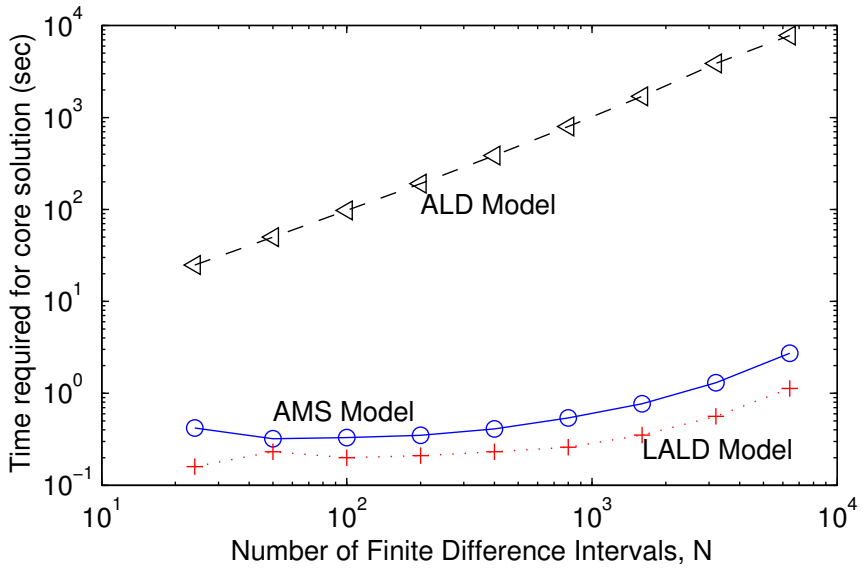

Figure 7.14: *Paraboloid-to-f/1-Paraboloid* benchmark problem, calculation time results — Time to calculate core solution over a range of finite difference interval counts and a single load case. The initial and final focal ratios are $f/1.001$ and $f/1$, respectively.

pressure is thus recommended as the parameter of choice for correlation to modelling error.

The data in Figure 7.15 provide the threshold values of the pressure, strain, and boundary-displacement parameters that are recorded in Tables 7.1, 7.2, and 7.3, respectively. The thresholds are estimated by linear interpolation and/ or extrapolation, as appropriate, from the log-log results presented earlier in this chapter. The upper threshold for optical quality is crossed for non-dimensional pressure loads in the range $10^{-7} < \bar{p} < 10^{-6}$ and lower threshold for $10^{-8} < \bar{p} < 10^{-7}$. In the $f/1$-forming case the ALD and LALD thresholds are three times the AMS thresholds. Similar threshold magnitudes are observed for the strain and displacement parameters in Tables 7.2 and 7.3. A scan of the exponents in the threshold tables provides the best insight into the thresholds.

Solution time represents another parameter of comparison. Comparing modelling error against the time required to calculate the solution provides a sort of "solution value" plot that indicates the practicality of different solution types. Figure 7.16 is such a plot. Solutions in the lower-left portion of the plot are desirable because of short solution times and small prediction error. The cases in the lower-left of Figure 7.16 correspond to small load

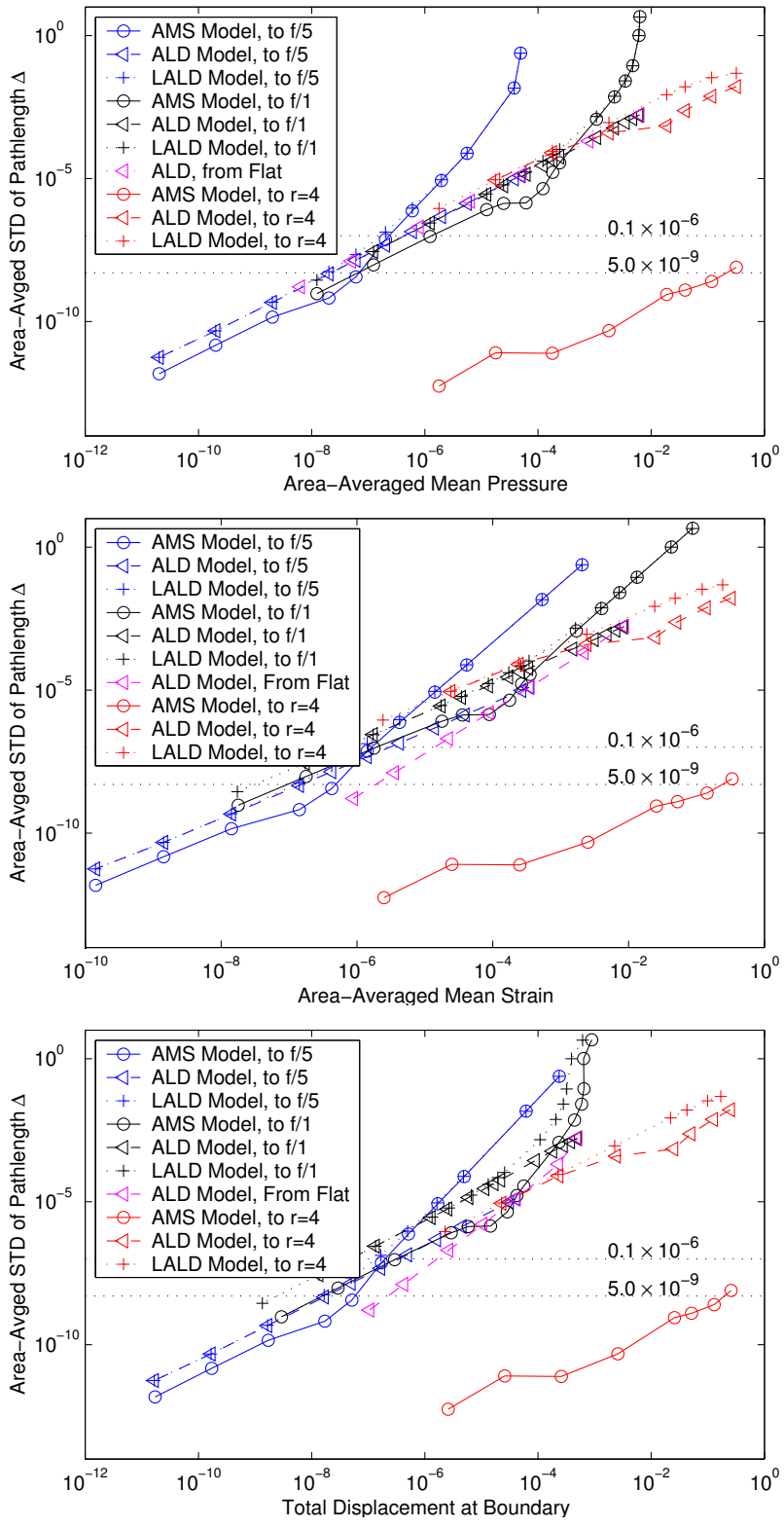

Figure 7.15: All benchmark problems, model accuracy results—Model prediction error, as measured by the area-averaged standard-deviation of pathlength error, for three different abscissas: (a) Area-averaged mean pressure, (b) Area-averaged mean strain, and (c) Total displacement at $r = r_{out}$.

Table 7.1: Values of *mean pressure* at which each model predicts the mission-critical performance to cross the upper and lower threshold values.

Benchmark	Geometry	Threshold	AMS	ALD	LALD
1	$\bar{r}_{sph}$=4	Upper	1.7×10^{0}	2.0×10^{-7}	2.0×10^{-7}
		Lower	2.3×10^{-1}	9.9×10^{-9}	9.9×10^{-9}
2	Flat	Upper	—	4.0×10^{-7}	—
		Lower	—	2.0×10^{-8}	—
3	$f/1$	Upper	1.3×10^{-6}	4.4×10^{-7}	4.4×10^{-7}
		Lower	6.5×10^{-8}	2.2×10^{-8}	2.2×10^{-8}
4	$f/5$	Upper	2.3×10^{-7}	4.3×10^{-7}	1.7×10^{-7}
		Lower	6.9×10^{-8}	2.2×10^{-8}	1.9×10^{-8}

Table 7.2: Values of *mean average strain* at which each model predicts the mission-critical performance to cross the upper and lower threshold values.

Benchmark	Geometry	Threshold	AMS	ALD	LALD
1	$\bar{r}_{sph}$=4	Upper	2.2×10^{0}	2.7×10^{-7}	2.7×10^{-7}
		Lower	2.6×10^{-1}	1.3×10^{-8}	1.3×10^{-8}
2	Flat	Upper	—	1.4×10^{-5}	—
		Lower	—	2.0×10^{-6}	—
3	$f/1$	Upper	1.9×10^{-6}	6.2×10^{-7}	6.2×10^{-7}
		Lower	9.4×10^{-8}	3.1×10^{-8}	3.1×10^{-8}
4	$f/5$	Upper	1.6×10^{-6}	3.0×10^{-6}	1.2×10^{-6}
		Lower	4.9×10^{-7}	1.5×10^{-7}	1.3×10^{-7}

Table 7.3: Values of *total* $\bar{r}$*=1 boundary displacement* at which each model predicts the mission-critical performance to cross the upper and lower threshold values.

Benchmark	Geometry	Threshold	AMS	ALD	LALD
1	$\bar{r}_{sph}$=4	Upper	2.1×10^{0}	2.5×10^{-7}	2.5×10^{-7}
		Lower	2.1×10^{-1}	1.3×10^{-8}	1.3×10^{-8}
2	Flat	Upper	—	2.0×10^{-6}	—
		Lower	—	3.2×10^{-7}	—
3	$f/1$	Upper	3.1×10^{-7}	4.8×10^{-8}	4.8×10^{-8}
		Lower	1.6×10^{-8}	2.4×10^{-9}	2.4×10^{-9}
4	$f/5$	Upper	2.0×10^{-7}	3.5×10^{-7}	1.4×10^{-7}
		Lower	5.9×10^{-8}	1.8×10^{-8}	1.5×10^{-8}

levels and linear models (ALD and AMS). The ALD solutions are seen to mostly have the undesirable properties of large solution time and medium-to-low accuracy.

7.3.2 Geometry and Model Error

In Figure 7.17 the plots of model error according to model rather than benchmark problem provides insight into the effect of geometry upon model error. Each subplot provides lessons about the models and the geometries:

- AMS in subplot (a): The AMS model returns solutions with consistently-low error, but no clear parametric trend is observed that relates the error directly to geometry across a range of problems. The extremely low error in the $\bar{r}_{sph}$=4-forming case again seems to indicate that the model is particularly-well suited for modelling constant pressure on spherical-shaped membranes.

- ALD in subplot (b): The pressure-error relationship is almost exactly linear for the ALD model, regardless of the geometry under consideration.

- LALD in subplot (c): The correlation between pressure and error is good for the LALD model except that the error increases rapidly at some load.

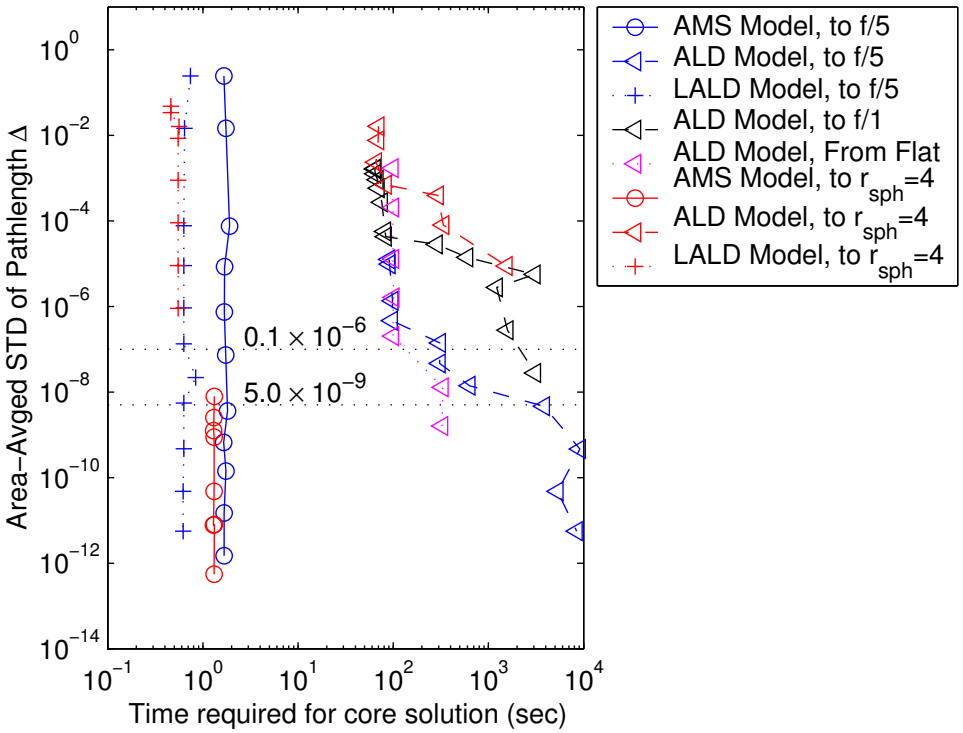

Figure 7.16: A "solution value" plot—Model prediction error, as measured by the area-averaged standard-deviation of pathlength error, over the range of associated times required to calculate the finite difference solutions. Each set of points represents a model-plus-geometry combination for a subset of benchmark problems.

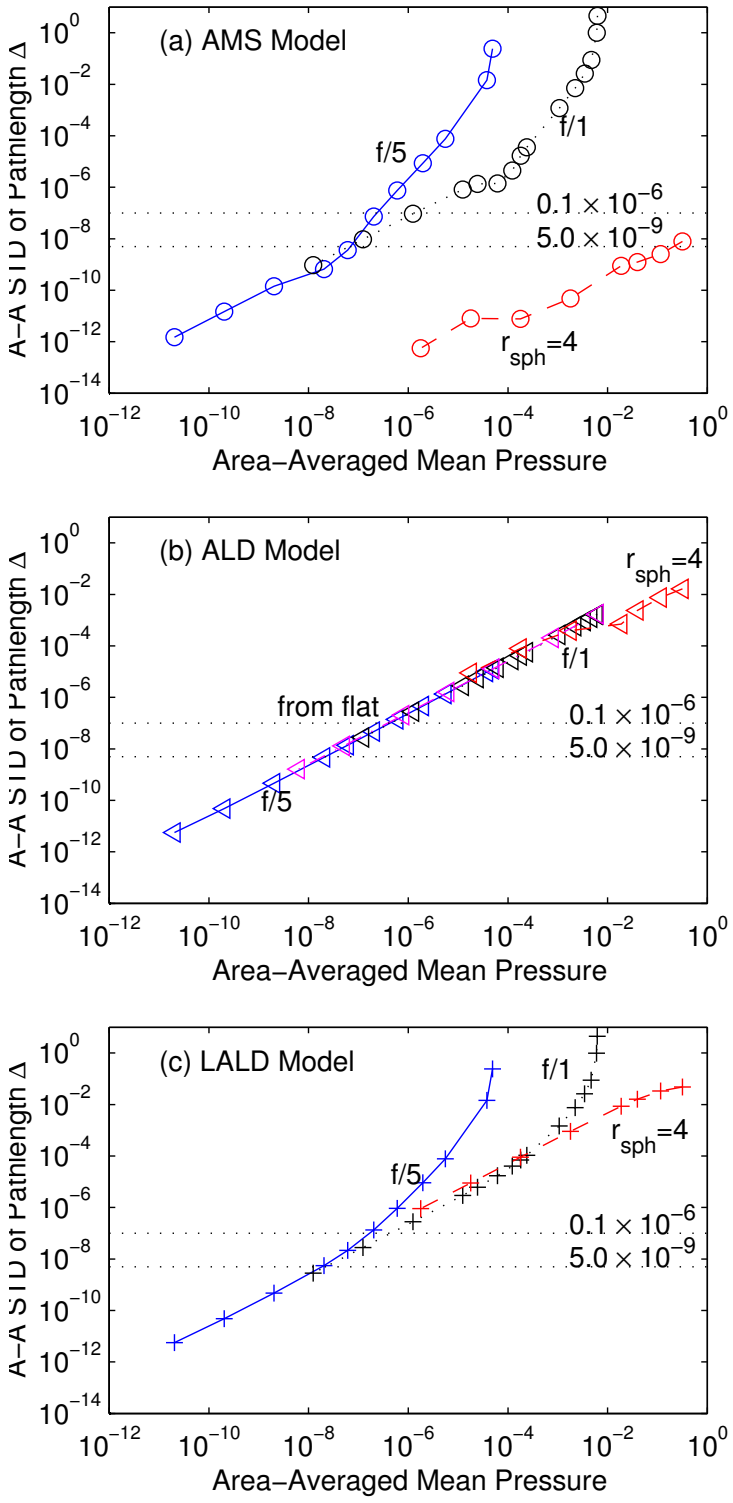

Figure 7.17: All benchmark problems, model accuracy results—Model prediction error, as measured by the area-averaged standard-deviation of pathlength error, over mean pressure for three different models: (a) AMS, (b) ALD, and (c) LALD. Two different geometries are shown in each subplot.

Figure 7.18 displays a new set of parameters, the difference between initial and final curvatures at $\bar{r} = 0$ against mean pressure. Each subplot is created from a single model. This choice of variables represents the set that would be available in any analysis because the calculated value of final curvature is used rather than the exact. The selection of symbols indicates whether the case represented has a modelling error below the lower threshold, between the thresholds, or above the upper thresholds. The $\times$ and ∇ symbols in the lower-left of the figure highlight the cases with optical-quality across all of the models and all of the benchmark problems. This region is indicated by a pressure band around $10^{-8} < \bar{p} < 10^{-6}$ and a curvature-difference band around $10^{-6} < \Delta\bar{\kappa} < 10^{-4}$. In addition, the highly accurate AMS solution to the $\bar{r}_{sph}$=4-forming problem once again provides outlying points in a model-accuracy plot. Thus optical quality predictions are achieved for a particular region of load-geometry parameter space that can be identified outside of the exact solution.

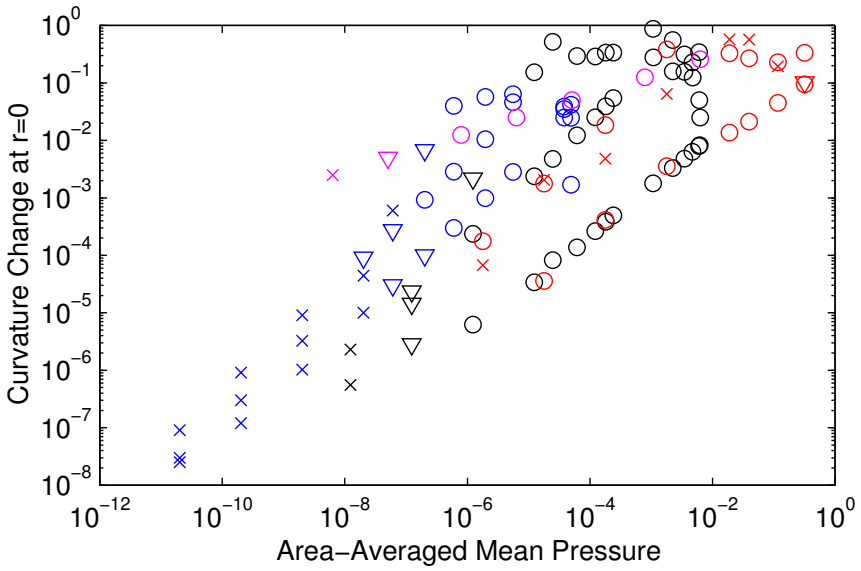

Figure 7.18: Model accuracy summary for all benchmark problems and models—Mean pressure versus difference in curvature at r=0 (also "load vs. geometry"). Symbols represent: "$\times$" = error well below optical tolerances; "∇" = error within banded threshold of interest for optics; and "o" = error larger than optical tolerances.

7.3.3 Correlation of Model Error to Model Assumption

The model accuracy results from Section 7.2 in conjunction with the model development from Section 3.2 provide the basis for making a correlation between modelling assumption and modelling error for a given geometry and load set. For any comparison parameter, the optical-level prediction errors are observed to increase from one model to another as modelling assumptions are added. The summary of the model assumptions in Figure 3.4 and Table 3.4 prove to be rather helpful with the correlation for both solution-precision and model-accuracy results:

- Based upon Figures 7.1 and 7.6, the graphics in Figure 7.19 label the model error according to assumption. The solution precision diagram in subplot (a) shows how the numerical component of AMS-model error decreases as the interval count increases. With the data represented on a logarithmic scale, the error due to the linear assumption in LALD is seen to be far greater than the AMS error. In fact, if the numerical error for the AMS model is similar in magnitude to the numerical error for the LALD model, the error due to the linearity assumption is seen to be orders of magnitude larger than the numerical errors.

- Subplot (b) of Figure 7.19 provides a model accuracy example and is patterned directly after Figure 7.6. For small load levels the linearity assumption is seen to be unobservable because no difference is observed between the LALD and ALD results; plainly stated, the behavior is linear at those load levels. The difference between AMS and ALD error is the amount of error from the geometric assumptions. For large loads, loads that normally lead to prediction errors well outside of the bounds of optical tolerances, the linearity assumption is seen to add significant error to the results.

The logic of Figure 7.19 thus allows an error-to-assumption correlation for any of the benchmark problems. A similar correlation from error to geometry can be constructed with Figure 7.17.

7.3.4 Utility of Results

The model-accuracy results can also form the basis of decisions about model linearity limits, Finite Element Model (FEM) element choice and element density, and proper choice of

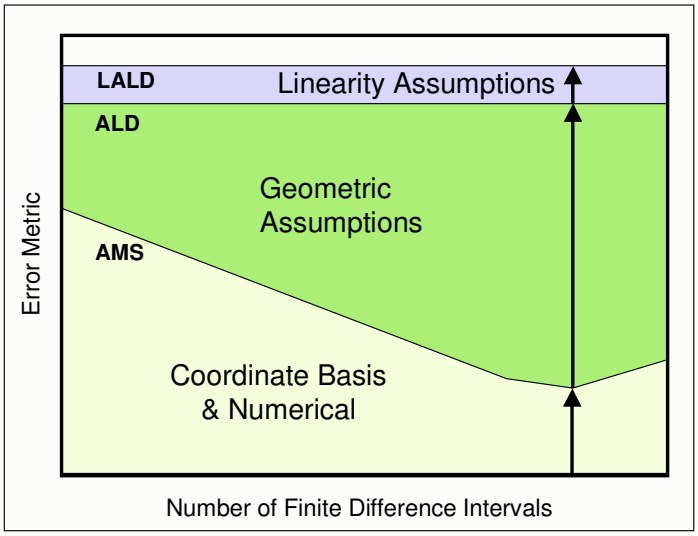

(a) Solution Precision

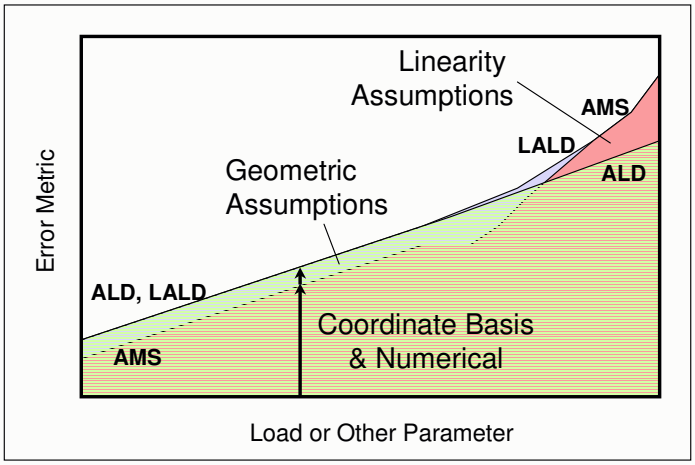

(b) Model Accuracy

Figure 7.19: Solution precision and model accuracy plots, broken down to emphasize effects of modelling decisions upon prediction error. Subplot (a) is based upon Figure 7.1, and subplot (b) upon Figure 7.6. Arrows indicate error components for a single solution.

models for dynamics.

- *Linearity*

  Linearity in models is important because the complexity of the solution is generally much less than for nonlinear and because many mathematical tools have been developed for linear models. In structures linearity is a modelling assumption with negligible error for small-magnitude loads; understanding the load limits over which the models are still valid for optics is relevant to the current problem. Of the models considered in this thesis, AMS and LALD are linear models.

  Linearity can be approached in two ways:

  1. Extent of a linear slope in the error-to-load results: the linear error/ load relationship in the AMS solutions, for example only lasts up to a particular load. At that point the slope increases to a new value. In subplot (a) of Figure 7.17, the change in slope on the log-log plot occurs at different loads for different geometries. This change in relationship order is seen around $\bar{p} \sim 10^{-4.3}$ for $f/1$-forming and around $\bar{p} \sim 10^{-7}$ for $f/5$-forming.
  2. Divergence of linearized version of model from nonlinear version: comparing LALD and ALD provides an additional indication of the range of model linearity. Again this departure from linearity varies according to geometry. In Figure 7.20 the departure between linear and non-linear models is observed around $\bar{p} \sim 10^{-4}$ for $f/1$-forming and $\bar{r}_{sph}$=4-forming and around $\bar{p} \sim 10^{-7}$ for $f/5$-forming.

- *Application to FEM*

  The results produced here correspond to a particular use of non-dimensional variables in a global reference frame. An interesting aspect of finite elements is that the equations are developed in the local coordinate system and then rotated to the global coordinate system after mass and stiffness are calculated. To use the current results in a local coordinate system, the local finite element would be viewed as an entire structure. Thus the scaling by the outer radius will change with element density because the "local" outer radius is the element size.

  With a non-dimensional pressure of $\bar{p} = \frac{pr_{out}}{Eh}$, or "pressure times outer radius over extensional stiffness", the results are scaled to a local element of length dimension

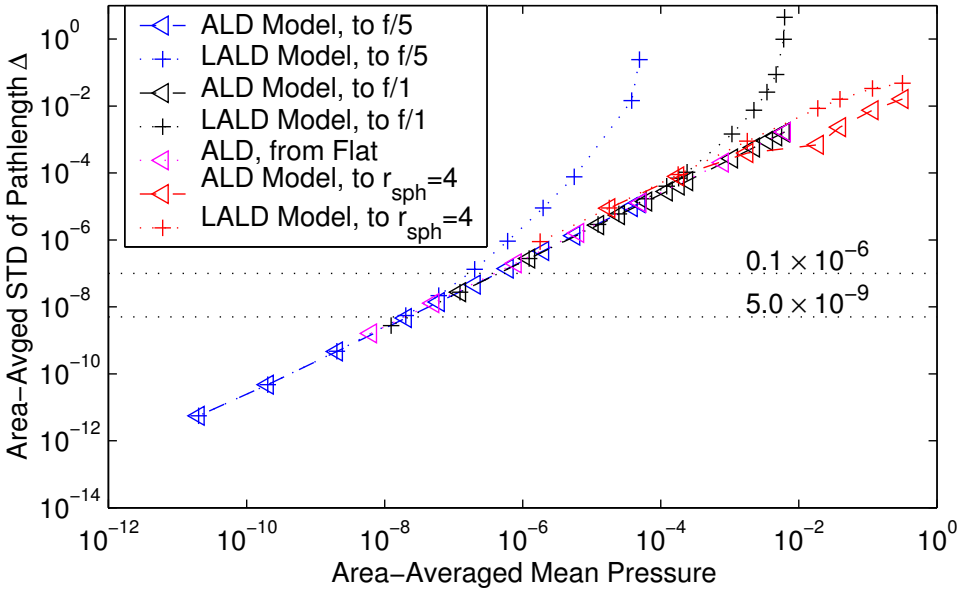

Figure 7.20: All benchmark problems, model accuracy results for Large Deflection models—Model prediction error, as measured by the area-averaged standard-deviation of pathlength error, over the range of load cases. Each set of points represents a model/ final-geometry combination.

$r_{element}$ by defining linear element order α.

$$\begin{aligned} \bar{p}_{element} &= \frac{pr_{element}}{Eh} \\ &= \frac{pr_{out}}{Eh}\frac{r_{element}}{r_{out}} \\ &= \frac{\bar{p}}{\alpha} \end{aligned} \tag{7.1}$$

This translation between local and global systems affects the interpretation of modelling-error limits. An element is considered with governing equations from some model "A". Model "A" is taken to have a known threshold of $\bar{p} < 10^{-6}$ for optical-level accuracy, but the applied pressure is known to be $O(10^{-2})$. To achieve a local pressure below the threshold, or $\bar{p}_{element} < 10^{-6}$, a linear order of $\alpha = 10^4$ would then be required to accurately represent the solution.

- *Dynamic Load Limits via Pressure/ Acceleration Duality*

  The dynamic equilibrium equation for curved membranes is typically written in units of pressure, and thus the linear inertia load $\rho h\ddot{w}$ is in units of pressure. If the same non-dimensional rules are applied to the inertia load term as the pressure term, a non-dimensional acceleration-type term is found. Appendix F contains the derivation of the non-dimensional transverse acceleration term $\frac{r_{out}\rho\ddot{w}}{E}\left(=\frac{r_{out}\rho h}{Eh}\ddot{w}\right)$ from the non-dimensional pressure parameter $\frac{pr_{out}}{Eh}$.

  Because the non-dimensional pressure and non-dimensional acceleration (or inertia load) enter the governing equations in the same manner, the effect of the loads upon the shape prediction will be the same. *The limitation of using a model based upon pressure load can thereby be extended to a limit upon the combination of pressure and inertia load for linear dynamic behavior.*

  In this manner an acceleration-based limit on model accuracy can be derived from statics and applied to dynamics. For a limit pressure $\bar{p}_{limit}$, the limit acceleration $\ddot{\bar{w}}_{limit}$ is thus

$$\ddot{\bar{w}}_{limit} = \bar{p}_{limit}$$

  From the results with the benchmark statics problems, similar models used for dynam-

ics will result in optical-quality-type errors when the non-dimensional transverse accelerations remain below the established non-dimensional pressure limit around 10^{-6}.

7.3.5 Example Dimensions

A couple of cases with actual dimensions illustrate the utility of the non-dimensional results. The pressure load is noted to be a model input that can be checked before solving the problem while the the acceleration is checked as a simulation output. Table 7.4 summarizes load limits for two cases:

1. Use of the AMS model to predict the behavior of a $0.5m$-diameter membrane with an $f/5$ parabolic shape. The thickness of the membrane is $20\mu m$, and the material properties correspond to NASA CP-1 (see Appendix C). The shape predictions can be considered optical quality for pressure loads $p < 0.0061Pa$ or even $p < 0.021Pa$ for advanced correction techniques. Similar limits for acceleration are $\ddot{w} < 0.22\frac{m}{s^2}$ and $\ddot{w} < 0.74\frac{m}{s^2}$.

2. Use of the AMS model to predict the behavior of a $10m$-diameter membrane with an $f/1$ parabolic shape ($f/1$ is deeper than $f/5$ of Case 1). Case 2 is a much larger and thinner membrane, and hence the two cases span the current space of interest for membrane primary mirrors. The thickness of the membrane is $10\mu m$, and the material properties again correspond to NASA CP-1. The shape predictions can be considered optical quality for pressure loads $p < 1.4 \times 10^{-4}Pa$ or possibly even $p < 2.9 \times 10^{-3}Pa$ for advanced correction techniques. The limits for acceleration are $\ddot{w} < 0.010\frac{m}{s^2}$ and $\ddot{w} < 0.21\frac{m}{s^2}$.

The limits for optical quality with the AMS-model predictions are observed in both cases to be rather small numbers. In compared to the standard atmosphere, the representative pressure is $10^{-3}Pa \times \frac{1ATM}{1.0125 \times 10^5 Pa} \sim 10^{-8}ATM$.

7.4 Modelling Guideline

The model-error results from throughout the thesis summarize in a guideline for optical-level modelling of ten-meter-class curved membrane mirrors. These lessons from the axisymmetric modelling of membrane shells aid future optical-level modelling efforts for large, curved

Table 7.4: Example values of pressure and acceleration limits for two cases. The limits are based upon use of the AMS model for shape predictions.

Parameter	Variable	Case 1	Case 2
Shape		$f/5$	$f/1$
Outer radius	r_{out}	$0.5m$	$10m$
Thickness	h	$2.0 \times 10^{-5}m$	$1.0 \times 10^{-5}m$
Elastic Modulus	E	$2.2 \times 10^{9}\ Pa$	$2.2 \times 10^{9}\ Pa$
Density	ρ	$1400\frac{kg}{m^3}$	$1400\frac{kg}{m^3}$
Non-dimensional Pressure Limits	$\bar{p}_{Upper}$	$2.3 \times 10^{-7}\ Pa$	$1.3 \times 10^{-6}\ Pa$
	$\bar{p}_{Lower}$	$6.9 \times 10^{-8}\ Pa$	$6.5 \times 10^{-8}\ Pa$
Pressure Limits	p_{Upper}	$2.1 \times 10^{-2}\ Pa$	$2.9 \times 10^{-3}\ Pa$
	p_{Lower}	$6.1 \times 10^{-3}\ Pa$	$1.4 \times 10^{-4}\ Pa$
Acceleration Limits	$\ddot{w}_{Upper}$	$0.74\ m/s^2$	$0.21\ m/s^2$
	$\ddot{w}_{Lower}$	$0.22\ m/s^2$	$0.010\ m/s^2$

membrane optics by identifying and explaining both required model elements and common solution pitfalls.

1. *Model Choice*: Many models are available and used in the literature, but a firm requirement on the accuracy of the shape prediction limits the range of geometry and loading over which certain models can be used.

   (a) If the non-dimensional loading remains below certain thresholds, then fairly common models may be used to obtain optical-quality thresholds. For small levels of loading, linearized models provide a good combination of simplicity, quick run time, and accuracy. Above the following approximate non-dimensional thresholds, a nonlinear, geometrically-exact solver must be implemented.

      i. Mean pressure loading $\rightarrow MEAN_{AA}(\bar{p}) >\sim 10^{-6}$

      ii. Mean strain $\rightarrow MEAN_{AA}(\frac{\epsilon_\phi+\epsilon_\theta}{2}) >\sim 10^{-6}$

      iii. Total boundary displacement $\rightarrow |\bar{u}(\bar{r}=1)| >\sim 10^{-7}$

   (b) Below the thresholds, membrane shell theory returns the most-accurate shape prediction. The error in membrane shell theory predictions increases rapidly at a geometry-dependent loading, however, whereas the error from the large-deflection models has a more reliable correlation to load regardless of geometry.

   (c) For large-deflection predictions without the need for optical quality, the Axisymmetric Large Deflection (ALD) model is the best choice because the solution does not "break down".

2. *Constitutive Law Choices*: A linear constitutive law is recommended when the material exhibits Hookean behavior.

   (a) An exact Hookean membrane relationship — linear between second-Piola-Kirchoff type stress resultant and Lagrangian strain — does not provide a significantly more accurate shape prediction than a law in which any stress resultant type is linearly related to any strain type.

   (b) The distinction between stress resultant and strain types is not important for shape predictions of membrane primary mirrors in that the error from choosing an improper field variable type is appreciably less than other modelling errors.

(c) A constitutive law from the literature, apparently "corrected" for the change in coordinate basis, results in greater prediction error than the linear law.

3. *Implementation of Solution*:

   (a) Density of points. For highly accurate results in axisymmetric problems, a few thousand finite difference points are required to achieve the best accuracy in the solution. For less-accurate results, or for problems in which the geometric errors swamp the numerical errors, tens of points can be used.

   (b) Numerical implementation: The numerical aspects of the solution should not introduce more error than the modelling assumptions introduce.

      i. When calculating the field variables such as radius of curvature, the slight change in the numerical expression at the endpoints –and resulting lack of smoothness– can result in 2 to 3 orders of magnitude greater error.

      ii. When applying the load, the reference frame of the load is critical for optical-quality predictions. Application of the deformed-basis pressure to the undeformed configuration can add $O(10^3)$ to the shape error.

4. The results attained in this work can be extended to (1) dynamics because of the duality of the non-dimensional pressure and acceleration terms in the equilibrium equation and (2) solution methods such as finite elements where the local coordinate systems effectively raise the thresholds with element density.

5. *Extension of Results*:

   (a) The limits upon model use can be extended to dynamics by according to the duality of the pressure and linear inertial load term in the governing equation. The non-dimensional acceleration has the same limit as the non-dimensional pressure.

   (b) The results herein are non-dimensional according to global parameters. For modelling methods such as finite elements, in which a local coordinate system is used for the governing equations, the limits on model use will scale with the linear density of elements. Adding elements has the equivalent effect of increasing the thresholds.

7.5 Summary

In this chapter the model comparison framework of Chapter 3 is utilized to determine parametric limits under which the shape predictions of a model exhibit optical quality. The results for four benchmark problems are presented, with the geometry of the benchmark problems covering a set of shapes both classic to the field and potentially viable for membrane primary mirrors. The area-averaged standard deviation of pathlength error captures the mission-critical shape-error and is hence used throughout the chapter as the error metric standard.

The errors are compared against three non-dimensional parameters: pressure, average strain, and outer-boundary displacement. Pressure is chosen as the standard because the parametric correlation to error is rather consistent across different models and geometries. The optical-quality-threshold values of all three parameters are calculated for all three models and provide practical limits upon the use of the models for high-quality shape predictions. These non-dimensional limits are noted as being rather small, generally on the order of 10^{-6}. Other parameters such as the calculated change in geometry are also shown to correlate to the prediction error and thus provide a basis of predicting model quality. Lastly, a duality is shown between non-dimensional pressure and non-dimensional acceleration/ inertia load and thereby extends the limit on static pressure for a given quality to a limit on acceleration.

Of the Axisymmetric Membrane Shell (AMS), Axisymmetric Large Deflection (ALD), and Linearized Axisymmetric Large Deflection (LALD) models, the AMS predictions are shown to generally return the smallest error. The AMS theory is shown to predict the constant-pressure expansion of a spherical shape with extremely low error, and for the other geometries the AMS results exhibits a trend similar to LALD. The error in the linear LALD and AMS models begins to rapidly increase at a modestly large load while the trend in the ALD results remains fairly constant with load. Records of the total time to generate the solutions shows that the ALD solution takes 100 to 1000 times as long as the AMS and LALD solutions. Combined with the difficulties in establishing the ALD nonlinear convergence parameters, the solution time required shows that the ALD is an undesirable model. In addition, the ALD model generally provides no benefit over the linearized LALD for optical-quality predictions.

The model-comparison framework thus accomplishes the task of identifying the parameter space for optical-quality predictions of doubly-curved membrane mirrors. Moreover, the modelling guideline captures the lessons of model selection, constitutive law, implementation, and results extension for future membrane-mirror modelling efforts.

Chapter 8

Summary and Conclusions

8.1 Summary

In this thesis modelling tools are developed for accurately predicting the optical-level behavior of membrane primary mirrors. An inverse solver is developed through a new approach to the geometrically-exact model, with initial and final shapes as model inputs and load distribution as output. The current approach opens the possibility of manufacturing-driven initial shapes and performance-driven final shapes. The inverse solver is used to establish a series of benchmark problems with geometries traceable to doubly-curved telescope mirrors. Finite difference solutions to the benchmark problems lead to relationships between geometry, load, and model error; in the correlation with model error, geometry and load limits for optical-quality predictions are established for a set of models. Model error is defined according to a metric significant to optics, the area-averaged standard deviation of the pathlength error created from the inexact shape prediction. Hookean constitutive law is exactly derived for curved membranes, and constitutive relations from the literature are demonstrated to be inconsistent and contain more error than simpler, consistently-derived relations. Numerical considerations, from level of discretization to endpoint handling, are also discussed for high-accuracy solutions. In general the models exhibit optical-quality accuracy in the shape prediction over some range of parameter space (strain, pressure, etc.), and the current methodology provides a framework for establishing those limits for optical-quality predictions in the parameter space. The model error limits, constitutive relation derivations, and numerical-implementation considerations are combined into a guideline for modelling the optical-level structural behavior of curved membrane mirrors.

8.2 Contributions

The basic theme of the contributions in this thesis is a methodology for modelling static and dynamic structural behavior of membrane mirrors at the optical level by quantifying the effects of modelling decisions. What follows is a listing by topic of the contributions in this thesis.

- A structured approach to classifying modelling assumptions.
  - Organization of existing models into a hierarchy according to assumptions applied to the geometrically exact model. The series of assumptions required to go from the exact equations to the most simple have been established.
- Method to design loaded membrane mirrors given the freedom to choose initial and final shapes according to manufacturing and performance needs, respectively.
  - Method to determine initial thickness distribution or pressure loading distribution required to deform manufacturable membrane shape into required mirror shape. Filled hole in literature by using both initial and final shapes as specifications for the inverse problem.
  - The pressure and stiffness distributions are solved by a new manipulation of the deformed-coordinate-equilibrium equations.
- Formal derivation of constitutive law.
  - The exact Hookean constitutive law is formally derived for stress resultants and strains in different coordinate bases.
- Comparison of constitutive laws which reveals that the commonly-accepted, simply-justified model from the literature is less appropriate than even the linearized model.
  - Demonstrated that the constitutive law from previous work by the author, originally taken from work by an established member of the community, is not consistent in terms of both (1) representing the energy in the structure and (2) using a consistent form (i.e., consistent in the order of strain terms retained).
  - Showed through derivation that the constitutive law used in much of the current work, which is taken from the literature, does not use conjugate variables

(conjugate variables are required for proper representation of the strain energy). In addition, the constitutive law from the literature uses a form which does not consistently reduce all orders in a strain expansion.

  - Showed through example cases that the relation used generally leads to greater error than even the linearized relations.
  - Quantified the errors for the different constitutive laws under axisymmetric membrane shells; result is a magnitude guideline for use of the constitutive laws.

- Load- and geometry-based guide to creating models with optical accuracy.
  - Developed a method to quantify the effects of modelling assumptions upon the ability to predict the optical-level behavior of a true membrane primary mirror. Demonstrated the method for representative problems over a range of geometry and load conditions.
  - Demonstrated method of model selection based upon model accuracy parameterized by load and geometry.
  - Demonstrated valid range for linear models.
  - Quantification of model errors for models used by many previous researchers.
  - Demonstrated extension of results to other solution methods such as finite elements.
  - Demonstrated extension of results to accurate prediction of dynamic behavior.

- Modifications to standard solution methods for optical modelling of membranes. Standard methods often added many orders of magnitude error to the shape predictions.
  - Thousands of discrete points are shown to be necessary in the axisymmetric case to reduce the numerical-type errors below the optical level. The error due to geometric assumptions is generally orders of magnitude greater than the discretization error, however, and so tens or hundreds of points are sufficient for most analyses.
  - Very minor changes in numerical expressions are shown to have significant effects upon error. A method is proposed to ensure the the smoothness in the original geometry is properly represented in the field variables.

– Showed that proper specification of basis of load is important for model accuracy.

8.3 Future Work/ Extensions to Current Work

- *Material Characterization:*

  Material properties, especially the elastic modulus and yield strength, are not well characterized in the literature over a range of temperature appropriate for a space telescope mirror. The form of the constitutive relations is a very important issue for achieving optical-quality shape predictions. In this work a linear relationship is assumed between the strain and the second-Piola-Kirchoff-type stress resultant; this implies a quadratic strain-energy-density. Proof of the quadratic form must come from experiments at representative ambient conditions. If the cubic term in the strain energy leads to a noticeable contribution to the deformation, the constitutive relations may currently have a (1+strain) level of error. Moreover, high-quality constitutive relations for membranes are not available in the literature.

  If some better representation of the constitutive behavior is developed, the methodology in this thesis would still apply for assessing model accuracy. Moreover, the higher-quality models identified in this thesis can be perturbed to assess the impact of new constitutive laws.

- *Continuation of results into sensitivity and dynamics.*

  The analysis flow in figure 1.3 provides several directions to take the current research. Sensitivity analysis can be used to establish manufacturing tolerances. Non-axisymmetric solutions will allow actuator schemes to be established for both static and dynamic behavior.

- *Characterization of the influence of actuators and the impact of disturbances, both static and dynamic, upon the mission-critical performance.*

  Telescope mirrors typically use point actuators distributed across the mirror surface; for true membranes point force inputs will influence too small a region about the actuator and hence a new system of actuation will be needed. The capabilities and limitations of actuators for true membrane systems need to be understood in order to be able to make system design decisions for the true membrane mirror systems.

- *Use of model-based autonomy.*

  The membrane exhibits multiple mechanical states, a possible list of which is listed below, and the control system will have to monitor the current state and apply the correct control solution.

  - Unloaded
  - Wrinkled
  - Within tolerance of final desired shape
  - Loaded yet outside of tolerance

  This list is significant because the shape prediction of membranes is only deterministic for certain loading regimes with certain assumptions satisfied. Transitions between the deterministic states will require another level of control, and model-based autonomy appears to be a viable approach.

  Future complex aerospace systems are expected to operate autonomously, and membrane mirrors, with the need to apply control systems based upon the current material state, may be well-served by model-based autonomy research [89]. Mechanical modelling might be made simple enough for the on-board computer to perform model-based diagnosis of the current state. Knowledge of the current state allows a planning program to to achieve the current desired goal (save power, maintain optical figure, etc.).

  Because the membrane exhibits multiple mechanical states and the modelling will only be correct if the correct state is identified, model-based autonomy technologies may be an enabling technology for membrane optics. Figure 8.1 provides a mapping of the transitions between membrane states.

  For example, knowing the tension distribution and out-of-figure displacement would provide information as to whether a wrinkled state exists. The identification of the wrinkled state would enable the control algorithm to be switched from the figure maintenance function of "Final Loading" to the startup procedure of "Initial Loading".

- *Dynamics and control for electrostatic-type pressure loading.*

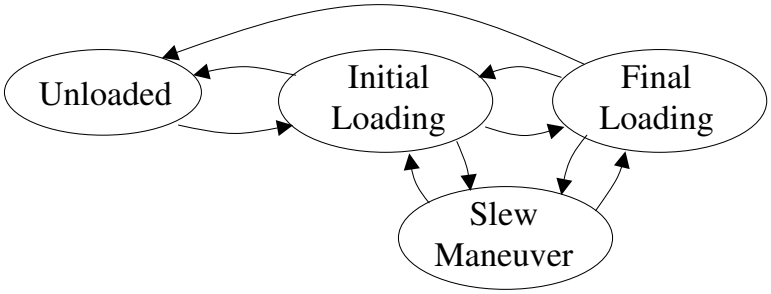

Figure 8.1: Example states and transitions for a membrane mirror.

Significant work has been performed on the dynamics and control of electrostatically-formed antennas and mirrors, yet more work is needed. For instance, the effect of a flexible back-plane or rim has not been considered. The small-deflection $f_\infty = 5$ subaperture geometry proposed in this thesis work also is not well-addressed by the $f_\infty = 1$ geometry typical of the literature. With the force at each point related to the the square of the distance between reflector and back-plane, a decrease in the maximum deflection means a significant decrease in the voltage requirement. Future research could address issues specific to electrostatic control for both the static forming and dynamic disturbance rejection problems.

- *Investigate importance of distributed moments to the optical-level behavior.*

  An early assumption of the static-shape-prediction models is that the structure is a true membrane and hence carries no distributed moment. The method used to quantify the effect of modelling assumptions for membrane shell models could be extended to include distributed moments. An example result would be to show, for a representative geometry and loading, the thickness at which distributed moments begin to significantly affect the shape predictions.

  Calculating the in-plane and bending components of the strain energy would provide an early indicator of the need to include moments in the models.

- *Include strain in the normal direction into the shape-design problem.*

For plane stress,

$$\begin{aligned} \sigma_z &= -\nu\left(\sigma_x + \sigma_y\right) && (8.1)\\ E_z\epsilon_z &= -\nu\left[\frac{E}{1-\nu^2}\left(\epsilon_x + \nu\epsilon_y\right) + \frac{E}{1-\nu^2}\left(\epsilon_y + \nu\epsilon_x\right)\right. && (8.2) \end{aligned}$$

For $E_x = E_y = E_z$,

$$\begin{aligned} \epsilon_z &= -\frac{\nu}{1-\nu^2}\left(\epsilon_x + \nu\epsilon_x + \epsilon_y + \nu\epsilon_y\right) && (8.3)\\ &= -\frac{\nu(1+\nu)}{1-\nu^2}\left(\epsilon_x + \epsilon_y\right) && (8.4)\\ &= -\frac{\nu}{1-\nu}\left(\epsilon_x + \epsilon_y\right) && (8.5) \end{aligned}$$

For the O(1%) strains and $\nu = 0.3$ conditions used in the static design work, the transverse strain is approximately

$$\begin{aligned} \epsilon_z &= -\frac{0.3}{1-0.3}\left(0.01 + 0.01\right) && (8.6)\\ &\approx -0.00857 && (8.7) \end{aligned}$$

For a $10\mu m$ thick membrane, this translates to a displacement of

$$\begin{aligned} \Delta_h &= \epsilon_z h && (8.8)\\ &= -0.0085710\mu m && (8.9)\\ &\approx -85.7nm && (8.10) \end{aligned}$$

Displacements in the range of tens of nanometers may be significant for some optics problems, and so a better understanding of the normal-direction displacement during loading could improve predictive capability.

Bibliography

[1] A.L. Adler, *Finite Element Approaches For Static And Dynamic Analysis Of Partially Wrinkled Membrane Structures*, PhD thesis, University of Colorado, 2000.

[2] G.S. Agnes and J.W. Wagner, Adaptive structures technology for membrane optical surfaces, 2001, AIAA Paper 2001-1199.

[3] D.R. Askeland, PWS-Kent Publishing, 2 edition.

[4] Standard test method for tensile properties of thin plastic sheeting, ASTM Standard, 2002, ASTM D882 - 02, Vol. 8.

[5] E.H. Baker, A.P. Cappelli, L. Kovalevsky, F.L. Rish, and R.M. Verette, *Shell Analysis Manual*, NASA CR-912, 1968.

[6] J.A. Bishop, Shape correction of initially flat inflated membranes by a genetic algorithm, In *Proceedings of the 39th AIAA/ASME/ASCE/AHS/ASC Structures, Structural Dynamics, and Materials Conference and Exhibit*, pages 2309–2312, 1998, AIAA Paper 98-1984.

[7] R.L. Bisplinghoff, H. Ashley, and R.L. Halfman, *Aeroelasticity*, Dover, 1996, originally published by Addison-Wesley, 1955.

[8] M. Born and E. Wolf, *Principles of Optics*, Cambridge University Press, 1980, 6th edition.

[9] E. Bromberg and J.J. Stoker, Non-linear theory of curved elastic sheets, *Quarterly of Applied Mathematics*, 3:246–265, 1945.

[10] A.L. Brooks, J.V. Coyner, W.J. Gardner, and D.J. Mihora, Conceptual design and analysis of a large antenna utilizing electrostatic membrane management, Technical report, NASA, 1982, NASA CR-3522.

[11] B. Budiansky, Notes on nonlinear shell theory, *Journal of Applied Mechanics*, 35:393–401, 1968.

[12] D.P. Cadogan, J.K. Lin, and M.S. Grahne, The development of inflatable space radar reflectarrays, In *Proceedings of the 40th AIAA/ASME/ASCE/AHS/ASC Structures, Structural Dynamics, and Materials Conference and Exhibit*, pages 2488–2494, 1999, AIAA Paper 99-1517.

[13] R. Carreras, On near-net shape membrane optics, 1999, AIAA Paper 99-4642.

[14] C. Cassapakis and M. Thomas, Inflatable structures technology development overview, 1995, AIAA Paper 95-3738.

[15] J.G.A. Croll, A tension field solution for non-linear circular plates, In D.J. Dawe, R.W. Horsington, A.G. Kamtekar, and G.H. Little, editors, *Aspects of the Analysis of Plate Structures*, Clarendon Press, 1985. Chapter 17.

[16] D.J. Davis and G.S. Agnes, Environmental disturbance modeling for inflatable space structures, 2002, AIAA Paper 2002-1266.

[17] B.J. de Blonk, Static shape-forming design of membrane mirrors for spaceborne telescopes, 2000, AIAA Paper 2000-1813.

[18] H. Fang and M.C. Lou, Analytical characterization of space inflatable structures – an overview, In *Proceedings of the 40th AIAA/ASME/ASCE/AHS/ASC Structures, Structural Dynamics, and Materials Conference and Exhibit*, pages 718–728, 1999, AIAA Paper 99-1272.

[19] W.B. Fichter, Some solutions for the large deflections of uniformly loaded circular membranes, Technical report, NASA, 1997, NASA TP 3658.

[20] R.E. Freeland, G.D. Bilyeu, G.R. Veal, and M.M. Mikulas, Inflatable deployable space structures technology summary, In *Proceedings of the* 49th *International Astronautical Congress*, International Astronautical Federation, 1998, IAF-98-I.5.01.

[21] R.F. Freeland, G.D. Bilyeu, G.R. Veal, M.D. Steiner, and D.E. Carson, Large inflatable deployable antenna flight experiment results, In *Proceedings of the 48th International Astronautical Congress*, International Astronautical Federation, 1997, IAF-97-I.3.01.

[22] A.E. Green and J.E. Atkins, *Large Elastic Deformations*, Clarendon Press, 2nd edition, 1970.

[23] G. Greschik, M.M. Mikulas, and A. Palisoc, Approximations and errors in pressurized axisymmetric membrane shape predictions, In *Proceedings of the 39th AIAA/ASME/ASCE/AHS/ASC Structures, Structural Dynamics, and Materials Conference and Exhibit*, pages 2761–2771, 1998, AIAA Paper 98-2101.

[24] G. Greschik, A. Palisoc, C. Cassapakis, G. Veal, and M.M. Mikulas, Approximating paraboloids with axisymmetric pressurized membranes, In *Proceedings of the 39th AIAA/ASME/ASCE/AHS/ASC Structures, Structural Dynamics, and Materials Conference and Exhibit*, pages 2772–2782, 1998, AIAA Paper 98-2102.

[25] G. Greschik, A. Palisoc, C. Cassapakis, G. Veal, and M.M. Mikulas, Sensitivity study of precision pressurized membrane reflector deformations, *AIAA Journal*, 39(2):308–314, 2001.

[26] M.T. Gruneisen, T. Martinez, and D.L. Lubin, Dynamic holography for high-dynamic-range two-dimensional laser wavefront control, In J.D. Gonglewski, M.A. Vorontsov, and M.T. Gruneisen, editors, *Proceedings of the SPIE Conference on High-Resolution Wavefront Control: Methods, Devices, and Applications III*, pages 224–238, 2002, Proceedings of the SPIE Vol 4493.

[27] K. Guidanean and G.T. Williams, An inflatable rigidizable truss structure with complex joints, In *Proceedings of the 39th AIAA/ASME/ASCE/AHS/ASC Structures, Structural Dynamics, and Materials Conference and Exhibit*, pages 2797–2806, 1998, AIAA Paper 98-2105.

[28] Homero Gutierrez, Mike Lieber, and Reese Hanes, Phase i study of an electrostatically controlled membrane mirror (ecmm), 1999, Ball Aerospace and Technologies Corp, Aerospace Systems Division, Final report for AFRL-DE on Prime Contract No. 2102202.

[29] L.J. Hart-Smith and J.D.C. Crisp, Large elastic deformations of thin rubber membranes, *International Journal of Engineering Science*, 5:1–24, 1967.

[30] H. Hencky, Über den Spannungszustand in Kreisrunden Platten mit verschwindender Biegungssteifigkeit (About the tensile state in circular plates with infinitesimal bending rigidity), *Z. Math. Phys.*, 63:311–317, 1915.

[31] C.H. Jenkins, R.E. Freeland, J.A. Bishop, and W.Z. Sadeh, An up-to-date review of inflatables structures technology for space-based applications, In R.G. Galloway and S. Lokaj, editors, *Proceedings of the* 6^{th} *International Conference and Exposition of Engineering, Construction, and Operations in Space (Space 98)*, pages 66–73, 1998.

[32] C.H. Jenkins, V.D. Kalanovic, K. Padmanabhan, and S.M. Faisal, Intelligent shape control for precision membrane antennae and reflectors in space, *Smart Materials and Structures*, 8:857–867, 1999.

[33] C.H. Jenkins and S. Kondareddy, Dynamics of seamed precision membranes, In *Proceedings of the* 40^{th} *AIAA/ASME/ASCE/AHS/ASC Structures, Structural Dynamics, and Materials Conference and Exhibit*, pages 2235–2546, 1999, AIAA Paper 99-1522.

[34] C.H. Jenkins and D.K. Marker, Surface precision of inflatable membrane reflectors, *Journal of Solar Energy Engineering*, 120(4):298–305, 1998.

[35] C.H. Jenkins and M. Tampi, Local membrane vibrations and inflatable space structures, In *Proceedings of Space 2000*, pages 410–416. American Society of Civil Engineers, 2000.

[36] C.H. Jenkins, J.M. Wilkes, and D.K. Marker, Improved surface accuracy of precision membrane reflectors through adaptive rim control, In *Proceedings of the* 39^{th} *AIAA/ASME/ASCE/AHS/ASC Structures, Structural Dynamics, and Materials Conference and Exhibit*, pages 2302–2308, 1998, AIAA-98-1983.

[37] C.H.M. Jenkins, W.W. Schur, and G. Greschik, Mechanics of membrane structures, In Christopher H.M. Jenkins, editor, *Gossamer Spacecraft: Membrane and Inflatable Structures Technology for Space Applications*, American Institute of Aeronautics and Astronautics, 2001. Chapter 3.

[38] Christopher H.M. Jenkins, editor, *Gossamer Spacecraft: Membrane and Inflatable Structures Technology for Space Applications*, American Institute of Aeronautics and Astronautics, 2001, Volume 191 in Progress in Aeronautics and Astronautics series.

[39] J.-N. Juang and W. Huang, Static shape forming for an electrostatically controlled membrane mirror, In *Proceedings of the 1983 American Control Conference*, pages 1310–1316, June 1983.

[40] W.T. Koiter, A consistent first approximation in the general theory of thin elastic shells, In *Proceedings of the Symposium on the Theory of Thin Elastic Shells*, pages 12–33, Interscience Publishers, 1960, Delft, 24–28 Aug 1959.

[41] I. Kolmanovsky, R.H. Miller, P.D. Washabaugh, and E.G. Gilbert, Nonlinear control of electrostatically shaped membrane with state and control constraints, In *Proceedings of the American Control Conference*, pages 2927–2931, June 1998.

[42] R. Kotaru and P.M. Bainum, On the dynamics and control of an orbiting shallow spherical shell in the presence of solar radiation, *The Journal of the Astronautical Sciences*, 42(4):395–419, 1994.

[43] A.D. Kydoniefs, Finite axisymmetric deformations of elastic membranes, *International Journal of Engineering Science*, 10:939–946, 1972.

[44] J.H. Lang, *Computer Control of Stochastic Distributed Systems with Applications to Very Large Electrostatically Figured Satellite Antennas*, PhD thesis, MIT, 1980.

[45] J.H. Lang, J.R. Gersh, and D.H. Staelin, Electrostatically controlled wire-mesh antennas, *Electronics Letters*, 14:655–656, September 1978.

[46] J.H. Lang and D.H. Staelin, The computer-controlled stabilization of a noisy two-dimensional hyperbolic system, *IEEE Transactions on Automatic Control*, 27(5):1033–1043, October 1982.

[47] J.H. Lang and D.H. Staelin, Electrostatically figured reflecting membrane antennas for satellites, *IEEE Transactions on Automatic Control*, 27(3):666–670, June 1982.

[48] W.J. Larson and J.R. Wertz, editors, *Space Mission Analysis and Design*, Kluwer Academic Publishers, 1992.

[49] J.W. Leonard, *Tension Structures*, McGraw-Hill, 1988.

[50] A. Libai and J.G. Simmonds, *The Nonlinear Theory of Elastic Shells*, Cambridge University Press, 2nd edition, 1998.

[51] A.E.H. Love, *Treatise on the Mathematical Theory of Elasticity*, Dover Publications, 1944, Fourth Edition.

[52] P.L. Luz and T. Rice, Mirror material properties compiled for preliminary design of the next generation space telescope (30 to 294 kelvin), Technical report, NASA Marshall Space Flight Center, 1998, NASA/TM-1998-208181.

[53] J.A. Main, R.A. Carlin, E. Garcia, S.W. Peterson, and A.M. Strauss, Dynamic analysis of space-based inflated beam structure, *J of the Acoustical Society of America*, 97(2):1035–1045, 1995.

[54] J.A. Main, S.W. Peterson, and A.M. Strauss, Load-deflection behavior of space-based inflatable beam structures, *Journal of Aerospace Engineering*, 7(2):225–238, 1994.

[55] L.E. Malvern, *Introduction to the Mechanics of a Continuous Medium*, Prentice-Hall, Inc, 1969.

[56] D.K. Marker, R.A. Carreras, J.M. Wilkes, C.H. Jenkins, D. Duneman, J.R. Rotge, and C.B. Hogge, Optical evaluation of membrane mirrors with curvature, In K.D. Bell, M.K. Powers, and J.M. Sasian, editors, *Novel Optical Systems and Large-Aperture Imaging*, pages 202–208, 1998, Proceedings of the SPIE Vol 3430.

[57] D.K. Marker and C.H. Jenkins, Surface precision of optical membranes with curvature, *Optics Express*, 1(11):324–331, 1997.

[58] D.K. Marker, J.M. Wilkes, R.A. Carreras, J.R. Rotge, C.H. Jenkins, and J.T. Ash, Fundamentals of membrane optics, In Christopher H.M. Jenkins, editor, *Gossamer Spacecraft: Membrane and Inflatable Structures Technology for Space Applications*, American Institute of Aeronautics and Astronautics, 2001, Chapter 4, Progress in Aeronautics and Astronautics Vol 191.

[59] A.B. Meinel and M.P. Meinel, Inflatable membrane mirrors for optical passband imagery, *Optical Engineering*, 39(2):541–550, 2000.

[60] V.M. Melnikov and V.A. Koshelev, *Large Space Structures Formed by Centrifugal Forces*, Gordon and Breach Science Publishers, 1998, Earth Space Institute Book Series, Translated by Nina Barabush, ISBN 90-5699-112-4.

[61] D.J. Mihora and P.J. Redmond, Electrostatically formed antennas, *Journal of Spacecraft*, 17(5):465–473, September–October 1980, Article No 79-0922R.

[62] M.M. Mikulas and M. Thomson, State of the art and technology needs for large space structures, In *Flight Vehicle Materials, Structures, and Dynamics – Assessment and Future Directions*, 1994, Chapter 3.

[63] R.K. Miller, M. Thomson, and J.M. Hedgepath, Concepts, analysis, and development for precision deployable space structures, Technical report, NASA CR 187622, 1991.

[64] L.M. Murphy, Moderate axisymmetric deformations of optical membrane surfaces, *Journal of Solar Energy Engineering*, 109:111–120, 1987.

[65] T.W. Murphy and M.M. Mikulas, Nonlinear effects of material wrinkles on the stiffness of thin polymer films, In *Proceedings of the 40th AIAA/ASME/ASCE/AHS/ASC Structures, Structural Dynamics, and Materials Conference and Exhibit*, pages 1227–1238, 1999, AIAA Paper 99-1341.

[66] A.H. Nayfeh, *Perturbation Methods*, Wiley-Interscience, 1973.

[67] V.V. Novozhilov, *Thin Shell Theory*, P. Noordhoff Ltd, 1964, Translated by P.G. Lowe, Edited by J.R.M. Radok, 2nd Augmented and Revised Edition.

[68] A. Palisoc, G. Veal, C. Cassapakis, G. Greschik, and M.M. Mikulas, Geometry attained by pressurized membranes, In *Space Telescopes and Instruments V*, pages 747–757, 1998, Proceedings of the SPIE Vol 3356.

[69] A.L. Palisoc and Y. Huang, Design tool for inflatable structures, In *Proceedings of the 38th AIAA/ASME/ASCE/AHS/ASC Structures, Structural Dynamics, and Materials Conference and Exhibit*, pages 2922–2930, 1997, AIAA Paper 97-1378.

[70] K.W. Peters, J.A. Bishop, and J.M. Wilkes, An analysis of membrane mirrors for use in large aperture imaging systems, In *Proceedings of the 1998 IEEE Aerospace Conference*, volume 2, pages 47–53, 1998.

[71] E. Reissner, On axisymmetrical deformations of thin shells of revolution, In *Proceedings of the Third Symposium in Applied Mathematics of the American Mathematical Society*, pages 27–52, 1950.

[72] L.M. Robertson, A systems engineering study of gossamer optical satellites, Technical report, Air Force Research Laboratory, Space Vehicles Directorate, 2002, AFRL-VS-TR-2002-1007.

[73] J.W. Rogers and G.S. Agnes, Modeling a piezothermoelastic string-beam, 2001, AIAA Paper 2001-1200.

[74] J.W. Rogers and G.S. Agnes, Formulation of asymptotic finite elements using the method of multiple scales, 2002, AIAA Paper 2002-1663.

[75] C.M Satter and R.E. Freeland, Inflatable structures technology applications and requirements, 1995, AIAA Paper 95-3737.

[76] M. Sheplak and J. Dugundji, Large deflections of clamped circular plates under initial tension and transitions to membrane behavior, *Journal of Applied Mechanics*, 65(1):107–115, 1998.

[77] W. Soedel, *Vibrations of Shells and Plates*, Marcel Dekker, Inc., 2nd edition, 1993.

[78] A.J.M. Spencer, The static theory of elasticity, *Journal of the Institute of Mathematics and Its Applications*, 6(3):164–200, 1970.

[79] B. Tabarrok and Z. Qin, Dynamic analysis of tension structures, *Computers and Structures*, 62(3):467–474, 1997.

[80] Thomas and Finney, Addison-Wesley, 7 edition, 1988.

[81] J.T. Tielking and W.W. Feng, The application of the minimum potential energy principle to nonlinear axisymmetric membrane problems, *Journal of Applied Mechanics*, 41:491–496, 1974.

[82] S. Timoshenko and S. Woinowsky-Krieger, *Theory of Plates and Shells*, McGraw-Hill, 2nd edition, 1959.

[83] R.K. Tyson, *Principles of Adaptive Optics*, Academic Press, 1998, 2nd edition.

[84] H. Vaughn, Pressurising a prestretched membrane to form a paraboloid, *International Journal of Engineering Science*, 18:99–107, 1980.

[85] P.K.C. Wang and F.Y. Hadaegh, Computation of static shapes and voltages for micromachined deformable mirrors with electrostatic actuators, *Journal of Microelectromechanical Systems*, 5(3):205–220, 1996.

[86] H.J. Weinitschke, Stable and unstable axisymmetric solutions for membranes of revolution, *Applied Mechanics Review*, 42(11):S289–S294, 1989.

[87] J.M. Wilkes, Applications of power series solutions of membrane equilibrium equations to the optical evaluation of membrane mirrors with curvature, Technical report, Air Force Research Laboratory, Directed Energy Directorate, 1998, AFRL-DE-PS-TR-1998-1069.

[88] J.M. Wilkes, Mechanics of a near net-shape stress-coated membrane, volume i: Theory development using the method of asymptotic expansions, Technical report, Air Force Research Laboratory, Directed Energy Directorate, 2002, AFRL-DE-PS-TR-2002-1023.

[89] B.C. Williams, M.D. Ingham, S.H. Chung, and P.H. Elliott, Model-based programming of intelligent embedded systems and robotic space explorers, In *Proceedings of the IEEE: Special Issue on Modeling and Design of Embedded Software*, volume 9, pages 212–237, 2003, Invited paper.

[90] Y. Yam, *Large Space Structure Model Reduction and Control System Design Based upon Sensor and Actuator Influence Functions*, PhD thesis, MIT, 1983.

Appendix A

Performance Metrics

Objectives of Appendix:

To identify the mission-critical performance metric for membrane primary mirrors.

A.1 Motivation

Modelling membrane mirror structural behavior with optical-level accuracy is a difficult task, and proper metrics are needed to evaluate differences between models. Since the performance strongly influences decisions in the structural control design process, the metrics must be chosen carefully. The difference between two predicted mirror shapes, often just in the axial direction, is commonly used as the basis of a metric. Since the mirror is an optical component, however, the impact of the actual mirror shape upon impinging wavefronts provides the information most critical to the mission. The effects of modelling decisions are then quantified properly when the effect on the wavefront is established.

A.2 Geometry

A telescope compresses the size of an incoming wavefront and projects an image onto a detector — eye, film, or CCD. For the light from the impinging wavefront to arrive in

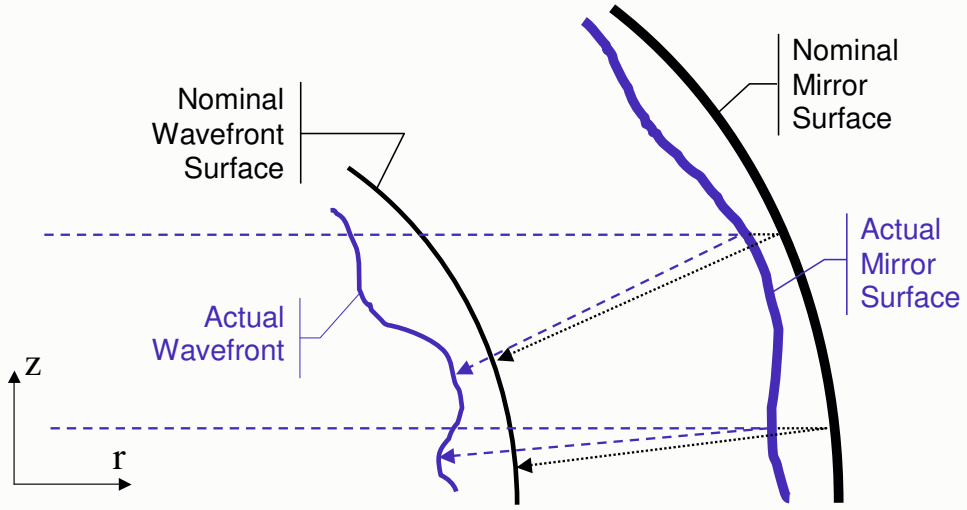

Figure A.1: Four surfaces of interest for reflection off a curved mirror. The lines shown are for a cut of the mirror and wavefront surfaces at some angle θ about the main telescope axis z.

phase at a single point — the focal point, the wavefront must have the form of a collapsing sphere. This sphere, represented in two dimensions in Figure A.1 by the "nominal wavefront surface," is known as the Gaussian reference sphere (chapter V of Born and Wolf [8]).

As shown in Figure A.1, four surfaces are relevant to the geometric analysis of curved-mirror performance. If the nominal mirror shape is a paraboloid, the nominal wavefront surface changes from planar to spherical as a product of reflection. Nominal shapes are mathematical abstractions, however, and so real surfaces always contain some level of shape error. Rather than make the assumption that the primary mirror is the final optical component that shapes the planar wavefront into a sphere, the error is defined generically as the difference between the wavefront reflected from the reference surface and that reflected from the actual surface. Pathlength error is measured in the nominal ray direction, toward the center of the sphere. Phase is the pathlength normalized by the wavelength of interest and converted to radians.

Figure A.3 provides a graphical representation of a general mirror error. The reference surface is shown in the middle part of the figure and includes point P_0. Point P_0 represents the location of point P for zero error. The reference ray is parallel to the z-axis and

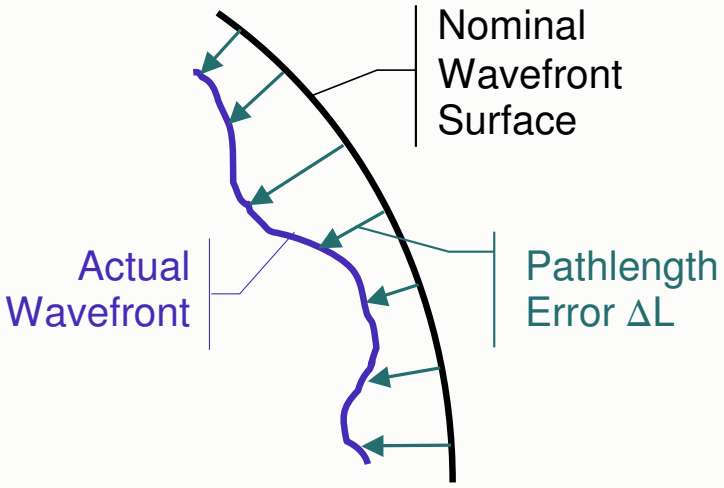

Figure A.2: Two-dimensional representation of pathlength error across a mirror surface.

terminates at a point in space according to the choice of ray length. A ray of the same length impinges upon the actual surface, shown at the bottom of the figure, and terminates at a different location. The vector difference between the two terminal locations is the pointwise vector error.

The sites at which the ray impinges upon the reference surface and the actual surface will have different locations and slopes. Since the reference mirror angle α_1 is generally not equal to the actual angle α, the direction of the ray reflected from the actual surface will have a different direction from the ray reflected from the reference surface.

The locus of equal-length-ray endpoints that have reflected across the entire mirror surface form a wavefront surface; generating the wavefront is the fundamental objective of a ray-trace analysis. The wavefront surface represents the state of the incoming signal as the signal is passed from the primary mirror subsystem to the secondary mirror or other optics subsystem. The pointwise shape difference between the wavefronts from a reference and an actual surface are integrated over the aperture to produce a single metric.

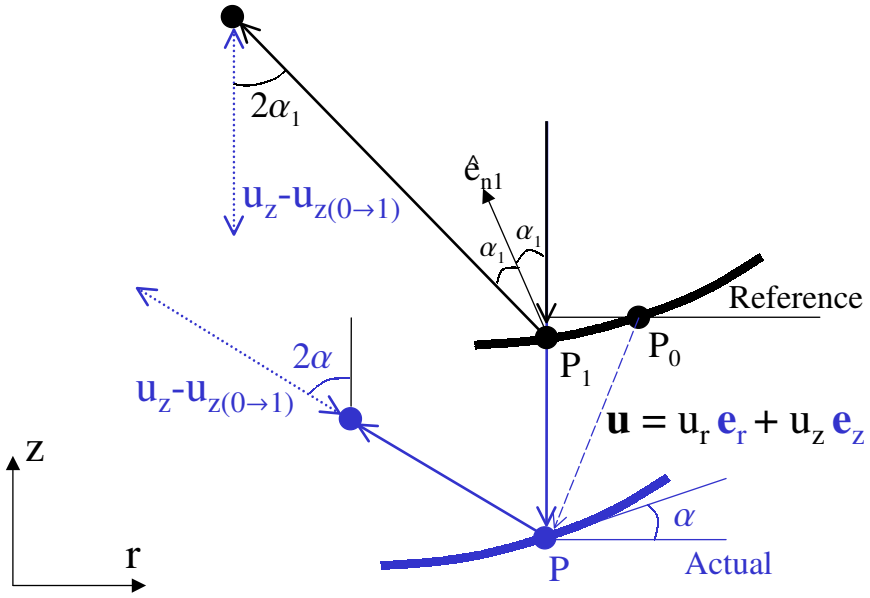

Figure A.3: Two-dimensional representation of reflection of a ray from both a reference mirror and an actual mirror with position and slope error. The dotted vectors of length $u_z - u_{z(0\to1)}$ show that adding the piston error to the pathlength is NOT equivalent to a piston motion of the reference ray terminus.

A.3 Metrics

The difference between the reference and actual mirror surfaces is captured in metrics such as the (common) *mirror piston RMS metric* $Z_{[u_{z_{RMS}}]}$. This RMS metric and those that follow are calculated by finding the area-weighted mean and then the area-weighted root-mean-square (also the bias and the variance). A_{Ref} is the axial projection of the area of the reference mirror surface.

$$\begin{aligned} \bar{u}_z &\equiv \frac{1}{A_M} \int_{A_M} (u_z)\, dA_M \\ &= \frac{1}{A_M} \int_{A_M} [(\mathbf{M}-\mathbf{m}) \cdot \hat{\mathbf{e}}_z]\, dA_M \\ Z_{[u_{z_{RMS}}]} &\equiv \sqrt{\frac{1}{A_M} \int_{A_M} (u_z - \bar{u}_z)^2\, dA_M} \end{aligned} \tag{A.1}$$

The remaining metrics are derived from the pointwise wavefront error as discussed throughout this report. The *pathlength STD metric* $Z_{[\Delta L_{STD}]}$, as discussed in the literature, is

$$\begin{aligned} \overline{\Delta L} &\equiv \frac{1}{A_{WF}} \int_{A_{WF}} (\Delta L)\, dA_{WF} \\ &= \frac{1}{A_{WF}} \int_{A_{WF}} [(\mathbf{W}-\mathbf{w}) \cdot \hat{\mathbf{e}}_L]\, dA_{WF} \\ Z_{[\Delta L_{STD}]} &\equiv \sqrt{\frac{1}{A_{WF}} \int_{A_{WF}} \left(\Delta L - \overline{\Delta L}\right)^2 dA_{WF}} \end{aligned} \tag{A.2}$$

where A_{WF} is the axial projection of the area of the reference wavefront surface.

The *wavefront piston RMS metric* $Z_{[\Delta w_{z_{RMS}}]}$ is calculated as

$$\begin{aligned} \overline{\Delta w_z} &\equiv \frac{1}{A_{WF}} \int_{A_{WF}} (\Delta w_z)\, dA_{WF} \\ &= \frac{1}{A_{WF}} \int_{A_{WF}} [(\mathbf{W}-\mathbf{w}) \cdot \hat{\mathbf{e}}_z]\, dA_{WF} \\ Z_{[\Delta w_{z_{RMS}}]} &\equiv \sqrt{\frac{1}{A_{WF}} \int_{A_{WF}} \left(\Delta w_z - \overline{\Delta w_z}\right)^2 dA_{WF}} \end{aligned} \tag{A.3}$$

Appendix B

Definition of Non-Dimensional Variables

The equations that describe the deflection behavior of large membrane mirrors can be placed into a non-dimensional form as discussed in chapter 11 of BAH [7]. In the non-dimensional form the independent or primary variables are normalized by a chosen set of values while the other parameters are placed into non-dimensional groupings called secondary variables. This formalism allows scaled problems or experiments to be studied to extract information about the behavior of the full-scale system; the only requirement is that the secondary parameters have identical values for both the full and reduced scale.

The choice of secondary variables for normalizing the entire variable set is a product of studying the governing equations. The constitutive equations scale readily when the extensional stiffness Eh is used to normalize the stress resultants. The equilibrium equations require a length-type variable for scaling, and use of the final outer radius r_{out} results in a better numerical scaling than if thickness were used. Table B.1 present the non-dimensional variable definitions for the model accuracy problem work in this thesis summarized by Figure 3.5. One discrepancy is allowed in Chapter 5, however: the thickness h is written as h_0 to emphasize that the undeformed-basis thickness is being used.

Table B.2 has the non-dimensional variable set use in the static-forming design work of Chapter 4. The variable are almost identical to Table B.1 except that the yield strength is used to normalize rather than the elastic modulus, or $\sigma_Y h$ rather than Eh. This variable choice allows a direct percent-of-yield design analysis applicable to creep design criteria.

Table B.1: Variables used to describe the geometry, field quantities, structural properties, and loading *for the model-accuracy analysis.*

Symbol	Description	Non-Dimensional Form
f_∞	Focal ratio of reflector	$\frac{f}{2r_{out}}$
$(\bar{h})^\dagger$	Thickness of the membrane	$\frac{h}{r_{out}}$
$\bar{r}_{in}$	Inner radius of mirror	$\frac{r_{in}}{r_{out}}$
(r_{out})	Outer radius of mirror	
$\bar{r}$	Radial position of deformed body	$\frac{r}{r_{out}}$
$\bar{R}$	Radial position of undeformed body	$\frac{R}{r_{out}}$
α	Angle of deformed membrane	α
$\bar{\kappa}$	Curvature of deformed membrane	κr_{out}
$\bar{r}_{sph}$	Radius of sphere	$\frac{r_{sph}}{r_{out}}$
$(\bar{E})$	Linear elastic modulus of material	
σ_Y	Yield stress of material	$\frac{\sigma_Y}{E}$
$\bar{p}$	Pressure loading	$\frac{p}{E}\frac{r_{out}}{h}$
$\bar{n}_\phi$	Meridional stress resultant (deformed basis)	$\frac{n_\phi}{Eh}$
$\bar{N}_\phi$	Meridional stress resultant (undeformed basis)	$\frac{N_\phi}{Eh}$
$\bar{n}_\theta$	Circumferential stress resultant (deformed basis)	$\frac{n_\theta}{Eh}$
$\bar{N}_\theta$	Circumferential stress resultant (undeformed basis)	$\frac{N_\theta}{Eh}$
ϵ_ϕ	Meridional strain	ϵ_ϕ
ϵ_θ	Circumferential strain	ϵ_θ

†Thickness of undeformed structure is h_0 in Chapter 5.

Table B.2: Variables used to describe the geometry, field quantities, structural properties, and loading *for the shape-forming design* work of Chapter 4.

Symbol	Description	Non-Dimensional Form
f_∞	Focal ratio of reflector	$\frac{f}{2r_{out}}$
$(\bar{h})$	Thickness of the membrane	$\frac{h}{r_{out}}$
$\bar{r}_{in}$	Inner radius of mirror	$\frac{r_{in}}{r_{out}}$
(r_{out})	Outer radius of mirror	
$\bar{r}$	Radial position of deformed body	$\frac{r}{r_{out}}$
$\bar{R}$	Radial position of undeformed body	$\frac{R}{r_{out}}$
α	Angle of deformed membrane	α
$\bar{\kappa}$	Curvature of deformed membrane	κr_{out}
$\bar{r}_{sph}$	Radius of sphere	$\frac{r_{sph}}{r_{out}}$
$\bar{E}$	Linear elastic modulus of material	$\frac{E}{\sigma_Y}$
$\bar{F}_v$	Vertical membrane force applied to inner rim	$\frac{F_v}{h\sigma_Y}$
(σ_Y)	Yield stress of material	
$\bar{p}$	Pressure loading	$\frac{p}{\sigma_Y}\frac{r_{out}}{h}$
$\bar{n}_\phi$	Meridional stress resultant	$\frac{n_\phi}{h\sigma_Y}$
$\bar{n}_\theta$	Circumferential stress resultant	$\frac{n_\theta}{h\sigma_Y}$
ϵ_ϕ	Meridional strain	ϵ_ϕ
ϵ_θ	Circumferential strain	ϵ_θ

Appendix C

Material Properties for Mirror Materials

This appendix contains a table of properties for two types of materials.

- Candidates for membrane mirrors — Tables C.1 and C.2
- Standards of research in current plate- or shell-like mirrors — Tables C.3 and C.4

The superscripts refer to the following set of notes:

1. Data from Luz and Rice [52].
2. Lunar Projects office at NASA-GSFC (*snoopy.gsfc.nasa.gov/∼lunartel/lun7.html* on 25Jul00)
3. Used data from *http://www.brytetech.com/pdf-ds/EX-1515.pdf*, the supplier for the project of Note 2 above, with a volume fraction of 60%.
4. Information from *ngst.gsfc.nasa.gov*, the "NGST 'Yardstick' Mission," July 1999.
5. Information listed in Askeland [3].
6. Measured results from [68].
7. Data from Du Pont web site.
8. Data sheet from SRS technologies of Huntsville, AL.

Table C.1: Mechanical properties of candidate membrane mirror materials.

Property (Temperature is 298K unless specified)	Variable	(Units)	Polyimide, thick CP-1[8]	Polyimide, thin Kapton[6]
Elastic Modulus	E	(MPa)	2170	3740 [3000–4800][7] [2500–5500$(4K)$][9]
Yield Strength	σ_Y	(MPa)	100	340 [230$(4K)$][9]
Poisson's Ratio	ν	(1)		0.3
Thermal Expansion	α_T	$(\frac{1}{^\circ C})$	51×10^{-6}	$[20 \times 10^{-6}]$[7] [20–80$\times 10^{-6}(78K)$][9]
Density	ρ	$(\frac{kg}{m^3})$	1430	[1420][7]

Table C.2: Structural properties of candidate membrane mirror materials.

Property	Variable	(Units)	Hubble Space Telescope	Polyimide, thick CP-1[8]	Polyimide, thin Kapton[6]
Area Density	ρ^*	$(\frac{kg}{m^2})$	186	$\Rightarrow$0.14	$\Rightarrow$0.018
Fundamental Length	L	(m)	2.4	15	15
Thickness	h	(mm)	[20][14]	0.100	0.0125
Tensile Load	P	(N)	0	$[\Rightarrow 500d]^{12}$	$[\Rightarrow 156d]^{12}$
Pressure Load	f_z	(Pa)	0	$[\Rightarrow 13.3]^{12}$	$[\Rightarrow 4.17]^{12}$
Inertia/ Area[11]	$\frac{I_y}{A}$	(m^2)		$\Rightarrow 8.33 \times 10^{-10}$	$\Rightarrow 1.20 \times 10^{-11}$
			(grid,$\frac{1}{4}h^2$)	(solid,$\frac{1}{12}h^2$)	(solid,$\frac{1}{12}h^2$)
Bending Inertia	I_y	(m^4)		$\Rightarrow 8.33 \times 10^{-14}d$	$\Rightarrow 1.63 \times 10^{-16}d$
Sandwich Thickness	h	(m)		0	0
Frequency	f	(Hz)	[60][4]		
Cross-section Area	A	(m^2)			

Table C.3: Mechanical properties of standard mirror materials.

Property (Temperature is 298K unless specified)	Variable	(Units)	NGST class[10]	ULE face-sheet[1]	Beryllium	CFRP replica[2]
Elastic Modulus	E	(MPa)		67600	$[2.9 \times 10^5]^5$	$[1–2 \times 10^5]^3$
				$64000(73K)$		
Yield Strength	σ_Y	(MPa)		ult = 49.8	$[210–340]^5$	$[100–500]^3$
Poisson's Ratio	ν	(1)		0.17		
				$0.158(73K)$		
Thermal	α_T	$(\frac{1}{^\circ C})$		2.00×10^{-8}		
Expansion				$-2.7 \times 10^{-7}(198K)$		
Density	ρ	$(\frac{kg}{m^3})$		2210	1850^5	2040

Table C.4: Structural properties of standard mirror materials.

Property	Variable (Units)	Hubble Space Telescope	NGST class	ULE face-sheet[1]	Beryllium	CFRP replica[2]
Area Density	ρ^* $(\frac{kg}{m^2})$	186	20	25[14]		
Fundamental Length	L (m)	2.4	2.7	2.5	2	0.6
Thickness	h (mm)	[20][14]	[2][14]	3	2	1.6
Tensile Load	P (N)	0	0	0	0	0
Pressure Load	f_z (Pa)	0	0	0	0	0
Inertia/ Area[11]	$\frac{I_y}{A}$ (m^2)	(grid, $\frac{1}{4}h^2$)	$\Rightarrow 729$ (grid, $\frac{1}{4}h^2$)	$\Rightarrow 2500$ (grid, $\frac{1}{4}h^2$)	$\Rightarrow 400$ (grid, $\frac{1}{4}h^2$)	$\Rightarrow 2.13 \times 10^{-7}$ (solid, $\frac{1}{12}h^2$)
Bending Inertia	I_y (m^4)					
Sandwich Thickness	h (m)		$[\sim 20L]$[14]	$[\sim 40L]$[10]	$[\sim 20L]$[14]	0
Frequency	f (Hz)	[60][4]	[10][4]			
Cross-Section Area	A (m^2)					

9. Data faxed from Du Pont, listed as "Report No. YR-66-15".

10. Data from U of Arizona-Steward Lab web site document.

11. Approximations from standard standard steel I-beam tables with $\frac{I_y}{A} \approx 0.038m^2$, $0.029m^2$, $0.032m^2$, and other, smaller ratios. These should be at the low end when considering a modern aerospace structure.

12. These quantities are calculated from guidelines in de Blonk [17], $\bar{p} = \frac{pR_{out}}{\sigma_Y t} \approx 0.02$ and $\bar{N} = \frac{N}{\sigma_Y t} \approx 0.05$.

13. The numbers for Kapton presented in this document do not reflect the (sometimes conflicting) data presented in other references.

14. Approximation by author with supporting evidence from the literature.

Appendix D

Differential Geometry of Surface

Objective of Appendix:

To review the mathematical description of a surface with an emphasis on orthogonal coordinates.

The length of an arc ds on a two-dimensional surface is defined in the orthogonal curvilinear coordinate system by

$$\begin{aligned}(ds)^2 &= (g_{\phi\phi}d\phi)^2 + (g_{\theta\theta}d\theta)^2 \\ &= (r_\phi d\phi)^2 + (r_\theta \sin\phi d\theta)^2\end{aligned}$$

The coordinate system is aligned with the two directions of principal curvature. The surface is assumed to be smooth, with each pair of coordinates ϕ and θ uniquely representing a single point on the surface.

$g_{\alpha\beta}$ is the first fundamental form of the surface, or "metric tensor" and $b_{\alpha\beta}$ is the second fundamental form of the surface. An approximate description of the two tensors is that the metric tensor maps the slope and the second fundamental form maps the curvature. The metric tensor is used to raise and lower the indices of the other tensors and vectors.

The following list provides an overview of the differential geometry relevant to membrane shells.

- The reason for significant formalism with shell geometry is that the derivatives of the unit vectors are nonzero. Hence there is a "normal-looking" derivative of a quantity plus that quantity times a less familiar term. Chapter 2 of Novozhilov [67] explicitly provides derivatives for the curvilinear unit vectors.

  The Christoffel symbol $\Gamma^{\gamma}_{\alpha\beta}$ helps with curvilinear coordinates in that it specifies second derivatives in the direction of the surface coordinates. This direction of the surface coordinate (ϕ and θ for most shell models) is the reason for the third index in the symbol. Appendix B of Leonard [49] has a readable description. In the notation of Libai and Simmonds [50]

$$\bar{\mathbf{y}}_{,\alpha\beta} = \bar{\Gamma}^{\gamma}_{\alpha\beta}\bar{\mathbf{y}}_{,\gamma} + \bar{b}_{\alpha\beta}\bar{\mathbf{b}}$$

- *Parametric description of the surface:*

  Baker et al [5] provide a table on p.16 that defines the primary radii of curvature as $\{R_1, R_2\}$ (also $\{R_\phi, R_\theta\}$) according to angle-from-vertical ϕ and radius of curvature R_0 defined at $\phi = 0$.

$$\begin{aligned} R_\phi &= \frac{R_0}{\left(1+\gamma \sin^2\phi\right)^{\frac{3}{2}}} \\ R_\theta &= \frac{R_0}{\left(1+\gamma \sin^2\phi\right)^{\frac{1}{2}}} \end{aligned}$$

  For a paraboloid, the factor gamma $\gamma = -1$; for a spherical cap, $\gamma = 0$.

- *First Fundamental Form/ Metric Tensor:*

  The fundamental forms are described well in

  - Appendix B of Leonard [49].
  - Section 1.12.1.A of Baker et al. [5], though the authors do not pose it directly as a "metric tensor."
  - Section I.A.3 of [37], where a good lower-case/ upper-case notation is used for deformed/ undeformed configurations.
  - Section 3 of Appendix I in Malvern [55] for a thorough description of the metric tensor (derivation and discussion of use).

For the differential length ds along the surface and the position vector $\mathbf{r}$, the metric tensor g_{mn} is defined as

$$\begin{aligned}(ds)^2 &= d\mathbf{r} \cdot d\mathbf{r} \\ &= \frac{\partial \mathbf{r}}{\partial x^p} \cdot \frac{\partial \mathbf{r}}{\partial x^q} \\ &= g_{mn} dx^m dx^n\end{aligned}$$

and so

$$g_{pq} \equiv \frac{\partial \mathbf{r}}{\partial x^p} \cdot \frac{\partial \mathbf{r}}{\partial x^q}$$

In addition, the conjugate metric tensor g^{mn} is defined such that

$$g_{mn} g^{np} = \delta_m^p$$

Figures B.2 and B.3 in Appendix B of Leonard [49] show how the metric tensor is used to determine the physical components of vector $\mathbf{T}$ with covariant components T_i and contravariant components T^i. That is, the physical component of $\mathbf{T}$ in the 1-direction is

$$\begin{aligned}\sqrt{g_{11}} T^1 &= \sqrt{g^{11}} T_1 \\ &= \frac{T_1}{\sqrt{g_{11}}}\end{aligned}$$

The metric tensor is used to translate between covariant and contravariant components of vectors and tensors, i.e. to raise and lower indices.

$$\mathbf{n}_\alpha = g_{\alpha\beta} \mathbf{n}^\beta$$

Every derivative term is affected by the metric tensor (or, alternatively, each is affected by being a part of a curvilinear system). A familiar example of a derivative that requires a pre-multiplier is

$$\frac{\partial}{\partial x_\phi} = \frac{1}{r_\phi} \frac{\partial}{\partial \phi}$$

Similarly, implementation of the gradient operator requires usage of the metric tensor (where we find the r_ϕ-type terms).

A graphical interpretation of the metric tensor determinant $\sqrt{g_{\alpha\alpha}}$ is given in Fig B.2, with accompanying description in the text, on p.386 of Leonard [49].

- *Second Fundamental Form:*

  The fundamental forms are described well in Appendix B of Leonard [49]. The general idea is that the second derivative of the vector position of a point on the surface has three vector components. The dot product of the vector is taken with respect to the in-plane and normal vectors, respectively, to discriminate between components. The tensor coefficient of the normal vector is the second fundamental form, B_{ij} in Leonard [49] and $b_{\alpha\beta}$ in Libai and Simmonds [50].

  Notable, too, is the alternate definition for the second fundamental form $b_{\alpha\beta}$ and normal vector $\mathbf{b}$ in Libai and Simmonds, Eqn (F.27) on p.399:

$$\mathbf{y}_{,\alpha}\big|_\beta = b_{\alpha\beta}\mathbf{b}$$

  The relation between the curvature and the second fundamental form is explored in Leonard [49]. In Leonard [49] a pedantic explanation is given as to how the curvature has two extreme values. The way to evaluate the extreme values is to set the $d\phi$ and then $d\theta$ components equal to zero. Setting $d\theta = 0$, the remaining components are

$$\begin{aligned} \kappa_\phi &= \frac{B_{\phi\phi}(d\phi)^2}{G_{\phi\phi}(d\phi)^2} \\ \frac{1}{R_\phi} &= \frac{B_{\phi\phi}}{R_\phi^2} \\ \therefore B_{\phi\phi} &= R_\phi \end{aligned}$$

- *Examples of the first and second fundamental forms*

  Section 6.4.1 of Leonard [49] gives values for the fundamental forms $G_{\alpha\beta}$ and $B_{\alpha\beta}$ in

the orthogonal curvilinear system as

$$\begin{aligned} G_{\alpha\beta} &= \begin{bmatrix} A^2 & 0 \\ 0 & r^2 \end{bmatrix} \\ B_{\alpha\beta} &= \begin{bmatrix} \frac{A^2}{R_1} & 0 \\ 0 & \frac{r^2}{R_2} \end{bmatrix} \end{aligned}$$

For an aximembrane, the tensors become

$$\begin{aligned} G_{\alpha\beta} &= \begin{bmatrix} R_\phi^2 & 0 \\ 0 & R_\theta^2 \sin^2\phi \end{bmatrix} \\ B_{\alpha\beta} &= \begin{bmatrix} R_\phi & 0 \\ 0 & R_\theta \sin^2\phi \end{bmatrix} \end{aligned}$$

Appendix E

Derivation of EAMS Governing Equations

In this appendix the scalar equations of motion are derived for the Exact Axisymmetric Membrane Shell (EAMS) model presented in Chapter 3.

E.1 Original Equations

In the explanation of the models (Chapter 3), the following form was provided for geometrically-exact equilibrium equations for a general shell without moments, i.e. a "membrane shell." Eqn 3.10 is repeated here,

$$\frac{1}{\sqrt{g}}\left(\sqrt{g}\mathbf{n}^{\alpha}\right)_{,\alpha} + \mathbf{p} \;=\; 0 \tag{E.1}$$

for determinant g of the metric tensor $g^{\alpha\beta}$ of the deformed basis.

E.2 Component Equations

Many tedious steps are required to get to equations 3.11 and 3.12. First, the equations will be divided into the scalar components: one equation for the normal direction and two for the in-plane directions. The stress-resultant vector $\mathbf{n}^{\alpha}$ is rewritten as

$$\mathbf{n}^{\alpha} \;=\; n^{\alpha\beta}\mathbf{y}_{,\beta} \tag{E.2}$$

for unit vector in the β direction of the deformed basis $\mathbf{y}_{,\beta}$. The metric tensor is also related via $g_{\alpha\beta} = \mathbf{y}_{,\alpha} \cdot \mathbf{y}_{,\alpha}$. The pressure term $\mathbf{p}$ is broken into vector components by

$$\mathbf{p} \quad = \quad p^{\beta}\mathbf{y}_{,\beta} + p\mathbf{b} \tag{E.3}$$

for base vector in the normal direction $\mathbf{b}$. Note that the pressures are reckoned with respect to the deformed area. The first term of Equation E.1 is expanded to reveal

$$\frac{1}{\sqrt{g}}\left(\sqrt{g}n^{\alpha\beta}\right)_{,\alpha}\mathbf{y}_{,\beta} + n^{\alpha\beta}\left(\mathbf{y}_{,\beta}\right)_{,\alpha} + \mathbf{p} \quad = \quad 0 \tag{E.4}$$

From differential geometry the double-derivative of the unit vector is defined with the Christoffel symbol $\Gamma^{\gamma}_{\beta\alpha}$ according to

$$\left(\mathbf{y}_{,\beta}\right)_{,\alpha} = \Gamma^{\gamma}_{\beta\alpha}\mathbf{y}_{,\gamma} + b_{\alpha\beta}\mathbf{b} \tag{E.5}$$

Equation E.4 then becomes, with the use of Eqn E.3,

$$\frac{1}{\sqrt{g}}\left(\sqrt{g}n^{\alpha\beta}\right)_{,\alpha}\mathbf{y}_{,\beta} + n^{\alpha\beta}\left[\Gamma^{\gamma}_{\beta\alpha}\mathbf{y}_{,\gamma} + b_{\alpha\beta}\mathbf{b}\right] + p^{\beta}\mathbf{y}_{,\beta} + p\mathbf{b} \quad = \quad 0 \tag{E.6}$$

$$\left[\frac{1}{\sqrt{g}}\left(\sqrt{g}n^{\alpha\beta}\right)_{,\alpha} + n^{\alpha\gamma}\Gamma^{\beta}_{\gamma\alpha} + p^{\beta}\right]\mathbf{y}_{,\beta} + \left[n^{\alpha\beta}b_{\alpha\beta} + p\right]\mathbf{b} \quad = \quad 0 \tag{E.7}$$

The dot product of Equation E.7 is taken with the normal vector $\mathbf{b}$ to find the scalar equilibrium equation in the normal direction.

$$n^{\alpha\beta}b_{\alpha\beta} + p \quad = \quad 0 \tag{E.8}$$

Equation E.8 is a common form of the equilibrium equation as formulated through differential geometry; see section 8.1 of Leonard [49] as an example.

Similarly, the dot product with the unit vectors in the in-plane directions is used to find the two in-plane equilibrium equations.

$$\frac{1}{\sqrt{g}}\left(\sqrt{g}n^{\alpha\beta}\right)_{,\alpha} + n^{\alpha\gamma}\Gamma^{\beta}_{\gamma\alpha} + p^{\beta} \quad = \quad 0 \tag{E.9}$$

A proper application of symmetry conditions and coordinate frame transformations leads to Eqns 3.11 and 3.12.

Appendix F

Non-Dimensional Acceleration

A typical equilibrium equation for membranes is written in units of pressure. The dynamic inertia component in the normal component of the equilibrium equation is written as the area density ρ^* times the transverse acceleration $\ddot{w}$.

$$p + \cdots = \rho^* \ddot{w} \tag{F.1}$$

In applying the non-dimensional parameters used in this work for pressure, $p = \frac{Eh}{r_{out}}\bar{p}$, both terms are converted over to a non-dimensional form. A constant extensional stiffness is assumed, or $\frac{\partial Eh}{\partial r} = 0$.

$$\left(\frac{r_{out}}{Eh}\right) p + \cdots = \frac{r_{out}}{Eh}\rho^* \ddot{w} \tag{F.2}$$

$$\bar{p} + \cdots = \left(\frac{r_{out}}{Eh}\right)(\rho h)\,\ddot{w} \tag{F.3}$$

$$= \frac{r_{out}^2 \rho}{E}\frac{\partial^2}{\partial t^2}\left(\frac{w}{r_{out}}\right) \tag{F.4}$$

$$= \frac{r_{out}^2 \rho}{E}\frac{\partial^2}{\partial t^2}(\bar{w}) \tag{F.5}$$

With time non-dimensionalized by $\bar{t} = t\frac{1}{r_{out}}\sqrt{\frac{E}{\rho}}$, the equilibrium equation becomes

$$\bar{p} + \cdots = \frac{\partial^2 \bar{w}}{\partial \bar{t}^2} \tag{F.6}$$

Thus the non-dimensional pressure parameter $\bar{p} \equiv \frac{p r_{out}}{Eh}$ is observed to enter the equilibrium equation in the same manner as the non-dimensional acceleration term $\ddot{\bar{w}} \equiv \frac{r_{out}\rho \ddot{w}}{E}$.